



Measurement of the $t\bar{t}$ production cross-section and lepton differential distributions in $e\mu$ dilepton events from pp collisions at $\sqrt{s} = 13$ TeV with the ATLAS detector

ATLAS Collaboration*

CERN, 1211 Geneva 23, Switzerland

Received: 20 October 2019 / Accepted: 6 April 2020 / Published online: 12 June 2020
© CERN for the benefit of the ATLAS collaboration 2020

Abstract The inclusive top quark pair ($t\bar{t}$) production cross-section $\sigma_{t\bar{t}}$ has been measured in proton–proton collisions at $\sqrt{s} = 13$ TeV, using 36.1 fb^{-1} of data collected in 2015–2016 by the ATLAS experiment at the LHC. Using events with an opposite-charge $e\mu$ pair and b -tagged jets, the cross-section is measured to be:

$$\sigma_{t\bar{t}} = 826.4 \pm 3.6 (\text{stat}) \pm 11.5 (\text{syst}) \pm 15.7 (\text{lumi}) \pm 1.9 (\text{beam}) \text{ pb},$$

where the uncertainties reflect the limited size of the data sample, experimental and theoretical systematic effects, the integrated luminosity, and the LHC beam energy, giving a total uncertainty of 2.4%. The result is consistent with theoretical QCD calculations at next-to-next-to-leading order. It is used to determine the top quark pole mass via the dependence of the predicted cross-section on m_t^{pole} , giving $m_t^{\text{pole}} = 173.1^{+2.0}_{-2.1}$ GeV. It is also combined with measurements at $\sqrt{s} = 7$ TeV and $\sqrt{s} = 8$ TeV to derive ratios and double ratios of $t\bar{t}$ and Z cross-sections at different energies. The same event sample is used to measure absolute and normalised differential cross-sections as functions of single-lepton and dilepton kinematic variables, and the results are compared with predictions from various Monte Carlo event generators.

Contents

1	Introduction	1
2	Data and simulated event samples	3
3	Event reconstruction and selection	4
4	Cross-section measurement	5
4.1	Inclusive cross-sections	5
4.2	Differential cross-sections	6
4.3	Background estimates	10
4.4	Validation of the differential measurements	11
5	Systematic uncertainties	14

5.1	$t\bar{t}$ modelling	15
5.2	Lepton identification and measurement	16
5.3	Jet measurement and b -tagging	18
5.4	Background modelling	19
5.5	Luminosity and beam energy	19
6	Inclusive cross-section results and interpretation	19
6.1	Total and fiducial cross-section results	20
6.2	Extraction of the top quark pole mass	22
6.3	$t\bar{t}$ and $t\bar{t}/Z$ cross-section ratios at different energies	23
7	Differential cross-section results	26
7.1	Results for measured distributions	27
7.2	Comparison with event generator predictions	31
8	Conclusions	35
	Appendix	42
	References	54

1 Introduction

The study of top quark–antiquark ($t\bar{t}$) production forms a cornerstone of the physics programme of the ATLAS experiment at the CERN Large Hadron Collider (LHC), allowing quantum chromodynamics (QCD) to be probed at some of the highest accessible energy scales. The large mass of the top quark, close to the scale of electroweak symmetry breaking, gives it a unique role in the Standard Model of particle physics and potential extensions, and $t\bar{t}$ production also forms an important background in many searches for physics beyond the Standard Model. Precise measurements of absolute rates and differential distributions in $t\bar{t}$ production are therefore a vital tool in fully exploiting the discovery potential of the LHC.

Predictions for the inclusive $t\bar{t}$ production cross-section in proton–proton (pp) collisions, $\sigma_{t\bar{t}}$, are available at next-to-next-to-leading-order (NNLO) accuracy in the strong coupling constant α_s , including the resummation of next-to-next-to-leading logarithmic (NNLL) soft gluon terms [1–6], and are in excellent agreement with measurements from

* e-mail: atlas.publications@cern.ch

ATLAS and CMS at $\sqrt{s} = 7, 8$ and 13 TeV [7–13]. At $\sqrt{s} = 13$ TeV, and assuming a fixed top quark mass of $m_t = 172.5$ GeV, the NNLO+NNLL prediction is $832 \pm 35_{-29}^{+20}$ pb, as calculated using the $\text{TOP}++ 2.0$ program [14]. The first uncertainty corresponds to parton distribution function (PDF) and α_S uncertainties, and the second to QCD scale variations. The former were calculated using the PDF4LHC prescription [15] with the MSTW2008 [16, 17], CT10 NNLO [18, 19] and NNPDF2.3 5f FFN [20] PDF sets.¹ The latter was calculated from the envelope of predictions with the QCD renormalisation and factorisation scales varied independently up or down by a factor of two from their default values of $\mu_F = \mu_R = m_t$, whilst never letting them differ by more than a factor of two [21, 22]. The total uncertainty corresponds to a relative precision of $_{-5.5}^{+4.8}\%$.

The predicted cross-section also depends strongly on m_t , decreasing by 2.7% for a 1 GeV increase in the top mass. The top quark mass parameter used in the cross-section prediction is actually the pole mass m_t^{pole} , corresponding to the definition of the mass of a free particle. This allows $\sigma_{t\bar{t}}$ measurements to be interpreted as measurements of m_t^{pole} , free of the theoretical ambiguities linked to the direct reconstruction of m_t from the invariant mass of its decay products [23–26]. Ratios of $t\bar{t}$ production cross-sections at different centre-of-mass energies are also of interest, e.g. $R_{13/7}^{t\bar{t}} = \sigma_{t\bar{t}}(13 \text{ TeV})/\sigma_{t\bar{t}}(7 \text{ TeV})$. Predictions for such ratios benefit from significant cancellations in the QCD scale and top quark mass uncertainties, but are still sensitive to the choice of PDF. The NNLO+NNLL predictions with the same set of assumptions as given for $\sigma_{t\bar{t}}$ above, and a 1 GeV uncertainty in m_t , are $R_{13/7}^{t\bar{t}} = 4.69 \pm 0.16$ and $R_{13/8}^{t\bar{t}} = 3.28 \pm 0.08$, i.e. relative uncertainties of 3.3% and 2.5%. Double ratios of $t\bar{t}$ to Z production cross-sections allow the experimental uncertainties to be further reduced, by normalising the $t\bar{t}$ cross-section at each energy to the corresponding cross-section for Z boson production [27].

Within the Standard Model, the top quark decays 99.8% of the time to a W boson and b -quark [28], making the final-state topologies in $t\bar{t}$ production dependent on the decay modes of the W bosons. The channel with an electron–muon pair with opposite electric charges, i.e. $t\bar{t} \rightarrow W^+ b W^- \bar{b} \rightarrow e^+ \mu^- \nu \bar{\nu} b \bar{b}$, is particularly clean.² It was exploited to make the most precise ATLAS measurements of $\sigma_{t\bar{t}}$ at $\sqrt{s} = 7, 8$ and 13 TeV [7, 9], based on events with an opposite-sign $e\mu$

pair and one or two jets tagged as likely to contain b -hadrons (b -tagged). The $\sqrt{s} = 13$ TeV measurement in Ref. [9] was based on the 3.2 fb^{-1} dataset recorded in 2015. This paper describes a new measurement of $\sigma_{t\bar{t}}$ at $\sqrt{s} = 13$ TeV using the same final state, but applied to the combined 2015–2016 ATLAS dataset of 36.1 fb^{-1} . The cross-section measurement is further used to determine the top quark pole mass via the dependence of the prediction on m_t^{pole} , complementing the analogous measurement with the $\sqrt{s} = 7$ and 8 TeV data [7]. This paper also updates the $t\bar{t}$ cross-section ratios $R_{13/7}^{t\bar{t}}$ and $R_{13/8}^{t\bar{t}}$, the $\sqrt{s} = 13$ TeV $t\bar{t}/Z$ ratio $R_{13}^{t\bar{t}/Z}$, and the double ratios of $t\bar{t}$ to Z cross-sections $R_{13/7}^{t\bar{t}/Z}$ and $R_{13/8}^{t\bar{t}/Z}$, using the new $\sigma_{t\bar{t}}$ result, superseding those derived from the previous $\sqrt{s} = 13$ TeV $\sigma_{t\bar{t}}$ measurement in Ref. [27].

The $e\mu + b$ -tagged jets sample also allows precise measurements of the differential distributions of the leptons produced in $t\bar{t}$ events to be made. ATLAS has published [29] measurements at $\sqrt{s} = 8$ TeV of the absolute and normalised differential cross-sections as functions of the transverse momentum p_T^ℓ and absolute pseudorapidity $|\eta^\ell|$ of the single leptons³ (combined for electrons and muons), the p_T , invariant mass and absolute rapidity of the $e\mu$ system ($p_T^{e\mu}$, $m^{e\mu}$ and $|y^{e\mu}|$), the absolute azimuthal angle $|\Delta\phi|$ between the two leptons in the transverse plane ($\Delta\phi^{e\mu}$), and the scalar sums of the transverse momenta ($p_T^e + p_T^\mu$) and energies ($E^e + E^\mu$) of the two leptons. These distributions were found to be generally well described by predictions from a variety of leading-order (LO) multileg and next-to-leading-order (NLO) $t\bar{t}$ matrix-element event generators interfaced to parton showers, and by NLO fixed-order QCD calculations. The sensitivity of the data to the gluon PDF and to the top quark pole mass was also demonstrated. This paper measures the same distributions at $\sqrt{s} = 13$ TeV, using $t\bar{t}$ samples which are about six times the size of those available at $\sqrt{s} = 8$ TeV. Two-dimensional distributions of $|\eta^\ell|$, $|y^{e\mu}|$ and $\Delta\phi^{e\mu}$ as functions of $m^{e\mu}$ are also reported. The data are again compared with the predictions of various NLO $t\bar{t}$ matrix-element event generators, but the interpretations in terms of PDF constraints and m_t^{pole} are left for future work.

The event selection, measurement methodology and uncertainty evaluations for both the inclusive $t\bar{t}$ cross-section and the differential distributions are similar to those used at

¹ The NLO prescription from Ref. [15] was used, but applied to the specified NNLO PDF sets. The PDF uncertainty envelope was defined to cover the positive and negative 68% confidence level uncertainties of each considered PDF set, and the $\sigma_{t\bar{t}}$ central value was defined as the midpoint of the envelope. The recommended α_S value was used for each PDF set (0.1170 ± 0.0014 for MSTW2008 and 0.1180 ± 0.0012 for CT10 and NNPDF2.3) and the α_S variations were included in the envelope uncertainties.

² Charge-conjugate decay modes are implied unless otherwise stated.

³ ATLAS uses a right-handed coordinate system with its origin at the nominal interaction point in the centre of the detector, and the z axis along the beam line. Pseudorapidity is defined in terms of the polar angle θ as $\eta = -\ln \tan \theta/2$, and transverse momentum and energy are defined relative to the beam line as $p_T = p \sin \theta$ and $E_T = E \sin \theta$. The azimuthal angle around the beam line is denoted by ϕ , and distances in (η, ϕ) space by $\Delta R = \sqrt{(\Delta\eta)^2 + (\Delta\phi)^2}$. The rapidity is defined as $y = \frac{1}{2} \ln \left(\frac{E+p_z}{E-p_z} \right)$, where p_z is the z -component of the momentum and E is the energy of the relevant object or system. The distance in (y, ϕ) space is given by $\Delta R_y = \sqrt{(\Delta y)^2 + (\Delta\phi)^2}$.

$\sqrt{s} = 7$ and 8 TeV [7,29], with the exception that the minimum lepton transverse momentum requirement has been lowered from 25 to 20 GeV, whilst still requiring at least one lepton to be above the lepton trigger threshold of 21–27 GeV. This increases the fraction of $t\bar{t} \rightarrow e\mu\nu\bar{b}b$ events that are selected by 16%, thus reducing the extrapolation uncertainties in the modelling of $t\bar{t}$ production and decay. The data and Monte Carlo simulation samples used in the analyses are described in Sect. 2, followed by the event reconstruction and selection in Sect. 3. The measurement methodology for both the inclusive and differential cross-sections is described in Sect. 4, and the evaluation of systematic uncertainties in Sect. 5. The inclusive cross-section results are given in Sect. 6, together with the derivation of the top quark pole mass from $\sigma_{t\bar{t}}$, and the corresponding $t\bar{t}$ and $t\bar{t}/Z$ cross-section ratios. The differential cross-section results are discussed in Sect. 7, and compared with the predictions of several $t\bar{t}$ event generators. Finally, conclusions are discussed in Sect. 8.

2 Data and simulated event samples

The ATLAS detector [30–32] at the LHC covers nearly the entire solid angle around the collision point. It consists of an inner tracking detector surrounded by a thin superconducting solenoid producing a 2T axial magnetic field, electromagnetic and hadronic calorimeters, and an external muon spectrometer incorporating three large toroidal magnet assemblies. The analysis was performed on samples of proton–proton collision data collected at $\sqrt{s} = 13$ TeV in 2015 and 2016, corresponding to total integrated luminosities of 3.2fb^{-1} in 2015 and 32.9fb^{-1} in 2016 after data quality requirements. Events were required to pass a single-electron or single-muon trigger [33,34], with transverse momentum thresholds that were progressively raised during the data-taking as the instantaneous luminosity increased. The electron trigger was fully efficient for electrons with reconstructed $p_T > 25$ GeV in 2015 and the first 6fb^{-1} of 2016 data, and for $p_T > 27$ GeV for the remainder. The corresponding muon trigger thresholds were $p_T > 21$ GeV for 2015 data, $p_T > 25$ GeV for the first 6fb^{-1} of 2016 data and $p_T > 27$ GeV for the rest. Each triggered event also includes the signals from on average 14 (25) additional inelastic pp collisions in 2015 (2016) data, referred to as pileup.

Monte Carlo simulated event samples were used to develop the analysis procedures, to evaluate signal and background contributions, and to compare with data. Samples were processed using either the full ATLAS detector simulation [35] based on GEANT4 [36], or with a faster simulation making use of parameterised showers in the calorimeters [37]. The effects of pileup were simulated by generating additional inelastic pp collisions with PYTHIA8 (v8.186) [38] using the A2 set of parameter values (tune) [39] and overlay-

ing them on the primary simulated events. These combined events were then processed using the same reconstruction and analysis chain as the data. Small corrections were applied to lepton trigger and reconstruction efficiencies to improve agreement with the response observed in data.

The baseline simulated $t\bar{t}$ sample was produced using the NLO matrix-element event generator POWHEG-BOX v2 (referred to hereafter as POWHEG) [40–43] with the NNPDF3.0 NLO PDF set [44], interfaced to PYTHIA8 (v8.210) with the NNPDF2.3 LO PDF set and the A14 tune [45] for the parton shower, hadronisation and underlying-event modelling. In the POWHEG configuration, the h_{damp} parameter, which gives a cut-off scale for the first gluon emission, was set to $\frac{3}{2}m_t$, and the factorisation and renormalisation scales were set to $\mu_F = \mu_R = \sqrt{(m_t^2 + (p_{T,t})^2)}$, where the top quark p_T is evaluated before radiation [46].

Alternative $t\bar{t}$ simulation samples used to assess systematic uncertainties were generated with POWHEG interfaced to HERWIG7 (v7.0.4) [47] with the H7UE tune, and with the MADGRAPH5_AMC@NLO (v2.3.3.p1) generator (referred to hereafter as AMC@NLO) [48] with the NNPDF3.0 NLO PDF set, interfaced to PYTHIA8 with the A14 tune. In the AMC@NLO sample, the renormalisation and factorisation scales were set in the same way as for POWHEG, and the MC@NLO prescription [49] was used for matching the NLO matrix element to the parton shower. Uncertainties related to the amount of initial- and final-state radiation were explored using two alternative POWHEG + PYTHIA8 samples: one with h_{damp} set to $3m_t$, μ_F and μ_R reduced by a factor of two from their default values, and the A14v3cUp tune variation, giving more parton-shower radiation; and a second sample with $h_{\text{damp}} = \frac{3}{2}m_t$, μ_F and μ_R increased by a factor of two and the A14v3cDo tune variation, giving less parton-shower radiation. These parameter variations were chosen in order to reproduce differential cross-section and jet multiplicity distributions measured in $t\bar{t}$ events, as discussed in Ref. [46]. The top quark mass was set to 172.5 GeV in all these samples, consistent with measurements from ATLAS [50] and CMS [51]. The $W \rightarrow \ell\nu$ branching ratio was set to the Standard Model prediction of 0.1082 per lepton flavour [52], and the EVTGEN program [53] was used to handle the decays of b - and c -flavoured hadrons. All the samples were normalised using the NNLO+NNLL inclusive cross-section prediction discussed in Sect. 1 when comparing simulation with data. Additional $t\bar{t}$ samples with different event generator configurations were used in comparisons with the measured normalised differential cross-sections as discussed in Sect. 7.2.

Backgrounds in these measurements are classified into two types: those with two real prompt leptons (electrons or muons) from W or Z boson decays (including those produced by leptonic decays of τ -leptons), and those where at least one of the reconstructed leptons is misidentified, i.e.

a non-prompt lepton from the decay of a bottom or charm hadron, an electron from a photon conversion, a hadronic jet misidentified as an electron, or a muon produced from the decay in flight of a pion or kaon. The background with two real prompt leptons is dominated by the associated production of a W boson and single top quark, Wt . This process was simulated using POWHEG v1 [54] with the CT10 NLO PDF set [18], interfaced to PYTHIA6 (v6.428) [55] with the P2012 tune [56]. The ‘diagram removal’ scheme [57] was used to handle the interference between the $t\bar{t}$ and Wt final states that occurs at NLO. The sample was normalised to a cross-section of 71.7 ± 3.8 pb, based on the approximate NNLO calculation [58, 59] using the MSTW2008 NNLO PDF set [16, 17], and taking into account PDF and QCD scale uncertainties. Smaller backgrounds result from $Z \rightarrow \tau\tau (\rightarrow e\mu)$ +jets, and from diboson production (WW , WZ and ZZ) in association with jets. These backgrounds were modelled using SHERPA 2.2.1 [60] (Z +jets) and SHERPA 2.1.1 (dibosons), as discussed in Ref. [61]. Production of $t\bar{t}$ in association with a leptonically decaying W , Z or Higgs boson gives a negligible contribution to the opposite-sign $e\mu$ samples compared to inclusive $t\bar{t}$ production, but is significant in the same-sign control samples used to assess the background from misidentified leptons. These processes were simulated using AMC@NLO + PYTHIA8 ($t\bar{t} + W/Z$) or POWHEG + PYTHIA8 ($t\bar{t} + H$) [61].

Backgrounds with one real and one misidentified lepton arise from $t\bar{t}$ events with one leptonically decaying and one hadronically decaying W , including $W \rightarrow \tau\nu$ with a hadronic τ decay. These processes were simulated with POWHEG + PYTHIA8 in the same way as for dileptonic $t\bar{t}$. Similar backgrounds also arise from W +jets production, modelled with SHERPA 2.2.1 as for Z +jets; and t -channel single top quark production, modelled with POWHEG + PYTHIA6 [62] with the CT10 PDF set and P2012 tune. The contributions of these backgrounds to the opposite-sign samples were determined with the help of the same-sign control samples in data. Other backgrounds, including processes with two misidentified leptons, are negligible after the event selections used in the analysis.

3 Event reconstruction and selection

The analysis makes use of reconstructed electrons, muons and b -tagged jets. Electron candidates were reconstructed from a localised cluster of energy deposits in the electromagnetic calorimeter matched to a track in the inner detector, passing the ‘Tight’ likelihood-based requirement of Ref. [63]. They were required to have transverse energy $E_T > 20$ GeV and pseudorapidity $|\eta| < 2.47$, excluding the transition region between the barrel and endcap electromagnetic calorimeters, $1.37 < |\eta| < 1.52$. To ensure they originated

from the event primary vertex, electrons were required to satisfy requirements on the transverse impact parameter significance calculated relative to the beam line of $|d_0|/\sigma_{d_0} < 5$, and on the longitudinal impact parameter calculated relative to the event primary vertex of $|\Delta z_0 \sin \theta| < 0.5$ mm, where θ is the polar angle of the track. The event primary vertex was defined as the reconstructed vertex with the highest sum of p_T^2 of associated tracks. To reduce background from non-prompt electrons, candidates were further required to be isolated, using p_T - and $|\eta|$ -dependent requirements on the summed calorimeter energy within a cone of size $\Delta R = 0.2$ around the electron cluster, and on the sum of track p_T within a cone of variable size $\Delta R = \min(0.2, 10 \text{ GeV}/p_T(e))$ around the electron track direction. The selections were tuned to give a 90% efficiency for electrons of $p_T = 25$ GeV in simulated $Z \rightarrow ee$ events, rising to 99% at 60 GeV.

Muon candidates were reconstructed by combining matching tracks reconstructed in the inner detector and muon spectrometer, and were required to have $p_T > 20$ GeV, $|\eta| < 2.5$ and to satisfy the ‘Medium’ requirements of Ref. [64]. Muons were also required to be isolated using calorimeter and track information in the same way as it was used for electrons, except that the track-based isolation was calculated with a cone of size $\Delta R = \min(0.3, 10 \text{ GeV}/p_T(\mu))$. The selections were again tuned to give efficiencies varying from 90% at $p_T = 25$ GeV to 99% at 60 GeV on simulated $Z \rightarrow \mu\mu$ events. No requirements were made on the muon impact parameters relative to the primary vertex, as they do not provide any useful additional background rejection in this event topology.

Jets were reconstructed using the anti- k_r algorithm [65, 66] with radius parameter $R = 0.4$, starting from topological clusters in the calorimeters [67]. After calibration using information from both simulation and data [68], jets were required to have $p_T > 25$ GeV and $|\eta| < 2.5$, and jets with $p_T < 60$ GeV and $|\eta| < 2.4$ were subject to additional pileup rejection criteria using the multivariate jet-vertex tagger (JVT) [69]. To prevent double counting of electron energy deposits as jets, the closest jet to an electron candidate was removed if it was within $\Delta R_y = 0.2$ of the electron. Furthermore, to reduce the contribution of leptons from heavy-flavour hadron decays inside jets, leptons within $\Delta R_y = 0.4$ of selected jets were discarded, unless the lepton was a muon and the jet had fewer than three associated tracks, in which case the jet was discarded (thus avoiding an efficiency loss for high-energy muons undergoing significant energy loss in the calorimeters).

Jets likely to contain b -hadrons were b -tagged using the MV2c10 algorithm [70], a multivariate discriminant making use of track impact parameters and reconstructed secondary vertices. A tagging working point corresponding to 70% efficiency for tagging b -quark jets from top quark decays in simulated $t\bar{t}$ events was used, corresponding to rejection fac-

Table 1 Summary of the main object and event selection requirements

Object	Identification	Selection
Electrons	Tight likelihood	$E_T > 20$ GeV, $ \eta < 1.37$ or $1.52 < \eta < 2.47$, isolation
Muons	Medium	$p_T > 20$ GeV, $ \eta < 2.5$, isolation
Jets	Anti- k_r $R = 0.4$	$p_T > 25$ GeV, $ \eta < 2.5$, b -tagging with MV2c10 at 70% efficiency
Event		1 electron+1 muon with opposite sign, 1 or 2 b -tagged jets

tors (i.e. the inverse of the mistag rates) of about 400 against light-quark and gluon jets and 12 against jets originating from charm quarks.

Selected events were required to have exactly one electron and exactly one muon passing the requirements detailed above, with at least one of the leptons matched to a corresponding electron or muon trigger. Events where the electron and muon were separated in angle by $|\Delta\theta| < 0.15$ and $|\Delta\phi| < 0.15$, or where at least one jet with $p_T > 20$ GeV failed quality requirements [71], were rejected. Events with an opposite-sign $e\mu$ pair formed the main analysis sample, whilst events with a same-sign $e\mu$ pair were used in the estimation of background from misidentified leptons. Table 1 summarises the main selection requirements.

4 Cross-section measurement

The same technique, employing the subsets of the opposite-sign $e\mu$ sample with exactly one and exactly two b -tagged jets, was used to measure both the inclusive $t\bar{t}$ cross-section and the differential distributions. The measurements are introduced in the following two subsections, followed by a discussion of the background estimate in Sect. 4.3 and the validation of the differential measurements using studies based on simulation in Sect. 4.4.

4.1 Inclusive cross-sections

The inclusive $t\bar{t}$ cross-section $\sigma_{t\bar{t}}$ was determined by counting the numbers of opposite-sign $e\mu$ events with exactly one (N_1) and exactly two (N_2) b -tagged jets. The two event counts satisfy the tagging equations:

$$\begin{aligned}
 N_1 &= L\sigma_{t\bar{t}} \epsilon_{e\mu} 2\epsilon_b(1 - C_b\epsilon_b) + N_1^{\text{bkg}}, \\
 N_2 &= L\sigma_{t\bar{t}} \epsilon_{e\mu} C_b\epsilon_b^2 + N_2^{\text{bkg}}
 \end{aligned}
 \tag{1}$$

where L is the integrated luminosity of the sample, $\epsilon_{e\mu}$ the efficiency for a $t\bar{t}$ event to pass the opposite-sign $e\mu$ selection, and C_b is a tagging correlation coefficient close to unity. The combined probability for a jet from the quark q in the $t \rightarrow Wq$ decay to fall within the acceptance of the detector, be reconstructed as a jet with transverse momentum above the selection threshold, and be tagged as a b -jet, is denoted

by ϵ_b . If the decays of the two top quarks and the reconstruction of the two associated b -tagged jets are completely independent, the probability ϵ_{bb} to reconstruct and tag both b -jets is given by $\epsilon_{bb} = \epsilon_b^2$. In practice, small correlations are present, due to kinematic correlations between the b -jets from the two top quarks, or the production of extra $b\bar{b}$ or $c\bar{c}$ pairs in the $t\bar{t}$ events. These effects are taken into account via the correlation coefficient $C_b = \epsilon_{bb}/\epsilon_b^2$, or equivalently $C_b = 4N_{e\mu}^{t\bar{t}} N_2^{t\bar{t}} / (N_1^{t\bar{t}} + 2N_2^{t\bar{t}})^2$, where $N_{e\mu}^{t\bar{t}}$ is the number of selected $e\mu$ $t\bar{t}$ events and $N_1^{t\bar{t}}$ and $N_2^{t\bar{t}}$ are the numbers of such events with one and two b -tagged jets. In the baseline $t\bar{t}$ simulation sample, $\epsilon_{e\mu} \approx 0.9\%$, including the branching ratio for a $t\bar{t}$ pair to produce an $e\mu$ final state. The corresponding value of C_b is 1.007 ± 0.001 (the uncertainty coming from the limited size of the simulation sample), indicating a small positive correlation between the reconstruction and b -tagging of the two quarks produced in the top quark decays. Background from sources other than $t\bar{t}$ events with two prompt leptons also contributes to N_1 and N_2 and is given by the terms N_1^{bkg} and N_2^{bkg} , evaluated using a combination of simulation and data control samples as discussed in Sect. 4.3 below. The values of $\epsilon_{e\mu}$ and C_b were taken from $t\bar{t}$ event simulation, allowing the tagging equations (1) to be solved to determine $\sigma_{t\bar{t}}$ and ϵ_b .

The selection efficiency $\epsilon_{e\mu}$ can be written as the product of two terms: $\epsilon_{e\mu} = A_{e\mu} G_{e\mu}$. The acceptance $A_{e\mu} \approx 1.7\%$ represents the fraction of $t\bar{t}$ events which have a true opposite-sign $e\mu$ pair from $t \rightarrow W \rightarrow e/\mu$ decays, with each lepton having $p_T > 20$ GeV and $|\eta| < 2.5$. The contributions via leptonic τ decays ($t \rightarrow W \rightarrow \tau \rightarrow e/\mu$) are included. The lepton four-momenta were taken after final-state radiation, and ‘dressed’ by including the four-momenta of any photons within a cone of size $\Delta R = 0.1$ around the lepton direction, excluding photons produced from hadron decays or interactions with the detector material. The reconstruction efficiency $G_{e\mu}$ represents the probability that the two leptons are reconstructed and pass all the identification and isolation requirements. A fiducial cross-section $\sigma_{t\bar{t}}^{\text{fid}}$, for the production of $t\bar{t}$ events with an electron and a muon satisfying the requirements on p_T and η , can then be defined as $\sigma_{t\bar{t}}^{\text{fid}} = A_{e\mu} \sigma_{t\bar{t}}$, and measured by replacing $\sigma_{t\bar{t}} \epsilon_{e\mu}$ with $\sigma_{t\bar{t}}^{\text{fid}} G_{e\mu}$ in Eq. (1). The fiducial cross-section definition makes no requirements on the presence of jets, as the tag-

Table 2 Observed numbers of opposite-sign $e\mu$ events with one (N_1) and two (N_2) b -tagged jets in 2015 and 2016 data, together with the estimates of backgrounds and associated uncertainties described in Sect. 5. Uncertainties shown as zero are less than 0.5 events

Sample	2015		2016	
Event counts	N_1	N_2	N_1	N_2
Data	14239	8351	133977	75853
Wt single top	1329 ± 92	261 ± 86	12490 ± 870	2430 ± 810
$Z(\rightarrow \tau\tau \rightarrow e\mu) + \text{jets}$	123 ± 15	7 ± 2	910 ± 110	37 ± 9
Diboson	42 ± 5	1 ± 0	481 ± 58	21 ± 7
Misidentified leptons	164 ± 54	58 ± 37	1720 ± 520	670 ± 390
Total background	1660 ± 110	327 ± 94	15600 ± 1000	3160 ± 890

ging formalism of Eq. (1) allows the number of $t\bar{t}$ events with no reconstructed and b -tagged jets to be inferred from the event counts N_1 and N_2 . Measurement of the fiducial cross-section avoids the systematic uncertainties associated with the evaluation of the acceptance, in particular estimation of the fraction of $t\bar{t} \rightarrow e\mu\nu\bar{\nu}b\bar{b}$ events where at least one lepton has $p_T < 20$ GeV or $|\eta| > 2.5$.

A total of 40680 data events passed the opposite-sign $e\mu$ selection in the 2015 data sample, and 358664 events in the 2016 data sample. They were subdivided according to the number of b -tagged jets, irrespective of the number of untagged jets. The numbers of events with one and two b -tagged jets in each sample are shown in Table 2, together with the expected non- $t\bar{t}$ contributions from Wt and dibosons evaluated from simulation, and $Z(\rightarrow \tau\tau \rightarrow e\mu) + \text{jets}$ and misidentified leptons evaluated using both data and simulation. The one b -tag sample is expected to be about 88% pure and the two b -tag sample 96% pure in $t\bar{t}$ events, with the largest backgrounds in both samples coming from Wt production. The distribution of the number of b -tagged jets is shown for the 2015 and 2016 data samples together in Fig. 1a, and compared with the expectations from simulation, broken down into contributions from $t\bar{t}$ events (modelled using the baseline POWHEG + PYTHIA8 sample), and various background processes. The predictions using alternative $t\bar{t}$ generator configurations (POWHEG + PYTHIA8 with more or less parton-shower radiation, denoted by ‘RadUp’ and ‘RadDn’, and AMC@NLO + PYTHIA8) are also shown. All expected contributions are normalised to the integrated luminosity of the data sample using the cross-sections discussed in Sects. 1 and 2. The excess of data events over the prediction in the zero b -tagged jets sample (which is not used in the measurement) was also observed previously [7,9] and is compatible with the expected uncertainties in modelling diboson and $Z + \text{jets}$ production.

Figure 1b–f show distributions of the p_T of the b -tagged jets, and the p_T and $|\eta|$ of the electron and muon, in opposite-sign $e\mu$ events with at least one b -tagged jet, a sample which is dominated by $t\bar{t}$ events. The total simulation prediction is normalised to the same number of events as the data to facilitate shape comparisons. The $|\eta|$ distributions for elec-

trons and muons reflect the differences in acceptance and efficiency, in particular the reduction in electron acceptance across the calorimeter transition region, and the reduced acceptance for muons around $|\eta| \approx 0$. In general, the simulation predictions give a good description of the data, although the baseline POWHEG + PYTHIA8 simulation predicts a significantly harder lepton p_T distribution than seen in data.

The inclusive cross-section was determined separately from the 2015 and 2016 datasets, and the results were combined, taking into account correlations in the systematic uncertainties. As the systematic uncertainties are much larger than the statistical uncertainties, and not fully correlated between the two samples (true in particular for the uncertainty in the integrated luminosity), this procedure gives a smaller overall uncertainty than treating the 2015–2016 data as a single sample. The selection efficiency $\epsilon_{e\mu}$ is about 10% lower in the 2016 data compared to the 2015 data, due to the harsher pileup conditions and higher- p_T trigger thresholds.

4.2 Differential cross-sections

The differential cross-sections as functions of the lepton and dilepton variables defined in Sect. 1 were measured using an extension of Eq. (1), by counting the number of leptons or events with one (N_1^i) or two (N_2^i) b -tagged jets where the lepton(s) falls in bin i of a differential distribution at reconstruction level. For the single-lepton distributions p_T^ℓ and $|\eta|^\ell$, there are two counts per event, in the two bins corresponding to the electron and muon. For the dilepton distributions, each event contributes a single count corresponding to the bin in which the appropriate dilepton variable falls. For each bin of each differential distribution, these counts satisfy the tagging equations:

$$\begin{aligned} N_1^i &= L\sigma_{t\bar{t}}^i G_{e\mu}^i 2\epsilon_b^i (1 - C_b^i \epsilon_b^i) + N_1^{i,\text{bkg}}, \\ N_2^i &= L\sigma_{t\bar{t}}^i G_{e\mu}^i C_b^i (\epsilon_b^i)^2 + N_2^{i,\text{bkg}}, \end{aligned} \quad (2)$$

where $\sigma_{t\bar{t}}^i$ is the absolute fiducial differential cross-section in bin i . The reconstruction efficiency $G_{e\mu}^i$ represents the ratio of the number of reconstructed $e\mu$ events (or leptons for p_T^ℓ and $|\eta|^\ell$) in bin i defined using the reconstructed lepton(s),

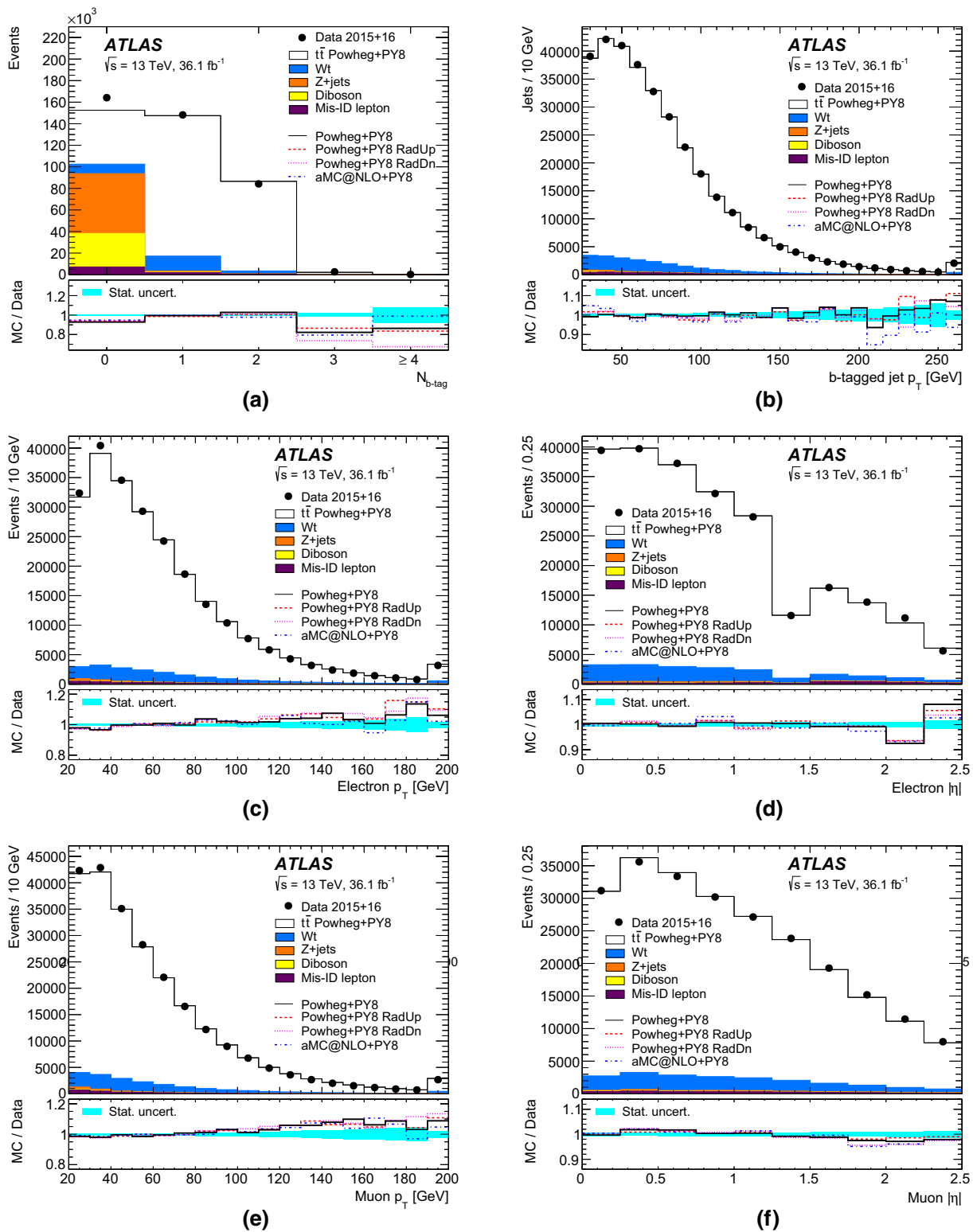


Fig. 1 Distributions of **a** the number of b -tagged jets in selected opposite-sign $e\mu$ events; and **b** the p_T of b -tagged jets, **c** the p_T of the electron, **d** the $|\eta|$ of the electron, **e** the p_T of the muon and **f** the $|\eta|$ of the muon, in events with an opposite-sign $e\mu$ pair and at least one b -tagged jet. The reconstruction-level data are compared with the expectation from simulation, broken down into contributions from $t\bar{t}$ (POWHEG + PYTHIA8), Wt , Z+jets, dibosons, and events with misiden-

tified electrons or muons. The simulation prediction is normalised to the same integrated luminosity as the data in **a** and to the same number of entries as the data in **b**–**f**. The lower parts of the figure show the ratios of simulation to data, using various $t\bar{t}$ signal samples and with the cyan shaded band indicating the statistical uncertainty. The last bin includes the overflow in panels **b**, **c** and **e**

to the number of true $e\mu$ events (or leptons) in the same bin i at particle level, evaluated using $t\bar{t}$ simulation. The true electron and muon were required to have $p_T > 20$ GeV and $|\eta| < 2.5$, but no requirements were made on reconstructed or particle-level jets. The efficiency $G_{e\mu}^i$ corrects for both the lepton reconstruction efficiency and the effects of event migration, where events in bin j at particle level appear in a different bin $i \neq j$ at reconstruction level. The integral of any dilepton differential cross-section is equal to the fiducial cross-section $\sigma_{t\bar{t}}^{\text{fid}}$ defined in Sect. 4.1, and the integrals of the single-lepton p_T^ℓ and $|\eta^\ell|$ distributions are equal to $2\sigma_{t\bar{t}}^{\text{fid}}$. The correlation coefficient C_b^i depends on the event counts in bin i analogously to the inclusive C_b appearing in Eq. (1). The values of $G_{e\mu}^i$ were taken from $t\bar{t}$ simulation, and are generally around 0.5–0.6. The corresponding values of C_b^i are always within 1–2% of unity, even at the edges of the differential distribution. The background term $N_1^{i,\text{bkg}}$ varies from 11% to 23% of the total event count N_1^i in each bin, and $N_2^{i,\text{bkg}}$ varies from 3% to 14% of N_2^i . They were determined from simulation and data control samples, allowing the tagging equations (2) to be solved to give the absolute fiducial differential cross-sections $\sigma_{t\bar{t}}^i$ and associated ϵ_b^i values for each bin i of each differential distribution.

The bin ranges for each differential distribution were based on those used at $\sqrt{s} = 8$ TeV [29], adding an additional bin for 20–25 GeV in the p_T^ℓ distribution and extending the lowest bin down to 40 GeV for $p_T^e + p_T^\mu$ and $E^e + E^\mu$ to accommodate the reduced minimum lepton p_T requirement of 20 GeV. The number and sizes of bins were chosen according to the experimental resolution in order to keep the bin purities (i.e. the fractions of events reconstructed in bin i that originate from bin i at particle level) above about 0.9, and to keep a maximum of around ten bins for the angular distributions ($|\eta^\ell|$, $|y^{e\mu}|$ and $\Delta\phi^{e\mu}$). The variations in the angular distributions predicted by different $t\bar{t}$ models do not motivate a finer binning, even though the experimental resolution would allow it. The chosen bin ranges can be seen in Tables 15, 16, 17, 18 in the Appendix. The last bin of the p_T^ℓ , $p_T^{e\mu}$, $m^{e\mu}$, $p_T^e + p_T^\mu$ and $E^e + E^\mu$ distributions includes overflow events falling above the last bin boundary.

The normalised fiducial differential cross-sections $\zeta_{t\bar{t}}^i$ were calculated from the absolute cross-sections $\sigma_{t\bar{t}}^i$ as follows:

$$\zeta_{t\bar{t}}^i = \frac{\sigma_{t\bar{t}}^i}{\sum_j \sigma_{t\bar{t}}^j} = \frac{\sigma_{t\bar{t}}^i}{\sigma_{t\bar{t}}^{\text{fid}}}, \quad (3)$$

where $\sigma_{t\bar{t}}^{\text{fid}}$ is the cross-section summed over all bins of the fiducial region, equal to the fiducial cross-section defined in Sect. 4.1, or twice that in the case of the single-lepton distributions. The $\zeta_{t\bar{t}}^i$ values were then divided by the bin widths W_i , to produce the cross-sections differential in the

variable x ($x = p_T^\ell$, $|\eta^\ell|$, etc.):

$$\frac{1}{\sigma} \left(\frac{d\sigma}{dx} \right)_i = \frac{\zeta_{t\bar{t}}^i}{W_i}. \quad (4)$$

The normalised differential cross-sections are correlated between bins because of the normalisation condition in Eq. (3). The absolute dilepton differential cross-sections are not statistically correlated between bins, but kinematic correlations between the electron and muon within one event introduce small correlations within the absolute single-lepton p_T^ℓ and $|\eta^\ell|$ distributions.

The larger number of selected $t\bar{t}$ events compared to the $\sqrt{s} = 8$ TeV analysis allows double-differential cross-sections to be measured, i.e. distributions that are functions of two variables. Three such distributions were measured, with $|\eta^\ell|$, $|y^{e\mu}|$ or $\Delta\phi^{e\mu}$ as the first variable, and $m^{e\mu}$ as the second variable, effectively measuring the $|\eta^\ell|$, $|y^{e\mu}|$ and $\Delta\phi^{e\mu}$ distributions in four bins of $m^{e\mu}$, chosen to be $m^{e\mu} < 80$ GeV, $80 < m^{e\mu} < 120$ GeV, $120 < m^{e\mu} < 200$ GeV and $m^{e\mu} > 200$ GeV. The excellent resolution in $|\eta^\ell|$, $|y^{e\mu}|$ and $\Delta\phi^{e\mu}$ results in migration effects being significant only between $m^{e\mu}$ bins. The formalism of Eq. (2) was used, with the index i running over the two-dimensional grid of bins in both variables. The normalised double-differential cross-sections were calculated with the sum in the denominator of Eq. (3) running over all bins, making the integral of the normalised double-differential cross-section equal to unity over the entire fiducial region, rather than normalising e.g. the $|\eta^\ell|$ distribution to unity in each $m^{e\mu}$ bin separately.

The measured differential cross-sections include contributions where one or both leptons are produced via leptonic decays of τ -leptons ($t \rightarrow W \rightarrow \tau \rightarrow e/\mu$). To enable comparisons with theoretical predictions which only include direct $t \rightarrow W \rightarrow e/\mu$ decays, a second set of cross-section results was derived with a bin-by-bin multiplicative correction $f_{\text{no-}\tau}^i$ to remove the τ contributions:

$$\sigma_{t\bar{t}}^i(\text{no-}\tau) = f_{\text{no-}\tau}^i \sigma_{t\bar{t}}^i, \quad (5)$$

and similarly for the normalised cross-sections $\zeta_{t\bar{t}}^i(\text{no-}\tau)$. The corrections $f_{\text{no-}\tau}^i$ were evaluated from the baseline POWHEG + PYTHIA8 $t\bar{t}$ simulation as the fractions of leptons or events in each particle-level bin which do not involve τ -lepton decays. They are typically in the range 0.8–0.9, the smaller values occurring in bins with a large contribution of low- p_T leptons where the τ contributions are largest.

Since the uncertainties in most of the differential cross-section bins are dominated by the data statistical uncertainties, and the luminosity uncertainty largely cancels out in the normalised differential cross-sections, the 2015–2016 data were treated as a single sample in the differential analysis. The varying lepton trigger thresholds and offline identification efficiencies were taken into account by calculating $G_{e\mu}^i$

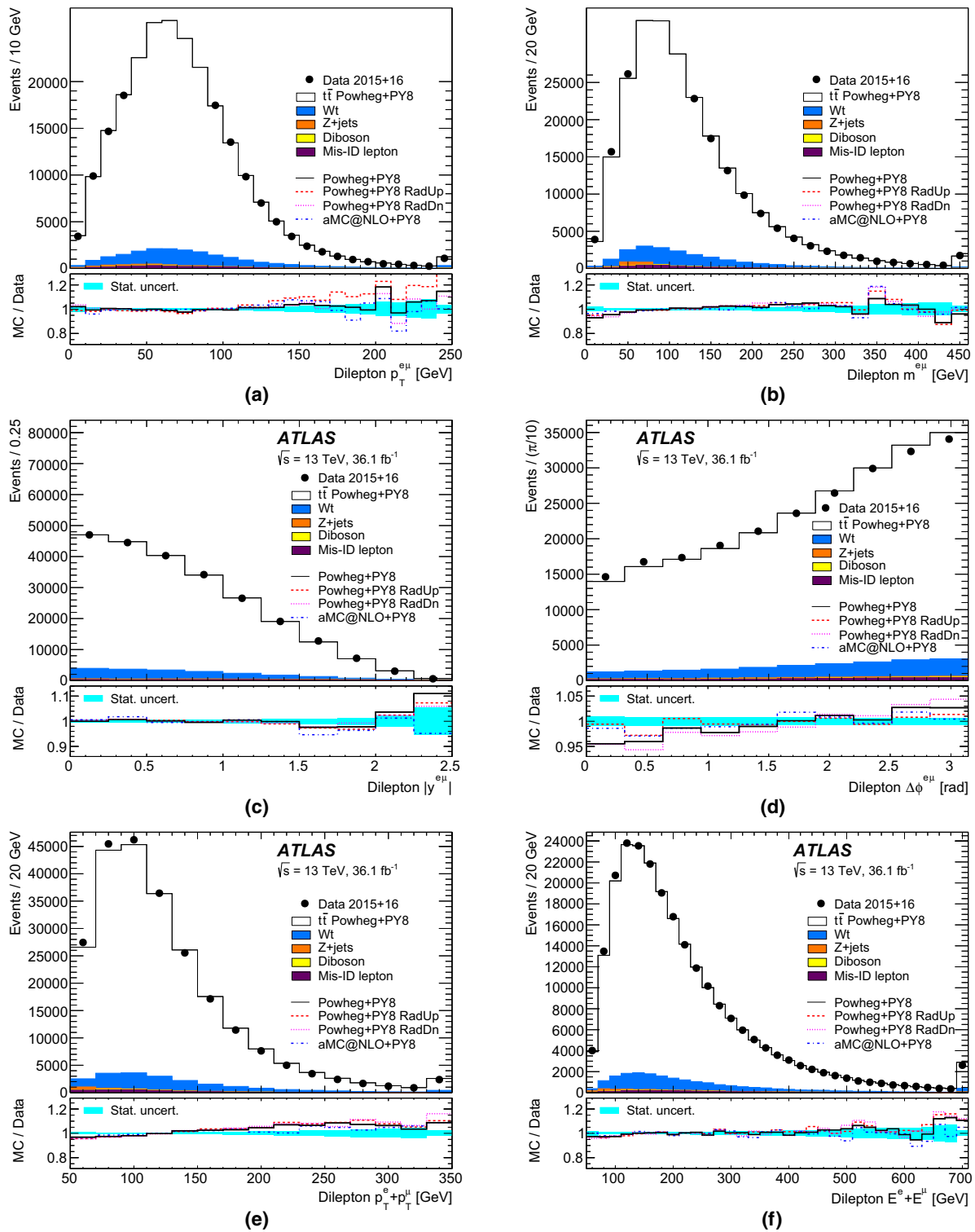


Fig. 2 Distributions of **a** the dilepton $p_T^{e\mu}$, **b** invariant mass $m^{e\mu}$, **c** rapidity $|y^{e\mu}|$, **d** azimuthal angle difference $\Delta\phi^{e\mu}$, **e** lepton p_T sum $p_T^e + p_T^\mu$ and **f** lepton energy sum $E^e + E^\mu$, in events with an opposite-sign $e\mu$ pair and at least one b -tagged jet. The reconstruction-level data are compared with the expectation from simulation, broken down into contributions from $t\bar{t}$ (POWHEG + PYTHIA8), Wt , Z+jets, dibosons,

and events with misidentified electrons or muons, normalised to the same number of entries as the data. The lower parts of the figure show the ratios of simulation to data, using various $t\bar{t}$ signal samples and with the cyan shaded band indicating the statistical uncertainty. The last bin includes the overflow in panels **a**, **b**, **e** and **f**

from an appropriately weighted mixture of simulated events. Figure 2 shows the reconstructed dilepton distributions for events with at least one b -tagged jet, comparing data with predictions using various $t\bar{t}$ generator configurations. As in Figure 1b–f, the predictions generally describe the data well, although in some regions there are significant differences between the data and all predictions, which are discussed further in Sect. 7.2 below.

4.3 Background estimates

The dominant background from Wt production, and the smaller contribution from diboson events (dominated by WW production) were evaluated from simulation, using the samples detailed in Sect. 2. The production of a Z boson accompanied by heavy-flavour jets is subject to large theoretical uncertainties, so the background contributions in the one and two b -tag samples predicted by SHERPA (normalised to the inclusive Z cross-section predictions from FEWZ [72]) were further scaled by factors of 1.10 ± 0.12 (one b -tag) and 1.20 ± 0.12 (two b -tags) obtained from data. These scale factors were derived from the ratio of data to simulation event yields for $Z \rightarrow ee/\mu\mu$ accompanied by one or by two b -tagged jets. The $Z \rightarrow ee/\mu\mu$ yields were obtained by requiring two opposite-sign electrons or muons passing the selections detailed in Sect. 3, and performing a template fit to the dilepton invariant mass distribution in the range $30 < m_{\ell\ell} < 150$ GeV in order to subtract the contributions from $t\bar{t}$ events and misidentified leptons. The uncertainties are dominated by variations in the scale factors as functions of Z boson p_T . Further uncertainties of 5% in the one b -tag sample and 23% in the two b -tag sample were assigned from the change in the final background prediction when replacing the SHERPA sample with one generated using MADGRAPH [73] interfaced to PYTHIA8, including re-evaluation of the scale factors. Similar procedures were used to evaluate the uncertainty in the Z +jets background prediction in every bin of the differential distributions, including a comparison of the per-bin predictions from SHERPA and MADGRAPH after normalising each sample to data in the inclusive $Z \rightarrow ee/\mu\mu$ control regions.

The background from events with one real and one misidentified lepton was evaluated with the help of the same-sign $e\mu$ control sample. For the inclusive cross-section analysis, the contributions $N_j^{\text{mis-id}}$ to the total numbers N_j of opposite-sign $e\mu$ events with $j = 1, 2$ b -tagged jets are given by:

$$N_j^{\text{mis-id}} = R_j \left(N_j^{\text{data,SS}} - N_j^{\text{sim,prompt,SS}} \right),$$

$$R_j = \frac{N_j^{\text{sim,mis-id,OS}}}{N_j^{\text{sim,mis-id,SS}}}, \quad (6)$$

where $N_j^{\text{data,SS}}$ is the number of observed same-sign events, $N_j^{\text{sim,prompt,SS}}$ is the number of same-sign events with two prompt leptons estimated from simulation, and R_j is the ratio in simulation of the number of opposite-sign ($N_j^{\text{sim,mis-id,OS}}$) to same-sign ($N_j^{\text{sim,mis-id,SS}}$) events with misidentified leptons, all with j b -tagged jets. This formalism relies on simulation to predict the ratio of opposite- to same-sign misidentified-lepton events, and the prompt same-sign contribution, but not the absolute number of misidentified-lepton events $N_j^{\text{mis-id}}$, which is calculated using the same-sign event counts in data. The same formalism in bins i of lepton differential variables was used to estimate the misidentified-lepton background contributions to $N_1^{i,\text{bkg}}$ and $N_2^{i,\text{bkg}}$ in each bin of the differential cross-section analysis.

Table 3 shows the estimates from simulation of misidentified-lepton contributions to the opposite- and same-sign event counts in the inclusive cross-section analysis, separately for the 2015 and 2016 selections. The prompt contributions (corresponding to $N_j^{\text{sim,prompt,SS}}$ in Eq. (6)) are about 25% of the one b -tag and 35% of the two b -tag same-sign samples. They include ‘wrong-sign’ contributions, dominated by dilepton $t\bar{t}$ events where the electron charge sign has been misidentified, and ‘right-sign’ contributions, with two genuine same-sign prompt leptons, from $t\bar{t} + V$ events ($V = W, Z$ or H), WZ, ZZ or same-sign WW production. The misidentified-lepton contributions are dominated by electrons from photon conversions, shown separately for events where the photon was radiated from a prompt electron in a $t\bar{t}$ dilepton event, or came from some other background source. These contributions are followed by electrons or muons from the semileptonic decays of heavy-flavour hadrons (e.g. b -hadrons produced from the top quark decays, or charm hadrons produced from hadronic W decays in single-lepton $t\bar{t}$ events), and other sources, such as misidentified hadrons or decays in flight of pions and kaons. Within each category and b -jet multiplicity, the numbers of opposite- and same-sign events are comparable, but with up to a factor two more opposite- than same-sign events in the major categories, and larger variations for the small contributions labelled ‘Other’. The reasons for this behaviour are complex, depending e.g. on details of the electron reconstruction, or on charge correlations between the decay products of the two top quarks.

The composition of the same-sign samples is also illustrated in Fig. 3, which shows electron and muon p_T and $|\eta|$ distributions in same-sign data events with at least one b -tagged jet, and the corresponding simulation predictions, broken down into prompt leptons (combining the right- and wrong-sign categories of Table 3) and various misidentified-lepton categories (again combining ‘other’ electrons and muons into a single category). Table 3 shows that the simulation reproduces the observed numbers of same-sign events

Table 3 Breakdown of estimated misidentified-lepton contributions in simulation to the one (1*b*) and two (2*b*) *b*-tag opposite- and same-sign (OS and SS) $e\mu$ event samples from 2015 and 2016 separately. The various misidentified-lepton categories are described in Sect. 4.3, and the contributions labelled ‘Other’ include all sources other than photon conversions and heavy-flavour decays. For the same-sign samples, the

estimated contributions of wrong-sign (where the electron charge sign is misidentified) and right-sign prompt lepton events are also shown, and the total expectations are compared with the data. The uncertainties are due to the limited size of the simulated samples, and values or uncertainties shown as zero are less than 0.5 events

Component	2015				2016			
	OS 1 <i>b</i>	SS 1 <i>b</i>	OS 2 <i>b</i>	SS 2 <i>b</i>	OS 1 <i>b</i>	SS 1 <i>b</i>	OS 2 <i>b</i>	SS 2 <i>b</i>
$t \rightarrow e \rightarrow \gamma$ conversion e	59 ± 5	41 ± 4	33 ± 3	21 ± 3	594 ± 15	360 ± 11	336 ± 11	191 ± 9
Background conversion e	53 ± 6	35 ± 4	19 ± 3	15 ± 2	424 ± 15	227 ± 36	185 ± 8	116 ± 6
Heavy-flavour e	27 ± 3	26 ± 3	3 ± 1	2 ± 1	208 ± 8	188 ± 8	20 ± 3	11 ± 2
Other e	2 ± 2	0 ± 0	1 ± 1	0 ± 0	48 ± 9	5 ± 1	19 ± 3	2 ± 1
Heavy-flavour μ	50 ± 5	46 ± 5	8 ± 2	2 ± 1	434 ± 14	335 ± 12	79 ± 6	27 ± 4
Other μ	11 ± 2	2 ± 1	4 ± 1	0 ± 0	54 ± 29	151 ± 126	46 ± 4	11 ± 2
Total misidentified	201 ± 10	149 ± 8	69 ± 5	40 ± 4	1761 ± 41	1266 ± 132	684 ± 16	358 ± 12
Wrong-sign prompt	–	24 ± 3	–	12 ± 2	–	224 ± 9	–	113 ± 6
Right-sign prompt	–	21 ± 1	–	9 ± 0	–	195 ± 4	–	88 ± 1
Total	–	194 ± 9	–	61 ± 4	–	1685 ± 132	–	560 ± 13
Data	–	167	–	55	–	1655	–	551

well, and the distributions shown in Fig. 3 demonstrate that it also reproduces the general features of the lepton kinematic distributions, the largest differences in individual bins being around 20%. These studies validate the overall modelling of misidentified leptons by the simulation, even though the background estimates determined via Eq. (6) do not rely on the simulation providing an accurate estimate of the absolute rates of such events. Additional studies were performed using same-sign control samples with relaxed electron or muon isolation criteria (increasing the relative contribution of heavy-flavour decays), and changing the lepton selection to $p_T > 40$ GeV (enhancing the fraction of photon conversions), and a similar level of agreement was seen both in rates and distribution shapes.

The ratios R_j in Eq. (6) were evaluated to be $R_1 = 1.4 \pm 0.3$ and $R_2 = 1.7 \pm 0.9$ for the 2015 data sample, and $R_1 = 1.4 \pm 0.4$ and $R_2 = 1.9 \pm 1.0$ for the 2016 sample. The uncertainties encompass the range of R_j values seen for the major sources of misidentified-lepton events; as can be seen from the entries in Table 3, the opposite- to same-sign event count ratios are different for the main categories, and the uncertainty allows for their relative contributions to be different from that predicted by the baseline simulation. The R_j values seen in the control samples with loosened isolation, and the predictions from alternative $t\bar{t}$ simulation samples using PYTHIA6 or HERWIG7 instead of PYTHIA8 hadronisation were also considered. A conservative 50% uncertainty in the prompt lepton same-sign contribution was also taken into account, covering the mismodelling of electron charge misidentification in simulation and the uncertainties in the

predicted cross-sections for $t\bar{t} + V$ and diboson processes. The final misidentified-lepton background estimates for the 2015 and 2016 opposite-sign data samples in the inclusive cross-section analysis are shown in Table 2.

Figure 4 shows the corresponding same-sign event distributions for the dilepton variables, showing a similar quality of modelling of these kinematic distributions by the simulation as seen for the single-lepton variables in Fig. 3. The R_1^i and R_2^i values in the binned version of Eq. (6) do not vary in simulation beyond the uncertainties assigned above to the inclusive R_1 and R_2 , so the same relative uncertainties in R_1 and R_2 were also used for the differential analysis, and taken to be correlated across all bins.

In the opposite-sign sample, the total non- $t\bar{t}$ background fraction from all sources varies significantly as a function of some of the differential variables, but remains dominated by Wt events in all bins. It reaches around 20% in the one *b*-tag sample and 10% of the two *b*-tag sample at the high ends of the single-lepton p_T^ℓ and dilepton $p_T^{e\mu}$ distributions, but varies little with lepton $|\eta^\ell|$.

4.4 Validation of the differential measurements

A set of tests using pseudo-experiment datasets generated from simulation were used to validate the analysis procedures for the differential measurements, as documented in detail for the $\sqrt{s} = 8$ TeV analysis [29]. These tests demonstrated that the method is unbiased and correctly estimates the statistical uncertainties in each bin of each distribution. Figure 5 shows examples for the p_T^ℓ , $p_T^{e\mu}$, $|\eta^\ell|$ and $|y^{e\mu}|$ distributions. The

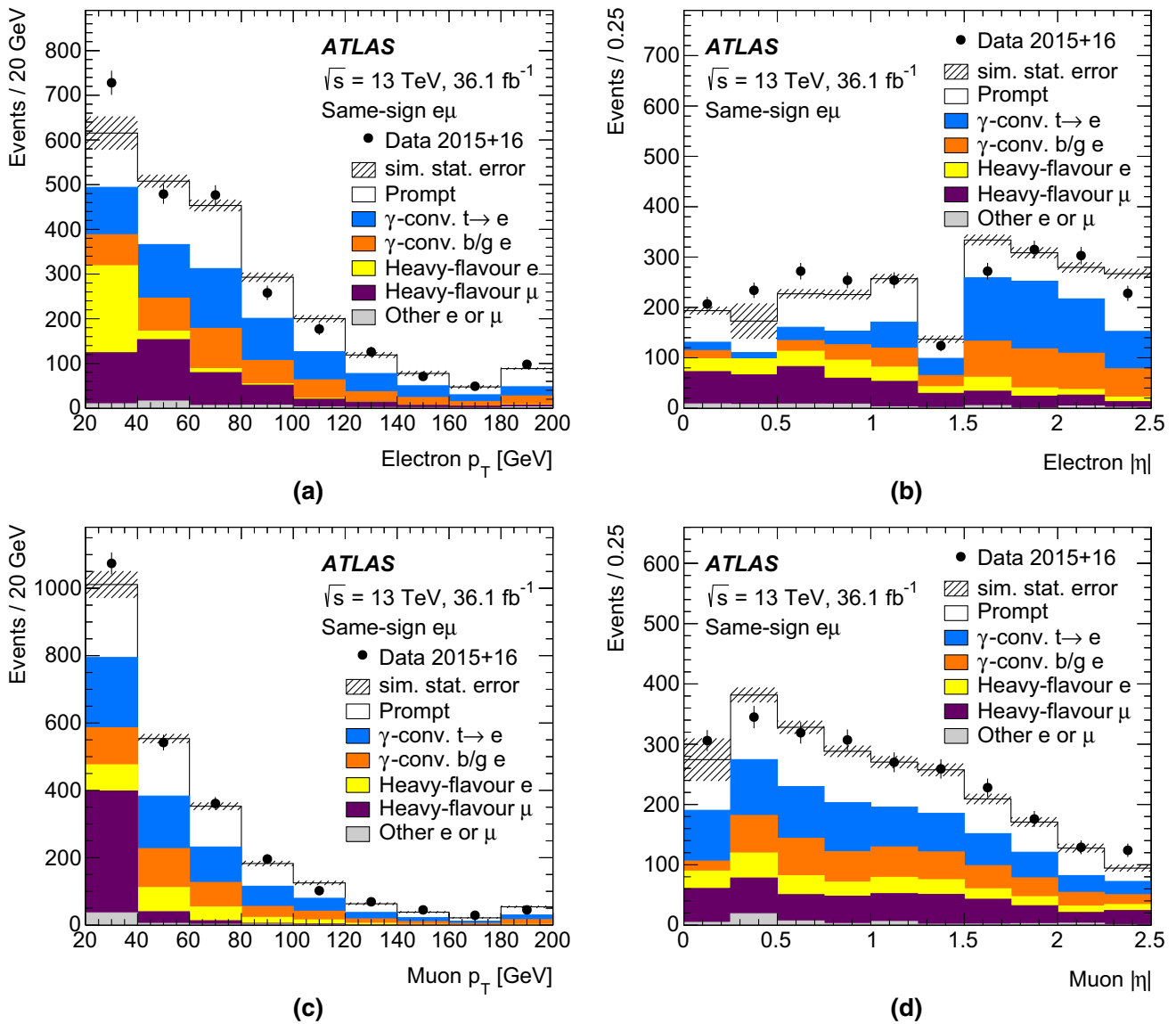


Fig. 3 Distributions of **a** the electron p_T , **b** the electron $|\eta|$, **c** the muon p_T and **d** the muon $|\eta|$, in events with a same-sign $e\mu$ pair and at least one b -tagged jet. The simulation prediction is normalised to the same integrated luminosity as the data, and broken down into contributions where both leptons are prompt, or one is a misidentified lepton from

a photon conversion originating from a top quark decay or from background, from heavy-flavour decay or from other sources. The statistical uncertainty in the total simulation prediction is significant in some bins, and is shown by the hatching. In the p_T distributions, the last bin includes the overflows

filled black points show the relative differences between the mean normalised differential cross-sections obtained from 1000 pseudo-experiments and the true cross-sections in each bin, divided by the true cross-sections to give fractional differences. The pseudo-experiments were generated from a reference $t\bar{t}$ sample, and the reference sample was also used to determine the values of $G_{e\mu}^i$ and C_b^i in each bin i of the distributions. The compatibility of the filled black points with zero within the statistical uncertainty of the reference sample confirms that the method is unbiased for this sample. The open red points and dotted lines show the mean pseudo-experiment results and true values for an alternative sample with different

underlying distributions, again expressed as fractional deviations from the true cross-sections in the reference sample, and obtained using $G_{e\mu}^i$ and C_b^i values from the reference sample. The alternative samples were chosen in order to produce a large variation in the distribution under test. An independent $t\bar{t}$ simulation sample with $m_t = 175$ GeV was used for the p_T^ℓ and $p_T^{e\mu}$ distributions, and the baseline $t\bar{t}$ sample generated with NNPDF3.0 was reweighted to the predictions of the CT14 PDF set [74] for $|\eta^\ell|$ and $|y^{e\mu}|$. In all cases, the results are consistent with the true values within the statistical uncertainties of the alternative samples, demonstrating that the simple bin-by-bin correction procedure correctly recov-

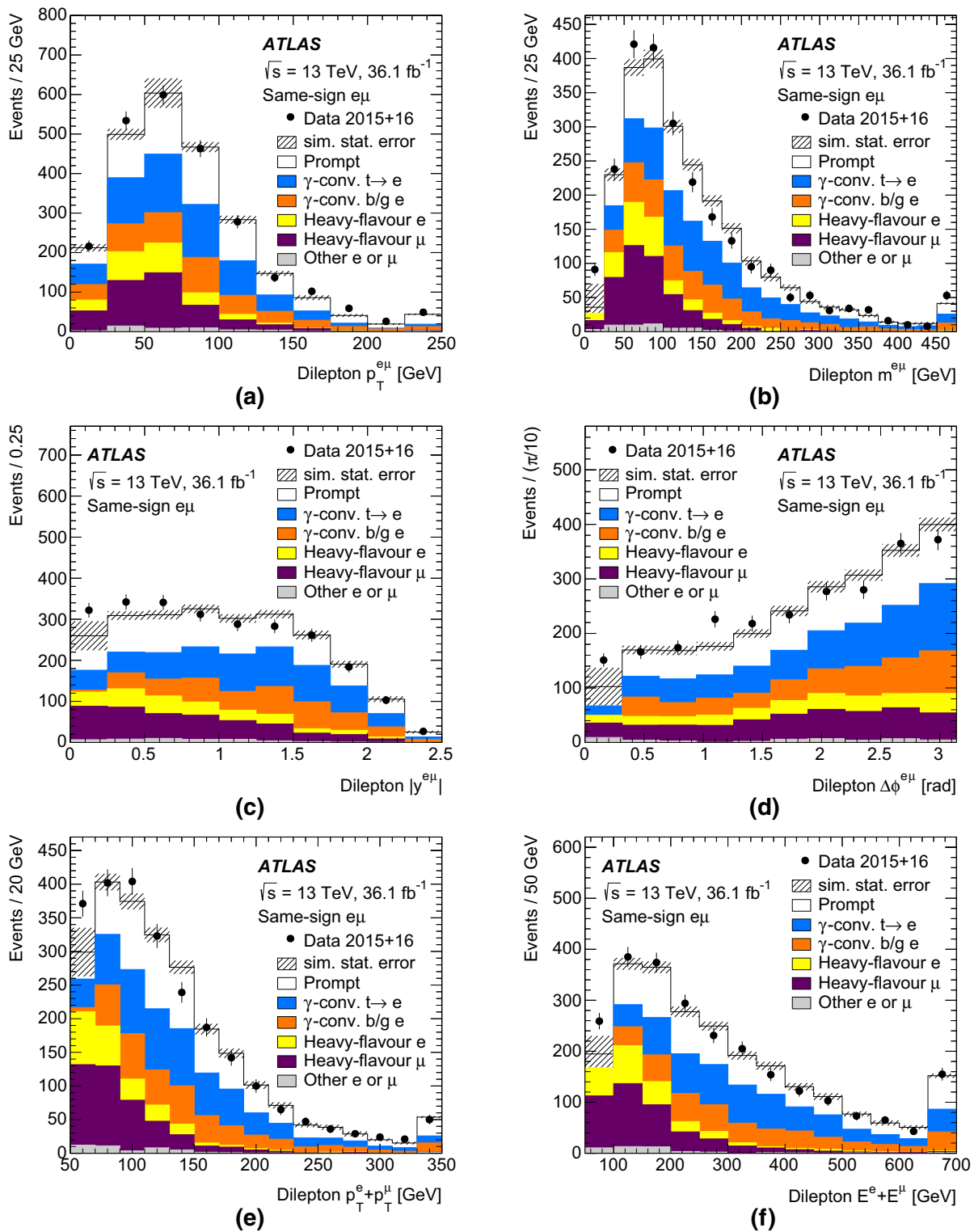


Fig. 4 Distributions of **a** the dilepton $p_T^{e\mu}$, **b** invariant mass $m^{e\mu}$, **c** rapidity $|y^{e\mu}|$, **d** azimuthal angle difference $\Delta\phi^{e\mu}$, **e** lepton p_T sum $p_T^e + p_T^\mu$ and **f** lepton energy sum $E^e + E^\mu$, in events with a same-sign $e\mu$ pair and at least one b -tagged jet. The simulation prediction is normalised to the same integrated luminosity as the data, and broken down into contributions where both leptons are prompt, or one is

a misidentified lepton from a photon conversion originating from a top quark decay or from background, from heavy-flavour decay or from other sources. The statistical uncertainty in the total simulation prediction is significant in some bins, and is shown by the hatching. In the $p_T^{e\mu}$, $m^{e\mu}$, $p_T^e + p_T^\mu$ and $E^e + E^\mu$ distributions, the last bin includes the overflows

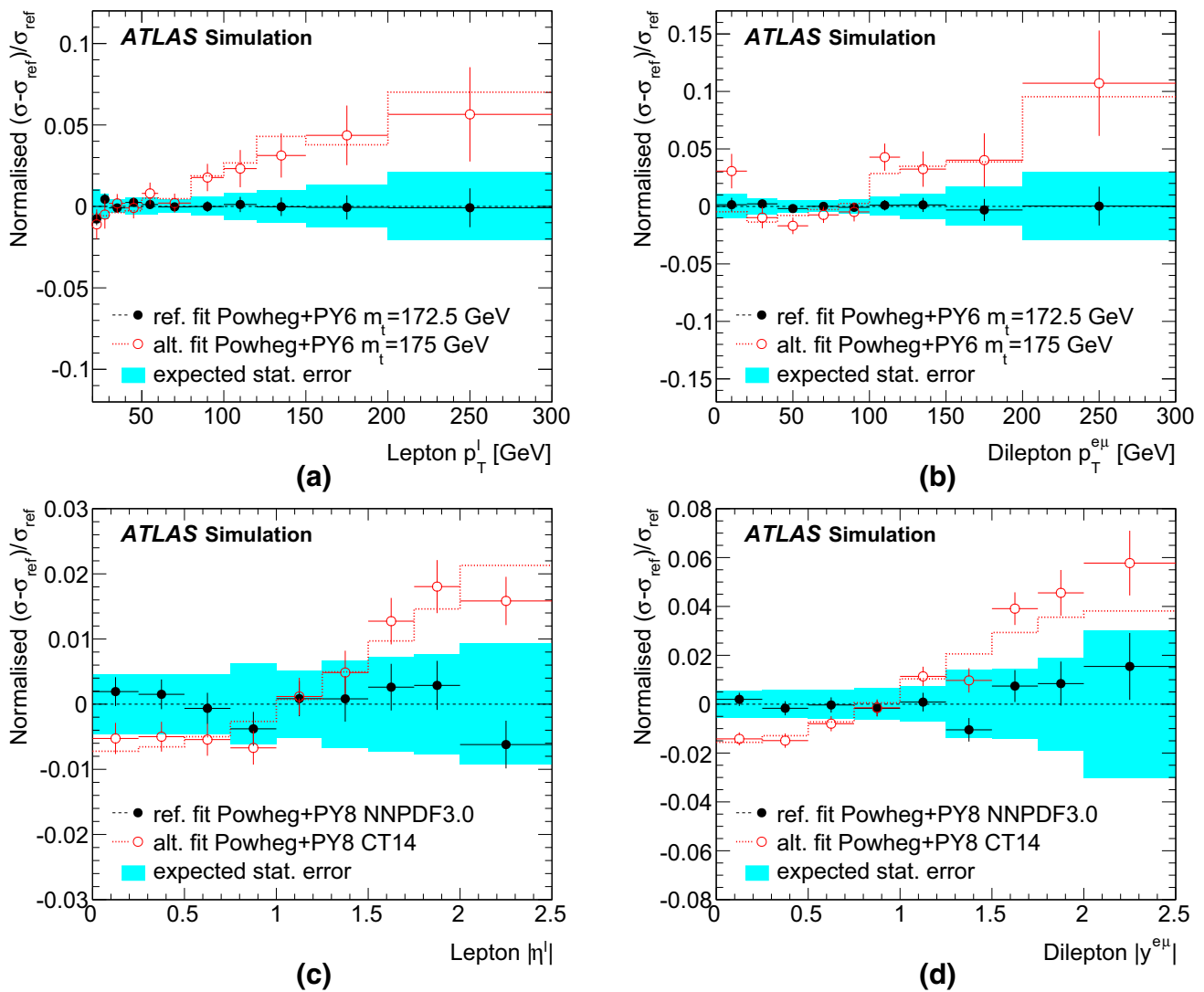


Fig. 5 Results of pseudo-experiment studies on simulated events for the extraction of the normalised differential cross-section distributions for **a** p_T^l , **b** $p_T^{e\mu}$, **c** $|\eta^l|$ and **d** $|y^{e\mu}|$, shown as relative deviations $(\sigma - \sigma_{\text{ref}})/\sigma_{\text{ref}}$ from the reference cross-section values in the POWHEG + PYTHIA6 CT10 (**a, b**) or POWHEG + PYTHIA8 NNPDF3.0 (**c, d**) samples with $m_t = 172.5$ GeV. The black filled points show the mean deviations from the reference values of the results from pseudo-data samples generated with the reference simulation sample, with error bars indicating the uncertainties due to the limited number of simulated events.

ers the alternative distributions, without the need for iteration or a matrix-based unfolding technique. Similar results were obtained for the analogous validation tests performed on the double-differential cross-section measurements. The various distributions shown in Fig. 5 also illustrate the sensitivity of the normalised differential cross-sections to m_t and different PDF sets.

The cyan shaded bands indicate the expected statistical uncertainties for a single sample corresponding to the data integrated luminosity. The open red points show the mean deviations from the reference values obtained from pseudo-experiments generated from an alternative simulation sample with $m_t = 175$ GeV (**a, b**) or by reweighting the baseline sample to the CT14 PDF (**c, d**). The red error bars represent the uncertainty due to the limited size of these alternative samples, and the red dotted lines show the true deviations from the reference in the alternative samples

5 Systematic uncertainties

Systematic uncertainties in the measured inclusive cross-section arise from uncertainties in the input quantities $\epsilon_{e\mu}$, C_b , N_1^{bkg} , N_2^{bkg} and L appearing in Eq. (1), and the corresponding quantities in Eq. (2) for the differential cross-sections. Each source of systematic uncertainty was evaluated by changing all relevant input quantities coherently and re-solving the tagging equations, thus taking into account systematic correlations between the different inputs (and

Table 4 Breakdown of the relative systematic uncertainties in $\epsilon_{e\mu}$, $G_{e\mu}$ and C_b , and the statistical, systematic (excluding luminosity and beam energy) and total uncertainties in the inclusive and fiducial $t\bar{t}$ cross-section measurements. The five groups of systematic uncertainties corresponding to the discussion in Sects. 5.1 to 5.5 are indicated in the leftmost column

	Uncertainty source	$\Delta\epsilon_{e\mu}/\epsilon_{e\mu}$ (%)	$\Delta G_{e\mu}/G_{e\mu}$ (%)	$\Delta C_b/C_b$ (%)	$\Delta\sigma_{t\bar{t}}/\sigma_{t\bar{t}}$ (%)	$\Delta\sigma_{t\bar{t}}^{\text{fid}}/\sigma_{t\bar{t}}^{\text{fid}}$ (%)
	Data statistics				0.44	0.44
$t\bar{t}$ mod.	$t\bar{t}$ generator	0.38	0.05	0.05	0.43	0.10
	$t\bar{t}$ hadronisation	0.24	0.42	0.25	0.49	0.67
	Initial/final-state radiation	0.30	0.26	0.16	0.45	0.41
	$t\bar{t}$ heavy-flavour production	0.01	0.01	0.26	0.26	0.26
	Parton distribution functions	0.44	0.05	–	0.45	0.07
	Simulation statistics	0.22	0.15	0.17	0.22	0.18
Lept.	Electron energy scale	0.06	0.06	–	0.06	0.06
	Electron energy resolution	0.01	0.01	–	0.01	0.01
	Electron identification	0.34	0.34	–	0.37	0.37
	Electron charge mis-id	0.09	0.09	–	0.10	0.10
	Electron isolation	0.22	0.22	–	0.24	0.24
	Muon momentum scale	0.03	0.03	–	0.03	0.03
	Muon momentum resolution	0.01	0.01	–	0.01	0.01
	Muon identification	0.28	0.28	–	0.30	0.30
	Muon isolation	0.16	0.16	–	0.18	0.18
	Lepton trigger	0.13	0.13	–	0.14	0.14
Jet/b	Jet energy scale	0.02	0.02	0.06	0.03	0.03
	Jet energy resolution	0.01	0.01	0.04	0.01	0.01
	Pileup jet veto	–	–	–	0.02	0.02
	b -tagging efficiency	–	–	0.04	0.20	0.20
	b -tag mistagging	–	–	0.06	0.06	0.06
Bkg.	Single-top cross-section	–	–	–	0.52	0.52
	Single-top/ $t\bar{t}$ interference	–	–	–	0.15	0.15
	Single-top modelling	–	–	–	0.34	0.34
	Z+jets extrapolation	–	–	–	0.09	0.09
	Diboson cross-sections	–	–	–	0.02	0.02
	Diboson modelling	–	–	–	0.03	0.03
	Misidentified leptons	–	–	–	0.43	0.43
	Analysis systematics	0.91	0.75	0.44	1.39	1.31
L/E_b	Integrated luminosity	–	–	–	1.90	1.90
	Beam energy	–	–	–	0.23	0.23
	Total uncertainty	0.91	0.75	0.44	2.40	2.36

between different bins in the differential analysis). The sources of systematic uncertainty are divided into the five groups discussed below, and are shown in detail for the inclusive and fiducial $t\bar{t}$ cross-sections in Table 4. The uncertainties are shown in groups for each bin of the single- and double-differential cross-sections in Tables 15, 16, 17, 18, 19, 20, 21, 22, 23, 24, and the uncertainties for the normalised single-differential cross-sections are also shown in Fig. 6.

5.1 $t\bar{t}$ modelling

The uncertainties in $\epsilon_{e\mu}$, $G_{e\mu}$, $G_{e\mu}^i$, C_b and C_b^i (and $f_{\text{no-}\tau}^i$ for the τ -corrected cross-sections) were evaluated using the alternative $t\bar{t}$ samples described in Sect. 2. The $t\bar{t}$ generator uncertainty was determined by comparing the baseline POWHEG + PYTHIA8 sample with AMC@NLO + PYTHIA8. The parton shower, hadronisation and underlying event uncertainty (referred to as ‘hadronisation’ below) was evaluated by comparing the baseline with POWHEG + HER-

WIG7. The initial/final-state radiation uncertainty was evaluated as half the difference between the POWHEG + PYTHIA8 model variations with more or less parton-shower radiation; as discussed in Sect. 2, these samples also include variations of μ_F and μ_R . As shown in Table 4, the $t\bar{t}$ generator uncertainty is larger for $\epsilon_{e\mu}$ than for $G_{e\mu}$, as the POWHEG + PYTHIA8 and AMC@NLO + PYTHIA8 samples predict different particle-level acceptances $A_{e\mu}$. In contrast, the differences in $A_{e\mu}$ and $G_{e\mu}$ for the $t\bar{t}$ hadronisation uncertainty have opposite signs, leading to a smaller shift in $\epsilon_{e\mu}$ than in $G_{e\mu}$. In the differential analyses, the bin-by-bin shifts in $G_{e\mu}^i$ and C_b^i were fitted with polynomial functions to reduce statistical fluctuations. All these comparisons were carried out without applying the lepton isolation requirements, as the isolation efficiencies were measured in situ in data as discussed in Sect. 5.2, and the simulation was only used to predict the lepton reconstruction, identification and overlap removal uncertainties. This procedure also reduces the sensitivity to the modelling of hadronisation, the underlying event and colour reconnection.

The values of C_b and C_b^i are sensitive to the fraction of $t\bar{t}$ events with extra $b\bar{b}$ or $c\bar{c}$ pairs. Such $t\bar{t}$ plus heavy-flavour production gives rise to events with three or more b -tagged jets; as can be seen from Fig. 1a and also measured in a dedicated analysis [75], this rate is underestimated by the available $t\bar{t}$ models that only produce extra $b\bar{b}$ or $c\bar{c}$ pairs through the parton shower. The potential effect on C_b was studied by reweighting the baseline POWHEG + PYTHIA8 $t\bar{t}$ sample so as to increase the fraction of events with at least three b -jets at generator level by 40%, an enhancement which reproduces both the rate of events with three b -tags and the p_T and η distributions of the third highest- p_T b -tagged jet in these events. The resulting shifts in C_b and C_b^i were assigned as additional systematic uncertainties due to the modelling of heavy-flavour production in $t\bar{t}$ events.

Parton distribution function uncertainties were evaluated by reweighting the baseline POWHEG + PYTHIA8 $t\bar{t}$ sample using generator weights associated with each of the 100 variations (replicas) provided by the NNPDF3.0 authors [44], and calculating the RMS of the changes induced in $\epsilon_{e\mu}$, $G_{e\mu}$ and $G_{e\mu}^i$. The resulting uncertainties are 0.45% in $\sigma_{t\bar{t}}$, but less than 0.1% in $\sigma_{t\bar{t}}^{\text{fid}}$, as variations of the PDF mainly affect the acceptance rather than the reconstruction efficiency. Similar uncertainties were found for the PDF4LHC15_NLO_30 meta-PDF [76], which is based on a Monte Carlo combination of the NNPDF3.0, CT14 [74] and MMHT14 [77] PDF sets. The central values from all these PDF sets lie within the uncertainty band obtained from NNPDF3.0.

The prediction for $\epsilon_{e\mu}$ is also sensitive to the assumed value of the top quark mass, as a heavier top quark increases the average lepton p_T and makes their $|\eta|$ slightly more central. This effect was evaluated using $t\bar{t}$ simulation samples

with m_t variations from 170 to 177.5 GeV, giving a relative change in $\epsilon_{e\mu}$ of 0.3% for a 1 GeV change in m_t . The effect is partially counterbalanced by changes in the Wt background prediction, which decreases with increasing m_t . By convention, the inclusive $t\bar{t}$ cross-section $\sigma_{t\bar{t}}$ is quoted at a fixed top quark mass value, but a ± 1 GeV variation in m_t is included in the uncertainties for the lepton differential distributions.

The total $t\bar{t}$ modelling uncertainties also include the small contributions due to the limited size of the baseline $t\bar{t}$ simulation sample, and are shown for the differential distributions by the green dotted lines in Fig. 6.

5.2 Lepton identification and measurement

The modelling of the electron and muon identification efficiencies was studied using $Z \rightarrow ee/\mu\mu$ events, as described in Refs. [63,64]. Small corrections were applied to the simulation, and the correlations in the associated systematic uncertainties as a function of lepton p_T and η were taken into account and propagated to all differential distributions. Similar procedures were used to measure the electron and muon trigger efficiencies with $Z \rightarrow ee/\mu\mu$ decays. Since only one lepton was required to pass the trigger requirements in order to accept the event, the trigger efficiencies for events passing the offline selection are high, around 97% for 2015 data and 94% for 2016 data. Most of the efficiency loss comes from events where one lepton has a transverse momentum below the trigger threshold and the other lepton is above the threshold but fails the trigger selection. The electron charge misidentification probability was measured as a function of p_T and $|\eta|$ using the ratio of same- to opposite-sign reconstructed $Z \rightarrow ee$ events, and the full difference between data and simulation, which is only significant for forward electrons with $|\eta| > 1.5$, was assigned as an uncertainty. The electron and muon energy/momentum scales and resolutions were determined using $Z \rightarrow ee/\mu\mu$, $Z \rightarrow \ell\ell\gamma$, $J/\psi \rightarrow ee/\mu\mu$ and $\Upsilon \rightarrow \mu\mu$ decays [64,78], and the residual uncertainties are typically much smaller than those associated with the lepton efficiency measurements.

The lepton isolation efficiencies were measured directly in the $t\bar{t}$ -dominated $e\mu$ plus b -tagged jet samples, by determining the fractions of events where either the electron or muon fails the isolation cut, as functions of lepton p_T and separately for the barrel ($|\eta| < 1.5$) and forward regions. The samples of leptons failing isolation cuts have significant contamination from misidentified leptons, reaching up to 10% in the $e\mu$ plus two b -tagged jet sample at low lepton p_T , and up to 50% in the one b -tagged jet sample, but in both cases decreasing strongly with increasing lepton p_T . The results were corrected for this contamination, estimated from data with the aid of leptons with large impact parameter significance ($|d_0|/\sigma_{d_0} > 5$), that provide a control sample enriched in misidentified leptons. Templates for the impact

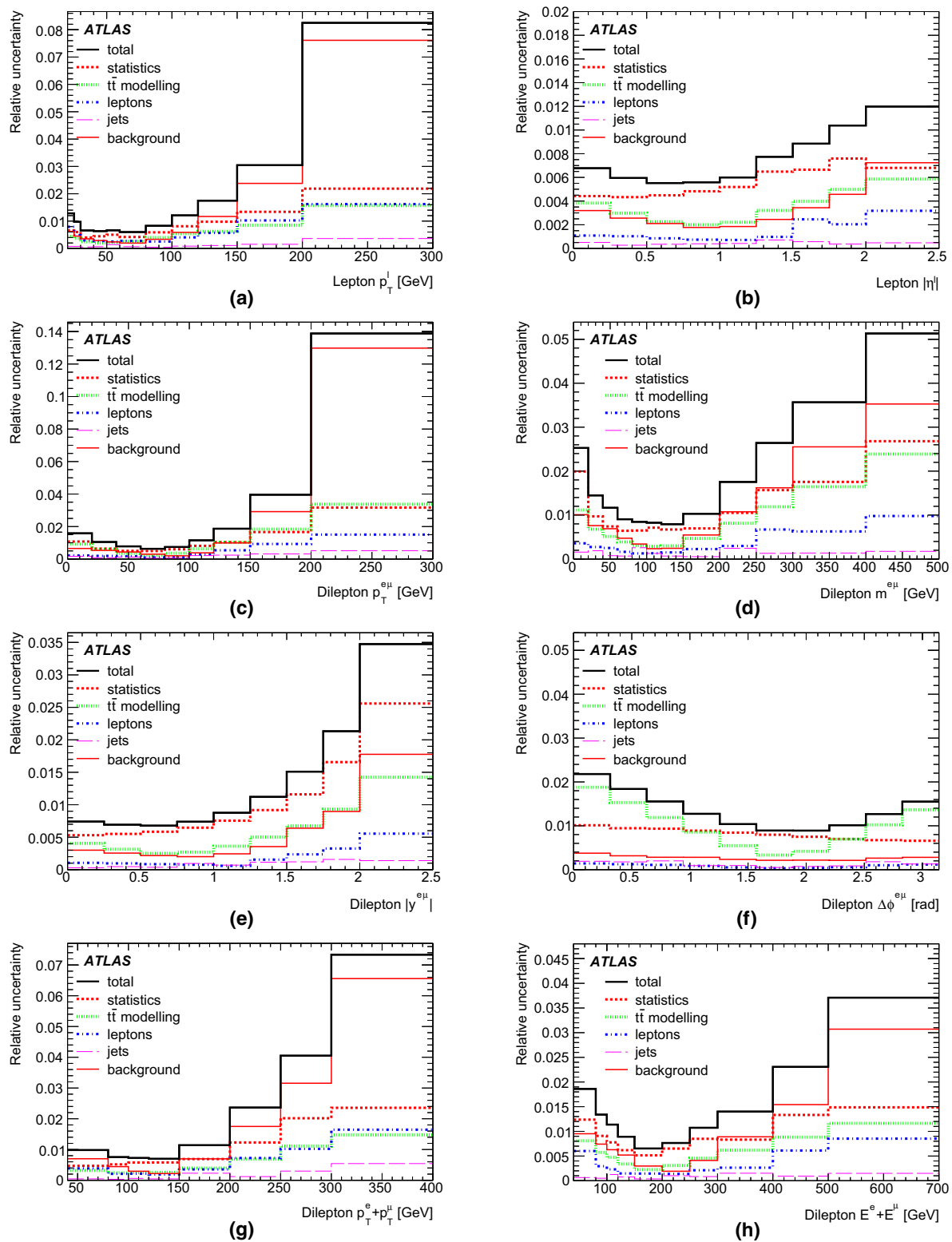


Fig. 6 Relative uncertainties in the measured normalised differential cross-sections coming from data statistics, $t\bar{t}$ modelling, leptons, jets and background, as a function of each lepton or dilepton differential

variable. The total uncertainty is shown by the thick black lines, and also includes small contributions from the integrated luminosity and LHC beam energy uncertainties

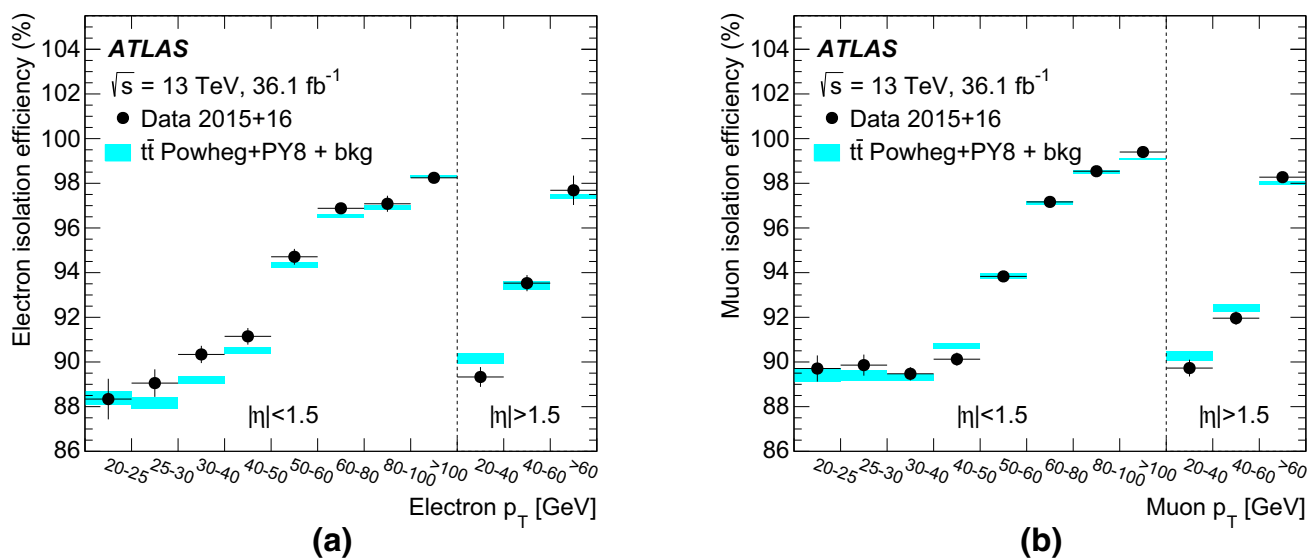


Fig. 7 Lepton isolation efficiencies for **a** electrons and **b** muons measured in the $t\bar{t}$ -dominated $e\mu$ plus b -tagged jets sample. The data measurements are shown by the black points with error bars indicating the total uncertainty, and the predictions of the baseline simulation

parameter significance distributions of misidentified leptons were obtained from the same-sign $e\mu$ samples, subtracting estimated prompt lepton contributions using simulation. The total uncertainties on the measured isolation efficiencies are up to 0.9% for electrons and 0.6% for muons at low lepton p_T , dominated by the dependence on the choice of impact parameter significance cut, and reduce to 0.1% at high p_T , where the isolation efficiency is around 98% and the misidentified lepton contributions are very small. The method was validated by using the various alternative $t\bar{t}$ simulation samples (which predict different isolation efficiencies) as pseudo-data, and by explicitly changing the lepton isolation efficiencies in simulation and verifying that the measurement procedure recovered the changes.

The isolation efficiencies measured on data are shown in Fig. 7, together with the prediction from simulation. The baseline $t\bar{t}$ simulation sample gives a good modelling of the muon isolation efficiency, but underestimates the electron isolation efficiency in data by up to 1% at low lepton p_T , leading to a total correction of about 0.4% for $\epsilon_{e\mu}$. The residual uncertainties on the p_T -integrated corrections are around 0.2% for both electrons and muons, dominated by the subtraction of misidentified-lepton background at low p_T . For comparison, the differing lepton isolation efficiency predictions from the various $t\bar{t}$ simulation samples would lead to differences in $\epsilon_{e\mu}$ of up to about 0.4%. The corresponding corrections as a function of lepton p_T and $|\eta|$ were propagated to the values of $G_{e\mu}^i$ in each bin of the differential distributions, and also applied to the estimates for the dominant Wt background. The total lepton-related uncertainties are shown by the blue dot-dashed lines in Fig. 6.

with POWHEG + PYTHIA8 $t\bar{t}$ events plus background shown by the cyan bands with width indicating the statistical uncertainty. The measurements are shown for eight bins of lepton p_T in the barrel region ($|\eta| < 1.5$) and three bins in the forward region ($|\eta| > 1.5$)

5.3 Jet measurement and b -tagging

Uncertainties in jet reconstruction and calibration affect the estimates of the background contributions from Wt and diboson events, and the values of C_b and C_b^i . They also have a very small effect on $\epsilon_{e\mu}$, $G_{e\mu}$ and $G_{e\mu}^i$ due to the removal of leptons within $\Delta R_y = 0.4$ of selected jets. The jet energy scale was determined using a combination of simulation, test beam and in situ measurements [68] and the corresponding uncertainties were evaluated using a model with 20 independent uncertainty components. The jet energy resolution was measured using Run 1 data [79] and the resulting uncertainties were extrapolated to the $\sqrt{s} = 13$ TeV data samples. The modelling of the JVT requirement used to reject jets coming from pileup was evaluated using jets in $Z \rightarrow \mu\mu$ events [69].

The efficiency for b -tagging jets in $t\bar{t}$ events was extracted from the data via Eq. (1), but simulation was used to predict the numbers of b -tagged jets in Wt and diboson background events. The values of C_b and C_b^i also depend weakly on the efficiencies for tagging both heavy- and light-flavoured jets. The modelling of the b -tagging performance in simulation was corrected using scale factors determined using dileptonic $t\bar{t}$ events for b -jets [70], single-lepton $t\bar{t}$ events for charm jets [80], and dijet events for light-quark and gluon jets [81]. The corresponding uncertainties were propagated to the background and correlation coefficient estimates. The uncertainties related to jets and b -tagging are shown by the purple dashed lines in Fig. 6, and are dominated by the effects of b -tagging uncertainties on the background estimates.

5.4 Background modelling

The normalisation of the Wt background was varied by 5.3%, corresponding to the PDF and QCD scale uncertainties on the approximate NNLO cross-section prediction discussed in Sect. 2. The potential effects of interference between the $t\bar{t}$ and Wt final states were assessed by comparing the predictions of POWHEG + PYTHIA6 samples with the diagram removal and diagram subtraction approaches to handling this interference [54, 57, 82]. The corresponding uncertainty in the inclusive cross-section result is small, but the diagram subtraction method predicts up to 30% less Wt background in the one b -tag sample and 60% less in the two b -tag sample at the high ends of the lepton p_T and dilepton $p_T^{e\mu}$, $m^{e\mu}$, $p_T^e + p_T^\mu$ and $E^e + E^\mu$ distributions, where interference effects become large and dominate the total uncertainty (see Fig. 6). However, a dedicated study of events with two leptons and two b -tagged jets [83] suggests that the data lie between the predictions of the models with diagram removal and diagram subtraction in the region where interference effects are important. Further modelling uncertainties were assessed by comparing the predictions from the baseline Wt sample with those of AMC@NLO interfaced to HERWIG++ [84], with POWHEG + PYTHIA6 samples with more or less parton-shower radiation, and with POWHEG + HERWIG7, in all cases normalising the total production cross-section to the approximate NNLO prediction. The small background acceptance uncertainties due to variations of the PDFs were evaluated using NNPDF3.0 replicas in the same way as for the $t\bar{t}$ signal. They were taken to be uncorrelated with the signal PDF uncertainties, but are included in the ‘Parton distribution functions’ entry in Table 4.

Uncertainties in the diboson background were assessed by varying the cross-sections by 6% based on calculations with MCFM [85] using the CT10 PDF set [18], and changing the QCD factorisation, renormalisation, resummation and CKKW matching scales by factors of two up and down within the SHERPA generator. The combined uncertainties amount to 12% of the diboson contribution to the one b -tag sample and 33% for the two b -tag sample.

The backgrounds from Z +jets and events with misidentified leptons were estimated using data control samples, and the corresponding uncertainties were evaluated as discussed in Sect. 4.3. The total background-related uncertainties in the normalised differential cross-sections are shown by the red solid lines in Fig. 6, and are dominated by those in the Wt background.

5.5 Luminosity and beam energy

The uncertainties in the integrated luminosity are 2.0% for the 2015 and 2.1% for the 2016 datasets, evaluated as discussed in Ref. [86] using a calibration of the LUCID-2

detector [87] obtained from x - y beam-separation scans in each year. For the inclusive cross-section analysis, the total luminosity uncertainties were broken down into individual components which were each considered correlated or uncorrelated between years, as appropriate, in the combination of the cross-section results from the two datasets [86]. A single luminosity uncertainty of 2.1% in the combined 2015–2016 sample was used for the differential cross-section analysis. In both cases, the luminosity-induced uncertainties in the measured cross-sections are around 10% larger than the uncertainty in the integrated luminosity itself, as the integrated luminosity is needed both for the conversion of the $t\bar{t}$ event yields to $\sigma_{t\bar{t}}$, and in order to normalise the simulation-based estimates of the Wt and diboson backgrounds.

The LHC beam energy is known to be within 0.1% of the nominal value of exactly 6.5 TeV per beam for $\sqrt{s} = 13$ TeV collisions, based on the LHC magnetic model and comparisons of the revolution frequencies of proton and lead-ion beams [88]. A 0.1% variation in \sqrt{s} corresponds to a 0.23% variation in $\sigma_{t\bar{t}}$, according to the NNLO+NNLL predictions of TOP++ [14]. Following the approach of previous analyses [7, 9], this uncertainty is included in the experimental uncertainty of $\sigma_{t\bar{t}}$, allowing the measurement to be compared with theoretical predictions for $\sigma_{t\bar{t}}$ at exactly $\sqrt{s} = 13$ TeV. The beam energy uncertainty also affects the predictions for both the absolute and normalised differential distributions, as e.g. the lepton p_T distributions become slightly harder and the $|\eta^\ell|$ distributions slightly more forward as \sqrt{s} increases. These shifts were evaluated by reweighting the AMC@NLO + PYTHIA8 $t\bar{t}$ sample using PDF weights calculated using LHAPDF [89] so as to vary the effective \sqrt{s} by $\pm 0.1\%$, and the resulting uncertainties were included in the differential cross-section results. The combined effects of the luminosity and beam energy uncertainties on the normalised differential cross-sections are listed in Tables 15, 16, 17, 18, and are at most 0.3%, always small compared with the other systematic and statistical uncertainties of the measurements.

6 Inclusive cross-section results and interpretation

The results of the inclusive $t\bar{t}$ cross-section analysis are given in Sect. 6.1, followed by the extraction of the top quark mass in Sect. 6.2 and the determination of ratios of cross-sections at different \sqrt{s} values in Sect. 6.3. The analyses were initially performed ‘blind’ by multiplying the $\sigma_{t\bar{t}}$ values by an unknown, randomly chosen scale factor which was only removed after verifying that consistent results were obtained from the 2015 and 2016 datasets, and after finalising all systematic uncertainties and stability studies. As a validation of the analysis procedures, the yields of $Z \rightarrow ee$

Table 5 Measurements of the inclusive total ($\sigma_{t\bar{t}}$) and fiducial ($\sigma_{t\bar{t}}^{\text{fid}}$) $t\bar{t}$ production cross-sections at $\sqrt{s} = 13$ TeV using the full dataset, the 2015 and 2016 datasets separately, and the combination of the 2015 and 2016 measurements. The fiducial cross-section requires an opposite-

sign $e\mu$ pair, with both leptons having $p_T > 20$ GeV and $|\eta| < 2.5$, as discussed in Sect. 4.1. The four uncertainties for each measurement correspond to the statistical, experimental and theoretical systematic, integrated luminosity, and beam energy uncertainties. The total uncertainty is given in parentheses after each result

Dataset	$\sigma_{t\bar{t}}$ (pb)	$\sigma_{t\bar{t}}^{\text{fid}}$ (pb)
All data	$830.7 \pm 2.2 \pm 11.6 \pm 18.4 \pm 1.9$ (22.0)	$14.14 \pm 0.04 \pm 0.19 \pm 0.31 \pm 0.03$ (0.37)
2015 data	$820.9 \pm 6.9 \pm 11.9 \pm 18.4 \pm 1.9$ (23.1)	$13.98 \pm 0.12 \pm 0.19 \pm 0.31 \pm 0.03$ (0.39)
2016 data	$831.8 \pm 2.3 \pm 11.6 \pm 19.5 \pm 1.9$ (22.9)	$14.16 \pm 0.04 \pm 0.19 \pm 0.33 \pm 0.03$ (0.39)
Combination	$826.4 \pm 3.6 \pm 11.5 \pm 15.7 \pm 1.9$ (19.9)	$14.07 \pm 0.06 \pm 0.18 \pm 0.27 \pm 0.03$ (0.33)

and $Z \rightarrow \mu\mu$ selections relative to the expectations from POWHEG + PYTHIA8-based $Z \rightarrow \ell\ell$ simulation were also compared across all data-taking periods and trigger selections, and found to be compatible within the assigned systematic and very small statistical uncertainties.

6.1 Total and fiducial cross-section results

Table 5 shows the results for $\sigma_{t\bar{t}}$ and $\sigma_{t\bar{t}}^{\text{fid}}$ from the entire 2015–2016 dataset treated as a single sample, the 2015 and 2016 datasets separately, and the combination of 2015 and 2016 results. The latter was performed using the best linear unbiased estimator technique [90,91], taking into account correlations in the systematic uncertainties. The combination gives the smallest total uncertainty, 9% smaller than that from all data treated as one sample, and gives the final results:

$$\sigma_{t\bar{t}} = 826.4 \pm 3.6 \pm 11.5 \pm 15.7 \pm 1.9 \text{ pb, and}$$

$$\sigma_{t\bar{t}}^{\text{fid}} = 14.07 \pm 0.06 \pm 0.18 \pm 0.27 \pm 0.03 \text{ pb,}$$

where the four uncertainties are due to data statistics, experimental and theoretical systematic effects internal to the analysis, the knowledge of the integrated luminosity, and the knowledge of the LHC beam energy. The total relative uncertainties are 2.4% for both $\sigma_{t\bar{t}}$ and $\sigma_{t\bar{t}}^{\text{fid}}$. The 2015 and 2016 datasets have relative weights of 0.49 and 0.51. The uncertainties due to the luminosity are only partially correlated and are similar in magnitude in both datasets, leading to approximately equal weights despite the much larger data sample from 2016. Other uncertainties are largely correlated between the two datasets, except for the statistical components of uncertainties estimated from data, such as the electron and muon identification efficiencies, and the misidentified-lepton background estimate. The χ^2 for the combination of 2015 and 2016 data is 0.23 for one degree of freedom, demonstrating good compatibility of the results. The values of ϵ_b obtained in 2015 data and simulation are very similar, and 1.6% lower in 2016 data than simulation, well within the expected uncertainties in the modelling of b -tagging performance [70]. The result for $\sigma_{t\bar{t}}$ is reported for a fixed top quark mass of $m_t = 172.5$ GeV, and depends on the assumed value

according to $(1/\sigma_{t\bar{t}})d\sigma_{t\bar{t}}/dm_t = -0.20\%/GeV$. The m_t dependence of $\sigma_{t\bar{t}}^{\text{fid}}$ is negligible. The fiducial cross-section was also corrected to remove the contribution of events with leptons from leptonic τ decays as discussed in Sect. 4.2, giving a result of $\sigma_{t\bar{t}, \text{no-}\tau}^{\text{fid}} = 12.05 \pm 0.05 \pm 0.16 \pm 0.23 \pm 0.03$ pb.

The breakdown of statistical and systematic uncertainties in the measurements is given in Table 4, which also shows the average uncertainty contributions to $\epsilon_{e\mu}$ and C_b , weighted as in the combination. The largest uncertainties come from the calibration of the integrated luminosity, followed by $t\bar{t}$ modelling (generator, hadronisation, radiation and PDFs), background modelling (Wt single-top cross-section and misidentified leptons), and lepton identification efficiencies. The uncertainties due to $t\bar{t}$ generator choices and PDFs are smaller for $\sigma_{t\bar{t}}^{\text{fid}}$ than for $\sigma_{t\bar{t}}$, but are offset by a larger uncertainty due to $t\bar{t}$ hadronisation, such that the total uncertainties in the two measurements are very similar.

The results are stable within the statistical uncertainties when increasing the minimum jet p_T requirement from the nominal value of 25 GeV up to 75 GeV, where the tagging correlations become much stronger ($C_b = 1.16$). The results are also stable when tightening the jet selection to $|\eta| < 1.0$ and changing the b -tagging selection to use the 60% or 77% efficiency working points. However, a significant trend was found when tightening the lepton p_T requirement from the nominal $p_T > 20$ GeV in several steps up to $p_T > 55$ GeV, where $\epsilon_{e\mu}$ is reduced by a factor 4.4 and $\sigma_{t\bar{t}}$ changes by $-3.9 \pm 0.7\%$, the uncertainty corresponding to the uncorrelated statistical component only. This is caused by the lepton p_T spectrum in data being significantly softer than that in the baseline POWHEG + PYTHIA8 simulation (see Fig. 1c, e, and Fig. 12a below). As discussed in Sect. 7.2 and shown in Fig. 16, the p_T^ℓ distribution is better described by the alternative AMC@NLO + PYTHIA8 $t\bar{t}$ sample, or by reweighting the baseline POWHEG + PYTHIA8 sample to better describe the measured top quark p_T spectrum [92]. Using either of these $t\bar{t}$ samples to calculate $\epsilon_{e\mu}$ increases the measured $\sigma_{t\bar{t}}$ with a lepton $p_T > 20$ GeV requirement by about 0.5%, and greatly improves the stability of the result against changes in the lepton p_T requirement. Since this change is similar

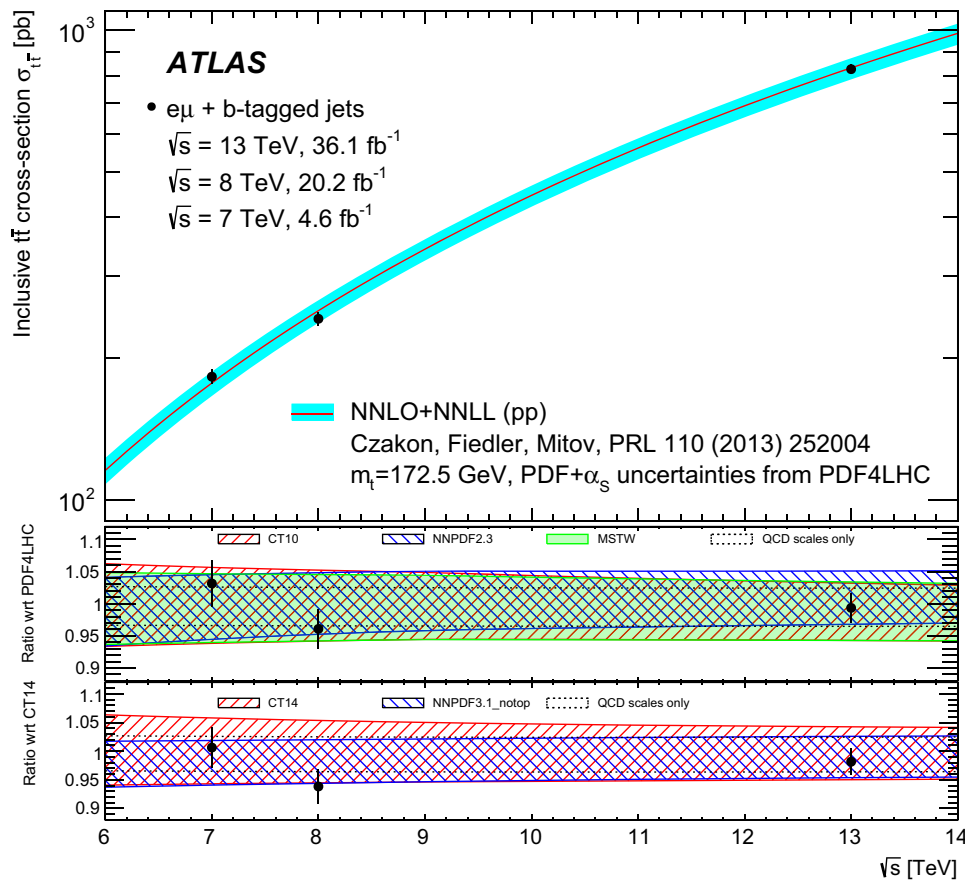


Fig. 8 The upper plot shows the inclusive $t\bar{t}$ cross-section $\sigma_{t\bar{t}}$ as a function of centre-of-mass energy \sqrt{s} , comparing ATLAS results from the $e\mu$ plus b -tagged jets final state at $\sqrt{s} = 7, 8$ and 13 TeV with NNLO+NNLL theoretical predictions [5] calculated using Top++ [14] using the PDF4LHC prescription for PDF and α_s uncertainties [15], and $m_t = 172.5$ GeV. The middle plot shows the ratios of the measurements and predictions to the central value of the prediction using PDF4LHC.

The total uncertainties when using the individual NNPDF2.3, MSTW and CT10 PDFs are shown as overlapping hatched or coloured bands, and the dotted lines show the QCD scale uncertainties alone. The lower plot shows the ratios of the measurements and predictions from the CT14 and NNPDF3.1_notop PDFs to the central value from CT14. The $\sqrt{s} = 7$ and 8 TeV results are taken from Ref. [7], with the LHC beam energy uncertainties reduced according to Ref. [88]

to the already assigned $t\bar{t}$ modelling uncertainties (in particular from the AMC@NLO vs POWHEG comparison), no additional uncertainty was included.

The inclusive cross-section result, together with previous measurements at $\sqrt{s} = 7$ TeV and $\sqrt{s} = 8$ TeV [7], is compared in Fig. 8 with the NNLO+NNLL QCD prediction described in Sect. 1. The measurement agrees with the predictions using the CT10, MSTW2008 and NNPDF2.3 PDF sets combined with the PDF4LHC prescription. It is significantly more precise than this prediction, demonstrating the power of the measurement to constrain the gluon PDF at high Bjorken- x . The lower ratio panel compares the measurements to predictions using the CT14 [74] and NNPDF3.1_notop [93] NNLO PDF sets, two recent PDF sets which do not use any $t\bar{t}$ data in their fits. The NNPDF3.1_notop PDF set does not include any variations of α_s from the nominal value of 0.118, so the α_s uncertainty obtained from an α_s variation of ± 0.0012 with the standard NNPDF3.1 PDF set was added

in quadrature to the PDF-alone uncertainty calculated with NNPDF3.1_notop. The $\sqrt{s} = 13$ TeV measurement is also in good agreement with the predictions from these PDF sets.

The result is also consistent with, and supersedes, the previous ATLAS measurement using the same technique applied to 2015 data alone, which had an uncertainty of 4.4% [9]. The smaller uncertainty of 2.4% in the updated analysis results from improvements in the modelling of $t\bar{t}$ production (including tuning to $t\bar{t}$ data at $\sqrt{s} = 13$ TeV), more precise calibration of the integrated luminosity and of the LHC beam energy, and better understanding of the lepton identification efficiencies and energy scales, as well as the larger data sample. The new result is also consistent with results from CMS in the dilepton [13] and lepton+jets [12] final states, but again has higher precision.

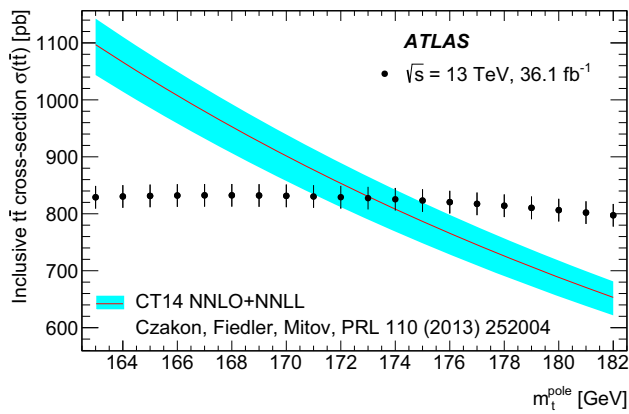


Fig. 9 Predicted inclusive $t\bar{t}$ cross-section at $\sqrt{s} = 13$ TeV as a function of the top quark pole mass m_t^{pole} , for the CT14 PDF set. The cyan band indicates the total uncertainty in the prediction from PDF+ α_S and QCD scale uncertainties. The experimental measurement with its uncertainty and dependence on the assumed value of m_t through acceptance and background corrections is shown by the black points with error bars

6.2 Extraction of the top quark pole mass

The strong dependence of the inclusive $t\bar{t}$ cross-section prediction on the top quark pole mass m_t^{pole} can be exploited to interpret precise measurements of $\sigma_{t\bar{t}}$ as measurements of m_t^{pole} , as discussed in Sect. 1. The ATLAS $\sqrt{s} = 7$ and 8 TeV measurements in the $e\mu$ channel were interpreted in this way, giving a combined value of $m_t^{\text{pole}} = 172.9^{+2.5}_{-2.6}$ GeV [7], and similar measurements have been performed by CMS at $\sqrt{s} = 7, 8$ and 13 TeV [10, 12, 13], as well as by D0 at the Tevatron $\bar{p}p$ collider [94].

The NNLO+NNLL prediction for $\sigma_{t\bar{t}}$ as a function of m_t^{pole} at $\sqrt{s} = 13$ TeV was calculated using TOP++ [14] and the CT14 NNLO PDF set [74] with uncertainties scaled to 68% confidence levels and $\alpha_S = 0.1180 \pm 0.0012$. CT14 was chosen as a recent PDF set which does not use any $t\bar{t}$ cross-section data as input. The resulting dependence was parameterised using the functional form proposed in Ref. [5]:

$$\sigma_{t\bar{t}}^{\text{theo}}(m_t^{\text{pole}}) = \sigma(m_t^{\text{ref}}) \left(\frac{m_t^{\text{ref}}}{m_t^{\text{pole}}} \right)^4 (1 + a_1 x + a_2 x^2).$$

Here, $x = (m_t^{\text{pole}} - m_t^{\text{ref}})/m_t^{\text{ref}}$, the constant $m_t^{\text{ref}} = 172.5$ GeV, and $\sigma(m_t^{\text{ref}})$, a_1 and a_2 are free parameters. The resulting function is shown in Fig. 9. The measurement of $\sigma_{t\bar{t}}$ given in Sect. 6.1 is also shown, with its small dependence on m_t due to variations of the experimental acceptance and Wt background discussed in Sect. 5.1. These variations were studied using $t\bar{t}$ and Wt simulation samples with several values of m_t , and the corresponding dependencies of $\epsilon_{e\mu}$, N_1^{bkg} and N_2^{bkg} on m_t were parameterised with second-order polynomials. The mass parameter used to characterise the dependence of the measured $\sigma_{t\bar{t}}$ on m_t represents the top

quark mass used in the Monte Carlo event generators rather than m_t^{pole} , but since the dependence of the measured $\sigma_{t\bar{t}}$ on m_t is small, this approximation causes negligible bias if m_t and m_t^{pole} differ by only a few GeV. Under these conditions, the intersection of the theoretical and experimental curves shown in Fig. 9 gives an unambiguous extraction of the top quark pole mass.

The mass extraction was performed by maximising the following Bayesian likelihood as a function of m_t^{pole} :

$$\mathcal{L}(m_t^{\text{pole}}) = \int G(\sigma'_{t\bar{t}} | \sigma_{t\bar{t}}(m_t^{\text{pole}}), s_{\text{exp}}) \cdot G(\sigma'_{t\bar{t}} | \sigma_{t\bar{t}}^{\text{theo}}(m_t^{\text{pole}}), s_{\text{theo}}^{\pm}) d\sigma'_{t\bar{t}}, \quad (7)$$

where $G(x | \mu, s)$ represents a Gaussian probability density in the variable x with mean μ and standard deviation s . The first Gaussian term in the integral represents the experimental measurement $\sigma_{t\bar{t}}$ with its dependence on m_t^{pole} and uncertainty s_{exp} , and the second term represents the theoretical prediction $\sigma_{t\bar{t}}^{\text{theo}}$ with its asymmetric uncertainty s_{theo}^{\pm} obtained from the quadrature sum of the combined PDF plus α_S uncertainty, and the QCD scale uncertainty, each evaluated as described in Sect. 1. The likelihood in Eq. (7) was maximised to obtain m_t^{pole} when using the CT14 NNLO PDF set to calculate $\sigma_{t\bar{t}}^{\text{theo}}$, and also when using the NNPDF3.1_notop NNLO PDF set, with α_S uncertainties inferred from NNPDF3.1 as discussed in Sect. 6.1. Results were also obtained using the individual CT10, MSTW and NNPDF2.3 NNLO PDF sets to calculate $\sigma_{t\bar{t}}^{\text{theo}}$, for comparison with the $\sqrt{s} = 7$ and 8 TeV results. The MMHT and NNPDF3.0 PDF sets were not considered, as they include $t\bar{t}$ cross-section data in order to constrain the gluon PDF, and hence cannot also be used to determine m_t^{pole} without introducing a circular dependence [95]. In each case, the value of $\sigma_{t\bar{t}}$ was recalculated using the corresponding NLO PDF set to calculate the value of $\epsilon_{e\mu}$. The results from each PDF set are shown in Table 6, together with the result using the PDF4LHC prescription to combine the CT10, MSTW and NNPDF2.3 results, keeping the CT10 central value but enlarging the uncertainty to cover the envelope of the positive and negative uncertainties of each individual PDF set. The NNPDF3.1_notop PDF set gives the smallest uncertainty of ± 1.7 GeV, demonstrating the power of recent improvements in the gluon PDF determination to reduce the uncertainty on m_t^{pole} . However, given the approximate procedure used to evaluate the α_S uncertainty for this PDF set, the CT14 PDF set was chosen for the baseline result.

Table 7 shows the breakdown of uncertainties in m_t^{pole} calculated using the CT14 PDF set, which are dominated by uncertainties in $\sigma_{t\bar{t}}^{\text{theo}}$ through PDF+ α_S and QCD scale variations. Improving the experimental measurement of $\sigma_{t\bar{t}}$ further would therefore have little effect on the determination of m_t^{pole} via this method. The result is compatible with other measurements of m_t^{pole} via lepton differential distri-

Table 6 Top quark pole mass results for various NNLO PDF sets, derived from the $t\bar{t}$ cross-section measurement at $\sqrt{s} = 13$ TeV. The uncertainties include PDF+ α_s , QCD scale and experimental sources. The PDF4LHC result spans the uncertainties of the CT10, MSTW and NNPDF2.3 PDF sets

PDF set	m_t^{pole} (GeV)
CT14	$173.1^{+2.0}_{-2.1}$
NNPDF3.1_notop	$172.9^{+1.7}_{-1.7}$
CT10	$172.1^{+2.0}_{-2.0}$
MSTW	$172.3^{+2.0}_{-2.1}$
NNPDF2.3	$173.4^{+1.9}_{-1.9}$
PDF4LHC	$172.1^{+3.1}_{-2.0}$

Table 7 Uncertainties in the top quark pole mass extracted from the $t\bar{t}$ production cross-section measurement at $\sqrt{s} = 13$ TeV, using the CT14 PDF set

Uncertainty source	Δm_t^{pole} (GeV)
Data statistics	0.2
Analysis systematics	0.6
Integrated luminosity	0.8
Beam energy	0.1
PDF+ α_s	$+1.5$ -1.4
QCD scales	$+1.0$ -1.5
Total uncertainty	$+2.0$ -2.1

butions [29], and via the reconstruction of top quark differential distributions in inclusive $t\bar{t}$ [96] and $t\bar{t}$ +jet [97,98] events, as well as previous measurements using the total $t\bar{t}$ cross-section [7, 10, 12, 13, 94]. It is also consistent with the Particle Data Group average of $m_t^{\text{pole}} = 173.1 \pm 0.9$ GeV [99] from a subset of these measurements. The result using the CT14 PDF improves upon the previous ATLAS result from $\sqrt{s} = 7$ and 8 TeV data using the CT10, MSTW and NNPDF2.3 PDFs combined with the PDF4LHC prescription [7]. However, using the PDF4LHC prescription with the $\sqrt{s} = 13$ TeV data gives a larger uncertainty of $^{+3.1}_{-2.0}$ GeV, as the prediction of $\sigma_{t\bar{t}}$ from NNPDF2.3 starts to diverge from

Table 8 Input inclusive $t\bar{t}$ and fiducial $Z \rightarrow ee/\mu\mu$ cross-sections used in the calculations of the $t\bar{t}$ and $t\bar{t}/Z$ cross-section ratios and double ratios shown in Tables 9 and 10. The three uncertainties in each cross-section are due to data statistics, experimental and theoretical systematic effects (including the LHC beam energy uncertainties) and knowledge of the integrated luminosities of the data samples. For $\sqrt{s} = 13$ TeV,

\sqrt{s} (TeV)	$\sigma_{t\bar{t}}$ (pb)	$\sigma_{Z \rightarrow ee}^{\text{fid}}$ (pb)	$\sigma_{Z \rightarrow \mu\mu}^{\text{fid}}$ (pb)
7	$182.9 \pm 3.1 \pm 4.2 \pm 3.6$	$451.2 \pm 0.5 \pm 1.7 \pm 8.1$	$450.0 \pm 0.4 \pm 2.0 \pm 8.1$
8	$242.9 \pm 1.7 \pm 5.5 \pm 5.1$	$507.0 \pm 0.2 \pm 4.3 \pm 9.6$	$504.7 \pm 0.2 \pm 3.6 \pm 9.6$
13	$824.7 \pm 6.9 \pm 12.1 \pm 18.4^{(a)}$ $830.2 \pm 3.6 \pm 11.7 \pm 15.7^{(b)}$	$778.3 \pm 0.7 \pm 4.1 \pm 15.9$	$774.4 \pm 0.7 \pm 6.3 \pm 15.8$

that of CT10 and MSTW at higher \sqrt{s} (see Fig. 8), leading to a larger spread in the m_t values from the different PDF sets.

6.3 $t\bar{t}$ and $t\bar{t}/Z$ cross-section ratios at different energies

The ratios $R_{13/7}^{t\bar{t}}$ and $R_{13/8}^{t\bar{t}}$ were calculated using the $\sqrt{s} = 13$ TeV $\sigma_{t\bar{t}}$ result discussed above and the $\sqrt{s} = 7$ and 8 TeV results from Refs. [7], corrected to reduce the LHC beam energy uncertainty to 0.1% [88]. The $\sigma_{t\bar{t}}$ values and uncertainties are summarised in Table 8; the largest systematic uncertainties come in all cases from $t\bar{t}$ modelling and the knowledge of the integrated luminosity. As the nominal $t\bar{t}$ simulation sample used at $\sqrt{s} = 7$ and 8 TeV was POWHEG + PYTHIA6 with the CT10 PDFs, the $\sqrt{s} = 13$ TeV result was rederived using a similar $t\bar{t}$ sample to calculate $\epsilon_{e\mu}$ and C_b , increasing the 13 TeV $\sigma_{t\bar{t}}$ value by 0.46%. PDF uncertainties were evaluated for each of the error sets or replicas of the CT10, MSTW and NNPDF2.3 PDF sets, considering the effect of each individual variation to be correlated between the numerator and denominator of the $\sigma_{t\bar{t}}$ ratio. Significant cancellations occur, leading to PDF uncertainties of about 0.5% in each ratio, significantly smaller than the 1% uncertainties for the $\sqrt{s} = 7$ and 8 TeV $\sigma_{t\bar{t}}$ measurements. The parton-shower radiation uncertainties were similarly evaluated using POWHEG + PYTHIA6 samples with more and less parton-shower radiation in all datasets, giving residual uncertainties of around 0.4% in the ratios. Other $t\bar{t}$ modelling uncertainties due to the choice of NLO generator and hadronisation model were conservatively taken to be uncorrelated, due to the different alternative generators used in the measurements. The uncertainties due to the Wt background cross-section and $t\bar{t}/Wt$ interference were assessed in the same way at all \sqrt{s} values and considered correlated. Lepton, jet and b -tagging uncertainties were mainly considered uncorrelated, due to the changes in detector configuration and lepton identification algorithms between measurements. The integrated luminosity measurements were based on different primary detectors at 7–8 TeV and 13 TeV, and the luminosity scale was calibrated using individual beam-separation scans

the $t\bar{t}$ cross-section labelled (a) uses 2015 data only and is used for the $t\bar{t}/Z$ ratio $R_{13}^{t\bar{t}/Z}$ and the double ratios $R_{13/7}^{t\bar{t}/Z}$ and $R_{13/8}^{t\bar{t}/Z}$, whilst the cross-section labelled (b) uses the combination of 2015 and 2016 data, and is used for the $t\bar{t}$ cross-section ratios $R_{13/7}^{t\bar{t}}$ and $R_{13/8}^{t\bar{t}}$. Both $t\bar{t}$ cross-sections have been calculated using a POWHEG + PYTHIA6 sample to derive the efficiencies (see text)

Table 9 Ratios of inclusive $t\bar{t}$ production cross-sections measured at $\sqrt{s} = 13, 7$ and 8 TeV, together with the corresponding NNLO+NNLL predictions using $T_{\text{OP}++}$ [14] with the PDF4LHC prescription for PDF and α_S uncertainties [15]. The three uncertainties in the measured ratios are due to data statistics, experimental and theoretical systematic effects

\sqrt{s} values (TeV)	Measured cross-section ratio	NNLO+NNLL prediction
13/7	$4.54 \pm 0.08 \pm 0.10 \pm 0.12$ (0.18)	4.69 ± 0.16
13/8	$3.42 \pm 0.03 \pm 0.07 \pm 0.10$ (0.12)	3.28 ± 0.08
8/7	$1.33 \pm 0.02 \pm 0.02 \pm 0.04$ (0.05)	1.43 ± 0.01

in each dataset [86, 100, 101] with only a fraction of the uncertainties being correlated. The total luminosity uncertainties were therefore conservatively taken to be uncorrelated in the $\sigma_{t\bar{t}}$ ratio measurements. The beam energy uncertainties are correlated between \sqrt{s} values, but the varying dependence of $\sigma_{t\bar{t}}$ on \sqrt{s} (see Fig. 8) leads to a small ($< 0.1\%$) residual uncertainty on the ratios.

The resulting cross-section ratios are shown in Table 9, together with the NNLO+NNLL predictions calculated using $T_{\text{OP}++}$ as described in Sect. 1, with the uncertainties from the CT10, MSTW and NNPDF2.3 PDFs combined according to the PDF4LHC prescription. The total uncertainties in the measurements are 3.9% for $R_{13/7}^{t\bar{t}}$ and 3.6% for $R_{13/8}^{t\bar{t}}$, improving on the uncertainties of 4.9% and 4.7% obtained using the 2015 $\sqrt{s} = 13$ TeV dataset alone in Ref. [27]. Figure 10 compares the measurements with the predictions using the CT10, MSTW and NNPDF2.3 PDF sets, as well as the more recent CT14 [74], ABM12LHC [102], ABMP16 [103], ATLAS-epWZ12 [104], HERAPDF2.0 [105], MMHT14 [77] and NNPDF3.0 [44] PDF sets, some of which include some LHC data (including $t\bar{t}$ cross-section measurements in the cases of ABM12LHC, ABMP16, MMHT and NNPDF3.0). The ratio $R_{13/7}^{t\bar{t}}$ is lower than all the predictions, and the ratio $R_{13/8}^{t\bar{t}}$ higher than all the predictions except ABM12LHC. However, both ratios are compatible with all the predictions except ABM12LHC within two standard deviations. Some of these results are also reflected in Fig. 8. The behaviour of ABM12LHC is attributed to the lower gluon density at high Bjorken- x compared to the other considered PDF sets, which leads to a larger relative increase in the $t\bar{t}$ cross-section as a function of \sqrt{s} . This behaviour is less apparent in the more recent ABMP16 PDF set, which includes more precise constraints from LHC top quark measurements. The current experimental uncertainties, dominated by the luminosity uncertainties which do not cancel in the ratios, do not allow the predictions using the other PDFs to be distinguished.

As discussed in Ref. [27], double ratios of $t\bar{t}$ to Z cross-sections at different energies can be used to reduce the luminosity uncertainty, potentially enhancing the sensitivity to

(including the LHC beam energy uncertainties) and knowledge of the integrated luminosities of the data samples. The ratio of $\sqrt{s} = 8$ and 7 TeV results is taken from Ref. [7]. The total uncertainty is given in parentheses after each result

PDF differences. The $t\bar{t}$ cross-section at a given energy can be normalised to the corresponding $Z \rightarrow \ell\ell$ fiducial cross-section $\sigma_{Z \rightarrow \ell\ell}^{\text{fid}}$ at the same energy by defining the ratio $R^{t\bar{t}/Z}$ as:

$$R^{t\bar{t}/Z} = \frac{\sigma_{t\bar{t}}}{0.5 \left(\sigma_{Z \rightarrow ee}^{\text{fid}} + \sigma_{Z \rightarrow \mu\mu}^{\text{fid}} \right)}, \quad (8)$$

where the use of the unweighted average of $Z \rightarrow ee$ and $Z \rightarrow \mu\mu$ cross-sections maximises the potential cancellation of electron- and muon-related systematic uncertainties when the $t\bar{t}$ cross-section is measured using events with one electron and one muon. Provided that the $t\bar{t}$ and Z cross-sections are measured using the same data sample, the integrated luminosity uncertainty cancels almost completely in the ratio $R^{t\bar{t}/Z}$. Double ratios $R_{i/j}^{t\bar{t}/Z}$ of $R^{t\bar{t}/Z}$ at two different energies i and j can then be defined:

$$R_{i/j}^{t\bar{t}/Z} = \frac{R^{t\bar{t}/Z}(i)}{R^{t\bar{t}/Z}(j)},$$

which benefit from cancellations of uncertainties between beam energies and production processes. In Ref. [27], the previous measurement of $\sigma_{t\bar{t}}$ at $\sqrt{s} = 13$ TeV from Ref. [9] was used together with the $\sqrt{s} = 7$ and 8 TeV $\sigma_{t\bar{t}}$ measurements from Refs. [7] and corresponding measurements of $\sigma_{Z \rightarrow \ell\ell}^{\text{fid}}$ at each energy to derive double ratios $R_{13/7}^{t\bar{t}/Z}$, $R_{13/8}^{t\bar{t}/Z}$ and $R_{8/7}^{t\bar{t}/Z}$, which were compared with the predictions from various PDF sets. The $Z \rightarrow \ell\ell$ cross-sections were measured in a fiducial volume corresponding to the lepton acceptance ($p_T > 25$ GeV and $|\eta| < 2.5$) with the dilepton invariant mass in the range $66 < m_{\ell\ell} < 116$ GeV.

The precision of the $t\bar{t}/Z$ ratio and double ratios involving $\sqrt{s} = 13$ TeV data were limited by the 4.4% uncertainty in the corresponding $\sigma_{t\bar{t}}$ measurement. These ratios have therefore been updated using the more precise $\sqrt{s} = 13$ TeV $\sigma_{t\bar{t}}$ measurement shown in Table 5. The result from 2015 data alone (with an uncertainty of 2.8%) was used in order to maintain the cancellation of luminosity uncertainties in Eq. (8), as the corresponding $\sigma_{Z \rightarrow \ell\ell}^{\text{fid}}$ measurements only used the 2015 data sample. Since the $\sigma_{t\bar{t}}$ result was derived using reoptimised lepton identification and updated calibrations, the

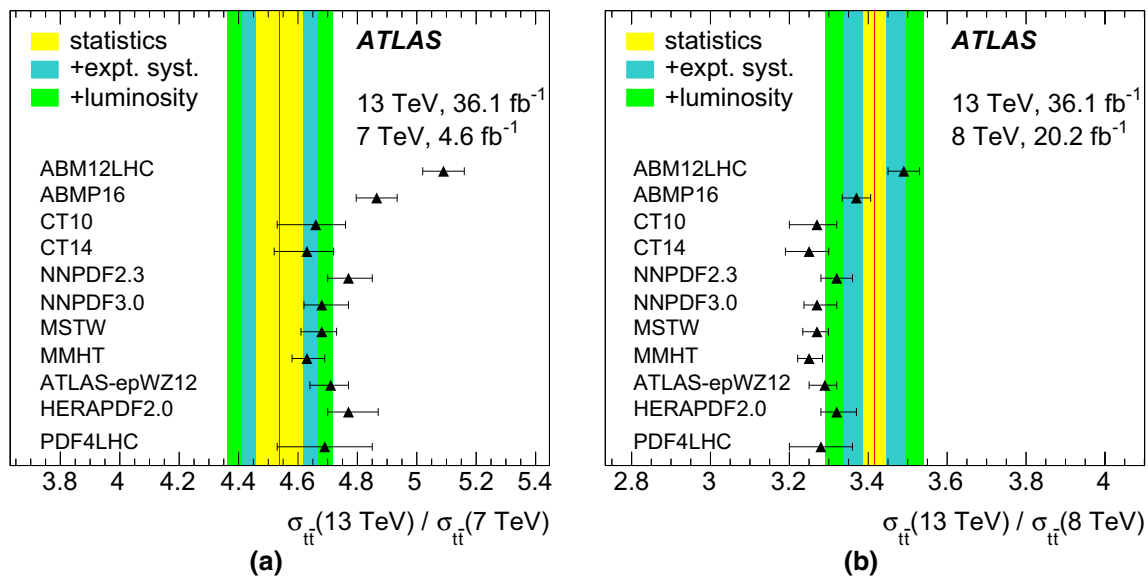


Fig. 10 Ratios of $t\bar{t}$ production cross-sections at different energies: **a** $R_{13/7}^{t\bar{t}}$, **b** $R_{13/8}^{t\bar{t}}$. The bands show the experimental measurements with the statistical (inner yellow bands), statistical plus experimental and theoretical systematic (middle cyan bands) and total including luminosity

(outer green bands) uncertainties. The black triangles with error bars show the predictions and uncertainties from various PDF sets. The last entry shows the prediction using the PDF4LHC recipe, encompassing the predictions from the CT10, MSTW and NNPDF2.3 PDF sets

Table 10 Measurements of the ratio of $t\bar{t}/Z$ cross-sections at $\sqrt{s} = 13$ TeV, and double ratios of $t\bar{t}/Z$ cross-sections at $\sqrt{s} = 13$ TeV and $\sqrt{s} = 7$ TeV or $\sqrt{s} = 8$ TeV, compared with predictions using the CT14 PDF set. The three uncertainties in the measurements are due to

data statistics, experimental and theoretical systematic effects (including the small uncertainty due to the LHC beam energy uncertainties) and knowledge of the integrated luminosities of the data samples. The total uncertainty is given in parentheses after each result

\sqrt{s} value (TeV)	$t\bar{t}/Z$ cross-section ratio	CT14 prediction
13	$1.062 \pm 0.009 \pm 0.016 \pm 0.002$ (0.018)	$1.132^{+0.078}_{-0.075}$
\sqrt{s} values (TeV)	$t\bar{t}/Z$ cross-section double ratio	
13/7	$2.617 \pm 0.049 \pm 0.060 \pm 0.007$ (0.078)	$2.691^{+0.045}_{-0.058}$
13/8	$2.212 \pm 0.024 \pm 0.049 \pm 0.006$ (0.055)	$2.124^{+0.026}_{-0.035}$

lepton uncertainties were conservatively treated as uncorrelated between the $\sqrt{s} = 13$ TeV $t\bar{t}$ and Z measurements. The largest uncertainties in the double ratio are associated with $t\bar{t}$ modelling, and these were treated in the same way as for the updated $t\bar{t}$ cross-section ratios discussed above, including the 0.46% increase of the $\sqrt{s} = 13$ TeV $\sigma_{t\bar{t}}$ value corresponding to the use of a POWHEG + PYTHIA6 CT10 nominal $t\bar{t}$ simulation sample. All other uncertainties were treated according to the correlation model described in Ref. [27], with the LHC beam energy uncertainties updated according to Ref. [88]. The input cross-sections are summarised in Table 8.

The resulting single and double ratios are shown in Table 10, together with the predictions using the CT14 PDF set, calculated as described in Ref. [27]. The total uncertainties are 1.7% for $R_{13}^{t\bar{t}/Z}$, 3.0% for $R_{13/7}^{t\bar{t}/Z}$ and 2.5% for $R_{13/8}^{t\bar{t}/Z}$,

which are significant improvements on the corresponding uncertainties of 3.5%, 3.8% and 3.6% in Ref. [27]. The largest uncertainties come from the $\sigma_{t\bar{t}}$ measurements, in particular the $t\bar{t}$ modelling uncertainties, which are mainly treated as uncorrelated between beam energies. Excluding PDF uncertainties, where the correlations between beam energies are fully accounted for, $t\bar{t}$ modelling uncertainties contribute 1.7% and 1.4% to the uncertainties on the ratios $R_{13/7}^{t\bar{t}/Z}$ and $R_{13/8}^{t\bar{t}/Z}$. In principle, these uncertainties could be reduced by using a fully coherent set of $t\bar{t}$ simulation samples and uncertainty model at all beam energies, but that has not been attempted here.

The results are compared with the predictions of the ABM12LHC, CT14, NNPDF3.0, MMHT, ATLAS-epWZ12 and HERAPDF2.0 PDF sets (the same sets as in Ref. [27])

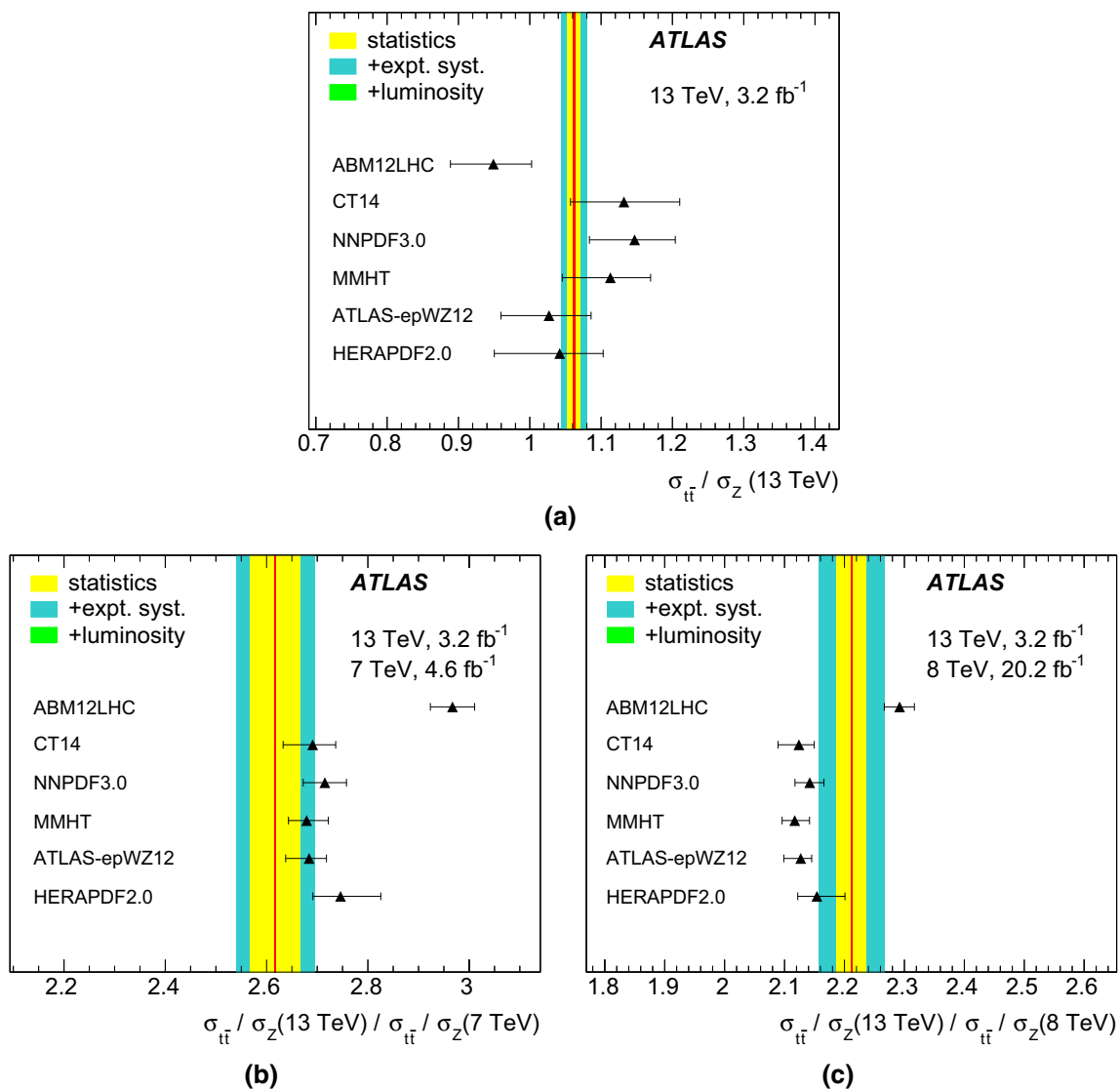


Fig. 11 **a** Ratio of $t\bar{t}$ to Z production cross-sections at $\sqrt{s} = 13$ TeV, and double ratios of $t\bar{t}$ to Z production cross-sections at different energies: **b** $R_{13/7}^{t\bar{t}/Z}$, **c** $R_{13/8}^{t\bar{t}/Z}$. The bands show the experimental measurements with the statistical (inner yellow bands), statistical plus experimental

and theoretical systematic (middle cyan bands) and total including luminosity (barely visible outer green bands) uncertainties. The black triangles with error bars show the predictions and uncertainties from various PDF sets. The $\sqrt{s} = 13$ TeV results use only the 3.2 fb⁻¹ data sample recorded in 2015

in Fig. 11. The measurement of the $t\bar{t}/Z$ cross-section ratio at $\sqrt{s} = 13$ TeV is compatible with all the predictions within two standard deviations. Although the experimental uncertainty is only 1.7%, the predictions have common uncertainties of $^{+4.0}_{-4.6}\%$ from QCD scale and top quark mass variations, limiting the sensitivity to PDF variations. The pattern for the double ratios is similar to that seen for the $t\bar{t}$ -only ratios in Fig. 10; the normalisation to $Z \rightarrow \ell\ell$ cross-sections serves mainly to reduce the luminosity-related uncertainties. The double ratio $R_{13/7}^{t\bar{t}/Z}$ lies below all the predictions, and $R_{13/8}^{t\bar{t}/Z}$ lies above all the predictions except that of ABM12LHC.

However, the measurements are consistent with all the predictions within two standard deviations, with the exception of ABM12LHC for $R_{13/7}^{t\bar{t}/Z}$. Similar trends were seen in Ref. [27], although with less separation between PDFs due to the larger uncertainties in the double ratios.

7 Differential cross-section results

The single-lepton and dilepton absolute fiducial differential cross-section results were obtained by solving Eq. (2) for

each bin i of each distribution, using the combined 2015–2016 data sample. The normalised differential cross-sections were obtained from the absolute results using Eq. (3) and (4). As in the inclusive cross-section analysis, the results were found to be stable when varying the jet p_T , $|\eta|$ and b -tagging requirements. The single-lepton p_T^ℓ and $|\eta^\ell|$ distributions were also measured for electrons and muons separately, instead of combining them into lepton distributions with two entries per event, and found to be compatible. The distributions of bin-by-bin differences in the electron and muon differential cross-sections have χ^2 per degree of freedom of 7/10 for p_T^ℓ and 13/8 for $|\eta^\ell|$, in both cases taking statistical and uncorrelated systematic uncertainties into account.

7.1 Results for measured distributions

The measured absolute and normalised fiducial differential cross-sections are shown in Table 15 (p_T^ℓ and $|\eta^\ell|$), Table 16 ($p_T^{e\mu}$ and $m^{e\mu}$), Table 17 ($|y^{e\mu}|$ and $\Delta\phi^{e\mu}$) and Table 18 ($p_T^e + p_T^\mu$ and $E^e + E^\mu$) in the Appendix. The double-differential cross-sections are shown in Tables 19, 20 ($|\eta^\ell| \times m^{e\mu}$), Tables 21, 22 ($|y^{e\mu}| \times m^{e\mu}$) and Tables 23, 24 ($|\Delta\phi^\ell| \times m^{e\mu}$). These tables show the measured cross-section values and uncertainties, together with a breakdown of the total uncertainties into components corresponding to data statistics ('Stat'), $t\bar{t}$ modelling (' $t\bar{t}$ mod. '), lepton identification and measurement ('Lept. '), jet and b -tagging uncertainties ('Jet/ b '), background uncertainties ('Bkg. ') and luminosity/beam energy uncertainties (' L/E_b '), matching the categories described in Sects. 5.1–5.5. The rightmost columns show the cross-sections corrected using Eq. (5) to remove the contributions where at least one lepton results from a leptonic

decay of a τ -lepton. As also visible in Fig. 6, the total uncertainties in the normalised differential cross-sections range from 0.6% to around 10%, and are typically around half those for the corresponding distributions measured at $\sqrt{s} = 8$ TeV [29]. The largest uncertainties are generally statistical, but background uncertainties (in particular from $t\bar{t}/Wt$ interference) become dominant at the high ends of the p_T^ℓ , $p_T^{e\mu}$, $m^{e\mu}$, $p_T^e + p_T^\mu$ and $E^e + E^\mu$ distributions, and $t\bar{t}$ modelling uncertainties from the comparison of AMC@NLO + PYTHIA8 and POWHEG + PYTHIA8 are dominant for most of the $\Delta\phi^{e\mu}$ distribution. Uncertainties related to leptons and jets generally play only a minor role; in particular those due to jet energy measurement and b -tagging are suppressed due to the determination of ϵ_b from data in Eq. (2). The systematic uncertainties in the normalised differential cross-sections benefit from significant cancellations between bins, and the uncertainties in the absolute cross-sections are substantially larger. The latter also suffer from the uncertainties in the integrated luminosity and beam energy, which contribute 2.3–2.8%, depending on the background level in each bin.

The measured normalised differential cross-sections are shown graphically in Figs. 12, 13, 14, 15. The different $m^{e\mu}$ bins for the double-differential cross-sections are shown sequentially on the x axes, separated by vertical dotted lines. The measured cross-sections are compared with the particle-level predictions from the baseline POWHEG + PYTHIA8 $t\bar{t}$ sample, POWHEG + PYTHIA8 samples with more or less parton-shower radiation, and AMC@NLO + PYTHIA8. The trends seen are similar to those visible in the reconstructed distributions shown in Figs. 1 and 2, and are discussed in the context of comparisons with a larger set of samples in the following.

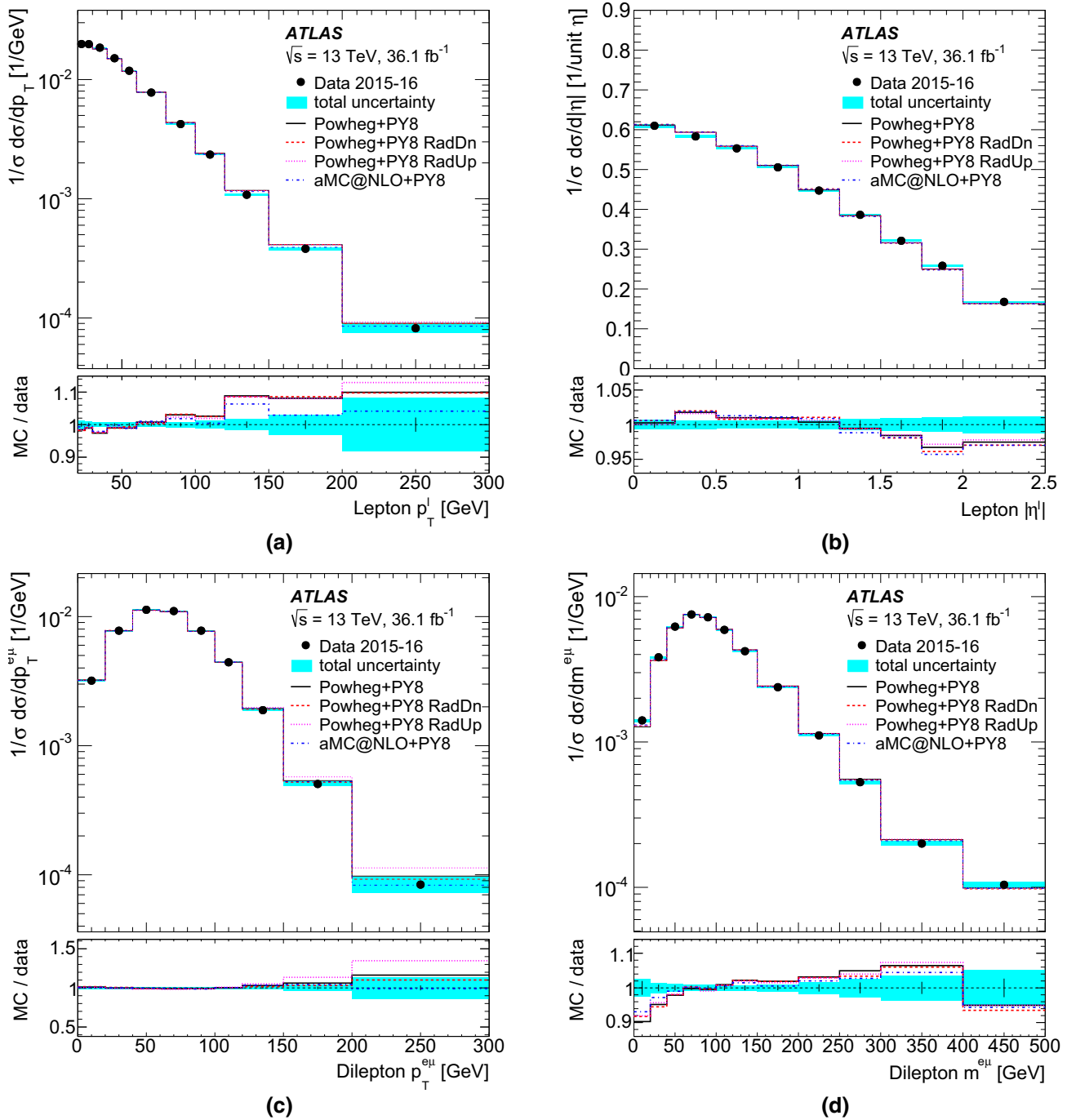


Fig. 12 Normalised differential cross-sections as a function of **a** p_T^ℓ , **b** $|\eta^\ell|$, **c** $p_T^{e\mu}$ and **d** $m^{e\mu}$. The measured values are shown by the black points with error bars corresponding to the data statistical uncertainties and cyan bands corresponding to the total uncertainties in each bin, and include the contributions via $W \rightarrow \tau \rightarrow e/\mu$ decays. The data points are placed at the centre of each bin. The results are compared with the

predictions from the baseline POWHEG + PYTHIA8 $t\bar{t}$ sample, POWHEG + PYTHIA8 samples with more or less parton-shower radiation (RadUp and RadDn), and an AMC@NLO + PYTHIA8 sample. The lower plots show the ratios of predictions to data, with the error bars indicating the data statistical uncertainties and the cyan bands indicating the total uncertainties in the measurements

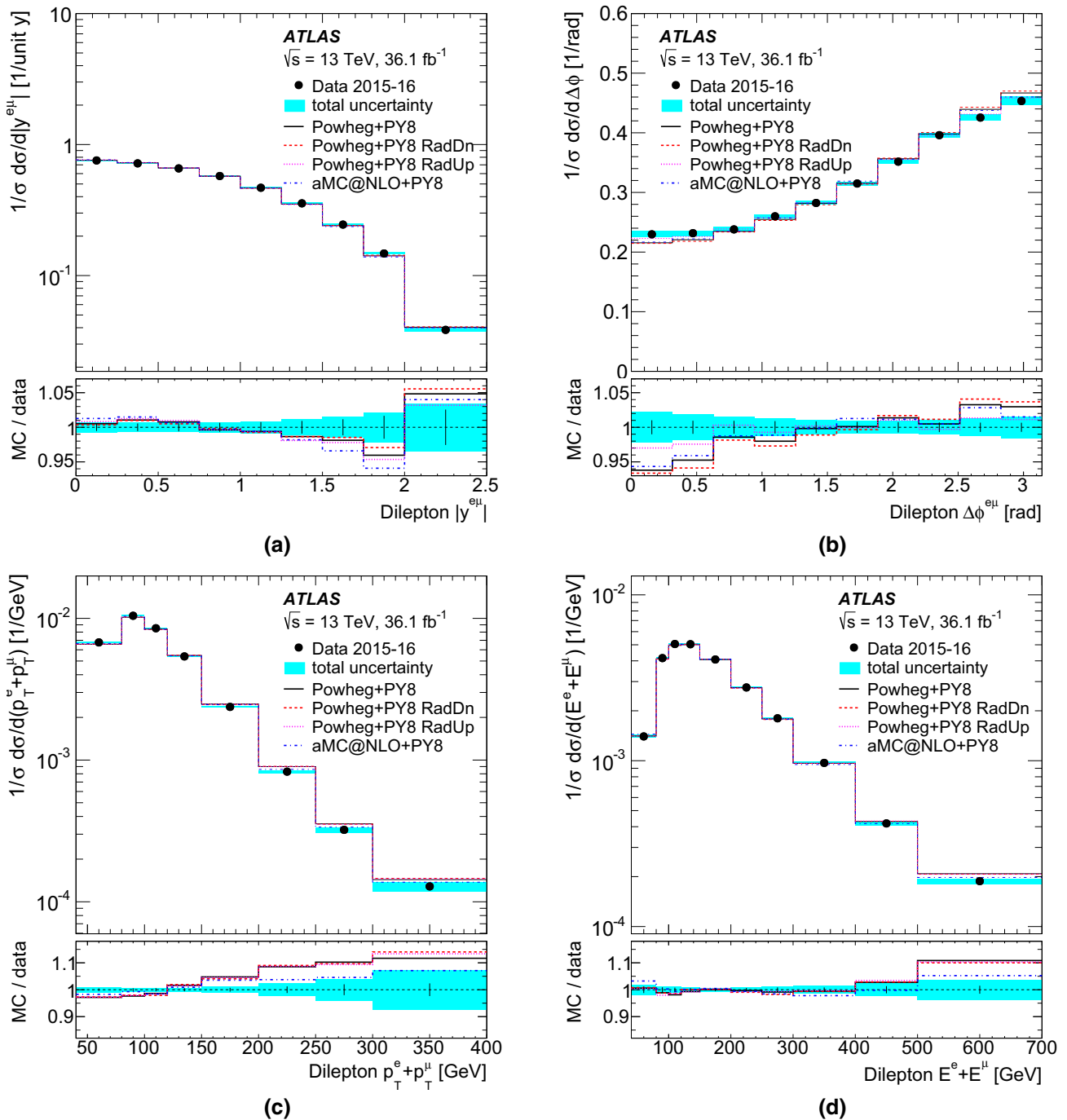


Fig. 13 Normalised differential cross-sections as a function of **a** $|y^{e\mu}|$, **b** $\Delta\phi^{e\mu}$, **c** $p_T^e + p_T^\mu$ and **d** $E^e + E^\mu$. The measured values are shown by the black points with error bars corresponding to the data statistical uncertainties and cyan bands corresponding to the total uncertainties in each bin, and include the contributions via $W \rightarrow \tau \rightarrow e/\mu$ decays. The lower plots show the ratios of predictions to data, with the error bars indicating the data statistical uncertainties and the cyan bands indicating the total uncertainties in the measurements

with the predictions from the baseline POWHEG + PYTHIA8 $t\bar{t}$ sample, POWHEG + PYTHIA8 samples with more or less parton-shower radiation (RadUp and RadDn), and an AMC@NLO + PYTHIA8 sample. The lower plots show the ratios of predictions to data, with the error bars indicating the data statistical uncertainties and the cyan bands indicating the total uncertainties in the measurements

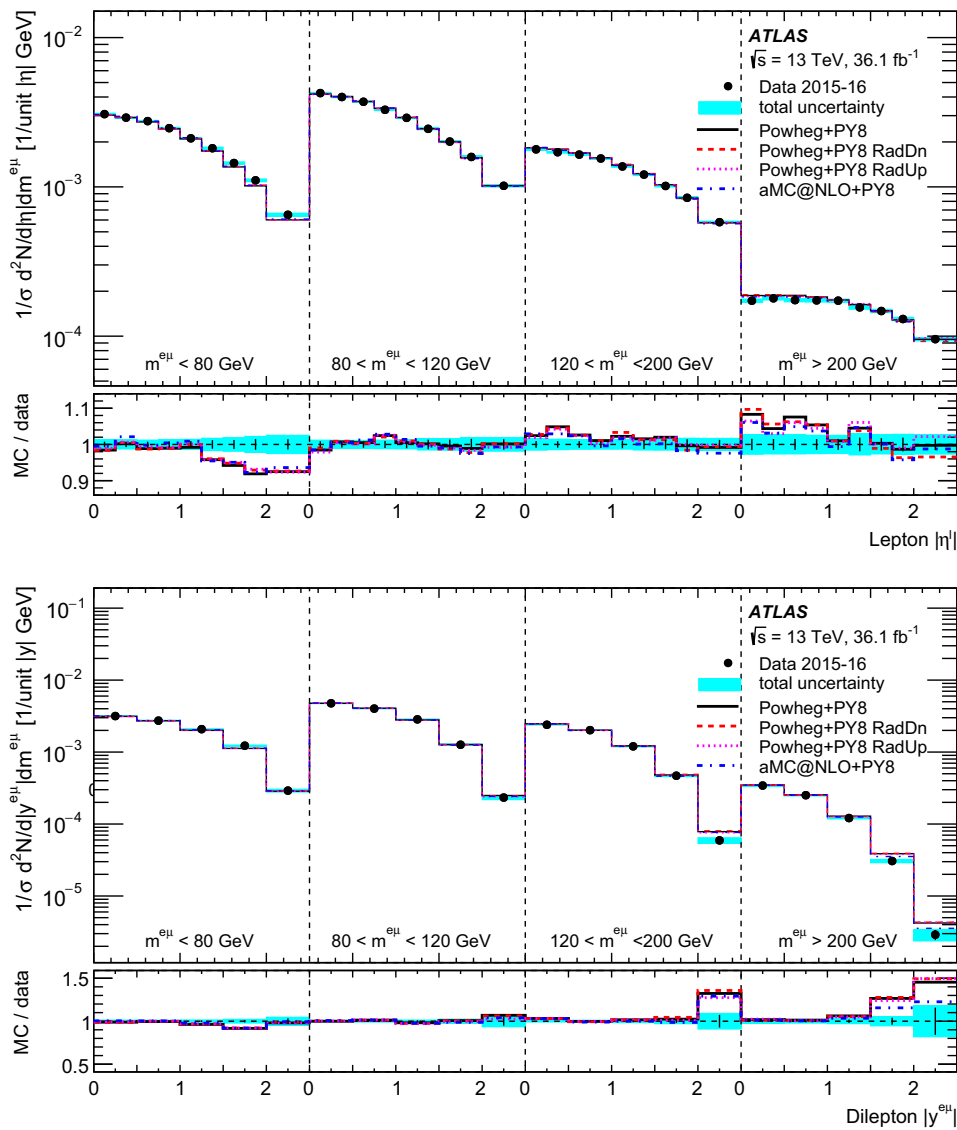


Fig. 14 Normalised double-differential cross-sections as functions of $|\eta^l|$ and $m^{e\mu}$ (top), and $|y^{e\mu}|$ and $m^{e\mu}$ (bottom). The measured values are shown by the black points with error bars corresponding to the data statistical uncertainties and cyan bands corresponding to the total uncertainties in each bin, and include the contributions via $W \rightarrow \tau \rightarrow e/\mu$ decays. The data points are placed at the centre of each bin. The

results are compared with the predictions from the baseline POWHEG + PYTHIA8 $t\bar{t}$ sample, POWHEG + PYTHIA8 samples with more or less parton-shower radiation (RadUp and RadDn), and an AMC@NLO + PYTHIA8 sample. The lower plots show the ratios of predictions to data, with the error bars indicating the data statistical uncertainties and the cyan bands indicating the total uncertainties in the measurements

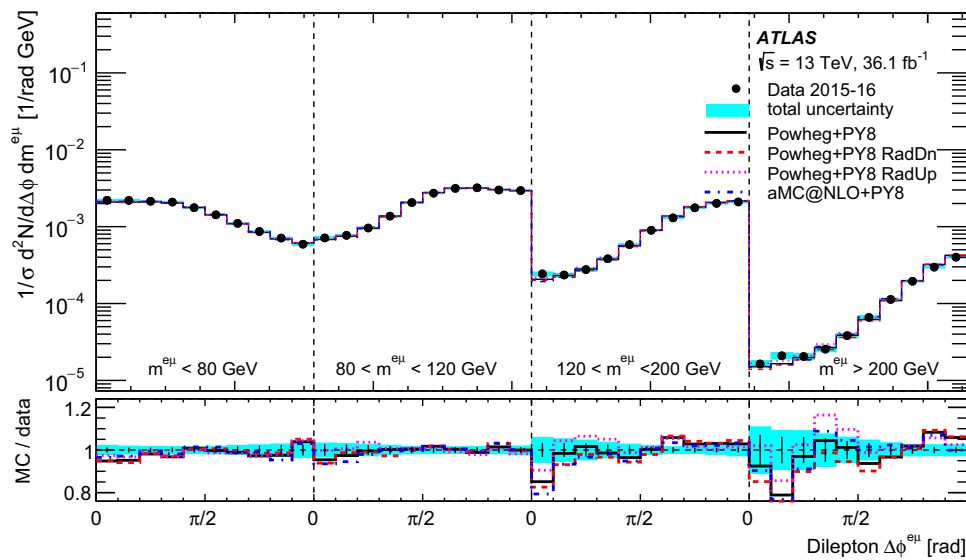


Fig. 15 Normalised double-differential cross-sections as a function of $\Delta\phi^{e\mu}$ and $m^{e\mu}$. The measured values are shown by the black points with error bars corresponding to the data statistical uncertainties and cyan bands corresponding to the total uncertainties in each bin, and include the contributions via $W \rightarrow \tau \rightarrow e/\mu$ decays. The data points are placed at the centre of each bin. The results are compared with the

predictions from the baseline POWHEG + PYTHIA8 $t\bar{t}$ sample, POWHEG + PYTHIA8 samples with more or less parton-shower radiation (RadUp and RadDn), and an AMC@NLO + PYTHIA8 sample. The lower plots show the ratios of predictions to data, with the error bars indicating the data statistical uncertainties and the cyan bands indicating the total uncertainties in the measurements

7.2 Comparison with event generator predictions

The measured normalised differential cross-sections are compared to a set of particle-level predictions from different Monte Carlo $t\bar{t}$ event generator configurations in Figs. 16, 17, 18, 19, 20, 21, 22. These figures show the ratios of each prediction to the data as functions of the differential variables, with the comparison organised into the four groups of samples summarised in Table 11. These include samples based on POWHEG or AMC@NLO for the NLO matrix-element generator, interfaced to PYTHIA8, PYTHIA6 or HERWIG7, and using various PDF sets. As well as NNPDF3.0 [44] used for the baseline samples, the global NLO PDF sets CT10 [18], CT14 [74], MMHT14 [77] and PDF4LHC_NLO_30 [76] are shown, together with the HERAPDF 2.0 PDF set, based mainly on deep inelastic scattering data [105]. Furthermore, the POWHEG + PYTHIA8 samples with more (denoted ‘RadUp’) or less (‘RadDn’) parton-shower radiation described in Sect. 2 are included, together with samples which differ from the baseline POWHEG + PYTHIA8 configuration only by changes of the factorisation and renormalisation scales μ_F and μ_R up and down by factors of two.

The baseline POWHEG + PYTHIA8 configuration is known to predict too hard a top quark p_T distribution compared to data at $\sqrt{s} = 13\text{ TeV}$ [92] and $\sqrt{s} = 8\text{ TeV}$ [106], and compared to NNLO QCD calculations [107]. To explore the effect of this mismodelling on the lepton differential distributions, the POWHEG + PYTHIA8 $t\bar{t}$ sample was reweighted accord-

ing to the top quark p_T in each event, using a linear function whose parameters were chosen so as to reproduce the measured top quark p_T distribution shown in Figure 19 of Ref. [92]; this sample is included in the first sample group and labelled ‘POWHEG + PY8 p_T rew’ in Figs. 16, 17, 18, 19, 20, 21, 22.

The compatibility of each prediction with each measured normalised distribution was tested using a χ^2 calculated as

$$\chi^2 = \mathbf{\Delta}_{(n-1)}^T \mathbf{S}_{(n-1)}^{-1} \mathbf{\Delta}_{(n-1)}, \tag{9}$$

where $\mathbf{\Delta}_{(n-1)}$ is the vector of differences between the measured and predicted normalised differential cross-section in each of the n bins, excluding the last one, and $\mathbf{S}_{(n-1)}^{-1}$ is the inverse of the corresponding covariance matrix, including both the experimental uncertainties in the measurement and the statistical uncertainties in the predictions. Correlations between the measurements in different bins were incorporated via off-diagonal terms in \mathbf{S} , and the last bin of each distribution was excluded to account for the degree of freedom lost to the normalisation condition. The resulting χ^2 values and corresponding probability p -values (for $n - 1$ degrees of freedom) are shown for each single-differential distribution and prediction in Table 12, and for the double-differential distributions and predictions in Table 13.

A number of observations can be made for the modelling of the individual lepton and dilepton distributions. The single-lepton p_T and dilepton $p_T^e + p_T^\mu$ distributions (Figs. 16a, 19a) are softer in the data than in all the POWHEG-

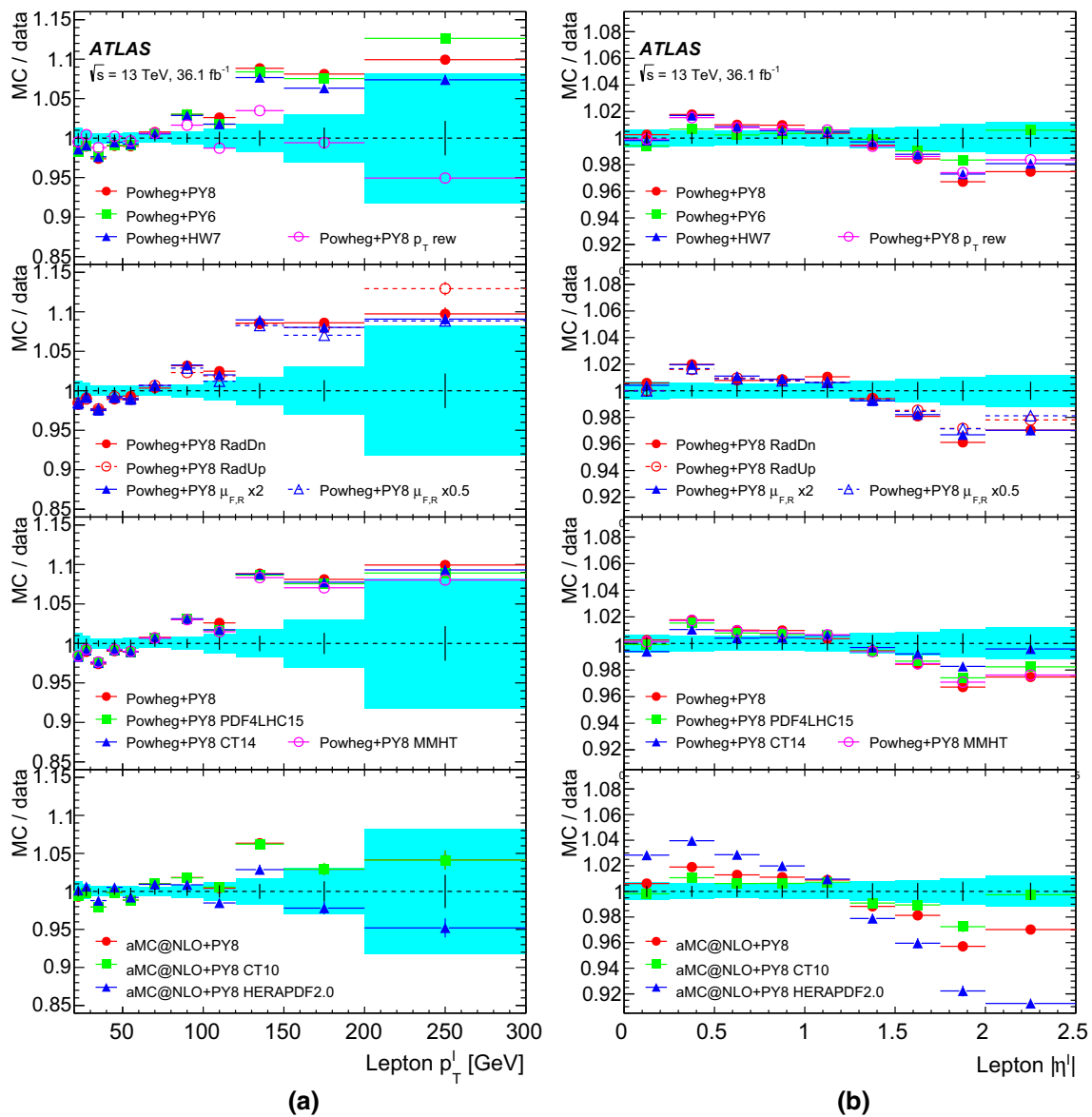


Fig. 16 Ratios of predictions of normalised differential cross-sections to data as a function of **a** p_T^ℓ and **b** $|\eta^\ell|$. The data statistical uncertainties are shown by the black error bars around a ratio of unity, and the total uncertainties are shown by the cyan bands. Several different $t\bar{t}$ predic-

tions are shown in each panel, grouped from top to bottom as shown in Table 11, and the error bars indicate the uncertainties due to the limited size of the simulated samples

based predictions, irrespective of the choice of parton shower, scale/tune settings or PDF. The AMC@NLO + PYTHIA8 samples agree better with data, especially when using the HERAPDF2.0 PDF set. Reweighting the top quark p_T in the POWHEG + PYTHIA8 sample also gives significantly better agreement. Similar features were seen in the comparisons of the p_T^ℓ and $p_T^e + p_T^\mu$ distributions at $\sqrt{s} = 8$ TeV [29], and in the p_T^ℓ distribution measured by CMS at $\sqrt{s} = 13$ TeV in a different fiducial region including requirements on jets [108].

The single-lepton $|\eta^\ell|$ distribution (Fig. 16b) is more forward than the predictions from either POWHEG + PYTHIA8

or AMC@NLO + PYTHIA8 with the NNPDF3.0 set, and agreement is improved by using CT10 or CT14. The MMHT and PDF4LHC15 PDF sets lie somewhere in between, but HERAPDF2.0 predicts much too central a distribution. The $|y^{e\mu}|$ distribution (Fig. 18a) shows a slightly different picture; again HERAPDF2.0 is in very poor agreement with the data, but all the other PDFs do reasonably well. These observations differ from those at $\sqrt{s} = 8$ TeV [29], where the HERAPDF 1.5 and 2.0 PDF sets were found to describe the data better than CT10, which was used as the default.

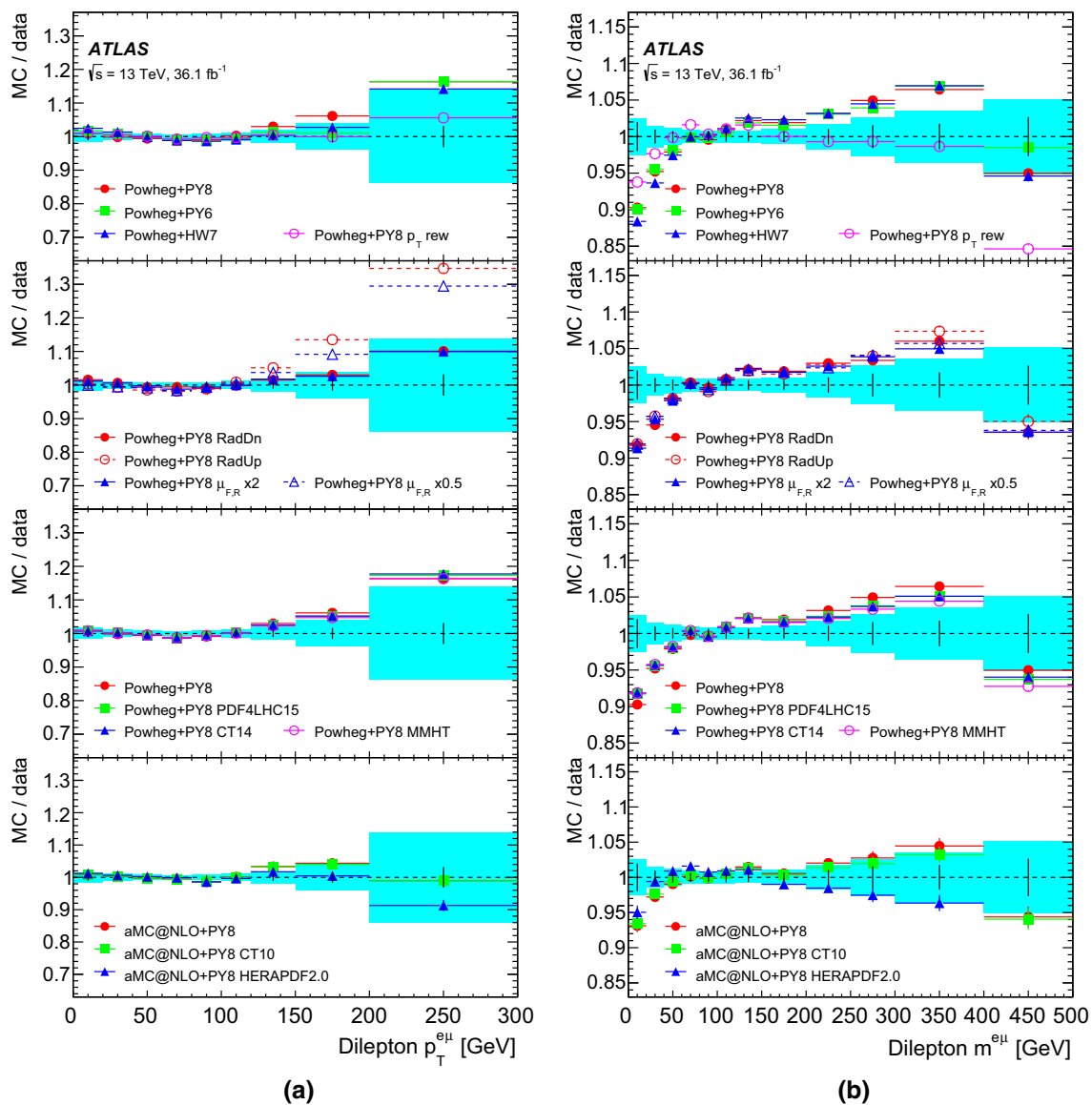


Fig. 17 Ratios of predictions of normalised differential cross-sections to data as a function of **a** $p_T^{e\mu}$ and **b** $m^{e\mu}$. The data statistical uncertainties are shown by the black error bars around a ratio of unity, and the total uncertainties are shown by the cyan bands. Several different

$t\bar{t}$ predictions are shown in each panel, grouped from top to bottom as shown in Table 11, and the error bars indicate the uncertainties due to the limited size of the simulated samples

All the generators model the $p_T^{e\mu}$ distribution well (Fig. 17a), with the exception of the POWHEG + PYTHIA8 RadUp configuration, and to a lesser extent, POWHEG + PYTHIA8 with reduced QCD scales. This distribution shows little sensitivity to PDFs. The $m^{e\mu}$ distribution (Fig. 17b) is poorly modelled by all POWHEG-based samples. The AMC@NLO + PYTHIA8 samples do better (except when HERAPDF2.0 is used), but still fail to describe the data at very low $m^{e\mu}$.

The data have a less steep $\Delta\phi^{e\mu}$ distribution than all the predictions (Fig. 18b), although the POWHEG + PYTHIA8 RadUp and reduced QCD scale samples come close, as does the sample with reweighted top quark p_T . The tensions

between data and predictions are smaller than in the dedicated ATLAS $t\bar{t}$ spin correlation analysis [109], but the latter analysis has a more restrictive fiducial region definition, with higher lepton p_T thresholds and a requirement of at least two jets.

Finally, the $E^e + E^\mu$ distribution (Fig. 19b) is reasonably described by the baseline POWHEG + PYTHIA8 prediction except at high $E^e + E^\mu$, where agreement is improved by top quark p_T reweighting. The distribution shows some sensitivity to PDFs, with NNPDF3.0 agreeing with data better than CT10, and HERAPDF2.0 again agreeing very poorly with data.

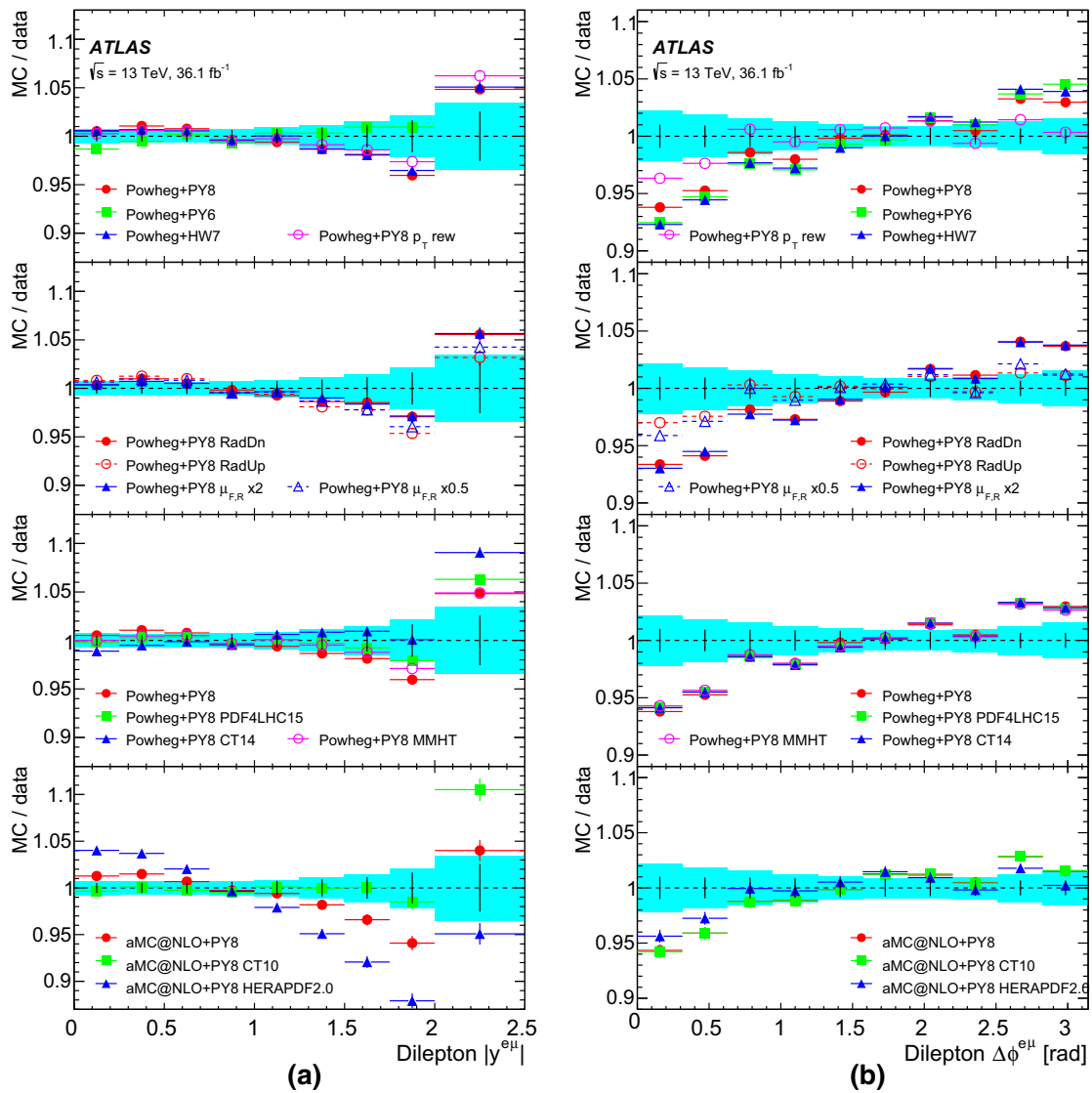


Fig. 18 Ratios of predictions of normalised differential cross-sections to data as a function of **a** $|\eta^{e\mu}|$ and **b** $\Delta\phi^{e\mu}$. The data statistical uncertainties are shown by the black error bars around a ratio of unity, and the total uncertainties are shown by the cyan bands. Several different

$t\bar{t}$ predictions are shown in each panel, grouped from top to bottom as shown in Table 11, and the error bars indicate the uncertainties due to the limited size of the simulated samples

The comparisons of normalised double-differential cross-section measurements and predictions in Figs. 20, 21, 22 reflect those seen in the single-differential results, although generally with reduced significance due to the larger per-bin statistical uncertainties. The χ^2 and probabilities shown in Table 13 are all poor, driven by poor agreement of the measured $m^{e\mu}$ distribution and predictions already visible in Fig. 17b. The largest differences between the models are seen at low $m^{e\mu}$ for $|\eta^\ell|$, whereas the differences become more pronounced at high $m^{e\mu}$ for $|y^{e\mu}|$. Similar trends in $\Delta\phi^{e\mu}$ are visible in all $m^{e\mu}$ bins in Fig. 22, despite the shape of the overall $\Delta\phi^{e\mu}$ distribution changing significantly across the $m^{e\mu}$ bins, as shown in Fig. 15. This distribution is

again best described by the POWHEG + PYTHIA8 predictions with increased radiation (RadUp), reduced QCD scales, or reweighted top quark p_T .

The χ^2 computation of Eq. (9) was extended to consider several normalised distributions simultaneously. The statistical correlations between distributions were evaluated using pseudo-experiments, and systematic uncertainties were assumed to be correlated between distributions. Five sets of combined distributions were considered: p_T^ℓ and $p_T^{e\mu}$; $p_T^{e\mu}$, $m^{e\mu}$ and $p_T^e + p_T^\mu$; $|\eta^\ell|$ and $|y^{e\mu}|$; $|\eta^\ell|$, $|y^{e\mu}|$ and $E^e + E^\mu$; and the combination of all eight single-differential distributions.

The resulting χ^2 and p -values are shown for each combination and prediction in Table 14. The best descriptions of

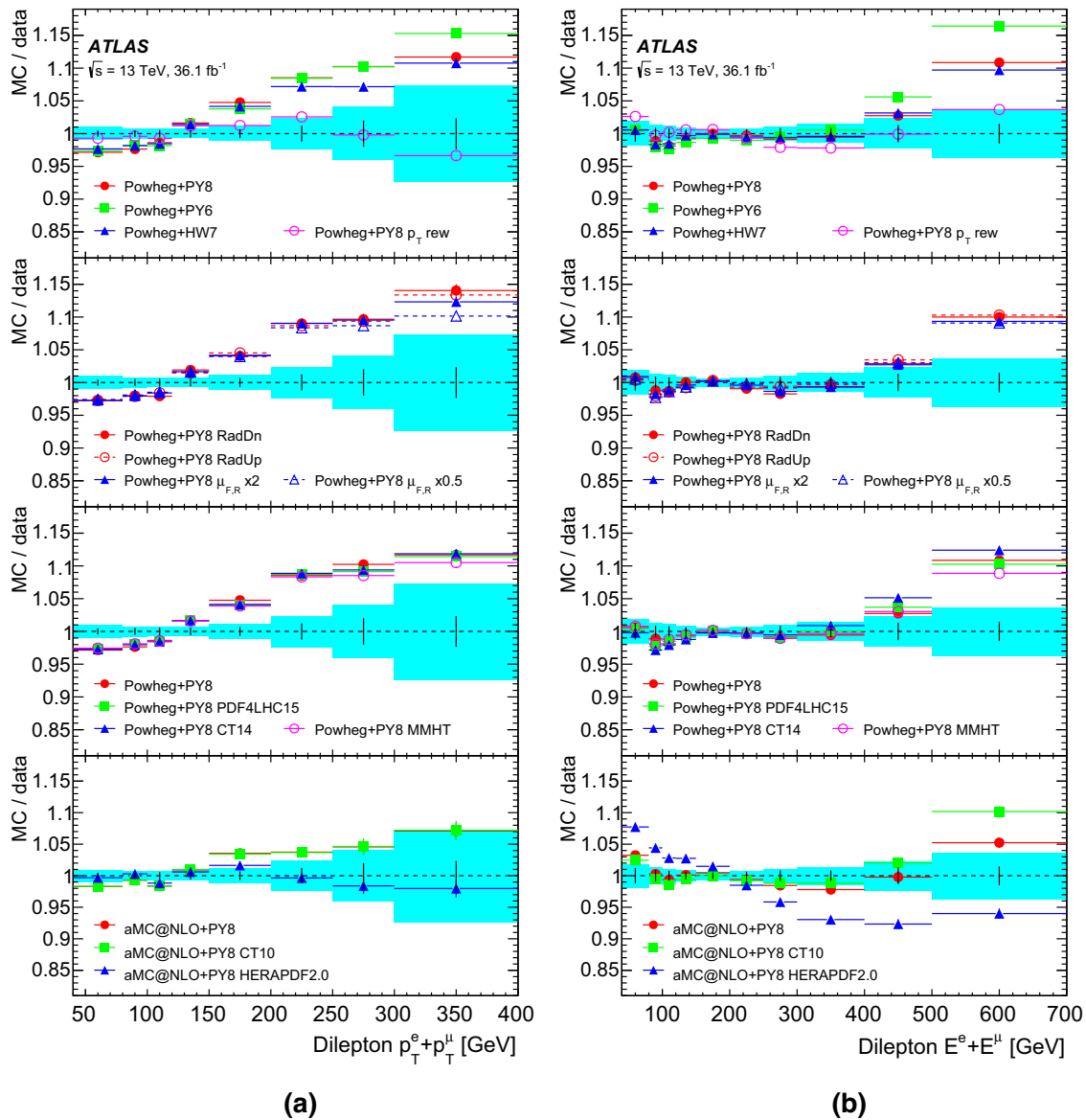


Fig. 19 Ratios of predictions of normalised differential cross-sections to data as a function of **a** $p_T^e + p_T^\mu$ and **b** $E^e + E^\mu$. The data statistical uncertainties are shown by the black error bars around a ratio of unity, and the total uncertainties are shown by the cyan bands. Several differ-

ent $t\bar{t}$ predictions are shown in each panel, grouped from top to bottom as shown in Table 11, and the error bars indicate the uncertainties due to the limited size of the simulated samples

p_T and $p_T^e + p_T^\mu$ are achieved by POWHEG + PYTHIA8 with top quark p_T reweighting, or by AMC@NLO + PYTHIA8, particularly with the HERAPDF2.0 PDF set. Either NLO generator combined with several PDF sets can describe the $|\eta^\ell|$ and $|y^{e\mu}|$ distributions, although only the sample with top quark p_T reweighting provides a reasonable description once $E^e + E^\mu$ is also included. No samples describe the combinations including $m^{e\mu}$, as this variable is not modelled by any of the generator configurations.

8 Conclusions

The inclusive $t\bar{t}$ production cross-section $\sigma_{t\bar{t}}$ has been measured in pp collisions at $\sqrt{s} = 13$ TeV using 36.1 fb^{-1} of data recorded by the ATLAS experiment at the LHC in 2015–2016. Using events with an opposite-sign $e\mu$ pair and one or two b -tagged jets, the result is:

$$\sigma_{t\bar{t}} = 826.4 \pm 3.6 \text{ (stat)} \pm 11.5 \text{ (syst)} \pm 15.7 \text{ (lumi)} \pm 1.9 \text{ (beam)} \text{ pb,}$$

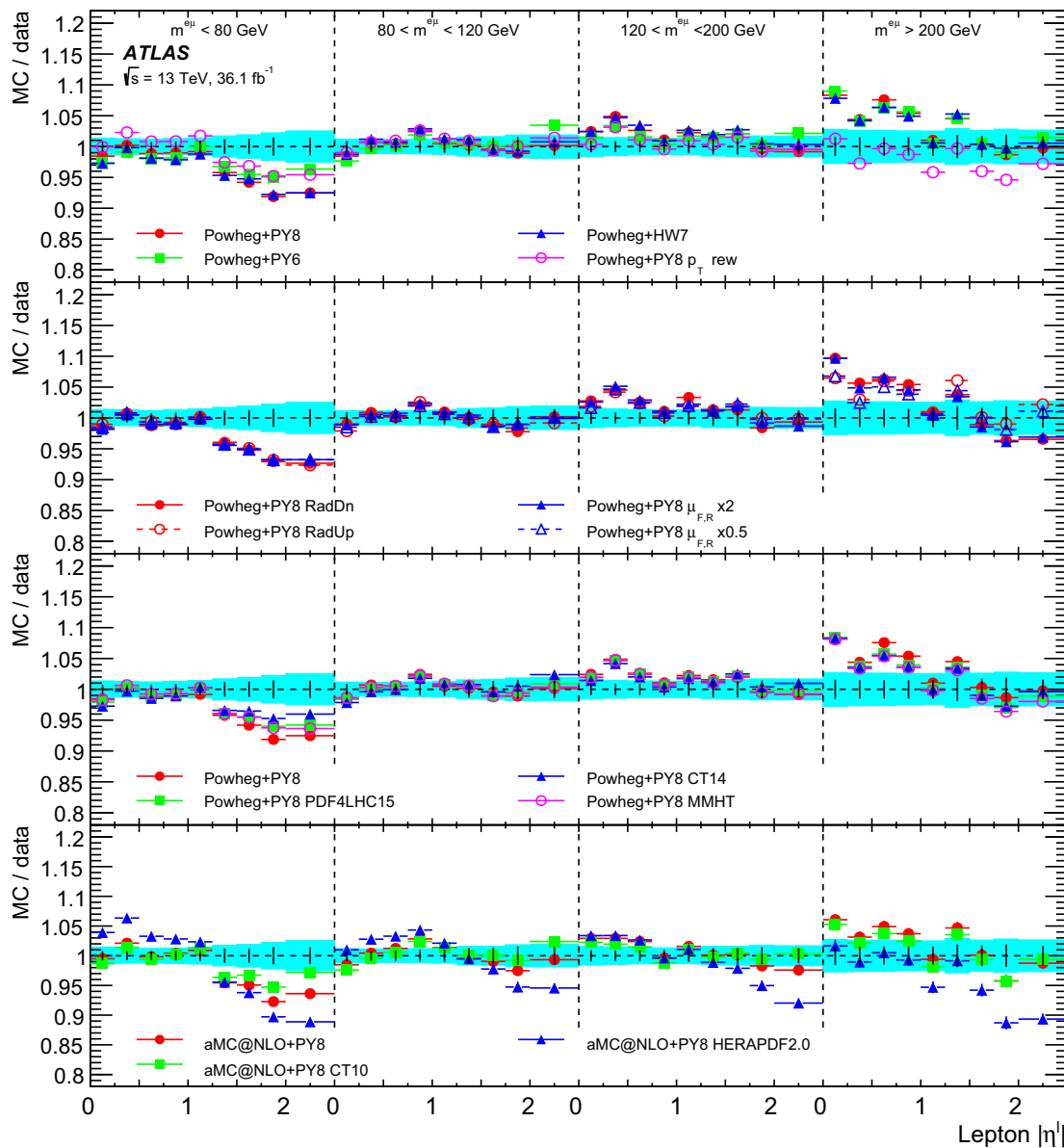


Fig. 20 Ratios of predictions of the normalised double-differential cross-sections to data as a function of $|\eta^\ell|$ and $m^{e\mu}$. The data statistical uncertainties are shown by the black error bars around a ratio of unity, and the total uncertainties are shown by the cyan bands. The

vertical dotted lines indicate the four bins of $m^{e\mu}$. Several different $t\bar{t}$ predictions are shown in each panel, grouped from top to bottom as shown in Table 11, and the error bars indicate the uncertainties due to the limited size of the simulated samples

where the four uncertainties are due to data statistics, experimental and theoretical systematic effects, and the knowledge of the integrated luminosity and of the LHC beam energy. The result is consistent with NNLO+NNLL QCD predictions. Fiducial cross-sections corresponding to the experimental acceptance for the leptons, with and without a correction for the contribution of leptons from leptonic τ decays, have also been measured. The dependence of predictions for $\sigma_{t\bar{t}}$ on the top quark pole mass m_t^{pole} has been exploited to

determine a mass value of

$$m_t^{\text{pole}} = 173.1^{+2.0}_{-2.1} \text{ GeV}$$

from the inclusive cross-section, using the predictions derived with the CT14 PDF set. This result is compatible with other top quark mass determinations using a variety of techniques. The inclusive cross-section has also been combined with previous measurements at $\sqrt{s} = 7$ and 8 TeV to determine ratios of $t\bar{t}$ cross-sections, and double ratios of $t\bar{t}$ to Z cross-

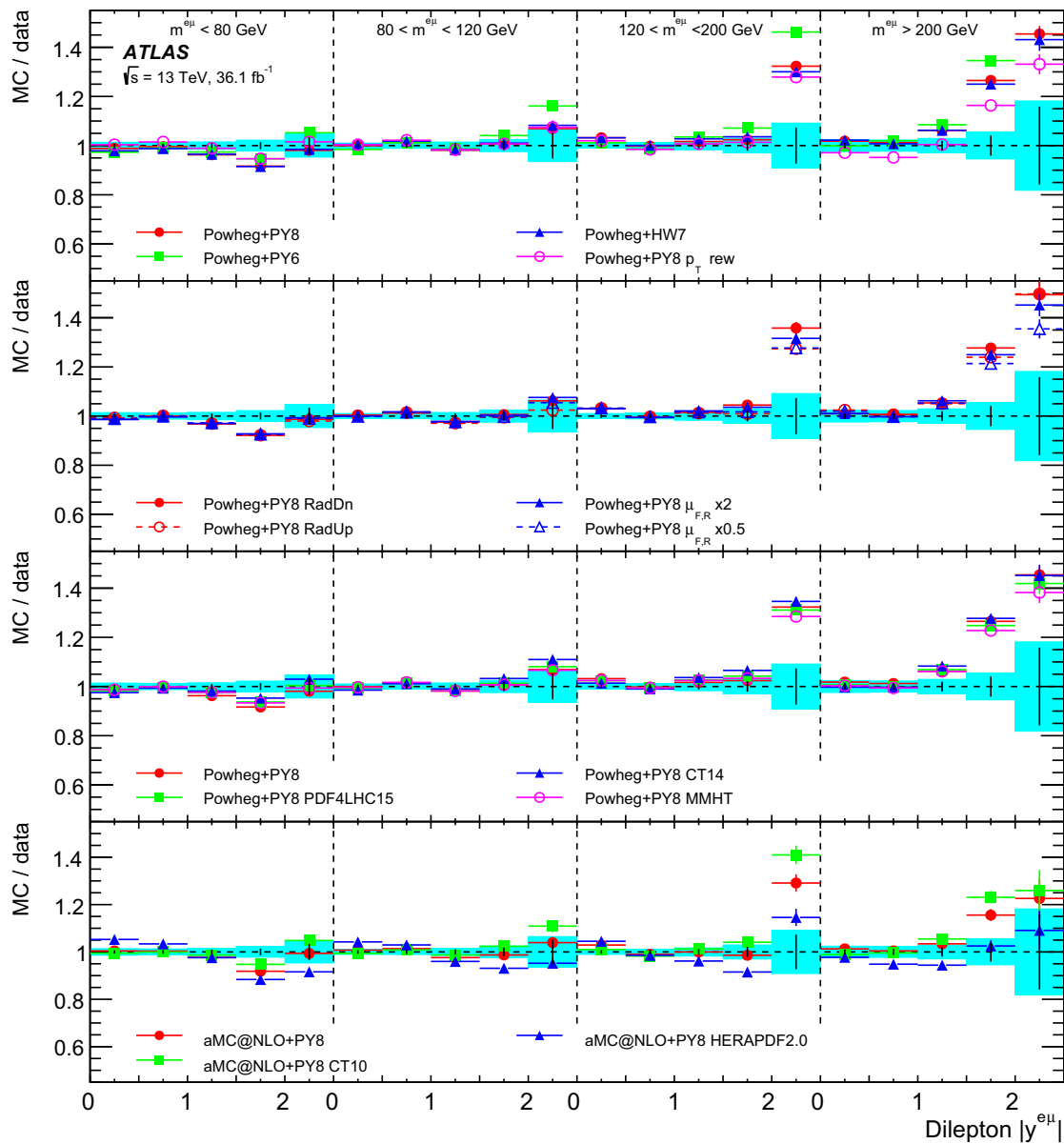


Fig. 21 Ratios of predictions of the normalised double-differential cross-sections to data as a function of $|y^{e\mu}|$ and $m^{e\mu}$. The data statistical uncertainties are shown by the black error bars around a ratio of unity, and the total uncertainties are shown by the cyan bands. The

vertical dotted lines indicate the four bins of $m^{e\mu}$. Several different $t\bar{t}$ predictions are shown in each panel, grouped from top to bottom as shown in Table 11, and the error bars indicate the uncertainties due to the limited size of the simulated samples

sections, at different energies, which are found to be compatible with predictions using a range of PDF sets.

The same data sample has been used to measure eight single-differential and three double-differential cross-sections as a function of lepton and dilepton kinematic variables, with uncertainties as small as 0.6% for normalised distributions in some parts of the fiducial region. The measured distributions are generally well described by the NLO matrix-element generators POWHEG and AMC@NLO when interfaced to PYTHIA or HERWIG for parton shower,

hadronisation and underlying-event modelling. However, the POWHEG-based predictions give lepton p_T spectra that are significantly harder than those observed in data, and none of the predictions describe the low-mass part of the dilepton invariant mass distribution. These differential cross-section results have sensitivity to PDFs and can be used as the basis for a precise determination of the top quark mass based on lepton kinematics.

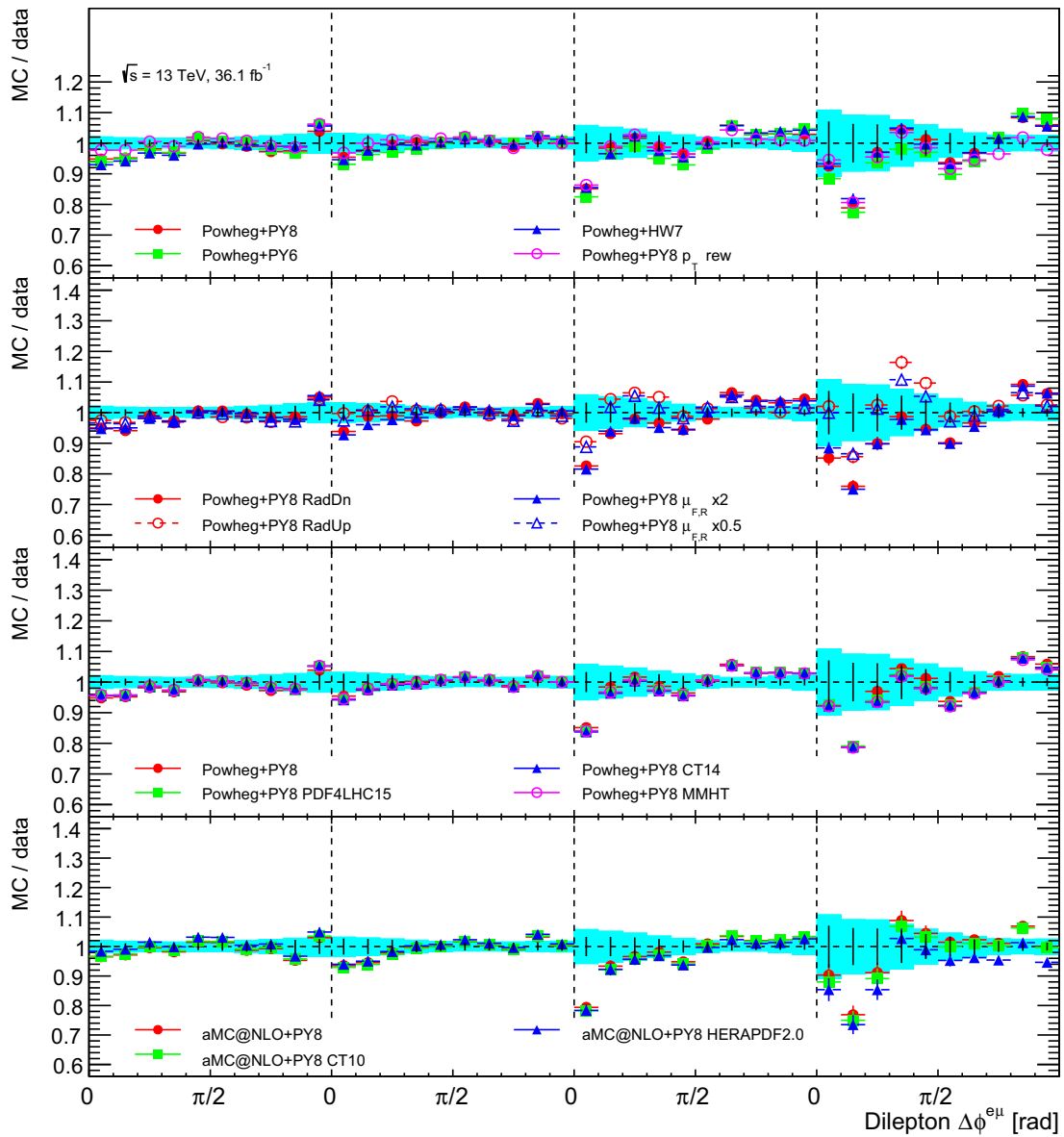


Fig. 22 Ratios of predictions of the normalised double-differential cross-sections to data as a function of $\Delta\phi^{e\mu}$ and $m^{e\mu}$. The data statistical uncertainties are shown by the black error bars around a ratio of unity, and the total uncertainties are shown by the cyan bands. The

vertical dotted lines indicate the four bins of $m^{e\mu}$. Several different $t\bar{t}$ predictions are shown in each panel, grouped from top to bottom as shown in Table 11, and the error bars indicate the uncertainties due to the limited size of the simulated samples

Table 11 Summary of particle-level simulation samples used in the comparison with the corrected data distributions in Sect. 7.2, giving the matrix-element generator, PDF set, parton shower and associated tune parameter set, and other relevant settings. The top quark

mass was set to $m_t = 172.5$ GeV in all samples. The four groups shown correspond to the four panels for each measured distribution shown in Figs. 16, 17, 18, 19, 20, 21, 22. The baseline POWHEG + PYTHIA8 configuration appears in both groups 1 and 3

	Matrix element	PDF	Parton shower/tune	Comments
1	POWHEG	NNPDF3.0	PYTHIA8 A14	$h_{\text{damp}} = \frac{3}{2}m_t$
	POWHEG	CT10	PYTHIA6 P2012	$h_{\text{damp}} = m_t$
	POWHEG	NNPDF3.0	HERWIG7 H7UE	$h_{\text{damp}} = \frac{3}{2}m_t$
	POWHEG	NNPDF3.0	PYTHIA8 A14	top quark p_T reweighted to Ref. [92]
2	POWHEG	NNPDF3.0	PYTHIA8 A14v3cDo	$h_{\text{damp}} = \frac{3}{2}m_t, 2\mu_{F,R}$ (RadDn)
	POWHEG	NNPDF3.0	PYTHIA8 A14v3cUp	$h_{\text{damp}} = 3m_t, \frac{1}{2}\mu_{F,R}$ (RadUp)
	POWHEG	NNPDF3.0	PYTHIA8 A14	$h_{\text{damp}} = \frac{3}{2}m_t, 2\mu_{F,R}$
	POWHEG	NNPDF3.0	PYTHIA8 A14	$h_{\text{damp}} = \frac{3}{2}m_t, \frac{1}{2}\mu_{F,R}$
3	POWHEG	NNPDF3.0	PYTHIA8 A14	$h_{\text{damp}} = \frac{3}{2}m_t$
	POWHEG	PDF4LHC15	PYTHIA8 A14	$h_{\text{damp}} = \frac{3}{2}m_t$
	POWHEG	CT14	PYTHIA8 A14	$h_{\text{damp}} = \frac{3}{2}m_t$
	POWHEG	MMHT	PYTHIA8 A14	$h_{\text{damp}} = \frac{3}{2}m_t$
4	AMC@NLO	NNPDF3.0	PYTHIA8 A14	
	AMC@NLO	CT10	PYTHIA8 A14	
	AMC@MLO	HERAPDF2.0	PYTHIA8 A14	

Table 12 χ^2 values (top) and associated probabilities (bottom) for comparison of normalised measured single-differential fiducial cross-sections with various $t\bar{t}$ simulation samples. Probabilities smaller than 10^{-10} are shown as zero

Generator N_{dof}	p_T^ℓ 10	$ \eta^\ell $ 8	$p_T^{e\mu}$ 8	$m^{e\mu}$ 11	$ y^{e\mu} $ 8	$\Delta\phi^{e\mu}$ 9	$p_T^e + p_T^\mu$ 7	$E^e + E^\mu$ 9
POWHEG + PY8	43.7	19.5	8.6	44.3	11.4	14.4	32.5	18.4
POWHEG + PY6 CT10	36.1	7.9	9.3	33.0	16.2	16.2	21.9	30.5
POWHEG + HW7	34.8	15.9	11.5	62.7	9.4	17.3	23.0	14.7
POWHEG + PY8 p_T rew.	20.2	14.7	2.3	38.3	8.4	12.7	9.4	14.0
POWHEG + PY8 RadDn	40.0	24.2	6.1	44.3	9.2	16.3	29.0	20.1
POWHEG + PY8 RadUp	33.0	16.3	21.9	35.3	12.3	6.4	26.7	16.5
POWHEG + PY8 $\mu_{F,R} \times 2$	46.5	21.6	6.2	42.6	8.5	16.5	28.9	17.1
POWHEG + PY8 $\mu_{F,R} \times 0.5$	39.8	17.3	11.4	38.0	10.7	10.9	27.6	14.2
POWHEG + PY8 PDF4LHC15	43.4	14.6	7.4	39.0	6.2	13.5	28.0	15.9
POWHEG + PY8 CT14	44.1	9.3	7.6	37.0	8.2	13.5	28.5	18.2
POWHEG + PY8 MMHT	41.2	17.7	6.9	39.0	6.3	13.2	26.3	14.3
AMC@NLO + PY8	26.2	25.7	11.4	19.7	16.7	13.2	12.5	14.0
AMC@NLO + PY8 CT10	24.9	11.7	10.6	16.9	10.0	13.4	12.0	19.0
AMC@NLO + PY8 HERA2	17.1	96.6	6.9	26.0	68.5	12.5	6.1	38.4
POWHEG + PY8	$4 \cdot 10^{-6}$	0.012	0.37	$6 \cdot 10^{-6}$	0.18	0.11	$3 \cdot 10^{-5}$	0.030
POWHEG + PY6 CT10	$8 \cdot 10^{-5}$	0.45	0.32	$5 \cdot 10^{-4}$	0.039	0.062	$3 \cdot 10^{-3}$	$4 \cdot 10^{-4}$
POWHEG + HW7	$1 \cdot 10^{-4}$	0.043	0.18	$3 \cdot 10^{-9}$	0.31	0.045	$2 \cdot 10^{-3}$	0.098
POWHEG + PY8 p_T rew.	0.028	0.065	0.97	$7 \cdot 10^{-5}$	0.39	0.18	0.23	0.12
POWHEG + PY8 RadDn	$2 \cdot 10^{-5}$	$2 \cdot 10^{-3}$	0.64	$6 \cdot 10^{-6}$	0.32	0.060	$1 \cdot 10^{-4}$	0.017
POWHEG + PY8 RadUp	$3 \cdot 10^{-4}$	0.038	$5 \cdot 10^{-3}$	$2 \cdot 10^{-4}$	0.14	0.70	$4 \cdot 10^{-4}$	0.057

Table 12 continued

Generator N_{dof}	p_T^ℓ 10	$ \eta^\ell $ 8	$p_T^{e\mu}$ 8	$m^{e\mu}$ 11	$ y^{e\mu} $ 8	$\Delta\phi^{e\mu}$ 9	$p_T^\ell + p_T^\mu$ 7	$E^e + E^\mu$ 9
POWHEG + PY8 $\mu_{F,R} \times 2$	$1 \cdot 10^{-6}$	$6 \cdot 10^{-3}$	0.62	$1 \cdot 10^{-5}$	0.39	0.056	$1 \cdot 10^{-4}$	0.048
POWHEG + PY8 $\mu_{F,R} \times 0.5$	$2 \cdot 10^{-5}$	0.027	0.18	$8 \cdot 10^{-5}$	0.22	0.28	$3 \cdot 10^{-4}$	0.12
POWHEG + PY8 PDF4LHC15	$4 \cdot 10^{-6}$	0.067	0.49	$5 \cdot 10^{-5}$	0.62	0.14	$2 \cdot 10^{-4}$	0.068
POWHEG + PY8 CT14	$3 \cdot 10^{-6}$	0.32	0.47	$1 \cdot 10^{-4}$	0.42	0.14	$2 \cdot 10^{-4}$	0.033
POWHEG + PY8 MMHT	$1 \cdot 10^{-5}$	0.024	0.55	$5 \cdot 10^{-5}$	0.62	0.15	$5 \cdot 10^{-4}$	0.11
AMC@NLO + PY8	$3 \cdot 10^{-3}$	$1 \cdot 10^{-3}$	0.18	0.049	0.034	0.15	0.086	0.12
AMC@NLO + PY8 CT10	$5 \cdot 10^{-3}$	0.16	0.23	0.11	0.27	0.15	0.10	0.025
AMC@NLO + PY8 HERA2	0.073	0	0.54	$6 \cdot 10^{-3}$	0	0.19	0.53	$1 \cdot 10^{-5}$

Table 13 χ^2 values (top) and associated probabilities (bottom) for comparison of normalised measured double-differential fiducial cross-sections with various $t\bar{t}$ simulation samples. Probabilities smaller than 10^{-10} are shown as zero

Generator N_{dof}	$ \eta^\ell \times m^{e\mu}$ 35	$ y^{e\mu} \times m^{e\mu}$ 19	$ \Delta\phi^\ell \times m^{e\mu}$ 39
POWHEG + PY8	53.1	72.3	65.4
POWHEG + PY6 CT10	45.9	92.9	79.5
POWHEG + HW7	49.3	67.4	63.7
POWHEG + PY8 p_T rew.	47.1	56.1	51.4
POWHEG + PY8 RadDn	57.1	74.2	69.9
POWHEG + PY8 RadUp	50.6	62.5	51.7
POWHEG + PY8 $\mu_{F,R} \times 2$	60.7	68.4	71.1
POWHEG + PY8 $\mu_{F,R} \times 0.5$	50.3	60.0	52.0
POWHEG + PY8 PDF4LHC15	51.5	61.5	59.7
POWHEG + PY8 CT14	50.6	67.3	60.0
POWHEG + PY8 MMHT	53.7	57.9	58.7
AMC@NLO + PY8	55.0	45.9	58.2
AMC@NLO + PY8 CT10	43.7	50.6	59.5
AMC@NLO + PY8 HERA2	130.3	97.6	58.0
POWHEG + PY8	0.026	$4 \cdot 10^{-8}$	$5 \cdot 10^{-3}$
POWHEG + PY6 CT10	0.10	0	$1 \cdot 10^{-4}$
POWHEG + HW7	0.055	$2 \cdot 10^{-7}$	$8 \cdot 10^{-3}$
POWHEG + PY8 p_T rew.	0.084	$2 \cdot 10^{-5}$	0.088
POWHEG + PY8 RadDn	0.011	$2 \cdot 10^{-8}$	$2 \cdot 10^{-3}$
POWHEG + PY8 RadUp	0.042	$2 \cdot 10^{-6}$	0.083
POWHEG + PY8 $\mu_{F,R} \times 2$	$5 \cdot 10^{-3}$	$2 \cdot 10^{-7}$	$1 \cdot 10^{-3}$
POWHEG + PY8 $\mu_{F,R} \times 0.5$	0.045	$4 \cdot 10^{-6}$	0.079
POWHEG + PY8 PDF4LHC15	0.036	$2 \cdot 10^{-6}$	0.018
POWHEG + PY8 CT14	0.042	$3 \cdot 10^{-7}$	0.017
POWHEG + PY8 MMHT	0.023	$8 \cdot 10^{-6}$	0.022
AMC@NLO + PY8	0.017	$5 \cdot 10^{-4}$	0.024
AMC@NLO + PY8 CT10	0.15	$1 \cdot 10^{-4}$	0.019
AMC@NLO + PY8 HERA2	0	0	0.026

Table 14 χ^2 values (top) and associated probabilities (bottom) for comparison of combinations of measured normalised differential fiducial cross-sections with various $t\bar{t}$ simulation samples. The last column gives the results for the combination of all eight measured single-differential distributions. Probabilities smaller than 10^{-10} are shown as zero

Generator	$p_T^\ell, p_T^e + p_T^\mu$	$p_T^{e\mu}, m^{e\mu}, p_T^e + p_T^\mu$	$ \eta^\ell , y^{e\mu} $	$ \eta^\ell , y^{e\mu} , E^e + E^\mu$	All 8 dists.
N_{dof}	17	26	16	25	70
POWHEG + PY8	52.2	92.8	31.2	51.5	176.5
POWHEG + PY6 CT10	42.9	87.9	31.0	58.0	176.6
POWHEG + HW7	42.5	97.4	25.7	41.6	169.8
POWHEG + PY8 p_T rew.	27.5	57.4	25.4	36.5	137.6
POWHEG + PY8 RadDn	49.7	110.8	37.8	58.3	193.9
POWHEG + PY8 RadUp	42.9	71.8	25.5	44.2	151.8
POWHEG + PY8 $\mu_{F,R} \times 2$	54.5	111.1	35.6	54.4	195.0
POWHEG + PY8 $\mu_{F,R} \times 0.5$	50.5	71.3	26.3	42.8	160.4
POWHEG + PY8 PDF4LHC15	52.2	89.7	26.7	44.1	167.1
POWHEG + PY8 CT14	52.9	91.5	26.6	44.8	170.2
POWHEG + PY8 MMHT	49.9	89.4	28.7	44.8	167.6
AMC@NLO + PY8	33.2	46.3	37.1	49.6	131.9
AMC@NLO + PY8 CT10	31.6	46.7	26.2	43.0	122.9
AMC@NLO + PY8 HERA2	23.1	51.5	119.0	132.8	229.8
POWHEG + PY8	$2 \cdot 10^{-5}$	$2 \cdot 10^{-9}$	0.013	$1 \cdot 10^{-3}$	0
POWHEG + PY6 CT10	$5 \cdot 10^{-4}$	$1 \cdot 10^{-8}$	0.014	$2 \cdot 10^{-4}$	0
POWHEG + HW7	$6 \cdot 10^{-4}$	$3 \cdot 10^{-10}$	0.058	0.020	$3 \cdot 10^{-10}$
POWHEG + PY8 p_T rew.	0.052	$4 \cdot 10^{-4}$	0.062	0.064	$3 \cdot 10^{-6}$
POWHEG + PY8 RadDn	$5 \cdot 10^{-5}$	0	$2 \cdot 10^{-3}$	$2 \cdot 10^{-4}$	0
POWHEG + PY8 RadUp	$5 \cdot 10^{-4}$	$4 \cdot 10^{-6}$	0.062	0.010	$6 \cdot 10^{-8}$
POWHEG + PY8 $\mu_{F,R} \times 2$	$8 \cdot 10^{-6}$	0	$3 \cdot 10^{-3}$	$6 \cdot 10^{-4}$	0
POWHEG + PY8 $\mu_{F,R} \times 0.5$	$4 \cdot 10^{-5}$	$4 \cdot 10^{-6}$	0.049	0.015	$5 \cdot 10^{-9}$
POWHEG + PY8 PDF4LHC15	$2 \cdot 10^{-5}$	$6 \cdot 10^{-9}$	0.045	0.011	$7 \cdot 10^{-10}$
POWHEG + PY8 CT14	$2 \cdot 10^{-5}$	$3 \cdot 10^{-9}$	0.046	$9 \cdot 10^{-3}$	$3 \cdot 10^{-10}$
POWHEG + PY8 MMHT	$4 \cdot 10^{-5}$	$7 \cdot 10^{-9}$	0.026	$9 \cdot 10^{-3}$	$6 \cdot 10^{-10}$
AMC@NLO + PY8	0.011	$9 \cdot 10^{-3}$	$2 \cdot 10^{-3}$	$2 \cdot 10^{-3}$	$1 \cdot 10^{-5}$
AMC@NLO + PY8 CT10	0.017	$8 \cdot 10^{-3}$	0.051	0.014	$1 \cdot 10^{-4}$
AMC@NLO + PY8 HERA2	0.14	$2 \cdot 10^{-3}$	0	0	0

Acknowledgements We thank CERN for the very successful operation of the LHC, as well as the support staff from our institutions without whom ATLAS could not be operated efficiently. We acknowledge the support of ANPCyT, Argentina; YerPhI, Armenia; ARC, Australia; BMWFW and FWF, Austria; ANAS, Azerbaijan; SSTC, Belarus; CNPq and FAPESP, Brazil; NSERC, NRC and CFI, Canada; CERN; CONICYT, Chile; CAS, MOST and NSFC, China; COLCIENCIAS, Colombia; MSMT CR, MPO CR and VSC CR, Czech Republic; DNRF and DNSRC, Denmark; IN2P3-CNRS and CEA-DRF/IRFU, France; SRNSFG, Georgia; BMBF, HGF and MPG, Germany; GSRT, Greece; RGC and Hong Kong SAR, China; ISF and Benozziyo Center, Israel; INFN, Italy; MEXT and JSPS, Japan; CNRST, Morocco; NWO, Netherlands; RCN, Norway; MNiSW and NCN, Poland; FCT, Portugal; MNE/IFA, Romania; MES of Russia and NRC KI, Russian Federation; JINR; MESTD, Serbia; MSSR, Slovakia; ARRS and MIZŠ, Slovenia; DST/NRF, South Africa; MINECO, Spain; SRC and Wallenberg Foundation, Sweden; SERI, SNSF and Cantons of Bern and Geneva, Switzerland; MOST, Taiwan; TAEC, Turkey; STFC, United Kingdom; DOE and NSF, United States of America. In addition, individual groups and members have received support from BCKDF, CANARIE, Compute Canada and CRC, Canada; ERC, ERDF, Horizon 2020, Marie Skłodowska-Curie Actions and COST, European Union; Investissements d’Avenir Labex, Investissements d’Avenir Idex and ANR, France; DFG and AvH Foundation, Germany; Herakleitos, Thales and Aristeia programmes co-financed by EU-ESF and the Greek NSRF, Greece; BSF-NSF and GIF, Israel; CERCA Programme Generalitat de Catalunya and PROMETEO Programme Generalitat Valenciana, Spain; Göran Gustafssons Stiftelse, Sweden; The Royal Society and Leverhulme Trust, United Kingdom. The crucial computing support from all WLCG partners is acknowledged gratefully, in particular from CERN, the ATLAS Tier-1 facilities at TRIUMF (Canada), NDGF (Denmark, Norway, Sweden), CC-IN2P3 (France), KIT/GridKA (Germany), INFN-CNAF (Italy), NL-T1 (Netherlands), PIC (Spain), ASGC (Taiwan), RAL (UK) and BNL (USA), the Tier-2 facilities worldwide and large non-WLCG resource providers. Major contributors of computing resources are listed in Ref. [110].

Data Availability Statement This manuscript has no associated data or the data will not be deposited. [Authors’ comment: All ATLAS scientific output is published in journals, and preliminary results are made available in Conference Notes. All are openly available, without restriction on use by external parties beyond copyright law and the standard conditions agreed by CERN. Data associated with journal publications are also made available: tables and data from plots (e.g. cross section

values, likelihood profiles, selection efficiencies, cross section limits, ...) are stored in appropriate repositories such as HEPDATA (<http://hepdata.cedar.ac.uk/>). ATLAS also strives to make additional material related to the paper available that allows a reinterpretation of the data in the context of new theoretical models. For example, an extended encapsulation of the analysis is often provided for measurements in the framework of RIVET (<http://rivet.hepforge.org/>). This information is taken from the ATLAS Data Access Policy, which is a public document that can be downloaded from <http://opendata.cern.ch/record/413> [<http://opendata.cern.ch/>.]

Open Access This article is licensed under a Creative Commons Attribution 4.0 International License, which permits use, sharing, adaptation, distribution and reproduction in any medium or format, as long as you give appropriate credit to the original author(s) and the source, provide a link to the Creative Commons licence, and indicate if changes were made. The images or other third party material in this article are included in the article’s Creative Commons licence, unless indicated otherwise in a credit line to the material. If material is not included in the article’s Creative Commons licence and your intended use is not permitted by statutory regulation or exceeds the permitted use, you will need to obtain permission directly from the copyright holder. To view a copy of this licence, visit <http://creativecommons.org/licenses/by/4.0/>.
Funded by SCOAP³.

Appendix

The measured absolute and normalised differential cross-sections as functions of individual lepton and dilepton variables are shown in Tables 15, 16, 17, 18. The absolute and normalised double-differential cross-sections as functions of $|\eta^\ell|$ and $m^{e\mu}$ are shown in Tables 19 and 20, those as a function of $|y^{e\mu}|$ and $m^{e\mu}$ in Tables 21 and 22, and those as a function of $\Delta\phi^{e\mu}$ and $m^{e\mu}$ in Tables 23 and 24. More details are given in Sect. 7.

Table 15 Absolute and normalised differential cross-sections as functions of p_T^ℓ (top) and $|\eta^\ell|$ (bottom). The columns show the bin ranges, measured cross-section and total uncertainty, relative statistical uncertainty, relative systematic uncertainties in various categories (see text),

total relative uncertainty, and differential cross-section corrected to remove contributions via $W \rightarrow \tau \rightarrow e/\mu$ decays. Relative uncertainties smaller than 0.05% are indicated by ‘0.0’. The last bin includes overflows where indicated by the ‘+’ sign

Absolute Bin (GeV)	$d\sigma/dp_T^\ell$ (fb/GeV)	Stat. (%)	$t\bar{t}$ mod. (%)	Lept. (%)	Jet/b (%)	Bkg. (%)	L/E_b (%)	Total (%)	$d\sigma/dp_T^\ell$ (no τ) (fb/GeV)
20–25	564 ± 17	0.7	0.9	1.4	0.2	1.0	2.3	3.1	436 ± 13
25–30	562 ± 16	0.6	0.9	1.1	0.2	0.8	2.3	2.9	456 ± 13
30–40	525 ± 14	0.4	0.9	0.7	0.2	0.7	2.3	2.7	441 ± 12
40–50	428 ± 12	0.5	0.9	0.6	0.2	0.7	2.3	2.7	369 ± 10
50–60	336.2 ± 9.2	0.5	0.9	0.6	0.3	0.7	2.3	2.7	294.8 ± 7.8
60–80	220.6 ± 6.0	0.4	1.0	0.6	0.2	0.7	2.3	2.7	195.9 ± 5.2
80–100	120.1 ± 3.4	0.6	1.1	0.7	0.2	0.8	2.3	2.9	107.4 ± 3.0
100–120	66.6 ± 2.0	0.8	1.1	0.7	0.2	1.0	2.3	3.0	59.7 ± 1.7
120–150	30.6 ± 1.0	1.0	1.2	0.8	0.3	1.5	2.4	3.3	27.4 ± 0.9
150–200	10.80 ± 0.45	1.4	1.2	1.0	0.2	2.6	2.5	4.1	9.64 ± 0.39
200–300+	2.33 ± 0.20	2.2	1.6	1.5	0.4	7.8	2.6	8.8	2.07 ± 0.18
Normalised Bin (GeV)	$\frac{1}{\sigma}d\sigma/dp_T^\ell$ (10^{-2} /GeV)	Stat. (%)	$t\bar{t}$ mod. (%)	Lept. (%)	Jet/b (%)	Bkg. (%)	L/E_b (%)	Total (%)	$\frac{1}{\sigma}d\sigma/dp_T^\ell$ (no τ) (10^{-2} /GeV)
20–25	1.987 ± 0.026	0.7	0.4	0.8	0.1	0.6	0.0	1.3	1.796 ± 0.023
25–30	1.982 ± 0.019	0.6	0.4	0.5	0.1	0.5	0.0	1.0	1.876 ± 0.018
30–40	1.852 ± 0.012	0.4	0.2	0.3	0.1	0.4	0.0	0.7	1.817 ± 0.012
40–50	1.5095 ± 0.0096	0.4	0.2	0.3	0.1	0.3	0.0	0.6	1.5212 ± 0.0097
50–60	1.1855 ± 0.0079	0.5	0.2	0.3	0.1	0.2	0.0	0.7	1.2142 ± 0.0080
60–80	0.7779 ± 0.0047	0.4	0.3	0.3	0.1	0.2	0.0	0.6	0.8067 ± 0.0047
80–100	0.4234 ± 0.0035	0.6	0.4	0.3	0.0	0.3	0.0	0.8	0.4423 ± 0.0035
100–120	0.2348 ± 0.0028	0.8	0.5	0.4	0.1	0.6	0.0	1.2	0.2459 ± 0.0029
120–150	0.1080 ± 0.0019	1.0	0.6	0.6	0.1	1.2	0.1	1.7	0.1129 ± 0.0019
150–200	0.0381 ± 0.0012	1.3	0.9	1.0	0.2	2.4	0.1	3.0	0.0397 ± 0.0012
200–300+	0.0082 ± 0.0007	2.2	1.6	1.6	0.4	7.6	0.3	8.2	0.0085 ± 0.0007
Absolute Bin (unit $ \eta $)	$d\sigma/d \eta^\ell $ (fb/unit $ \eta $)	Stat. (%)	$t\bar{t}$ mod. (%)	Lept. (%)	Jet/b (%)	Bkg. (%)	L/E_b (%)	Total (%)	$d\sigma/d \eta^\ell $ (no τ) (fb/unit $ \eta $)
0.00–0.25	17270 ± 460	0.5	0.8	0.7	0.2	0.7	2.3	2.7	14750 ± 390
0.25–0.50	16520 ± 440	0.5	0.8	0.6	0.2	0.7	2.3	2.7	14110 ± 370
0.50–0.75	15660 ± 420	0.5	0.8	0.6	0.2	0.7	2.3	2.7	13390 ± 350
0.75–1.00	14320 ± 390	0.5	0.9	0.7	0.2	0.7	2.3	2.7	12250 ± 330
1.00–1.25	12660 ± 350	0.5	1.0	0.7	0.2	0.8	2.3	2.8	10850 ± 290
1.25–1.50	10940 ± 310	0.7	1.0	0.7	0.2	0.8	2.3	2.8	9370 ± 260
1.50–1.75	9090 ± 260	0.7	1.1	0.7	0.2	0.9	2.3	2.9	7810 ± 220
1.75–2.00	7320 ± 220	0.8	1.2	0.8	0.2	1.0	2.3	3.0	6310 ± 180
2.00–2.50	4750 ± 150	0.7	1.3	0.9	0.2	1.2	2.3	3.2	4100 ± 130

Table 15 continued

Normalised Bin (unit $ \eta $)	$\frac{1}{\sigma} d\sigma/d \eta^\ell $ ($10^{-1}/\text{unit } \eta $)	Stat. (%)	$t\bar{t}$ mod. (%)	Lept. (%)	Jet/ b (%)	Bkg. (%)	L/E_b (%)	Total (%)	$\frac{1}{\sigma} d\sigma/d \eta^\ell $ (no τ) ($10^{-1}/\text{unit } \eta $)
0.00–0.25	6.099 ± 0.041	0.4	0.4	0.1	0.1	0.3	0.0	0.7	6.082 ± 0.041
0.25–0.50	5.832 ± 0.035	0.4	0.3	0.1	0.0	0.3	0.0	0.6	5.816 ± 0.035
0.50–0.75	5.531 ± 0.031	0.4	0.2	0.1	0.0	0.2	0.0	0.6	5.521 ± 0.031
0.75–1.00	5.056 ± 0.028	0.5	0.2	0.1	0.0	0.2	0.0	0.6	5.049 ± 0.028
1.00–1.25	4.472 ± 0.027	0.5	0.2	0.1	0.0	0.2	0.0	0.6	4.473 ± 0.027
1.25–1.50	3.863 ± 0.030	0.6	0.3	0.1	0.1	0.2	0.0	0.8	3.863 ± 0.030
1.50–1.75	3.211 ± 0.028	0.7	0.4	0.2	0.1	0.3	0.0	0.9	3.217 ± 0.028
1.75–2.00	2.584 ± 0.027	0.8	0.5	0.2	0.0	0.5	0.0	1.0	2.599 ± 0.027
2.00–2.50	1.676 ± 0.020	0.7	0.6	0.3	0.0	0.7	0.0	1.2	1.690 ± 0.020

Table 16 Absolute and normalised differential cross-sections as functions of $p_T^{e\mu}$ (top) and $m^{e\mu}$ (bottom). The columns show the bin ranges, measured cross-section and total uncertainty, relative statistical uncertainty, relative systematic uncertainties in various categories (see text),total relative uncertainty, and differential cross-section corrected to remove contributions via $W \rightarrow \tau \rightarrow e/\mu$ decays. Relative uncertainties smaller than 0.05% are indicated by ‘0.0’. The last bin includes overflows where indicated by the ‘+’ sign

Absolute Bin (GeV)	$d\sigma/dp_T^{e\mu}$ (fb/GeV)	Stat. (%)	$t\bar{t}$ mod. (%)	Lept. (%)	Jet/ b (%)	Bkg. (%)	L/E_b (%)	Total (%)	$d\sigma/dp_T^{e\mu}$ (no τ) (fb/GeV)
0–20	45.1 ± 1.4	1.1	1.2	0.7	0.3	0.9	2.3	3.1	36.5 ± 1.1
20–40	110.1 ± 3.1	0.7	1.0	0.7	0.3	0.8	2.3	2.9	89.7 ± 2.5
40–60	159.8 ± 4.5	0.6	1.0	0.8	0.3	0.8	2.3	2.8	132.2 ± 3.6
60–80	156.2 ± 4.3	0.6	1.0	0.7	0.2	0.7	2.3	2.8	134.8 ± 3.6
80–100	110.1 ± 3.1	0.7	1.1	0.7	0.2	0.7	2.3	2.8	98.2 ± 2.7
100–120	62.6 ± 1.9	0.8	1.2	0.7	0.2	0.9	2.3	3.0	56.9 ± 1.6
120–150	26.67 ± 0.90	1.1	1.4	0.8	0.3	1.4	2.4	3.4	24.29 ± 0.80
150–200	7.15 ± 0.35	1.7	2.0	1.0	0.3	3.2	2.5	5.0	6.45 ± 0.32
200–300+	1.19 ± 0.17	3.2	3.4	1.5	0.6	13.2	2.8	14.3	1.06 ± 0.15
Normalised Bin (GeV)	$\frac{1}{\sigma} d\sigma/dp_T^{e\mu}$ ($10^{-2}/\text{GeV}$)	Stat. (%)	$t\bar{t}$ mod. (%)	Lept. (%)	Jet/ b (%)	Bkg. (%)	L/E_b (%)	Total (%)	$\frac{1}{\sigma} d\sigma/dp_T^{e\mu}$ (no τ) ($10^{-2}/\text{GeV}$)
0–20	0.3189 ± 0.0051	1.1	0.9	0.2	0.2	0.7	0.0	1.6	0.3011 ± 0.0049
20–40	0.7776 ± 0.0082	0.6	0.6	0.2	0.1	0.5	0.0	1.1	0.7402 ± 0.0081
40–60	1.1286 ± 0.0088	0.5	0.4	0.2	0.1	0.4	0.0	0.8	1.0905 ± 0.0089
60–80	1.1035 ± 0.0070	0.5	0.2	0.1	0.1	0.3	0.0	0.6	1.1121 ± 0.0072
80–100	0.7780 ± 0.0058	0.6	0.4	0.1	0.1	0.2	0.0	0.7	0.8098 ± 0.0059
100–120	0.4425 ± 0.0051	0.8	0.6	0.3	0.2	0.4	0.0	1.2	0.4694 ± 0.0054
120–150	0.1884 ± 0.0035	1.0	1.0	0.5	0.2	1.0	0.1	1.9	0.2003 ± 0.0038
150–200	0.0505 ± 0.0020	1.7	1.8	0.9	0.3	2.9	0.2	4.0	0.0532 ± 0.0021
200–300+	0.0084 ± 0.0012	3.2	3.4	1.5	0.5	13.0	0.5	13.9	0.0087 ± 0.0012
Absolute Bin (GeV)	$d\sigma/dm^{e\mu}$ (fb/GeV)	Stat. (%)	$t\bar{t}$ mod. (%)	Lept. (%)	Jet/ b (%)	Bkg. (%)	L/E_b (%)	Total (%)	$d\sigma/dm^{e\mu}$ (no τ) (fb/GeV)
0–20	19.98 ± 0.74	2.0	1.3	1.0	0.3	1.2	2.3	3.7	16.57 ± 0.60
20–40	54.3 ± 1.6	1.0	1.0	0.9	0.2	1.0	2.3	3.0	45.6 ± 1.3
40–60	88.2 ± 2.6	0.8	0.9	0.9	0.2	1.0	2.3	2.9	73.1 ± 2.1
60–80	107.0 ± 3.0	0.7	0.8	0.8	0.2	0.9	2.3	2.8	88.9 ± 2.4
80–100	102.3 ± 2.9	0.7	0.9	0.7	0.3	0.8	2.3	2.8	86.4 ± 2.4
100–120	83.8 ± 2.3	0.8	0.9	0.6	0.3	0.7	2.3	2.8	71.7 ± 2.0
120–150	59.8 ± 1.7	0.7	0.9	0.6	0.2	0.7	2.3	2.8	51.9 ± 1.4

Table 16 continued

Normalised Bin (GeV)	$\frac{1}{\sigma}d\sigma/dm^{e\mu}$ ($10^{-3}/\text{GeV}$)	Stat. (%)	$t\bar{t}$ mod. (%)	Lept. (%)	Jet/ b (%)	Bkg. (%)	L/E_b (%)	Total (%)	$\frac{1}{\sigma}d\sigma/dm^{e\mu}$ (no τ) ($10^{-3}/\text{GeV}$)
150–200	33.80 ± 0.97	0.7	1.0	0.6	0.2	0.9	2.3	2.9	29.96 ± 0.84
200–250	15.75 ± 0.51	1.1	1.2	0.6	0.4	1.3	2.4	3.2	14.21 ± 0.45
250–300	7.51 ± 0.29	1.6	1.5	0.8	0.2	1.8	2.4	3.8	6.85 ± 0.25
300–400	2.84 ± 0.13	1.8	2.0	0.7	0.2	2.7	2.4	4.5	2.62 ± 0.11
400–500+	1.48 ± 0.09	2.7	2.7	0.9	0.3	3.7	2.4	5.9	1.38 ± 0.08
0–20	1.408 ± 0.036	2.0	1.1	0.4	0.2	1.0	0.0	2.5	1.364 ± 0.034
20–40	3.826 ± 0.055	1.0	0.7	0.3	0.2	0.8	0.0	1.4	3.751 ± 0.053
40–60	6.218 ± 0.073	0.7	0.5	0.3	0.1	0.7	0.0	1.2	6.017 ± 0.069
60–80	7.541 ± 0.068	0.6	0.4	0.2	0.1	0.5	0.0	0.9	7.315 ± 0.066
80–100	7.210 ± 0.061	0.6	0.3	0.1	0.3	0.3	0.0	0.8	7.108 ± 0.060
100–120	5.907 ± 0.049	0.7	0.3	0.1	0.1	0.2	0.0	0.8	5.898 ± 0.049
120–150	4.212 ± 0.033	0.7	0.3	0.2	0.1	0.2	0.0	0.8	4.270 ± 0.034
150–200	2.382 ± 0.025	0.7	0.5	0.2	0.1	0.5	0.0	1.0	2.466 ± 0.024
200–250	1.110 ± 0.019	1.1	0.8	0.3	0.2	1.1	0.0	1.8	1.169 ± 0.019
250–300	0.529 ± 0.014	1.6	1.2	0.7	0.1	1.6	0.1	2.6	0.564 ± 0.014
300–400	0.2000 ± 0.0071	1.8	1.6	0.6	0.1	2.6	0.1	3.6	0.2154 ± 0.0073
400–500+	0.1041 ± 0.0053	2.7	2.4	1.0	0.2	3.5	0.1	5.1	0.1132 ± 0.0055

Table 17 Absolute and normalised differential cross-sections as functions of $|y^{e\mu}|$ (top) and $\Delta\phi^{e\mu}$ (bottom). The columns show the bin ranges, measured cross-section and total uncertainty, relative statistical uncertainty, relative systematic uncertainties in various categories (see text), total relative uncertainty, and differential cross-section corrected

to remove contributions via $W \rightarrow \tau \rightarrow e/\mu$ decays. Relative uncertainties smaller than 0.05% are indicated by ‘0.0’. The bin boundaries for $\Delta\phi^{e\mu}$ correspond to exact multiples of $\pi/10$ but are quoted to two decimal places

Absolute Bin (unit $ y $)	$d\sigma/d y^{e\mu} $ (fb/unit $ y $)	Stat. (%)	$t\bar{t}$ mod. (%)	Lept. (%)	Jet/ b (%)	Bkg. (%)	L/E_b (%)	Total (%)	$d\sigma/d y^{e\mu} $ (no τ) (fb/unit $ y $)
0.00–0.25	10700 ± 290	0.6	0.7	0.6	0.2	0.7	2.3	2.7	9150 ± 240
0.25–0.50	10160 ± 270	0.6	0.8	0.6	0.2	0.7	2.3	2.7	8700 ± 230
0.50–0.75	9300 ± 260	0.6	0.9	0.7	0.2	0.7	2.3	2.8	7970 ± 210
0.75–1.00	8140 ± 230	0.7	1.0	0.7	0.2	0.8	2.3	2.8	6970 ± 190
1.00–1.25	6620 ± 190	0.8	1.1	0.7	0.2	0.8	2.3	2.9	5680 ± 160
1.25–1.50	5030 ± 150	1.0	1.2	0.8	0.3	0.9	2.3	3.0	4320 ± 130
1.50–1.75	3460 ± 110	1.2	1.4	0.8	0.2	1.1	2.3	3.3	2969 ± 96
1.75–2.00	2085 ± 76	1.7	1.6	0.9	0.2	1.3	2.3	3.7	1790 ± 65
2.00–2.50	545 ± 26	2.6	2.1	1.1	0.3	2.2	2.4	4.8	467 ± 22
Normalised Bin (unit $ y $)	$\frac{1}{\sigma}d\sigma/d y^{e\mu} $ ($10^{-1}/\text{unit } y $)	Stat. (%)	$t\bar{t}$ mod. (%)	Lept. (%)	Jet/ b (%)	Bkg. (%)	L/E_b (%)	Total (%)	$\frac{1}{\sigma}d\sigma/d y^{e\mu} $ (no τ) ($10^{-1}/\text{unit } y $)
0.00–0.25	7.560 ± 0.056	0.5	0.4	0.1	0.0	0.3	0.0	0.7	7.550 ± 0.056
0.25–0.50	7.184 ± 0.050	0.6	0.3	0.1	0.0	0.3	0.0	0.7	7.182 ± 0.050
0.50–0.75	6.574 ± 0.045	0.6	0.3	0.1	0.0	0.2	0.0	0.7	6.574 ± 0.045
0.75–1.00	5.752 ± 0.042	0.6	0.3	0.1	0.1	0.2	0.0	0.7	5.748 ± 0.043
1.00–1.25	4.679 ± 0.041	0.8	0.4	0.1	0.1	0.2	0.0	0.9	4.688 ± 0.041
1.25–1.50	3.558 ± 0.040	0.9	0.5	0.2	0.1	0.4	0.0	1.1	3.562 ± 0.040
1.50–1.75	2.449 ± 0.037	1.2	0.7	0.2	0.1	0.6	0.0	1.5	2.449 ± 0.037

Table 17 continued

Normalised Bin (unit y)	$\frac{1}{\sigma} d\sigma/d y^{e\mu} $ ($10^{-1}/\text{unit } y $)	Stat. (%)	$t\bar{t}$ mod. (%)	Lept. (%)	Jet/b (%)	Bkg. (%)	L/E_b (%)	Total (%)	$\frac{1}{\sigma} d\sigma/d y^{e\mu} $ (no τ) ($10^{-1}/\text{unit } y $)
1.75–2.00	1.474 ± 0.031	1.7	0.9	0.3	0.2	0.9	0.0	2.1	1.477 ± 0.032
2.00–2.50	0.385 ± 0.013	2.6	1.4	0.6	0.1	1.8	0.1	3.5	0.386 ± 0.014
Absolute Bin (rad)	$d\sigma/d\Delta\phi^{e\mu}$ (fb/rad)	Stat. (%)	$t\bar{t}$ mod. (%)	Lept. (%)	Jet/b (%)	Bkg. (%)	L/E_b (%)	Total (%)	$d\sigma/d\Delta\phi^{e\mu}$ (no τ) (fb/rad)
0.00–0.31	3250 ± 110	1.1	2.0	0.8	0.2	0.8	2.3	3.4	2847 ± 90
0.31–0.63	3280 ± 110	1.0	1.7	0.8	0.1	0.8	2.3	3.2	2882 ± 87
0.63–0.94	3370 ± 100	1.0	1.4	0.8	0.3	0.8	2.3	3.1	2965 ± 88
0.94–1.26	3680 ± 110	0.9	1.2	0.7	0.2	0.8	2.3	3.0	3219 ± 93
1.26–1.57	4000 ± 120	0.9	1.0	0.7	0.2	0.8	2.3	2.9	3476 ± 98
1.57–1.88	4460 ± 130	0.8	0.9	0.7	0.2	0.8	2.3	2.8	3850 ± 110
1.88–2.20	4980 ± 140	0.8	1.0	0.7	0.3	0.8	2.3	2.8	4260 ± 120
2.20–2.51	5610 ± 160	0.7	1.1	0.6	0.3	0.7	2.3	2.9	4740 ± 130
2.51–2.83	6030 ± 180	0.7	1.3	0.6	0.3	0.8	2.3	3.0	5060 ± 150
2.83–3.14	6420 ± 200	0.7	1.6	0.6	0.3	0.8	2.3	3.1	5350 ± 170
Normalised Bin (rad)	$\frac{1}{\sigma} d\sigma/d\Delta\phi^{e\mu}$ [$10^{-1}/\text{rad}$]	Stat. (%)	$t\bar{t}$ mod. (%)	Lept. (%)	Jet/b (%)	Bkg. (%)	L/E_b (%)	Total (%)	$\frac{1}{\sigma} d\sigma/d\Delta\phi^{e\mu}$ (no τ) ($10^{-1}/\text{rad}$)
0.00–0.31	2.298 ± 0.050	1.0	1.9	0.1	0.2	0.4	0.0	2.2	2.345 ± 0.044
0.31–0.63	2.316 ± 0.043	0.9	1.5	0.1	0.2	0.3	0.0	1.8	2.374 ± 0.040
0.63–0.94	2.380 ± 0.037	0.9	1.2	0.1	0.2	0.3	0.0	1.6	2.442 ± 0.036
0.94–1.26	2.600 ± 0.033	0.9	0.9	0.1	0.1	0.3	0.0	1.3	2.651 ± 0.034
1.26–1.57	2.823 ± 0.029	0.8	0.5	0.1	0.1	0.2	0.0	1.0	2.864 ± 0.031
1.57–1.88	3.149 ± 0.028	0.8	0.3	0.0	0.1	0.2	0.0	0.9	3.172 ± 0.029
1.88–2.20	3.516 ± 0.031	0.7	0.4	0.0	0.1	0.2	0.0	0.9	3.505 ± 0.030
2.20–2.51	3.960 ± 0.040	0.7	0.7	0.1	0.1	0.2	0.0	1.0	3.908 ± 0.038
2.51–2.83	4.255 ± 0.054	0.7	1.0	0.1	0.2	0.3	0.0	1.3	4.164 ± 0.052
2.83–3.14	4.533 ± 0.070	0.7	1.4	0.1	0.1	0.3	0.0	1.6	4.405 ± 0.071

Table 18 Absolute and normalised differential cross-sections as functions of $p_T^e + p_T^\mu$ (top) and $E^e + E^\mu$ (bottom). The columns show the bin ranges, measured cross-section and total uncertainty, relative statistical uncertainty, relative systematic uncertainties in various categories (see

text), total relative uncertainty, and differential cross-section corrected to remove contributions via $W \rightarrow \tau \rightarrow e/\mu$ decays. Relative uncertainties smaller than 0.05% are indicated by ‘0.0’. The last bin includes overflows where indicated by the ‘+’ sign

Absolute Bin (GeV)	$d\sigma/d(p_T^e + p_T^\mu)$ (fb/GeV)	Stat. (%)	$t\bar{t}$ mod. (%)	Lept. (%)	Jet/b (%)	Bkg. (%)	L/E_b (%)	Total (%)	$d\sigma/d(p_T^e + p_T^\mu)$ (no τ) (fb/GeV)
40–80	96.1 ± 2.8	0.6	0.9	1.0	0.2	0.9	2.3	2.9	76.1 ± 2.2
80–100	148.2 ± 4.1	0.6	1.0	0.7	0.2	0.8	2.3	2.8	126.3 ± 3.4
100–120	120.9 ± 3.4	0.6	1.0	0.7	0.2	0.7	2.3	2.8	105.9 ± 2.9
120–150	76.5 ± 2.1	0.6	1.0	0.6	0.2	0.8	2.3	2.8	68.1 ± 1.8
150–200	33.7 ± 1.0	0.7	1.1	0.7	0.3	1.1	2.4	3.0	30.3 ± 0.9
200–250	11.77 ± 0.43	1.3	1.2	0.8	0.3	2.0	2.4	3.7	10.65 ± 0.38

Table 18 continued

Absolute Bin (GeV)	$d\sigma/d(p_T^e + p_T^\mu)$ (fb/GeV)	Stat. (%)	$t\bar{t}$ mod. (%)	Lept. (%)	Jet/ b (%)	Bkg. (%)	L/E_b (%)	Total (%)	$d\sigma/d(p_T^e + p_T^\mu)$ (no τ) (fb/GeV)
250–300	4.57 ± 0.23	2.0	1.4	1.0	0.3	3.3	2.5	4.9	4.18 ± 0.20
300–400+	1.82 ± 0.14	2.4	1.6	1.5	0.6	6.7	2.6	7.9	1.68 ± 0.13
Normalised Bin (GeV)	$\frac{1}{\sigma}d\sigma/d(p_T^e + p_T^\mu)$ (10^{-2} /GeV)	Stat. (%)	$t\bar{t}$ mod. (%)	Lept. (%)	Jet/ b (%)	Bkg. (%)	L/E_b (%)	Total (%)	$\frac{1}{\sigma}d\sigma/d(p_T^e + p_T^\mu)$ (no τ) (10^{-2} /GeV)
40–80	0.6764 ± 0.0066	0.5	0.3	0.4	0.0	0.7	0.0	1.0	0.6263 ± 0.0063
80–100	1.0429 ± 0.0079	0.5	0.2	0.2	0.0	0.4	0.0	0.8	1.0393 ± 0.0080
100–120	0.8512 ± 0.0062	0.6	0.2	0.2	0.1	0.3	0.0	0.7	0.8717 ± 0.0064
120–150	0.5387 ± 0.0038	0.6	0.3	0.2	0.0	0.2	0.0	0.7	0.5601 ± 0.0039
150–200	0.2373 ± 0.0027	0.7	0.4	0.4	0.2	0.7	0.0	1.1	0.2490 ± 0.0027
200–250	0.0829 ± 0.0020	1.2	0.7	0.7	0.1	1.8	0.1	2.4	0.0876 ± 0.0020
250–300	0.0322 ± 0.0013	2.0	1.1	1.0	0.3	3.2	0.1	4.1	0.0344 ± 0.0014
300–400+	0.0128 ± 0.0009	2.4	1.5	1.6	0.5	6.6	0.3	7.3	0.0138 ± 0.0010
Absolute Bin (GeV)	$d\sigma/d(E^e + E^\mu)$ (fb/GeV)	Stat. (%)	$t\bar{t}$ mod. (%)	Lept. (%)	Jet/ b (%)	Bkg. (%)	L/E_b (%)	Total (%)	$d\sigma/d(E^e + E^\mu)$ (no τ) (fb/GeV)
40–80	19.82 ± 0.63	1.3	0.8	1.2	0.2	1.1	2.3	3.2	14.95 ± 0.47
80–100	58.8 ± 1.7	1.0	0.7	0.9	0.2	0.9	2.3	2.9	47.3 ± 1.4
100–120	71.5 ± 2.0	0.8	0.8	0.8	0.2	0.8	2.3	2.8	59.4 ± 1.6
120–150	71.3 ± 2.0	0.7	0.8	0.7	0.2	0.8	2.3	2.8	60.5 ± 1.6
150–200	57.7 ± 1.6	0.6	0.9	0.7	0.2	0.7	2.3	2.7	49.8 ± 1.3
200–250	39.1 ± 1.1	0.7	1.0	0.7	0.3	0.7	2.3	2.8	34.2 ± 0.9
250–300	25.49 ± 0.76	0.9	1.2	0.6	0.2	0.9	2.3	3.0	22.57 ± 0.65
300–400	13.72 ± 0.44	0.9	1.3	0.6	0.2	1.3	2.4	3.2	12.24 ± 0.38
400–500	5.92 ± 0.22	1.4	1.6	0.8	0.2	1.9	2.4	3.8	5.33 ± 0.19
500–700+	2.66 ± 0.13	1.5	1.7	1.0	0.3	3.4	2.4	4.9	2.42 ± 0.12
Normalised Bin (GeV)	$\frac{1}{\sigma}d\sigma/d(E^e + E^\mu)$ (10^{-3} /GeV)	Stat. (%)	$t\bar{t}$ mod. (%)	Lept. (%)	Jet/ b (%)	Bkg. (%)	L/E_b (%)	Total (%)	$\frac{1}{\sigma}d\sigma/d(E^e + E^\mu)$ (no τ) (10^{-3} /GeV)
40–80	1.401 ± 0.026	1.2	0.8	0.6	0.1	1.0	0.1	1.9	1.234 ± 0.023
80–100	4.157 ± 0.056	0.9	0.6	0.3	0.1	0.7	0.0	1.3	3.905 ± 0.053
100–120	5.054 ± 0.057	0.8	0.5	0.2	0.1	0.6	0.0	1.1	4.900 ± 0.056
120–150	5.039 ± 0.045	0.6	0.3	0.1	0.1	0.5	0.0	0.9	4.995 ± 0.045
150–200	4.076 ± 0.027	0.5	0.2	0.1	0.0	0.3	0.0	0.7	4.107 ± 0.027
200–250	2.765 ± 0.021	0.7	0.3	0.1	0.1	0.2	0.0	0.8	2.826 ± 0.022
250–300	1.802 ± 0.019	0.8	0.5	0.2	0.1	0.4	0.0	1.1	1.863 ± 0.020
300–400	0.970 ± 0.014	0.8	0.6	0.3	0.2	0.9	0.0	1.4	1.010 ± 0.014
400–500	0.4187 ± 0.0097	1.3	0.9	0.6	0.1	1.5	0.1	2.3	0.4397 ± 0.0099
500–700+	0.1879 ± 0.0070	1.5	1.2	0.9	0.1	3.1	0.1	3.7	0.1998 ± 0.0074

Table 19 Absolute differential cross-sections as a function of $|\eta^\ell| \times m^{e\mu}$. The columns show the bin ranges, measured cross-section and total uncertainty, relative statistical uncertainty, relative systematic uncertainties in various categories (see text), total relative uncertainty, and differential cross-section corrected to remove contributions via $W \rightarrow \tau \rightarrow e/\mu$ decays. Relative uncertainties smaller than 0.05% are indicated by ‘0.0’. The last bin includes overflows where indicated by the ‘+’ sign

Absolute	$d^2\sigma/d \eta^\ell dm^{e\mu}$	Stat.	$t\bar{t}$ mod.	Lept.	Jet/b	Bkg.	L/E_b	Total	$d^2\sigma/d \eta^\ell dm^{e\mu}$ (no τ)
Bin (unit $ \eta $ GeV)	(fb/unit $ \eta $ GeV)	(%)	(%)	(%)	(%)	(%)	(%)	(%)	(fb/unit $ \eta $ GeV)
$0 < m^{e\mu} < 80$ GeV									
0.00–0.25	87.2 ± 2.5	0.8	0.7	0.8	0.1	1.0	2.3	2.8	72.3 ± 2.0
0.25–0.50	82.6 ± 2.3	0.8	0.8	0.8	0.1	0.9	2.3	2.8	68.5 ± 1.9
0.50–0.75	78.2 ± 2.2	0.8	0.9	0.8	0.2	0.8	2.3	2.9	65.0 ± 1.8
0.75–1.00	70.2 ± 2.1	0.9	1.1	0.9	0.2	0.9	2.3	3.0	58.3 ± 1.7
1.00–1.25	60.0 ± 1.9	0.9	1.3	0.9	0.2	0.9	2.3	3.1	50.0 ± 1.5
1.25–1.50	51.5 ± 1.7	1.2	1.5	0.9	0.1	1.0	2.3	3.3	42.9 ± 1.3
1.50–1.75	41.0 ± 1.4	1.3	1.7	1.0	0.2	1.0	2.3	3.4	34.2 ± 1.1
1.75–2.00	31.4 ± 1.2	1.5	1.8	1.0	0.2	1.2	2.3	3.7	26.2 ± 0.9
2.00–2.50	18.45 ± 0.73	1.5	2.2	1.1	0.3	1.5	2.3	4.0	15.42 ± 0.57
$80 < m^{e\mu} < 120$ GeV									
0.00–0.25	120.6 ± 3.4	0.9	0.9	0.7	0.3	0.8	2.3	2.9	102.2 ± 3.0
0.25–0.50	113.5 ± 3.2	0.9	0.9	0.6	0.3	0.7	2.3	2.8	96.3 ± 2.7
0.50–0.75	105.5 ± 3.0	0.9	0.8	0.6	0.3	0.7	2.3	2.8	89.5 ± 2.5
0.75–1.00	93.2 ± 2.7	1.0	0.9	0.7	0.3	0.7	2.3	2.9	79.1 ± 2.3
1.00–1.25	82.3 ± 2.4	1.1	0.9	0.7	0.3	0.7	2.3	2.9	69.9 ± 2.0
1.25–1.50	69.5 ± 2.1	1.3	1.0	0.7	0.3	0.8	2.3	3.0	58.9 ± 1.8
1.50–1.75	57.1 ± 1.8	1.4	1.0	0.7	0.3	0.9	2.3	3.1	48.4 ± 1.5
1.75–2.00	45.0 ± 1.5	1.6	1.0	0.8	0.3	1.0	2.3	3.2	38.4 ± 1.2
2.00–2.50	28.85 ± 0.97	1.5	1.1	0.9	0.3	1.3	2.3	3.4	24.53 ± 0.83
$120 < m^{e\mu} < 200$ GeV									
0.00–0.25	50.6 ± 1.6	0.9	1.7	0.6	0.3	0.8	2.3	3.2	44.5 ± 1.3
0.25–0.50	48.4 ± 1.5	0.9	1.6	0.5	0.2	0.8	2.3	3.1	42.5 ± 1.3
0.50–0.75	46.7 ± 1.4	0.9	1.5	0.6	0.2	0.7	2.3	3.1	40.9 ± 1.2
0.75–1.00	44.0 ± 1.3	1.0	1.4	0.6	0.2	0.7	2.3	3.0	38.6 ± 1.1
1.00–1.25	38.9 ± 1.2	1.1	1.3	0.6	0.3	0.8	2.3	3.1	34.1 ± 1.0
1.25–1.50	34.3 ± 1.1	1.3	1.3	0.6	0.2	0.8	2.3	3.2	30.0 ± 0.9
1.50–1.75	28.79 ± 0.92	1.3	1.3	0.7	0.3	1.0	2.3	3.2	25.20 ± 0.79
1.75–2.00	23.97 ± 0.78	1.4	1.3	0.7	0.2	1.0	2.3	3.2	20.98 ± 0.67
2.00–2.50	16.46 ± 0.54	1.3	1.2	0.8	0.2	1.3	2.3	3.3	14.43 ± 0.47
$200 < m^{e\mu} < 500 +$ GeV									
0.00–0.25	4.90 ± 0.18	1.6	1.3	0.6	0.3	1.8	2.4	3.7	4.47 ± 0.17
0.25–0.50	5.09 ± 0.19	1.5	1.2	0.6	0.3	1.9	2.4	3.7	4.65 ± 0.17
0.50–0.75	4.95 ± 0.18	1.5	1.2	0.6	0.3	2.0	2.4	3.7	4.52 ± 0.17
0.75–1.00	4.93 ± 0.18	1.5	1.2	0.6	0.4	1.9	2.4	3.7	4.50 ± 0.16
1.00–1.25	4.91 ± 0.18	1.5	1.3	0.6	0.2	1.9	2.4	3.7	4.46 ± 0.16
1.25–1.50	4.42 ± 0.18	1.9	1.5	0.7	0.6	2.0	2.4	4.0	4.01 ± 0.16
1.50–1.75	4.18 ± 0.16	1.7	1.5	0.7	0.3	1.8	2.3	3.9	3.80 ± 0.14
1.75–2.00	3.70 ± 0.15	1.9	1.8	0.7	0.3	1.9	2.3	4.0	3.36 ± 0.13
2.00–2.50	2.71 ± 0.11	1.6	2.0	0.8	0.3	1.9	2.3	4.0	2.46 ± 0.10

Table 20 Normalised differential cross-sections as a function of $|\eta^\ell| \times m^{e\mu}$. The columns show the bin ranges, measured cross-section and total uncertainty, relative statistical uncertainty, relative systematic uncertainties in various categories (see text), total relative uncertainty, and differential cross-section corrected to remove contributions via $W \rightarrow \tau \rightarrow e/\mu$ decays. Relative uncertainties smaller than 0.05% are indicated by ‘0.0’. The last bin includes overflows where indicated by the ‘+’ sign

Normalised	$\frac{1}{\sigma} d^2\sigma/d \eta^\ell dm^{e\mu}$	Stat.	$t\bar{t}$ mod.	Lept.	Jet/ b	Bkg.	L/E_b	Total	$\frac{1}{\sigma} d^2\sigma/d \eta^\ell dm^{e\mu}$ (no τ)
Bin (unit $ \eta $ GeV)	(10^{-3} /unit $ \eta $ GeV)	(%)	(%)	(%)	(%)	(%)	(%)	(%)	(10^{-3} /unit $ \eta $ GeV)
0 < $m^{e\mu}$ < 80 GeV									
0.00–0.25	3.072 ± 0.042	0.8	0.8	0.2	0.1	0.8	0.0	1.4	2.977 ± 0.039
0.25–0.50	2.909 ± 0.037	0.7	0.7	0.2	0.1	0.7	0.0	1.3	2.819 ± 0.034
0.50–0.75	2.757 ± 0.034	0.8	0.7	0.2	0.1	0.6	0.0	1.2	2.675 ± 0.031
0.75–1.00	2.473 ± 0.032	0.8	0.8	0.2	0.1	0.6	0.0	1.3	2.398 ± 0.030
1.00–1.25	2.115 ± 0.030	0.9	0.9	0.3	0.1	0.6	0.0	1.4	2.057 ± 0.028
1.25–1.50	1.815 ± 0.031	1.2	1.0	0.3	0.1	0.6	0.0	1.7	1.765 ± 0.029
1.50–1.75	1.444 ± 0.028	1.2	1.2	0.4	0.1	0.7	0.0	1.9	1.406 ± 0.025
1.75–2.00	1.106 ± 0.025	1.5	1.4	0.4	0.1	0.9	0.0	2.2	1.079 ± 0.023
2.00–2.50	0.650 ± 0.016	1.4	1.6	0.5	0.2	1.2	0.0	2.5	0.635 ± 0.015
80 < $m^{e\mu}$ < 120 GeV									
0.00–0.25	4.248 ± 0.051	0.9	0.7	0.2	0.1	0.4	0.0	1.2	4.208 ± 0.054
0.25–0.50	3.999 ± 0.045	0.9	0.6	0.2	0.1	0.4	0.0	1.1	3.963 ± 0.046
0.50–0.75	3.716 ± 0.043	0.9	0.6	0.1	0.1	0.4	0.0	1.1	3.685 ± 0.042
0.75–1.00	3.283 ± 0.040	1.0	0.6	0.1	0.2	0.4	0.0	1.2	3.255 ± 0.039
1.00–1.25	2.900 ± 0.036	1.0	0.6	0.1	0.1	0.3	0.0	1.3	2.878 ± 0.036
1.25–1.50	2.448 ± 0.038	1.3	0.7	0.1	0.2	0.4	0.0	1.6	2.425 ± 0.038
1.50–1.75	2.011 ± 0.032	1.4	0.7	0.2	0.1	0.4	0.0	1.6	1.992 ± 0.032
1.75–2.00	1.586 ± 0.029	1.5	0.8	0.2	0.2	0.6	0.0	1.9	1.581 ± 0.030
2.00–2.50	1.017 ± 0.019	1.4	0.8	0.4	0.1	0.8	0.0	1.9	1.010 ± 0.019
120 < $m^{e\mu}$ < 200 GeV									
0.00–0.25	1.783 ± 0.028	0.9	1.2	0.2	0.1	0.5	0.0	1.6	1.832 ± 0.025
0.25–0.50	1.706 ± 0.025	0.9	1.0	0.2	0.1	0.4	0.0	1.5	1.751 ± 0.023
0.50–0.75	1.645 ± 0.022	0.9	0.9	0.2	0.1	0.4	0.0	1.4	1.685 ± 0.022
0.75–1.00	1.549 ± 0.021	1.0	0.8	0.2	0.1	0.3	0.0	1.3	1.587 ± 0.021
1.00–1.25	1.370 ± 0.018	1.0	0.7	0.2	0.1	0.4	0.0	1.3	1.402 ± 0.019
1.25–1.50	1.208 ± 0.019	1.3	0.7	0.2	0.1	0.4	0.0	1.6	1.235 ± 0.019
1.50–1.75	1.014 ± 0.016	1.3	0.7	0.3	0.1	0.5	0.0	1.6	1.037 ± 0.016
1.75–2.00	0.845 ± 0.015	1.4	0.7	0.2	0.1	0.6	0.0	1.7	0.863 ± 0.015
2.00–2.50	0.5801 ± 0.0098	1.3	0.6	0.3	0.1	0.9	0.0	1.7	0.5938 ± 0.0100
200 < $m^{e\mu}$ < 500 + GeV									
0.00–0.25	0.1728 ± 0.0047	1.6	1.5	0.5	0.2	1.6	0.1	2.7	0.1840 ± 0.0050
0.25–0.50	0.1793 ± 0.0047	1.5	1.3	0.6	0.2	1.7	0.1	2.6	0.1914 ± 0.0050
0.50–0.75	0.1744 ± 0.0046	1.5	1.1	0.5	0.1	1.8	0.1	2.6	0.1859 ± 0.0048
0.75–1.00	0.1736 ± 0.0044	1.5	1.0	0.5	0.2	1.7	0.0	2.6	0.1853 ± 0.0047
1.00–1.25	0.1729 ± 0.0043	1.5	0.9	0.5	0.2	1.7	0.0	2.5	0.1837 ± 0.0046
1.25–1.50	0.1559 ± 0.0045	1.9	1.0	0.6	0.6	1.8	0.0	2.9	0.1652 ± 0.0048
1.50–1.75	0.1474 ± 0.0039	1.7	1.0	0.5	0.2	1.6	0.0	2.6	0.1563 ± 0.0041
1.75–2.00	0.1303 ± 0.0037	1.9	1.1	0.5	0.2	1.6	0.0	2.8	0.1382 ± 0.0039
2.00–2.50	0.0955 ± 0.0026	1.6	1.3	0.4	0.3	1.7	0.1	2.7	0.1012 ± 0.0027

Table 21 Absolute differential cross-sections as a function of $|y^{e\mu}| \times m^{e\mu}$. The columns show the bin ranges, measured cross-section and total uncertainty, relative statistical uncertainty, relative systematic uncertainties in various categories (see text), total relative uncertainty, and differential cross-section corrected to remove contributions via $W \rightarrow \tau \rightarrow e/\mu$ decays. Relative uncertainties smaller than 0.05% are indicated by ‘0.0’. The last bin includes overflows where indicated by the ‘+’ sign

Absolute Bin (unit $ y $ GeV)	$d^2\sigma/d y^{e\mu} dm^{e\mu}$ (fb/unit $ y $ GeV)	Stat. (%)	$t\bar{t}$ mod. (%)	Lept. (%)	Jet/ b (%)	Bkg. (%)	L/E_b (%)	Total (%)	$d^2\sigma/d y^{e\mu} dm^{e\mu}$ (no τ) (fb/unit $ y $ GeV)
$0 < m^{e\mu} < 80$ GeV									
0.00–0.50	44.9 ± 1.3	0.7	0.8	0.8	0.2	0.9	2.3	2.8	37.1 ± 1.0
0.50–1.00	38.7 ± 1.1	0.8	1.0	0.8	0.2	0.9	2.3	2.9	32.1 ± 0.9
1.00–1.50	29.48 ± 0.95	1.0	1.4	0.9	0.2	1.0	2.3	3.2	24.56 ± 0.74
1.50–2.00	17.38 ± 0.65	1.5	1.9	1.0	0.4	1.3	2.3	3.8	14.58 ± 0.52
2.00–2.50	4.13 ± 0.24	3.4	2.9	1.2	0.5	2.5	2.4	5.8	3.49 ± 0.20
$80 < m^{e\mu} < 120$ GeV									
0.00–0.50	67.4 ± 1.9	0.8	0.7	0.7	0.3	0.8	2.3	2.7	57.0 ± 1.6
0.50–1.00	56.9 ± 1.6	0.9	0.8	0.7	0.3	0.7	2.3	2.8	48.2 ± 1.4
1.00–1.50	40.3 ± 1.2	1.2	1.2	0.7	0.3	0.7	2.3	3.0	34.5 ± 1.1
1.50–2.00	17.92 ± 0.68	1.9	1.7	0.8	0.3	1.4	2.3	3.8	15.33 ± 0.60
2.00–2.50	3.30 ± 0.24	5.3	2.9	1.2	1.1	2.8	2.4	7.3	2.86 ± 0.21
$120 < m^{e\mu} < 200$ GeV									
0.00–0.50	33.95 ± 0.98	0.8	1.2	0.6	0.2	0.7	2.3	2.9	29.66 ± 0.84
0.50–1.00	28.57 ± 0.85	0.9	1.3	0.6	0.3	0.8	2.3	3.0	25.02 ± 0.72
1.00–1.50	17.01 ± 0.56	1.2	1.5	0.6	0.2	1.1	2.3	3.3	14.98 ± 0.48
1.50–2.00	6.65 ± 0.28	2.1	2.0	0.8	0.3	1.6	2.3	4.2	5.89 ± 0.25
2.00–2.50	0.84 ± 0.08	7.4	3.6	1.6	1.2	4.2	2.5	9.8	0.74 ± 0.07
$200 < m^{e\mu} < 500 +$ GeV									
0.00–0.50	4.85 ± 0.18	1.1	1.7	0.6	0.3	1.8	2.4	3.6	4.41 ± 0.16
0.50–1.00	3.56 ± 0.13	1.3	1.2	0.6	0.3	1.9	2.4	3.6	3.25 ± 0.11
1.00–1.50	1.72 ± 0.07	2.0	1.5	0.9	0.3	2.1	2.4	4.1	1.57 ± 0.06
1.50–2.00	0.43 ± 0.03	4.1	2.6	1.2	0.3	2.9	2.4	6.2	0.40 ± 0.02
2.00–2.50	0.04 ± 0.01	15.9	7.1	2.4	1.5	5.2	2.7	18.6	0.04 ± 0.01

Table 22 Normalised differential cross-sections as a function of $|y^{e\mu}| \times m^{e\mu}$. The columns show the bin ranges, measured cross-section and total uncertainty, relative statistical uncertainty, relative systematic uncertainties in various categories (see text), total relative uncertainty, and differential cross-section corrected to remove contributions via $W \rightarrow \tau \rightarrow e/\mu$ decays. Relative uncertainties smaller than 0.05% are indicated by ‘0.0’. The last bin includes overflows where indicated by the ‘+’ sign

Normalised	$\frac{1}{\sigma} d^2\sigma/d y^{e\mu} dm^{e\mu}$	Stat.	$t\bar{t}$ mod.	Lept.	Jet/ b	Bkg.	L/E_b	Total	$\frac{1}{\sigma} d^2\sigma/d y^{e\mu} dm^{e\mu}$ (no τ)
Bin (unit $ y $ GeV)	(10^{-3} /unit $ y $ GeV)	(%)	(%)	(%)	(%)	(%)	(%)	(%)	(10^{-3} /unit $ y $ GeV)
0 < $m^{e\mu}$ < 80 GeV									
0.00–0.50	3.165 ± 0.044	0.7	1.0	0.2	0.1	0.7	0.0	1.4	3.061 ± 0.040
0.50–1.00	2.733 ± 0.035	0.8	0.8	0.2	0.1	0.6	0.0	1.3	2.649 ± 0.032
1.00–1.50	2.080 ± 0.032	1.0	0.9	0.3	0.1	0.6	0.0	1.5	2.024 ± 0.029
1.50–2.00	1.226 ± 0.027	1.4	1.3	0.4	0.4	0.9	0.0	2.2	1.202 ± 0.026
2.00–2.50	0.291 ± 0.014	3.4	2.3	0.7	0.4	2.2	0.1	4.7	0.287 ± 0.013
80 < $m^{e\mu}$ < 120 GeV									
0.00–0.50	4.758 ± 0.049	0.8	0.5	0.2	0.1	0.4	0.0	1.0	4.696 ± 0.048
0.50–1.00	4.017 ± 0.044	0.9	0.5	0.1	0.1	0.4	0.0	1.1	3.974 ± 0.045
1.00–1.50	2.846 ± 0.041	1.1	0.8	0.2	0.2	0.4	0.0	1.5	2.840 ± 0.043
1.50–2.00	1.264 ± 0.031	1.8	1.3	0.2	0.1	1.0	0.0	2.5	1.263 ± 0.033
2.00–2.50	0.233 ± 0.015	5.3	2.6	0.7	1.1	2.5	0.1	6.5	0.236 ± 0.016
120 < $m^{e\mu}$ < 200 GeV									
0.00–0.50	2.395 ± 0.024	0.8	0.5	0.2	0.1	0.3	0.0	1.0	2.444 ± 0.025
0.50–1.00	2.016 ± 0.024	0.8	0.7	0.2	0.1	0.4	0.0	1.2	2.062 ± 0.023
1.00–1.50	1.200 ± 0.021	1.2	1.0	0.2	0.1	0.7	0.0	1.7	1.234 ± 0.021
1.50–2.00	0.469 ± 0.014	2.1	1.6	0.4	0.3	1.2	0.1	3.0	0.485 ± 0.015
2.00–2.50	0.0592 ± 0.0054	7.4	3.4	1.3	1.2	3.9	0.2	9.2	0.0611 ± 0.0056
200 < $m^{e\mu}$ < 500 + GeV									
0.00–0.50	0.3425 ± 0.0084	1.1	1.5	0.4	0.1	1.6	0.0	2.5	0.3634 ± 0.0086
0.50–1.00	0.2513 ± 0.0058	1.3	0.7	0.5	0.3	1.6	0.0	2.3	0.2676 ± 0.0061
1.00–1.50	0.1211 ± 0.0036	2.0	1.0	0.7	0.1	1.8	0.1	2.9	0.1292 ± 0.0038
1.50–2.00	0.0306 ± 0.0017	4.1	2.3	1.0	0.3	2.5	0.1	5.4	0.0327 ± 0.0018
2.00–2.50	0.0029 ± 0.0005	15.9	6.9	2.1	1.5	4.9	0.4	18.2	0.0031 ± 0.0006

Table 23 Absolute differential cross-sections as a function of $|\Delta\phi^\ell| \times m^{e\mu}$. The columns show the bin ranges, measured cross-section and total uncertainty, relative statistical uncertainty, relative systematic uncertainties in various categories (see text), total relative uncertainty, and differential cross-section corrected to remove contributions via $W \rightarrow \tau \rightarrow e/\mu$ decays. Relative uncertainties smaller than 0.05% are indicated by ‘0.0’. The bin boundaries for $\Delta\phi^{e\mu}$ correspond to exact multiples of $\pi/10$ but are quoted to two decimal places

Absolute	$d^2\sigma/d\Delta\phi^{e\mu}dm^{e\mu}$	Stat.	$t\bar{t}$ mod.	Lept.	Jet/b	Bkg.	L/E_b	Total	$d^2\sigma/d\Delta\phi^{e\mu}dm^{e\mu}$ (no τ)
Bin (rad GeV)	(fb/rad GeV)	(%)	(%)	(%)	(%)	(%)	(%)	(%)	(fb/rad GeV)
$0 < m^{e\mu} < 80$ GeV									
0.00–0.31	31.2 ± 1.0	1.2	1.6	0.8	0.1	1.0	2.3	3.4	27.0 ± 0.9
0.31–0.63	31.13 ± 0.99	1.1	1.4	0.8	0.1	0.9	2.3	3.2	27.04 ± 0.82
0.63–0.94	30.34 ± 0.95	1.2	1.3	0.8	0.2	0.9	2.3	3.1	26.31 ± 0.79
0.94–1.26	29.60 ± 0.92	1.2	1.1	0.8	0.2	0.9	2.3	3.1	25.31 ± 0.76
1.26–1.57	25.05 ± 0.80	1.3	1.1	0.9	0.2	1.0	2.3	3.2	20.89 ± 0.64
1.57–1.88	20.21 ± 0.66	1.5	1.1	0.9	0.3	1.0	2.3	3.3	16.31 ± 0.52
1.88–2.20	15.63 ± 0.55	1.8	1.3	1.0	0.2	1.1	2.3	3.5	12.16 ± 0.42
2.20–2.51	12.27 ± 0.46	2.1	1.4	1.0	0.3	1.1	2.3	3.7	9.27 ± 0.34
2.51–2.83	10.07 ± 0.40	2.3	1.6	1.1	0.2	1.3	2.3	4.0	7.53 ± 0.29
2.83–3.14	8.38 ± 0.37	2.6	1.8	1.1	0.6	1.7	2.3	4.4	6.20 ± 0.27
$80 < m^{e\mu} < 120$ GeV									
0.00–0.31	10.11 ± 0.44	2.8	1.9	0.8	0.4	1.3	2.3	4.3	9.13 ± 0.40
0.31–0.63	10.92 ± 0.45	2.6	1.7	0.8	0.4	1.0	2.3	4.1	9.84 ± 0.40
0.63–0.94	13.61 ± 0.52	2.3	1.5	0.7	0.4	1.0	2.3	3.8	12.28 ± 0.46
0.94–1.26	19.44 ± 0.68	1.9	1.3	0.7	0.2	0.9	2.3	3.5	17.50 ± 0.60
1.26–1.57	29.17 ± 0.94	1.6	1.1	0.6	0.4	0.9	2.3	3.2	26.19 ± 0.83
1.57–1.88	38.7 ± 1.2	1.4	1.0	0.7	0.2	0.8	2.3	3.1	34.1 ± 1.0
1.88–2.20	44.6 ± 1.4	1.3	0.9	0.7	0.4	0.8	2.3	3.1	37.9 ± 1.1
2.20–2.51	45.4 ± 1.4	1.3	0.9	0.7	0.3	0.8	2.3	3.0	37.3 ± 1.1
2.51–2.83	42.5 ± 1.3	1.4	0.9	0.7	0.4	0.8	2.3	3.1	34.1 ± 1.1
2.83–3.14	41.8 ± 1.3	1.4	1.1	0.7	0.4	0.8	2.3	3.1	33.1 ± 1.1
$120 < m^{e\mu} < 200$ GeV									
0.00–0.31	3.44 ± 0.22	3.3	4.8	0.8	0.3	1.3	2.3	6.5	3.17 ± 0.21
0.31–0.63	3.33 ± 0.20	3.3	4.1	0.8	0.2	1.3	2.3	6.0	3.05 ± 0.19
0.63–0.94	3.92 ± 0.21	3.1	3.4	0.8	0.5	1.5	2.3	5.5	3.59 ± 0.20
0.94–1.26	5.41 ± 0.25	2.6	2.7	0.7	0.2	1.2	2.3	4.6	4.94 ± 0.24
1.26–1.57	8.28 ± 0.32	2.1	2.0	0.7	0.4	1.0	2.3	3.9	7.55 ± 0.31
1.57–1.88	12.70 ± 0.44	1.7	1.5	0.6	0.2	1.0	2.4	3.5	11.52 ± 0.40
1.88–2.20	18.44 ± 0.59	1.4	1.3	0.6	0.2	0.9	2.3	3.2	16.55 ± 0.52
2.20–2.51	24.92 ± 0.80	1.2	1.5	0.6	0.3	0.8	2.3	3.2	21.86 ± 0.68
2.51–2.83	28.48 ± 0.99	1.2	2.0	0.6	0.4	0.8	2.3	3.5	24.35 ± 0.85
2.83–3.14	29.7 ± 1.1	1.1	2.7	0.6	0.2	0.8	2.3	3.8	25.0 ± 1.0
$200 < m^{e\mu} < 500 +$ GeV									
0.00–0.31	0.23 ± 0.03	7.1	6.3	0.9	1.0	5.6	2.3	11.4	0.22 ± 0.02
0.31–0.63	0.30 ± 0.03	6.3	5.6	0.8	0.7	4.3	2.3	9.8	0.28 ± 0.03
0.63–0.94	0.29 ± 0.03	6.2	4.8	0.8	0.8	5.0	2.4	9.7	0.27 ± 0.03
0.94–1.26	0.36 ± 0.03	5.6	3.9	0.7	0.8	3.7	2.3	8.2	0.34 ± 0.03
1.26–1.57	0.54 ± 0.04	4.3	3.1	0.8	0.5	3.2	2.4	6.7	0.51 ± 0.03
1.57–1.88	0.93 ± 0.05	3.3	2.4	0.8	0.4	2.7	2.3	5.5	0.87 ± 0.05
1.88–2.20	1.60 ± 0.07	2.4	1.7	0.7	0.5	2.1	2.3	4.4	1.48 ± 0.07
2.20–2.51	2.76 ± 0.11	1.9	1.4	0.7	0.4	1.9	2.4	3.9	2.54 ± 0.10
2.51–2.83	4.22 ± 0.16	1.5	1.5	0.6	0.3	1.7	2.4	3.7	3.83 ± 0.14
2.83–3.14	5.68 ± 0.21	1.3	2.0	0.6	0.3	1.3	2.4	3.7	5.08 ± 0.18

Table 24 Normalised differential cross-sections as a function of $|\Delta\phi^\ell| \times m^{e\mu}$. The columns show the bin ranges, measured cross-section and total uncertainty, relative statistical uncertainty, relative systematic uncertainties in various categories (see text), total relative uncertainty, and differential cross-section corrected to remove contributions via $W \rightarrow \tau \rightarrow e/\mu$ decays. Relative uncertainties smaller than 0.05% are indicated by ‘0.0’. The bin boundaries for $\Delta\phi^{e\mu}$ correspond to exact multiples of $\pi/10$ but are quoted to two decimal places

Normalised	$\frac{1}{\sigma} \frac{d^2\sigma}{d\Delta\phi^{e\mu} dm^{e\mu}}$	Stat.	$t\bar{t}$ mod.	Lept.	Jet/b	Bkg.	L/E_b	Total	$\frac{1}{\sigma} \frac{d^2\sigma}{d\Delta\phi^{e\mu} dm^{e\mu}}$ (no τ)
Bin (rad GeV)	($10^{-3}/\text{rad GeV}$)	(%)	(%)	(%)	(%)	(%)	(%)	(%)	($10^{-3}/\text{rad GeV}$)
0 < m^{eμ} < 80 GeV									
0.00–0.31	2.204 ± 0.047	1.2	1.6	0.2	0.2	0.7	0.0	2.1	2.224 ± 0.045
0.31–0.63	2.196 ± 0.041	1.1	1.3	0.1	0.2	0.6	0.0	1.8	2.227 ± 0.038
0.63–0.94	2.140 ± 0.036	1.1	1.1	0.1	0.1	0.6	0.0	1.7	2.167 ± 0.034
0.94–1.26	2.088 ± 0.033	1.2	0.9	0.2	0.1	0.6	0.0	1.6	2.084 ± 0.032
1.26–1.57	1.767 ± 0.029	1.3	0.8	0.2	0.2	0.7	0.0	1.7	1.720 ± 0.028
1.57–1.88	1.426 ± 0.026	1.5	0.7	0.3	0.1	0.7	0.0	1.8	1.343 ± 0.024
1.88–2.20	1.103 ± 0.023	1.7	0.9	0.3	0.1	0.8	0.0	2.1	1.001 ± 0.022
2.20–2.51	0.865 ± 0.021	2.0	1.0	0.4	0.1	0.8	0.0	2.5	0.763 ± 0.019
2.51–2.83	0.710 ± 0.020	2.3	1.2	0.5	0.2	1.1	0.1	2.8	0.620 ± 0.018
2.83–3.14	0.591 ± 0.020	2.5	1.4	0.5	0.5	1.5	0.0	3.3	0.511 ± 0.017
80 < m^{eμ} < 120 GeV									
0.00–0.31	0.713 ± 0.023	2.7	1.4	0.2	0.3	1.0	0.0	3.3	0.751 ± 0.026
0.31–0.63	0.770 ± 0.023	2.6	1.3	0.2	0.4	0.7	0.0	3.0	0.810 ± 0.025
0.63–0.94	0.960 ± 0.026	2.3	1.1	0.1	0.4	0.6	0.0	2.7	1.011 ± 0.027
0.94–1.26	1.371 ± 0.030	1.9	0.9	0.2	0.2	0.4	0.0	2.2	1.441 ± 0.031
1.26–1.57	2.057 ± 0.037	1.6	0.7	0.1	0.3	0.4	0.0	1.8	2.156 ± 0.038
1.57–1.88	2.729 ± 0.042	1.4	0.6	0.1	0.1	0.4	0.0	1.5	2.809 ± 0.043
1.88–2.20	3.145 ± 0.049	1.3	0.6	0.2	0.3	0.5	0.0	1.6	3.124 ± 0.048
2.20–2.51	3.201 ± 0.052	1.3	0.8	0.2	0.2	0.5	0.0	1.6	3.075 ± 0.050
2.51–2.83	2.998 ± 0.053	1.4	0.9	0.2	0.3	0.5	0.0	1.8	2.811 ± 0.051
2.83–3.14	2.948 ± 0.056	1.4	1.1	0.2	0.3	0.5	0.0	1.9	2.722 ± 0.058
120 < m^{eμ} < 200 GeV									
0.00–0.31	0.243 ± 0.014	3.3	4.7	0.3	0.4	1.2	0.1	5.9	0.261 ± 0.016
0.31–0.63	0.235 ± 0.012	3.3	3.9	0.3	0.3	1.2	0.0	5.3	0.251 ± 0.014
0.63–0.94	0.276 ± 0.013	3.1	3.2	0.3	0.4	1.3	0.0	4.7	0.296 ± 0.015
0.94–1.26	0.382 ± 0.014	2.6	2.4	0.2	0.2	0.9	0.0	3.7	0.407 ± 0.017
1.26–1.57	0.584 ± 0.016	2.1	1.7	0.3	0.4	0.7	0.0	2.8	0.621 ± 0.020
1.57–1.88	0.896 ± 0.018	1.7	1.0	0.2	0.1	0.6	0.0	2.0	0.948 ± 0.022
1.88–2.20	1.300 ± 0.021	1.3	0.7	0.2	0.1	0.5	0.0	1.6	1.363 ± 0.022
2.20–2.51	1.758 ± 0.029	1.2	1.1	0.2	0.2	0.3	0.0	1.6	1.800 ± 0.028
2.51–2.83	2.009 ± 0.042	1.1	1.7	0.2	0.2	0.3	0.0	2.1	2.005 ± 0.043
2.83–3.14	2.095 ± 0.057	1.1	2.5	0.2	0.1	0.3	0.0	2.7	2.062 ± 0.063
200 < m^{eμ} < 500 + GeV									
0.00–0.31	0.0164 ± 0.0018	7.1	6.0	0.7	1.0	5.5	0.0	10.9	0.0179 ± 0.0020
0.31–0.63	0.0209 ± 0.0019	6.3	5.3	0.4	0.7	4.1	0.0	9.2	0.0227 ± 0.0021
0.63–0.94	0.0205 ± 0.0019	6.1	4.5	0.5	0.8	4.9	0.1	9.1	0.0224 ± 0.0021
0.94–1.26	0.0255 ± 0.0019	5.6	3.6	0.3	0.8	3.5	0.0	7.6	0.0279 ± 0.0022
1.26–1.57	0.0382 ± 0.0023	4.2	2.8	0.6	0.6	3.1	0.0	6.0	0.0416 ± 0.0026
1.57–1.88	0.0659 ± 0.0031	3.3	2.0	0.6	0.2	2.5	0.0	4.7	0.0717 ± 0.0034
1.88–2.20	0.1130 ± 0.0039	2.4	1.3	0.5	0.4	2.0	0.0	3.4	0.1221 ± 0.0043
2.20–2.51	0.1949 ± 0.0053	1.8	1.0	0.6	0.2	1.7	0.0	2.7	0.2094 ± 0.0056
2.51–2.83	0.2974 ± 0.0075	1.5	1.3	0.5	0.3	1.5	0.1	2.5	0.3154 ± 0.0075
2.83–3.14	0.401 ± 0.011	1.3	2.0	0.4	0.1	1.0	0.1	2.6	0.418 ± 0.010

References

- M. Cacciari, M. Czakon, M. Mangano, A. Mitov, P. Nason, Top-pair production at hadron colliders with next-to-next-to-leading logarithmic soft-gluon resummation. *Phys. Lett. B* **710**, 612 (2012). <https://doi.org/10.1016/j.physletb.2012.03.013>. arXiv:1111.5869 [hep-ph]
- P. Barnreuther, M. Czakon, A. Mitov, Percent-level-precision physics at the tevatron: first genuine NNLO QCD corrections to $q\bar{q} \rightarrow t\bar{t} + X$. *Phys. Rev. Lett.* **109**, 132001 (2012). <https://doi.org/10.1103/PhysRevLett.109.132001>. arXiv:1204.5201 [hep-ph]
- M. Czakon, A. Mitov, NNLO corrections to top-pair production at hadron colliders: the all-fermionic scattering channels. *JHEP* **12**, 054 (2012). [https://doi.org/10.1007/JHEP12\(2012\)054](https://doi.org/10.1007/JHEP12(2012)054). arXiv:1207.0236 [hep-ph]
- M. Czakon, A. Mitov, NNLO corrections to top pair production at hadron colliders: the quark-gluon reaction. *JHEP* **01**, 080 (2013). [https://doi.org/10.1007/JHEP01\(2013\)080](https://doi.org/10.1007/JHEP01(2013)080). arXiv:1210.6832 [hep-ph]
- M. Czakon, P. Fiedler, A. Mitov, Total top-quark pair production cross section at hadron colliders through $O(\alpha_s^4)$. *Phys. Rev. Lett.* **110**, 252004 (2013). <https://doi.org/10.1103/PhysRevLett.110.252004>. arXiv:1303.6254 [hep-ph]
- S. Catani et al., Top-quark pair hadroproduction at next-to-next-to-leading order in QCD. *Phys. Rev. D* **99**, 051501 (2019). <https://doi.org/10.1103/PhysRevD.99.051501>. arXiv:1901.04005 [hep-ph]
- ATLAS Collaboration, Measurement of the $t\bar{t}$ production cross-section using ep events with b-tagged jets in pp collisions at $\sqrt{s} = 7$ and 8 TeV with the ATLAS detector. *Eur. Phys. J. C* **74**, 3109 (2014). <https://doi.org/10.1140/epjc/s10052-014-3109-7> arXiv:1406.5375 [hep-ex] [Addendum: *Eur. Phys. J. C* **76**, 642 (2016). <https://doi.org/10.1140/epjc/s10052-016-4501-2>]
- ATLAS Collaboration, Measurement of the inclusive and fiducial $t\bar{t}$ production cross-sections in the lepton + jets channel in pp collisions at $\sqrt{s} = 8$ TeV with the ATLAS detector. *Eur. Phys. J. C* **78**, 487 (2018). <https://doi.org/10.1140/epjc/s10052-018-5904-z>. arXiv:1712.06857 [hep-ex]
- ATLAS Collaboration, Measurement of the $t\bar{t}$ production cross-section using ep events with b-tagged jets in pp collisions at $\sqrt{s} = 13$ TeV with the ATLAS detector. *Phys. Lett. B* **761**, 136 (2016). <https://doi.org/10.1016/j.physletb.2016.08.019>. arXiv:1606.02699 [hep-ex] [Erratum: *Phys. Lett. B* **772**, 879 (2017). <https://doi.org/10.1016/j.physletb.2017.09.027>]
- CMS Collaboration, Measurement of the $t\bar{t}$ production cross section in the ep channel in proton-proton collisions at $\sqrt{s} = 7$ and 8 TeV. *JHEP* **08**, 029 (2016). [https://doi.org/10.1007/JHEP08\(2016\)029](https://doi.org/10.1007/JHEP08(2016)029). arXiv:1603.02303 [hep-ex]
- CMS Collaboration, Measurements of the $t\bar{t}$ production cross section in lepton + jets final states in pp collisions at 8 TeV and ratio of 8 to 7 TeV cross sections. *Eur. Phys. J. C* **77**, 15 (2017). <https://doi.org/10.1140/epjc/s10052-016-4504-z>. arXiv:1602.09024 [hep-ex]
- CMS Collaboration, Measurement of the $t\bar{t}$ production cross section using events with one lepton and at least one jet in pp collisions at $\sqrt{s} = 13$ TeV. *JHEP* **09**, 051 (2017). [https://doi.org/10.1007/JHEP09\(2017\)051](https://doi.org/10.1007/JHEP09(2017)051). arXiv:1701.06228 [hep-ex]
- CMS Collaboration, Measurement of the $t\bar{t}$ production cross section, the top quark mass, and the strong coupling constant using dilepton events in pp collisions at $\sqrt{s} = 13$ TeV. *Eur. Phys. J. C* **79**, 368 (2019). <https://doi.org/10.1140/epjc/s10052-019-6863-8>. arXiv:1812.10505 [hep-ex]
- M. Czakon, A. Mitov, Top ++: a program for the calculation of the top-pair cross-section at hadron colliders. *Comput. Phys. Commun.* **185**, 2930 (2014). <https://doi.org/10.1016/j.cpc.2014.06.021>. arXiv:1112.5675 [hep-ph]
- M. Botje et al., The PDF4LHC Working Group Interim Recommendations (2011). arXiv:1101.0538 [hep-ph]
- A.D. Martin, W.J. Stirling, R.S. Thorne, G. Watt, Parton distributions for the LHC. *Eur. Phys. J. C* **63**, 189 (2009). <https://doi.org/10.1140/epjc/s10052-009-1072-5>. arXiv:0901.0002 [hep-ph]
- A.D. Martin, W.J. Stirling, R.S. Thorne, G. Watt, Uncertainties on a α_s in global PDF analyses and implications for predicted hadronic cross sections. *Eur. Phys. J. C* **64**, 653 (2009). <https://doi.org/10.1140/epjc/s10052-009-1164-2>. arXiv:0905.3531 [hep-ph]
- H.-L. Lai et al., New parton distributions for collider physics. *Phys. Rev. D* **82**, 074024 (2010). <https://doi.org/10.1103/PhysRevD.82.074024>. arXiv:1007.2241 [hep-ph]
- J. Gao et al., CT10 next-to-next-to-leading order global analysis of QCD. *Phys. Rev. D* **89**, 033009 (2014). <https://doi.org/10.1103/PhysRevD.89.033009>. arXiv:1302.6246 [hep-ph]
- R.D. Ball et al., Parton distributions with LHC data. *Nucl. Phys. B* **867**, 244 (2013). <https://doi.org/10.1016/j.nuclphysb.2012.10.003>. arXiv:1207.1303 [hep-ph]
- M. Cacciari, S. Frixione, M.L. Mangano, P. Nason, G. Ridolfi, The $t\bar{t}$ cross-section at 1.8 TeV and 1.96 TeV: a study of the systematics due to parton densities and scale dependence. *JHEP* **04**, 068 (2004). <https://doi.org/10.1088/1126-6708/2004/04/068>. arXiv:hep-ph/0303085
- S. Catani, D. de Florian, M. Grazzini, P. Nason, Soft-gluon resummation for Higgs boson production at hadron colliders. *JHEP* **07**, 028 (2003). <https://doi.org/10.1088/1126-6708/2003/07/028>. arXiv:hep-ph/0306211
- A. Buckley et al., General-purpose event generators for LHC physics. *Phys. Rep.* **504**, 145 (2011). <https://doi.org/10.1016/j.physrep.2011.03.005>. arXiv:1101.2599 [hep-ph]
- S. Moch et al., High precision fundamental constants at the TeV scale (2014). arXiv:1405.4781 [hep-ph]
- M. Butenschoen et al., Top quark mass calibration for Monte Carlo event generators. *Phys. Rev. Lett.* **117**, 232001 (2016). <https://doi.org/10.1103/PhysRevLett.117.232001>. arXiv:1608.01318 [hep-ph]
- S. Ferrario Ravasio, T. Jezo, P. Nason, C. Oleari, A theoretical study of top-mass measurements at the LHC using NLO + PS generators of increasing accuracy. *Eur. Phys. J. C* **78**, 458 (2018). <https://doi.org/10.1140/epjc/s10052-018-5909-7>. arXiv:1801.03944 [hep-ph]
- ATLAS Collaboration, Measurements of top-quark pair to Z-boson cross-section ratios at $\sqrt{s} = 13, 8, 7$ TeV with the ATLAS detector. *JHEP* **02**, 117 (2017). [https://doi.org/10.1007/JHEP02\(2017\)117](https://doi.org/10.1007/JHEP02(2017)117). arXiv:1612.03636 [hep-ex]
- A. Ceccucci, Z. Ligeti, Y. Sakai, CKM quark-mixing matrix, in Review of Particle Physics. *Phys. Rev. D* **98**, 030001 (2018). <https://doi.org/10.1103/PhysRevD.98.030001>
- ATLAS Collaboration, Measurement of lepton differential distributions and the top quark mass in $t\bar{t}$ production in pp collisions at $\sqrt{s} = 8$ TeV with the ATLAS detector. *Eur. Phys. J. C* **77**, 804 (2017). <https://doi.org/10.1140/epjc/s10052-017-5349-9>. arXiv:1709.09407 [hep-ex]
- ATLAS Collaboration, The ATLAS experiment at the CERN large hadron collider. *JINST* **3**, S08003 (2008). <https://doi.org/10.1088/1748-0221/3/08/S08003>
- B. Abbott et al., Production and integration of the ATLAS insertable B-layer. *JINST* **13**, T05008 (2018). <https://doi.org/10.1088/1748-0221/13/05/T05008>. arXiv:1803.00844 [physics.ins-det]
- ATLAS Collaboration, ATLAS Insertable B-Layer Technical Design Report, ATLAS-TDR-19 (2010). <https://cds.cern.ch/record/1291633> (ATLAS Insertable B-Layer Technical Design

- Report Addendum, ATLAS-TDR-19-ADD-1, 2012. <https://cds.cern.ch/record/1451888>
33. ATLAS Collaboration, Performance of the ATLAS trigger system in 2015. *Eur. Phys. J. C* **77**, 317 (2017). <https://doi.org/10.1140/epjc/s10052-017-4852-3>. arXiv:1611.09661 [hep-ex]
 34. ATLAS Collaboration, Performance of electron and photon triggers in ATLAS during LHC Run 2, (2019). arXiv:1909.00761 [hep-ex]
 35. ATLAS Collaboration, The ATLAS simulation infrastructure. *Eur. Phys. J. C* **70**, 823 (2010). <https://doi.org/10.1140/epjc/s10052-010-1429-9>. arXiv:1005.4568 [physics.ins-det]
 36. S. Agostinelli et al., GEANT4—a simulation toolkit. *Nucl. Instrum. Methods A* **506**, 250 (2003). [https://doi.org/10.1016/S0168-9002\(03\)01368-8](https://doi.org/10.1016/S0168-9002(03)01368-8)
 37. ATLAS Collaboration, The simulation principle and performance of the ATLAS fast calorimeter simulation FastCaloSim, ATL-PHYS-PUB-2010-013 (2010). <https://cds.cern.ch/record/1300517>
 38. T. Sjostrand, S. Mrenna, P.Z. Skands, A brief introduction to PYTHIA 8.1. *Comput. Phys. Commun.* **178**, 852 (2008). <https://doi.org/10.1016/j.cpc.2008.01.036>. arXiv:0710.3820 [hep-ph]
 39. ATLAS Collaboration, Further ATLAS tunes of Pythia 6 and Pythia 8, ATL-PHYS-PUB-2011-014 (2011). <https://cds.cern.ch/record/1400677>
 40. P. Nason, A new method for combining NLO QCD with shower Monte Carlo algorithms. *JHEP* **11**, 040 (2004). <https://doi.org/10.1088/1126-6708/2004/11/040>. arXiv:hep-ph/0409146
 41. S. Frixione, P. Nason, C. Oleari, Matching NLO QCD computations with parton shower simulations: the POWHEG method. *JHEP* **11**, 070 (2007). <https://doi.org/10.1088/1126-6708/2007/11/070>. arXiv:0709.2092 [hep-ph]
 42. S. Alioli, P. Nason, C. Oleari, E. Re, A general framework for implementing NLO calculations in shower Monte Carlo programs: the POWHEG BOX. *JHEP* **06**, 043 (2010). [https://doi.org/10.1007/JHEP06\(2010\)043](https://doi.org/10.1007/JHEP06(2010)043). arXiv:1002.2581 [hep-ph]
 43. S. Frixione, G. Ridolfi, P. Nason, A positive-weight next-to-leading-order Monte Carlo for heavy flavour hadroproduction. *JHEP* **09**, 126 (2007). <https://doi.org/10.1088/1126-6708/2007/09/126>. arXiv:0707.3088 [hep-ph]
 44. R.D. Ball et al., Parton distributions for the LHC Run II. *JHEP* **04**, 040 (2015). [https://doi.org/10.1007/JHEP04\(2015\)040](https://doi.org/10.1007/JHEP04(2015)040). arXiv:1410.8849 [hep-ph]
 45. ATLAS Collaboration, ATLAS Pythia 8 tunes to 7 TeV data, ATL-PHYS-PUB-2014-021 (2014). <https://cds.cern.ch/record/1966419>
 46. ATLAS Collaboration, Studies on top-quark Monte Carlo modelling for Top2016, ATL-PHYS-PUB-2016-020 (2016). <https://cds.cern.ch/record/2216168>
 47. J. Bellm et al., Herwig 7.0/Herwig ++ 3.0 release note. *Eur. Phys. J. C* **76**, 196 (2016). <https://doi.org/10.1140/epjc/s10052-016-4018-8>. arXiv:1512.01178 [hep-ph]
 48. J. Alwall et al., The automated computation of tree-level and next-to-leading order differential cross sections, and their matching to parton shower simulations. *JHEP* **07**, 079 (2014). [https://doi.org/10.1007/JHEP07\(2014\)079](https://doi.org/10.1007/JHEP07(2014)079). arXiv:1405.0301 [hep-ph]
 49. S. Frixione, B.R. Webber, Matching NLO QCD computations and parton shower simulations. *JHEP* **06**, 029 (2002). <https://doi.org/10.1088/1126-6708/2002/06/029>. arXiv:hep-ph/0204244 [hep-ph]
 50. ATLAS Collaboration, Measurement of the top quark mass in the $t\bar{t} \rightarrow \text{lepton} + \text{jets}$ channel from $\sqrt{s} = 8$ TeV ATLAS data and combination with previous results. *Eur. Phys. J. C* **79**, 290 (2019). <https://doi.org/10.1140/epjc/s10052-019-6757-9>. arXiv:1810.01772 [hep-ex]
 51. CMS Collaboration, Measurement of the top quark mass using proton–proton data at $\sqrt{s} = 7$ and 8 TeV. *Phys. Rev. D* **93**, 072004 (2016). <https://doi.org/10.1103/PhysRevD.93.072004>. arXiv:1509.04044 [hep-ex]
 52. J. Erler, P. Langacker, Electroweak model and constraints on new physics, in Review of Particle Physics. *Phys. Rev. D* **98**, 030001 (2018). <https://doi.org/10.1103/PhysRevD.98.030001>
 53. D.J. Lange, The EvtGen particle decay simulation package. *Nucl. Instrum. Methods A* **462**, 152 (2001). [https://doi.org/10.1016/S0168-9002\(01\)00089-4](https://doi.org/10.1016/S0168-9002(01)00089-4)
 54. E. Re, Single-top Wt -channel production matched with parton showers using the POWHEG method. *Eur. Phys. J. C* **71**, 1547 (2011). <https://doi.org/10.1140/epjc/s10052-011-1547-z>. arXiv:1009.2450 [hep-ph]
 55. T. Sjostrand, S. Mrenna, P.Z. Skands, Pythia 6.4 physics and manual. *JHEP* **05**, 026 (2006). <https://doi.org/10.1088/1126-6708/2006/05/026>. arXiv:hep-ph/0603175
 56. P.Z. Skands, Tuning Monte Carlo generators: the Perugia tunes. *Phys. Rev. D* **82**, 074018 (2010). <https://doi.org/10.1103/PhysRevD.82.074018>. arXiv:1005.3457 [hep-ph]
 57. S. Frixione, E. Laenen, P. Motylinski, B.R. Webber, C.D. White, Single-top hadroproduction in association with a W boson. *JHEP* **07**, 029 (2008). <https://doi.org/10.1088/1126-6708/2008/07/029>. arXiv:0805.3067 [hep-ph]
 58. N. Kidonakis, Two-loop soft anomalous dimensions for single top quark associated production with a W^- or H^- . *Phys. Rev. D* **82**, 054018 (2010). <https://doi.org/10.1103/PhysRevD.82.054018>. arXiv:1005.4451 [hep-ph]
 59. N. Kidonakis, Top quark production, in Proceedings, Helmholtz International Summer School on Physics of Heavy Quarks and Hadrons (HQ 2013): JINR, Dubna, July 15–28, 2013 (2014). <https://doi.org/10.3204/DESY-PROC-2013-03/Kidonakis>. arXiv:1311.0283 [hep-ph]
 60. T. Gleisberg et al., Event generation with SHERPA 1.1. *JHEP* **02**, 007 (2009). <https://doi.org/10.1088/1126-6708/2009/02/007>. arXiv:0811.4622 [hep-ph]
 61. ATLAS Collaboration, Measurement of the $t\bar{t}Z$ and $t\bar{t}W$ cross sections in proton–proton collisions at $\sqrt{s} = 13$ TeV with the ATLAS detector. *Phys. Rev. D* **99**, 072009 (2019). <https://doi.org/10.1103/PhysRevD.99.072009>. arXiv:1901.03584 [hep-ex]
 62. R. Frederix, E. Re, P. Torrielli, Single-top t -channel hadroproduction in the four-flavour scheme with POWHEG and aMC@NLO. *JHEP* **09**, 130 (2012). [https://doi.org/10.1007/JHEP09\(2012\)130](https://doi.org/10.1007/JHEP09(2012)130). arXiv:1207.5391 [hep-ph]
 63. ATLAS Collaboration, Electron reconstruction and identification in the ATLAS experiment using the 2015 and 2016 LHC proton–proton collision data at $\sqrt{s} = 13$ TeV. *Eur. Phys. J. C* **79**, 639 (2019). <https://doi.org/10.1140/epjc/s10052-019-7140-6>. arXiv:1902.04655 [hep-ex]
 64. ATLAS Collaboration, Muon reconstruction performance of the ATLAS detector in proton–proton collision data at $\sqrt{s} = 13$ TeV. *Eur. Phys. J. C* **76**, 292 (2016). <https://doi.org/10.1140/epjc/s10052-016-4120-y>. arXiv:1603.05598 [hep-ex]
 65. M. Cacciari, G.P. Salam, G. Soyez, The anti- k_t jet clustering algorithm. *JHEP* **04**, 063 (2008). <https://doi.org/10.1088/1126-6708/2008/04/063>. arXiv:0802.1189 [hep-ph]
 66. M. Cacciari, G.P. Salam, G. Soyez, FastJet user manual. *Eur. Phys. J. C* **72**, 1896 (2012). <https://doi.org/10.1140/epjc/s10052-012-1896-2>. arXiv:1111.6097 [hep-ph]
 67. ATLAS Collaboration, Topological cell clustering in the ATLAS calorimeters and its performance in LHC Run 1. *Eur. Phys. J. C* **77**, 490 (2017). <https://doi.org/10.1140/epjc/s10052-017-5004-5>. arXiv:1603.02934 [hep-ex]
 68. ATLAS Collaboration, Jet energy scale measurements and their systematic uncertainties in proton–proton collisions at $\sqrt{s} = 13$ TeV with the ATLAS detector. *Phys. Rev. D* **96**, 072002 (2017). <https://doi.org/10.1103/PhysRevD.96.072002>. arXiv:1703.09665 [hep-ex]

69. ATLAS Collaboration, Performance of pile-up mitigation techniques for jets in pp collisions at $\sqrt{s} = 8$ TeV using the ATLAS detector. *Eur. Phys. J. C* **76**, 581 (2016). <https://doi.org/10.1140/epjc/s10052-016-4395-z>. arXiv:1510.03823 [hep-ex]
70. ATLAS Collaboration, Measurements of b-jet tagging efficiency with the ATLAS detector using $t\bar{t}$ events at $\sqrt{s} = 13$ TeV. *JHEP* **08**, 089 (2018). [https://doi.org/10.1007/JHEP08\(2018\)089](https://doi.org/10.1007/JHEP08(2018)089). arXiv:1805.01845 [hep-ex]
71. ATLAS Collaboration, Jet energy measurement and its systematic uncertainty in proton–proton collisions at $\sqrt{s} = 7$ TeV with the ATLAS detector. *Eur. Phys. J. C* **75**, 17 (2015). <https://doi.org/10.1140/epjc/s10052-014-3190-y>. arXiv:1406.0076 [hep-ex]
72. R. Gavin, Y. Li, F. Petriello, S. Quackenbush, FEWZ 2.0: a code for hadronic Z production at next-to-next-to-leading order. *Comput. Phys. Commun.* **182**, 2388 (2011). <https://doi.org/10.1016/j.cpc.2011.06.008>. arXiv:1011.3540 [hep-ph]
73. J. Alwall, M. Herquet, F. Maltoni, O. Mattelaer, T. Stelzer, MadGraph 5: going beyond. *JHEP* **06**, 128 (2011). [https://doi.org/10.1007/JHEP06\(2011\)128](https://doi.org/10.1007/JHEP06(2011)128). arXiv:1106.0522 [hep-ph]
74. S. Dulat et al., New parton distribution functions from a global analysis of quantum chromodynamics. *Phys. Rev. D* **93**, 033006 (2016). <https://doi.org/10.1103/PhysRevD.93.033006>. arXiv:1506.07443 [hep-ph]
75. ATLAS Collaboration, Measurements of inclusive and differential fiducial cross-sections of $t\bar{t}$ production with additional heavy-flavour jets in proton–proton collisions at $\sqrt{s} = 13$ TeV with the ATLAS detector. *JHEP* **04**, 046 (2019). [https://doi.org/10.1007/JHEP04\(2019\)046](https://doi.org/10.1007/JHEP04(2019)046). arXiv:1811.12113 [hep-ex]
76. J. Butterworth et al., PDF4LHC recommendations for LHC Run II. *J. Phys. G* **43**, 023001 (2016). <https://doi.org/10.1088/0954-3899/43/2/023001>. arXiv:1510.03865 [hep-ph]
77. L.A. Harland-Lang, A.D. Martin, P. Motylinski, R.S. Thorne, Parton distributions in the LHC era: MMHT2014 PDFs. *Eur. Phys. J. C* **75**, 204 (2015). <https://doi.org/10.1140/epjc/s10052-015-3397-6>. arXiv:1412.3989 [hep-ph]
78. ATLAS Collaboration, Electron and photon energy calibration with the ATLAS detector using 2015–2016 LHC proton–proton collision data. *JINST* **14**, P03017 (2019). <https://doi.org/10.1088/1748-0221/14/03/P03017>. arXiv:1812.03848 [hep-ex]
79. ATLAS Collaboration, Jet energy resolution in proton–proton collisions at $\sqrt{s} = 7$ TeV recorded in 2010 with the ATLAS detector. *Eur. Phys. J. C* **73**, 2306 (2013). <https://doi.org/10.1140/epjc/s10052-013-2306-0>. arXiv:1210.6210 [hep-ex]
80. ATLAS Collaboration, Measurement of b-tagging efficiency of c-jets in $t\bar{t}$ events using a likelihood approach with the ATLAS detector, ATLAS-CONF-2018-001 (2018). <https://cds.cern.ch/record/2306649>
81. ATLAS Collaboration, Calibration of light-flavour b-jet mistagging rates using ATLAS proton–proton collision data at $\sqrt{s} = 13$ TeV, ATLAS-CONF-2018-006 (2018). <https://cds.cern.ch/record/2314418>
82. C.D. White, S. Frixione, E. Laenen, F. Maltoni, Isolating Wt production at the LHC. *JHEP* **11**, 074 (2009). <https://doi.org/10.1088/1126-6708/2009/11/074>. arXiv:0908.0631 [hep-ph]
83. ATLAS Collaboration, Probing the quantum interference between singly and doubly resonant top-quark production in pp collisions at $\sqrt{s} = 13$ TeV with the ATLAS detector. *Phys. Rev. Lett.* **121**, 152002 (2018). <https://doi.org/10.1103/PhysRevLett.121.152002>. arXiv:1806.04667 [hep-ex]
84. M. Bahr et al., Herwig ++ physics and manual. *Eur. Phys. J. C* **58**, 639 (2008). <https://doi.org/10.1140/epjc/s10052-008-0798-9>. arXiv:0803.0883 [hep-ph]
85. J.M. Campbell, R.K. Ellis, MCFM for the Tevatron and the LHC. *Nucl. Phys. Proc. Suppl.* **205–206**, 10 (2010). <https://doi.org/10.1016/j.nuclphysbps.2010.08.011>. arXiv:1007.3492 [hep-ph]
86. ATLAS Collaboration, Luminosity determination in pp collisions at $\sqrt{s} = 13$ TeV using the ATLAS detector at the LHC, ATLAS-CONF-2019-021 (2019). <https://cds.cern.ch/record/2677054>
87. G. Avoni et al., The new LUCID-2 detector for luminosity measurement and monitoring in ATLAS. *JINST* **13**, P07017 (2018). <https://doi.org/10.1088/1748-0221/13/07/P07017>
88. E. Todesco, J. Wenninger, Large Hadron Collider momentum calibration and accuracy. *Phys. Rev. Accel. Beams* **20**, 081003 (2017). <https://doi.org/10.1103/PhysRevAccelBeams.20.081003>
89. A. Buckley et al., LHAPDF6: parton density access in the LHC precision era. *Eur. Phys. J. C* **75**, 132 (2015). <https://doi.org/10.1140/epjc/s10052-015-3318-8>. arXiv:1412.7420 [hep-ph]
90. L. Lyons, D. Gibaut, P. Clifford, How to combine correlated estimates of a single physical quantity. *Nucl. Instrum. Methods A* **270**, 110 (1988). [https://doi.org/10.1016/0168-9002\(88\)90018-6](https://doi.org/10.1016/0168-9002(88)90018-6)
91. A. Valassi, Combining correlated measurements of several different physical quantities. *Nucl. Instrum. Methods A* **500**, 391 (2003). [https://doi.org/10.1016/S0168-9002\(03\)00329-2](https://doi.org/10.1016/S0168-9002(03)00329-2)
92. ATLAS Collaboration, Measurements of top-quark pair differential cross-sections in the lepton + jets channel in pp collisions at $\sqrt{s} = 13$ TeV using the ATLAS detector. *JHEP* **11**, 191 (2017). [https://doi.org/10.1007/JHEP11\(2017\)191](https://doi.org/10.1007/JHEP11(2017)191). arXiv:1708.00727 [hep-ex]
93. R.D. Ball et al., Parton distributions from high-precision collider data. *Eur. Phys. J. C* **77**, 663 (2017). <https://doi.org/10.1140/epjc/s10052-017-5199-5>. arXiv:1706.00428 [hep-ph]
94. D0 Collaboration, Determination of the pole and MS masses of the top quark from the $t\bar{t}$ cross section. *Phys. Lett. B* **703**, 422 (2011). <https://doi.org/10.1016/j.physletb.2011.08.015>. arXiv:1104.2887 [hep-ex]
95. T. Kljinsma, S. Bethke, G. Dissertori, G.P. Salam, Determination of the strong coupling constant $\alpha_s(m_Z)$ from measurements of the total cross section for top-antitop quark production. *Eur. Phys. J. C* **77**, 778 (2017). <https://doi.org/10.1140/epjc/s10052-017-5340-5>. arXiv:1708.07495 [hep-ph]
96. CMS Collaboration, Measurement of $t\bar{t}$ normalised multi-differential cross sections in pp collisions at $\sqrt{s} = 13$ TeV, and simultaneous determination of the strong coupling strength, top quark pole mass, and parton distribution functions (2019). arXiv:1904.05237 [hep-ex]
97. ATLAS Collaboration, Determination of the top-quark pole mass using $t\bar{t} + 1$ -jet events collected with the ATLAS experiment in 7 TeV pp collisions. *JHEP* **10**, 121 (2015). [https://doi.org/10.1007/JHEP10\(2015\)121](https://doi.org/10.1007/JHEP10(2015)121). arXiv:1507.01769 [hep-ex]
98. ATLAS Collaboration, Measurement of the top-quark mass in $t\bar{t} + 1$ -jet events collected with the ATLAS detector in pp collisions at $\sqrt{s} = 8$ TeV (2019). arXiv:1905.02302 [hep-ex]
99. M. Tanabashi et al., (Particle Data Group), Review of Particle Physics. *Phys. Rev. D* **98**, 030001 (2018). <https://doi.org/10.1103/PhysRevD.98.030001> (and 2019 update)
100. ATLAS Collaboration, Improved luminosity determination in pp collisions at $\sqrt{s} = 7$ TeV using the ATLAS detector at the LHC. *Eur. Phys. J. C* **73**, 2518 (2013). <https://doi.org/10.1140/epjc/s10052-013-2518-3>. arXiv:1302.4393 [hep-ex]
101. ATLAS Collaboration, Luminosity determination in pp collisions at $\sqrt{s} = 8$ TeV using the ATLAS detector at the LHC. *Eur. Phys. J. C* **76**, 653 (2016). <https://doi.org/10.1140/epjc/s10052-016-4466-1>. arXiv:1608.03953 [hep-ex]
102. S. Alekhin, J. Blumlein, S. Moch, The ABM parton distributions tuned to LHC data. *Phys. Rev. D* **89**, 054028 (2014). <https://doi.org/10.1103/PhysRevD.89.054028>. arXiv:1310.3059 [hep-ph]
103. S. Alekhin, J. Blumlein, S. Moch, R. Placakyte, Parton distribution functions, α_s , and heavy-quark masses for LHC Run II. *Phys. Rev. D* **96**, 014011 (2017). <https://doi.org/10.1103/PhysRevD.96.014011>. arXiv:1701.05838 [hep-ph]

104. ATLAS Collaboration, Determination of the strange-quark density of the proton from ATLAS measurements of the $W \rightarrow \ell\nu$ and $Z \rightarrow \ell\ell$ cross sections. *Phys. Rev. Lett.* **109**, 012001. (2012). <https://doi.org/10.1103/PhysRevLett.109.012001>. arXiv:1203.4051 [hep-ex]
105. H1 and ZEUS Collaborations, Combination of measurements of inclusive deep inelastic $e^\pm p$ scattering cross sections and QCD analysis of HERA data. *Eur. Phys. J. C* **75**, 580 (2015). <https://doi.org/10.1140/epjc/s10052-015-3710-4>. arXiv:1506.06042 [hep-ex]
106. ATLAS Collaboration, Measurements of top-quark pair differential cross-sections in the lepton + jets channel in pp collisions at $\sqrt{s} = 8$ TeV using the ATLAS detector. *Eur. Phys. J. C* **76**, 538 (2016). <https://doi.org/10.1140/epjc/s10052-016-4366-4>. arXiv:1511.04716 [hep-ex]
107. M. Czakon, D. Heymes, A. Mitov, High-precision differential predictions for top-quark pairs at the LHC. *Phys. Rev. Lett.* **116**, 082003 (2016). <https://doi.org/10.1103/PhysRevLett.116.082003>. arXiv:1511.00549 [hep-ph]
108. CMS Collaboration, Measurements of $t\bar{t}$ differential cross sections in proton–proton collisions at $\sqrt{s} = 13$ TeV using events containing two leptons. *JHEP* **02**, 149 (2019). [https://doi.org/10.1007/JHEP02\(2019\)149](https://doi.org/10.1007/JHEP02(2019)149). arXiv:1811.06625 [hep-ex]
109. ATLAS Collaboration, Measurements of top-quark pair spin correlations in the $e\mu$ channel at $\sqrt{s} = 13$ TeV using pp collisions in the ATLAS detector (2019). arXiv:1903.07570 [hep-ex]
110. ATLAS Collaboration, ATLAS Computing Acknowledgements, ATL-GEN-PUB-2016-002. <https://cds.cern.ch/record/2202407>

ATLAS Collaboration

G. Aad¹⁰², B. Abbott¹²⁹, D. C. Abbott¹⁰³, A. Abed Abud^{71a,71b}, K. Abeling⁵³, D. K. Abhayasinghe⁹⁴, S. H. Abidi¹⁶⁷, O. S. AbouZeid⁴⁰, N. L. Abraham¹⁵⁶, H. Abramowicz¹⁶¹, H. Abreu¹⁶⁰, Y. Abulaiti⁶, B. S. Acharya^{67a,67b,n}, B. Achkar⁵³, S. Adachi¹⁶³, L. Adam¹⁰⁰, C. Adam Bourdarios⁵, L. Adamczyk^{84a}, L. Adamek¹⁶⁷, J. Adelman¹²¹, M. Adersberger¹¹⁴, A. Adiguzel^{12c}, S. Adorni⁵⁴, T. Adye¹⁴⁴, A. A. Affolder¹⁴⁶, Y. Afik¹⁶⁰, C. Agapopoulou⁶⁵, M. N. Agaras³⁸, A. Aggarwal¹¹⁹, C. Agheorghiesei^{27c}, J. A. Aguilar-Saavedra^{140a,140f,ag}, F. Ahmadov⁸⁰, W. S. Ahmed¹⁰⁴, X. Ai¹⁸, G. Aielli^{74a,74b}, S. Akatsuka⁸⁶, T. P. A. Åkesson⁹⁷, E. Akilli⁵⁴, A. V. Akimov¹¹¹, K. Al Khoury⁶⁵, G. L. Alberghi^{23a,23b}, J. Albert¹⁷⁶, M. J. Alconada Verzini¹⁶¹, S. Alderweireldt³⁶, M. Aleksa³⁶, I. N. Aleksandrov⁸⁰, C. Alexa^{27b}, T. Alexopoulos¹⁰, A. Alfonsi¹²⁰, F. Alfonsi^{23a,23b}, M. Alhroob¹²⁹, B. Ali¹⁴², M. Aliev¹⁶⁶, G. Alimonti^{69a}, S. P. Alkire¹⁴⁸, C. Allaire⁶⁵, B. M. M. Allbrooke¹⁵⁶, B. W. Allen¹³², P. P. Allport²¹, A. Aloisio^{70a,70b}, A. Alonso⁴⁰, F. Alonso⁸⁹, C. Alpigiani¹⁴⁸, A. A. Alshehri⁵⁷, M. Alvarez Estevez⁹⁹, D. Álvarez Piqueras¹⁷⁴, M. G. Alviggi^{70a,70b}, Y. Amaral Coutinho^{81b}, A. Ambler¹⁰⁴, L. Ambroz¹³⁵, C. Amelung²⁶, D. Amidei¹⁰⁶, S. P. Amor Dos Santos^{140a}, S. Amoroso⁴⁶, C. S. Amrouche⁵⁴, F. An⁷⁹, C. Anastopoulos¹⁴⁹, N. Andari¹⁴⁵, T. Andeen¹¹, C. F. Anders^{61b}, J. K. Anders²⁰, A. Andreazza^{69a,69b}, V. Andrei^{61a}, C. R. Anelli¹⁷⁶, S. Angelidakis³⁸, A. Angerami³⁹, A. V. Anisenkov^{122a,122b}, A. Annovi^{72a}, C. Antel⁵⁴, M. T. Anthony¹⁴⁹, E. Antipov¹³⁰, M. Antonelli⁵¹, D. J. A. Antrim¹⁷¹, F. Anulli^{73a}, M. Aoki⁸², J. A. Aparisi Pozo¹⁷⁴, L. Aperio Bella^{15a}, J. P. Araque^{140a}, V. Araujo Ferraz^{81b}, R. Araujo Pereira^{81b}, C. Arcangeletti⁵¹, A. T. H. Arce⁴⁹, F. A. Arduh⁸⁹, J-F. Arguin¹¹⁰, S. Argyropoulos⁷⁸, J.-H. Arling⁴⁶, A. J. Armbruster³⁶, A. Armstrong¹⁷¹, O. Arnaez¹⁶⁷, H. Arnold¹²⁰, Z. P. Arrubarrena Tame¹¹⁴, G. Artoni¹³⁵, S. Artz¹⁰⁰, S. Asai¹⁶³, N. Asbah⁵⁹, E. M. Asimakopoulou¹⁷², L. Asquith¹⁵⁶, J. Assahsah^{35d}, K. Assamagan²⁹, R. Astalos^{28a}, R. J. Atkin^{33a}, M. Atkinson¹⁷³, N. B. Atlay¹⁹, H. Atmani⁶⁵, K. Augsten¹⁴², G. Avolio³⁶, R. Avramidou^{60a}, M. K. Ayoub^{15a}, A. M. Azoulay^{168b}, G. Azuelos^{110,as}, H. Bachacou¹⁴⁵, K. Bachas^{68a,68b}, M. Backes¹³⁵, F. Backman^{45a,45b}, P. Bagnaia^{73a,73b}, M. Bahmani⁸⁵, H. Bahrasemani¹⁵², A. J. Bailey¹⁷⁴, V. R. Bailey¹⁷³, J. T. Baines¹⁴⁴, M. Bajic⁴⁰, C. Bakalis¹⁰, O. K. Baker¹⁸³, P. J. Bakker¹²⁰, D. Bakshi Gupta⁸, S. Balaji¹⁵⁷, E. M. Baldin^{122a,122b}, P. Balek¹⁸⁰, F. Balli¹⁴⁵, W. K. Balunas¹³⁵, J. Balz¹⁰⁰, E. Banas⁸⁵, A. Bandyopadhyay²⁴, Sw. Banerjee^{181,i}, A. A. E. Bannoura¹⁸², L. Barak¹⁶¹, W. M. Barbe³⁸, E. L. Barberio¹⁰⁵, D. Barberis^{55a,55b}, M. Barbero¹⁰², G. Barbour⁹⁵, T. Barillari¹¹⁵, M-S. Barisits³⁶, J. Barkeloo¹³², T. Barklow¹⁵³, R. Barnea¹⁶⁰, S. L. Barnes^{60c}, B. M. Barnett¹⁴⁴, R. M. Barnett¹⁸, Z. Barnovska-Blenessy^{60a}, A. Baroncelli^{60a}, G. Barone²⁹, A. J. Barr¹³⁵, L. Barranco Navarro^{45a,45b}, F. Barreiro⁹⁹, J. Barreiro Guimarães da Costa^{15a}, S. Barsov¹³⁸, R. Bartoldus¹⁵³, G. Bartolini¹⁰², A. E. Barton⁹⁰, P. Bartos^{28a}, A. Basalae⁴⁶, A. Basan¹⁰⁰, A. Bassalat^{65,am}, M. J. Basso¹⁶⁷, R. L. Bates⁵⁷, S. Batlamous^{35e}, J. R. Batley³², B. Batool¹⁵¹, M. Battaglia¹⁴⁶, M. Bauce^{73a,73b}, F. Bauer¹⁴⁵, K. T. Bauer¹⁷¹, H. S. Bawa^{31,1}, J. B. Beacham⁴⁹, T. Beau¹³⁶, P. H. Beauchemin¹⁷⁰, F. Becherer⁵², P. Bechtel²⁴, H. C. Beck⁵³, H. P. Beck^{20,r}, K. Becker⁵², M. Becker¹⁰⁰, C. Becot⁴⁶, A. Beddall^{12d}, A. J. Beddall^{12a}, V. A. Bednyakov⁸⁰, M. Bedognetti¹²⁰, C. P. Bee¹⁵⁵, T. A. Beermann¹⁸², M. Begalli^{81b}, M. Begel²⁹, A. Behara¹⁵⁵, J. K. Behr⁴⁶, F. Beisiegel²⁴, A. S. Bell⁹⁵, G. Bella¹⁶¹, L. Bellagamba^{23b}, A. Bellerive³⁴, P. Bellos⁹, K. Beloborodov^{122a,122b}, K. Belotskiy¹¹², N. L. Belyaev¹¹², D. Bencheekroun^{35a}, N. Benekos¹⁰, Y. Benhammou¹⁶¹, D. P. Benjamin⁶, M. Benoit⁵⁴, J. R. Bensinger²⁶, S. Bentvelsen¹²⁰, L. Beresford¹³⁵, M. Beretta⁵¹, D. Berge⁴⁶, E. Bergeaas Kuutmann¹⁷², N. Berger⁵, B. Bergmann¹⁴², L. J. Bergsten²⁶, J. Beringer¹⁸, S. Berlendis⁷, G. Bernardi¹³⁶, C. Bernius¹⁵³, F. U. Bernlochner²⁴, T. Berry⁹⁴, P. Berta¹⁰⁰, C. Bertella^{15a}, I. A. Bertram⁹⁰, O. Bessidskaia Bylund¹⁸², N. Besson¹⁴⁵, A. Bethani¹⁰¹,

S. Bethke¹¹⁵, A. Betti⁴², A. J. Bevan⁹³, J. Beyer¹¹⁵, D. S. Bhattacharya¹⁷⁷, P. Bhattacharai²⁶, R. Bi¹³⁹, R. M. Bianchi¹³⁹, O. Biebel¹¹⁴, D. Biedermann¹⁹, R. Bielski³⁶, K. Bierwagen¹⁰⁰, N. V. Biesuz^{72a,72b}, M. Biglietti^{75a}, T. R. V. Billoud¹¹⁰, M. Bindi⁵³, A. Bingul^{12d}, C. Bini^{73a,73b}, S. Biondi^{23a,23b}, M. Birman¹⁸⁰, T. Bisanz⁵³, J. P. Biswal¹⁶¹, D. Biswas^{181.i}, A. Bitadze¹⁰¹, C. Bittrich⁴⁸, K. Björke¹³⁴, K. M. Black²⁵, T. Blazek^{28a}, I. Bloch⁴⁶, C. Blocker²⁶, A. Blue⁵⁷, U. Blumenschein⁹³, G. J. Bobbink¹²⁰, V. S. Bobrovnikov^{122a,122b}, S. S. Bocchetta⁹⁷, A. Bocci⁴⁹, D. Boerner⁴⁶, D. Bogavac¹⁴, A. G. Bogdanchikov^{122a,122b}, C. Bohm^{45a}, V. Boisvert⁹⁴, P. Bokan^{53,172}, T. Bold^{84a}, A. S. Boldyrev¹¹³, A. E. Bolz^{61b}, M. Bomben¹³⁶, M. Bona⁹³, J. S. Bonilla¹³², M. Boonekamp¹⁴⁵, C. D. Booth⁹⁴, H. M. Borecka-Bielska⁹¹, A. Borisov¹²³, G. Borissov⁹⁰, J. Bortfeldt³⁶, D. Bortoletto¹³⁵, D. Boscherini^{23b}, M. Bosman¹⁴, J. D. Bossio Sola¹⁰⁴, K. Bouaouda^{35a}, J. Boudreau¹³⁹, E. V. Bouhova-Thacker⁹⁰, D. Boumediene³⁸, S. K. Boutle⁵⁷, A. Boveia¹²⁷, J. Boyd³⁶, D. Boye^{33c.an}, I. R. Boyko⁸⁰, A. J. Bozson⁹⁴, J. Bracinik²¹, N. Brahimi¹⁰², G. Brandt¹⁸², O. Brandt³², F. Braren⁴⁶, B. Brau¹⁰³, J. E. Brau¹³², W. D. Breaden Madden⁵⁷, K. Brendlinger⁴⁶, L. Brenner⁴⁶, R. Brenner¹⁷², S. Bressler¹⁸⁰, B. Brickwedde¹⁰⁰, D. L. Briglin²¹, D. Britton⁵⁷, D. Britzger¹¹⁵, I. Brock²⁴, R. Brock¹⁰⁷, G. Brooijmans³⁹, W. K. Brooks^{147c}, E. Brost¹²¹, J. H. Broughton²¹, P. A. Bruckman de Renstrom⁸⁵, D. Bruncko^{28b}, A. Bruni^{23b}, G. Bruni^{23b}, L. S. Bruni¹²⁰, S. Bruno^{74a,74b}, M. Bruschi^{23b}, N. Bruscino^{73a,73b}, P. Bryant³⁷, L. Bryngemark⁹⁷, T. Buanes¹⁷, Q. Buat³⁶, P. Buchholz¹⁵¹, A. G. Buckley⁵⁷, I. A. Budagov⁸⁰, M. K. Bugge¹³⁴, F. Bühner⁵², O. Bulekov¹¹², T. J. Burch¹²¹, S. Burdin⁹¹, C. D. Burgard¹²⁰, A. M. Burger¹³⁰, B. Burghgrave⁸, J. T. P. Burr⁴⁶, C. D. Burton¹¹, J. C. Burzynski¹⁰³, V. Büscher¹⁰⁰, E. Buschmann⁵³, P. J. Bussey⁵⁷, J. M. Butler²⁵, C. M. Buttar⁵⁷, J. M. Butterworth⁹⁵, P. Butti³⁶, W. Buttinger³⁶, C. J. Buxo Vazquez¹⁰⁷, A. Buzatu¹⁵⁸, A. R. Buzykaev^{122a,122b}, G. Cabras^{23a,23b}, S. Cabrera Urbán¹⁷⁴, D. Caforio⁵⁶, H. Cai¹⁷³, V. M. M. Cairo¹⁵³, O. Cakir^{4a}, N. Calace³⁶, P. Calafiura¹⁸, A. Calandri¹⁰², G. Calderini¹³⁶, P. Calfayan⁶⁶, G. Callea⁵⁷, L. P. Caloba^{81b}, A. Caltabiano^{74a,74b}, S. Calvente Lopez⁹⁹, D. Calvet³⁸, S. Calvet³⁸, T. P. Calvet¹⁵⁵, M. Calvetti^{72a,72b}, R. Camacho Toro¹³⁶, S. Camarda³⁶, D. Camarero Munoz⁹⁹, P. Camarri^{74a,74b}, D. Cameron¹³⁴, R. Caminal Armadans¹⁰³, C. Camincher³⁶, S. Campana³⁶, M. Campanelli⁹⁵, A. Camplani⁴⁰, A. Campoverde¹⁵¹, V. Canale^{70a,70b}, A. Canesse¹⁰⁴, M. Cano Bret^{60c}, J. Cantero¹³⁰, T. Cao¹⁶¹, Y. Cao¹⁷³, M. D. M. Capeans Garrido³⁶, M. Capua^{41a,41b}, R. Cardarelli^{74a}, F. Cardillo¹⁴⁹, G. Carducci^{41a,41b}, I. Carli¹⁴³, T. Carli³⁶, G. Carlino^{70a}, B. T. Carlson¹³⁹, L. Carminati^{69a,69b}, R. M. D. Carney^{45a,45b}, S. Caron¹¹⁹, E. Carquin^{147c}, S. Carrá⁴⁶, J. W. S. Carter¹⁶⁷, M. P. Casado^{14.e}, A. F. Casha¹⁶⁷, D. W. Casper¹⁷¹, R. Castelijin¹²⁰, F. L. Castillo¹⁷⁴, V. Castillo Gimenez¹⁷⁴, N. F. Castro^{140a,140e}, A. Catinaccio³⁶, J. R. Catmore¹³⁴, A. Cattai³⁶, V. Cavaliere²⁹, E. Cavallaro¹⁴, M. Cavalli-Sforza¹⁴, V. Cavasinni^{72a,72b}, E. Celebi^{12b}, F. Ceradini^{75a,75b}, L. Cerda Alberich¹⁷⁴, K. Cerny¹³¹, A. S. Cerqueira^{81a}, A. Cerri¹⁵⁶, L. Cerrito^{74a,74b}, F. Cerutti¹⁸, A. Cervelli^{23a,23b}, S. A. Cetin^{12b}, Z. Chadi^{35a}, D. Chakraborty¹²¹, W. S. Chan¹²⁰, W. Y. Chan⁹¹, J. D. Chapman³², B. Chargeishvili^{159b}, D. G. Charlton²¹, T. P. Charman⁹³, C. C. Chau³⁴, S. Che¹²⁷, S. Chekanov⁶, S. V. Chekulaev^{168a}, G. A. Chelkov^{80.ar}, M. A. Chelstowska³⁶, B. Chen⁷⁹, C. Chen^{60a}, C. H. Chen⁷⁹, H. Chen²⁹, J. Chen^{60a}, J. Chen³⁹, S. Chen¹³⁷, S. J. Chen^{15c}, X. Chen^{15b}, Y.-H. Chen⁴⁶, H. C. Cheng^{63a}, H. J. Cheng^{15a}, A. Cheplakov⁸⁰, E. Cheremushkina¹²³, R. Cherkaoui El Moursli^{35e}, E. Cheu⁷, K. Cheung⁶⁴, T. J. A. Chevaléras¹⁴⁵, L. Chevalier¹⁴⁵, V. Chiarella⁵¹, G. Chiarelli^{72a}, G. Chiodini^{68a}, A. S. Chisholm²¹, A. Chitan^{27b}, I. Chiu¹⁶³, Y. H. Chiu¹⁷⁶, M. V. Chizhov⁸⁰, K. Choi⁶⁶, A. R. Chomont^{73a,73b}, S. Chouridou¹⁶², Y. S. Chow¹²⁰, M. C. Chu^{63a}, X. Chu^{15a,15d}, J. Chudoba¹⁴¹, A. J. Chuinard¹⁰⁴, J. J. Chwastowski⁸⁵, L. Chytka¹³¹, D. Cieri¹¹⁵, K. M. Ciesla⁸⁵, D. Cinca⁴⁷, V. Cindro⁹², I. A. Cioară^{27b}, A. Ciocio¹⁸, F. Ciroto^{70a,70b}, Z. H. Citron^{180j}, M. Citterio^{69a}, D. A. Ciubotaru^{27b}, B. M. Ciungu¹⁶⁷, A. Clark⁵⁴, M. R. Clark³⁹, P. J. Clark⁵⁰, C. Clement^{45a,45b}, Y. Coadou¹⁰², M. Cobl^{67a,67c}, A. Coccaro^{55b}, J. Cochran⁷⁹, H. Cohen¹⁶¹, A. E. C. Coimbra³⁶, L. Colasurdo¹¹⁹, B. Cole³⁹, A. P. Colijn¹²⁰, J. Collot⁵⁸, P. Conde Muiño^{140a,140h}, S. H. Connell^{33c}, I. A. Connelly⁵⁷, S. Constantinescu^{27b}, F. Conventi^{70a.at}, A. M. Cooper-Sarkar¹³⁵, F. Cormier¹⁷⁵, K. J. R. Cormier¹⁶⁷, L. D. Corpe⁹⁵, M. Corradi^{73a,73b}, E. E. Corrigan⁹⁷, F. Corriveau^{104.ac}, A. Cortes-Gonzalez³⁶, M. J. Costa¹⁷⁴, F. Costanza⁵, D. Costanzo¹⁴⁹, G. Cowan⁹⁴, J. W. Cowley³², J. Crane¹⁰¹, K. Cranmer¹²⁵, S. J. Crawley⁵⁷, R. A. Creager¹³⁷, S. Crépe-Renaudin⁵⁸, F. Crescioli¹³⁶, M. Cristinziani²⁴, V. Croft¹²⁰, G. Crosetti^{41a,41b}, A. Cueto⁵, T. Cuhadar Donszelmann¹⁴⁹, A. R. Cukierman¹⁵³, W. R. Cunningham⁵⁷, S. Czekerda⁸⁵, P. Czodrowski³⁶, M. J. Da Cunha Sargedas De Sousa^{60b}, J. V. Da Fonseca Pinto^{81b}, C. Da Via¹⁰¹, W. Dabrowski^{84a}, F. Dachs³⁶, T. Dado^{28a}, S. Dahbi^{35e}, T. Dai¹⁰⁶, C. Dallapiccola¹⁰³, M. Dam⁴⁰, G. D'amen²⁹, V. D'Amico^{75a,75b}, J. Damp¹⁰⁰, J. R. Dandoy¹³⁷, M. F. Daneri³⁰, N. P. Dang^{181.i}, N. S. Dann¹⁰¹, M. Danninger¹⁷⁵, V. Dao³⁶, G. Darbo^{55b}, O. Dartsis⁵, A. Dattagupta¹³², T. Daubney⁴⁶, S. D'Auria^{69a,69b}, C. David⁴⁶, T. Davidek¹⁴³, D. R. Davis⁴⁹, I. Dawson¹⁴⁹, K. De⁸, R. De Asmundis^{70a}, M. De Beurs¹²⁰, S. De Castro^{23a,23b}, S. De Cecco^{73a,73b}, N. De Groot¹¹⁹, P. de Jong¹²⁰, H. De la Torre¹⁰⁷, A. De Maria^{15c}, D. De Pedis^{73a}, A. De Salvo^{73a}, U. De Sanctis^{74a,74b}, M. De Santis^{74a,74b}, A. De Santo¹⁵⁶, K. De Vasconcelos Corga¹⁰², J. B. De Vivie De Regie⁶⁵, C. Debenedetti¹⁴⁶, D. V. Dedovich⁸⁰, A. M. Deiana⁴², J. Del Peso⁹⁹, Y. Delabat Diaz⁴⁶, D. Delgove⁶⁵, F. Deliot^{145.q}, C. M. Delitzsch⁷, M. Della Pietra^{70a,70b}, D. Della Volpe⁵⁴, A. Dell'Acqua³⁶, L. Dell'Asta^{74a,74b}, M. Delmastro⁵, C. Delporte⁶⁵, P. A. Delsart⁵⁸, D. A. DeMarco¹⁶⁷,

S. Demers¹⁸³, M. Demichev⁸⁰, G. Demontigny¹¹⁰, S. P. Denisov¹²³, L. D'Eramo¹³⁶, D. Derendarz⁸⁵, J. E. Derkaoui^{35d}, F. Derue¹³⁶, P. Dervan⁹¹, K. Desch²⁴, C. Deterre⁴⁶, K. Dette¹⁶⁷, C. Deutsch²⁴, M. R. Devesa³⁰, P. O. Deviveiros³⁶, A. Dewhurst¹⁴⁴, F. A. Di Bello⁵⁴, A. Di Ciaccio^{74a,74b}, L. Di Ciaccio⁵, W. K. Di Clemente¹³⁷, C. Di Donato^{70a,70b}, A. Di Girolamo³⁶, G. Di Gregorio^{72a,72b}, B. Di Micco^{75a,75b}, R. Di Nardo¹⁰³, K. F. Di Petrillo⁵⁹, R. Di Sipio¹⁶⁷, D. Di Valentino³⁴, C. Diaconu¹⁰², F. A. Dias⁴⁰, T. Dias Do Vale^{140a}, M. A. Diaz^{147a}, J. Dickinson¹⁸, E. B. Diehl¹⁰⁶, J. Dietrich¹⁹, S. Díez Cornell⁴⁶, A. Dimitrievska¹⁸, W. Ding^{15b}, J. Dingfelder²⁴, F. Dittus³⁶, F. Djama¹⁰², T. Djobava^{159b}, J. I. Djuvsland¹⁷, M. A. B. Do Vale^{81c}, M. Dobre^{27b}, D. Dodsworth²⁶, C. Doglioni⁹⁷, J. Dolejsi¹⁴³, Z. Dolezal¹⁴³, M. Donadelli^{81d}, B. Dong^{60c}, J. Donini³⁸, A. D'onofrio^{15c}, M. D'Onofrio⁹¹, J. Dopke¹⁴⁴, A. Doria^{70a}, M. T. Dova⁸⁹, A. T. Doyle⁵⁷, E. Drechsler¹⁵², E. Dreyer¹⁵², T. Dreyer⁵³, A. S. Drobac¹⁷⁰, D. Du^{60b}, Y. Duan^{60b}, F. Dubinin¹¹¹, M. Dubovsky^{28a}, A. Dubreuil⁵⁴, E. Duchovni¹⁸⁰, G. Duckeck¹¹⁴, A. Ducourthial¹³⁶, O. A. Ducu¹¹⁰, D. Duda¹¹⁵, A. Dudarev³⁶, A. C. Dudder¹⁰⁰, E. M. Duffield¹⁸, L. Duflot⁶⁵, M. Dührssen³⁶, C. Dülsen¹⁸², M. Dumancic¹⁸⁰, A. E. Dumitriu^{27b}, A. K. Duncan⁵⁷, M. Dunford^{61a}, A. Duperrin¹⁰², H. Duran Yildiz^{4a}, M. Düren⁵⁶, A. Durglishvili^{159b}, D. Duschinger⁴⁸, B. Dutta⁴⁶, D. Duvnjak¹, G. I. Dyckes¹³⁷, M. Dyndal³⁶, S. Dysch¹⁰¹, B. S. Dzedzic⁸⁵, K. M. Ecker¹¹⁵, R. C. Edgar¹⁰⁶, M. G. Eggleston⁴⁹, T. Eifert³⁶, G. Eigen¹⁷, K. Einsweiler¹⁸, T. Ekelof¹⁷², H. El Jarrari^{35e}, M. El Kacimi^{35c}, R. El Kosseifi¹⁰², V. Ellajosyula¹⁷², M. Ellert¹⁷², F. Ellinghaus¹⁸², A. A. Elliot⁹³, N. Ellis³⁶, J. Elmsheuser²⁹, M. Elsing³⁶, D. Emeliyanov¹⁴⁴, A. Emerman³⁹, Y. Enari¹⁶³, M. B. Epland⁴⁹, J. Erdmann⁴⁷, A. Ereditato²⁰, M. Errenst³⁶, M. Escalier⁶⁵, C. Escobar¹⁷⁴, O. Estrada Pastor¹⁷⁴, E. Etzion¹⁶¹, H. Evans⁶⁶, A. Ezhilov¹³⁸, F. Fabbri⁵⁷, L. Fabbri^{23a,23b}, V. Fabiani¹¹⁹, G. Facini⁹⁵, R. M. Faisca Rodrigues Pereira^{140a}, R. M. Fakhruddinov¹²³, S. Falciano^{73a}, P. J. Falke⁵, S. Falke⁵, J. Faltova¹⁴³, Y. Fang^{15a}, Y. Fang^{15a}, G. Fanourakis⁴⁴, M. Fanti^{69a,69b}, M. Faraj^{67a,67c,t}, A. Farbin⁸, A. Farilla^{75a}, E. M. Farina^{71a,71b}, T. Farooque¹⁰⁷, S. Farrell¹⁸, S. M. Farrington⁵⁰, P. Farthouat³⁶, F. Fassi^{35e}, P. Fassnacht³⁶, D. Fassouliotis⁹, M. Fauci Giannelli⁵⁰, W. J. Fawcett³², L. Fayard⁶⁵, O. L. Fedin^{138,o}, W. Fedorko¹⁷⁵, A. Fehr²⁰, M. Feickert⁴², L. Feligioni¹⁰², A. Fell¹⁴⁹, C. Feng^{60b}, M. Feng⁴⁹, M. J. Fenton⁵⁷, A. B. Fenyuk¹²³, S. W. Ferguson⁴³, J. Ferrando⁴⁶, A. Ferrante¹⁷³, A. Ferrari¹⁷², P. Ferrari¹²⁰, R. Ferrari^{71a}, D. E. Ferreira de Lima^{61b}, A. Ferrer¹⁷⁴, D. Ferrere⁵⁴, C. Ferretti¹⁰⁶, F. Fiedler¹⁰⁰, A. Filipčić⁹², F. Filthaut¹¹⁹, K. D. Finelli²⁵, M. C. N. Fiolhais^{140a,140c,a}, L. Fiorini¹⁷⁴, F. Fischer¹¹⁴, W. C. Fisher¹⁰⁷, I. Fleck¹⁵¹, P. Fleischmann¹⁰⁶, R. R. M. Fletcher¹³⁷, T. Flick¹⁸², B. M. Flierl¹¹⁴, L. Flores¹³⁷, L. R. Flores Castillo^{63a}, F. M. Follega^{76a,76b}, N. Fomin¹⁷, J. H. Foo¹⁶⁷, G. T. Forcolin^{76a,76b}, A. Formica¹⁴⁵, F. A. Förster¹⁴, A. C. Forti¹⁰¹, A. G. Foster²¹, M. G. Foti¹³⁵, D. Fournier⁶⁵, H. Fox⁹⁰, P. Francavilla^{72a,72b}, S. Francescato^{73a,73b}, M. Franchini^{23a,23b}, S. Franchino^{61a}, D. Francis³⁶, L. Franconi²⁰, M. Franklin⁵⁹, A. N. Fray⁹³, P. M. Freeman²¹, B. Freund¹¹⁰, W. S. Freund^{81b}, E. M. Freundlich⁴⁷, D. C. Frizzell¹²⁹, D. Froidevaux³⁶, J. A. Frost¹³⁵, C. Fukunaga¹⁶⁴, E. Fullana Torregrosa¹⁷⁴, E. Fumagalli^{55a,55b}, T. Fusayasu¹¹⁶, J. Fuster¹⁷⁴, A. Gabrielli^{23a,23b}, A. Gabrielli¹⁸, S. Gadatsch⁵⁴, P. Gadow¹¹⁵, G. Gagliardi^{55a,55b}, L. G. Gagnon¹¹⁰, C. Galea^{27b}, B. Galhardo^{140a}, G. E. Gallardo¹³⁵, E. J. Gallas¹³⁵, B. J. Gallop¹⁴⁴, G. Galster⁴⁰, R. Gamboa Goni⁹³, K. K. Gan¹²⁷, S. Ganguly¹⁸⁰, J. Gao^{60a}, Y. Gao⁵⁰, Y. S. Gao^{31,l}, C. García¹⁷⁴, J. E. García Navarro¹⁷⁴, J. A. García Pascual^{15a}, C. Garcia-Argos⁵², M. Garcia-Sciveres¹⁸, R. W. Gardner³⁷, N. Garelli¹⁵³, S. Gargiulo⁵², C. A. Garner¹⁶⁷, V. Garonne¹³⁴, S. J. Gasiorowski¹⁴⁸, P. Gaspar^{81b}, A. Gaudiello^{55a,55b}, G. Gaudio^{71a}, I. L. Gavrilenko¹¹¹, A. Gavrilyuk¹²⁴, C. Gay¹⁷⁵, G. Gaycken⁴⁶, E. N. Gazis¹⁰, A. A. Geanta^{27b}, C. M. Gee¹⁴⁶, C. N. P. Gee¹⁴⁴, J. Geisen⁵³, M. Geisen¹⁰⁰, C. Gemme^{55b}, M. H. Genest⁵⁸, C. Geng¹⁰⁶, S. Gentile^{73a,73b}, S. George⁹⁴, T. Gerialis⁴⁴, L. O. Gerlach⁵³, P. Gessinger-Befurt¹⁰⁰, G. Gessner⁴⁷, S. Ghasemi¹⁵¹, M. Ghasemi Bostanabad¹⁷⁶, M. Ghneimat¹⁵¹, A. Ghosh⁶⁵, A. Ghosh⁷⁸, B. Giacobbe^{23b}, S. Giagu^{73a,73b}, N. Giangiacomi^{23a,23b}, P. Giannetti^{72a}, A. Giannini^{70a,70b}, G. Giannini¹⁴, S. M. Gibson⁹⁴, M. Gignac¹⁴⁶, D. Gillberg³⁴, G. Gilles¹⁸², D. M. Gingrich^{3,as}, M. P. Giordani^{67a,67c}, F. M. Giorgi^{23b}, P. F. Giraud¹⁴⁵, G. Giugliarelli^{67a,67c}, D. Giugni^{69a}, F. Giuli^{74a,74b}, S. Gkaitatzis¹⁶², I. Gkialas^{9,g}, E. L. Gkougkousis¹⁴, P. Gkoutoumis¹⁰, L. K. Gladilin¹¹³, C. Glasman⁹⁹, J. Glatzer¹⁴, P. C. F. Glaysheer⁴⁶, A. Glazov⁴⁶, G. R. Gledhill¹³², M. Goblirsch-Kolb²⁶, D. Godin¹¹⁰, S. Goldfarb¹⁰⁵, T. Golling⁵⁴, D. Golubkov¹²³, A. Gomes^{140a,140b}, R. Goncalves Gama⁵³, R. Gonçalo^{140a}, G. Gonella⁵², L. Gonella²¹, A. Gongadze⁸⁰, F. Gonnella²¹, J. L. Gonski³⁹, S. González de la Hoz¹⁷⁴, S. Gonzalez-Sevilla⁵⁴, G. R. Gonzalvo Rodriguez¹⁷⁴, L. Goossens³⁶, N. A. Gorasia²¹, P. A. Gorbounov¹²⁴, H. A. Gordon²⁹, B. Gorini³⁶, E. Gorini^{68a,68b}, A. Gorišek⁹², A. T. Goshaw⁴⁹, M. I. Gostkin⁸⁰, C. A. Gottardo¹¹⁹, M. Gouighri^{35b}, D. Goujdami^{35c}, A. G. Goussiou¹⁴⁸, N. Govender^{33c}, C. Goy⁵, E. Gozani¹⁶⁰, I. Grabowska-Bold^{84a}, E. C. Graham⁹¹, J. Gramling¹⁷¹, E. Gramstad¹³⁴, S. Grancagnolo¹⁹, M. Grandi¹⁵⁶, V. Gratchev¹³⁸, P. M. Gravila^{27f}, F. G. Gravili^{68a,68b}, C. Gray⁵⁷, H. M. Gray¹⁸, C. Greife²⁴, K. Gregersen⁹⁷, I. M. Gregor⁴⁶, P. Grenier¹⁵³, K. Grevtsov⁴⁶, C. Grieco¹⁴, N. A. Grieser¹²⁹, A. A. Grillo¹⁴⁶, K. Grimm^{31,k}, S. Grinstein^{14,z}, J.-F. Grivaz⁶⁵, S. Groh¹⁰⁰, E. Gross¹⁸⁰, J. Grosse-Knetter⁵³, Z. J. Grout⁹⁵, C. Grud¹⁰⁶, A. Grummer¹¹⁸, L. Guan¹⁰⁶, W. Guan¹⁸¹, C. Gubbels¹⁷⁵, J. Guenther³⁶, A. Guerguichon⁶⁵, J. G. R. Guerrero Rojas¹⁷⁴, F. Guescini¹¹⁵, D. Guest¹⁷¹, R. Gugel⁵², T. Guillemain⁵, S. Guindon³⁶, U. Gul⁵⁷, J. Guo^{60c}, W. Guo¹⁰⁶, Y. Guo^{60a,s}, Z. Guo¹⁰², R. Gupta⁴⁶, S. Gurbuz^{12c}, G. Gustavino¹²⁹, M. Guth⁵², P. Gutierrez¹²⁹, C. Gutschow⁹⁵, C. Guyot¹⁴⁵, C. Gwenlan¹³⁵, C. B. Gwilliam⁹¹, A. Haas¹²⁵,

C. Haber¹⁸, H. K. Hadavand⁸, N. Haddad^{35e}, A. Hader^{60a}, S. Hageböck³⁶, M. Haleem¹⁷⁷, J. Haley¹³⁰, G. Halladjian¹⁰⁷, G. D. Hallewell¹⁰², K. Hamacher¹⁸², P. Hamal¹³¹, K. Hamano¹⁷⁶, H. Hamdaoui^{35e}, M. Hamer²⁴, G. N. Hamity⁵⁰, K. Han^{60a,y}, L. Han^{60a}, S. Han^{15a}, Y. F. Han¹⁶⁷, K. Hanagaki^{82,w}, M. Hance¹⁴⁶, D. M. Handl¹¹⁴, B. Haney¹³⁷, R. Hankache¹³⁶, E. Hansen⁹⁷, J. B. Hansen⁴⁰, J. D. Hansen⁴⁰, M. C. Hansen²⁴, P. H. Hansen⁴⁰, E. C. Hanson¹⁰¹, K. Hara¹⁶⁹, T. Harenberg¹⁸², S. Harkusha¹⁰⁸, P. F. Harrison¹⁷⁸, N. M. Hartmann¹¹⁴, Y. Hasegawa¹⁵⁰, A. Hasib⁵⁰, S. Hassani¹⁴⁵, S. Haug²⁰, R. Hauser¹⁰⁷, L. B. Havener³⁹, M. Havranek¹⁴², C. M. Hawkes²¹, R. J. Hawkins³⁶, D. Hayden¹⁰⁷, C. Hayes¹⁰⁶, R. L. Hayes¹⁷⁵, C. P. Hays¹³⁵, J. M. Hays⁹³, H. S. Hayward⁹¹, S. J. Haywood¹⁴⁴, F. He^{60a}, M. P. Heath⁵⁰, V. Hedberg⁹⁷, L. Heelan⁸, S. Heer²⁴, K. K. Heidegger⁵², W. D. Heidorn⁷⁹, J. Heilman³⁴, S. Heim⁴⁶, T. Heim¹⁸, B. Heinemann^{46,ao}, J. J. Heinrich¹³², L. Heinrich³⁶, J. Hejbal¹⁴¹, L. Helary^{61b}, A. Held¹⁷⁵, S. Hellesund¹³⁴, C. M. Helling¹⁴⁶, S. Hellman^{45a,45b}, C. Helsens³⁶, R. C. W. Henderson⁹⁰, Y. Heng¹⁸¹, L. Henkelmann^{61a}, S. Henkelmann¹⁷⁵, A. M. Henriques Correia³⁶, G. H. Herbert¹⁹, H. Herde²⁶, V. Herget¹⁷⁷, Y. Hernández Jiménez^{33e}, H. Herr¹⁰⁰, M. G. Herrmann¹¹⁴, T. Herrmann⁴⁸, G. Herten⁵², R. Hertenberger¹¹⁴, L. Hervas³⁶, T. C. Herwig¹³⁷, G. G. Hesketh⁹⁵, N. P. Hessey^{168a}, A. Higashida¹⁶³, S. Higashino⁸², E. Higón-Rodríguez¹⁷⁴, K. Hildebrand³⁷, E. Hill¹⁷⁶, J. C. Hill³², K. K. Hill²⁹, K. H. Hiller⁴⁶, S. J. Hillier²¹, M. Hils⁴⁸, I. Hinchliffe¹⁸, F. Hinterkeuser²⁴, M. Hirose¹³³, S. Hirose⁵², D. Hirschbuehl¹⁸², B. Hiti⁹², O. Hladik¹⁴¹, D. R. Hlaluku^{33e}, X. Hoad⁵⁰, J. Hobbs¹⁵⁵, N. Hod¹⁸⁰, M. C. Hodgkinson¹⁴⁹, A. Hoecker³⁶, D. Hohn⁵², D. Hohov⁶⁵, T. Holm²⁴, T. R. Holmes³⁷, M. Holzbock¹¹⁴, L. B. A. H. Hommels³², S. Honda¹⁶⁹, T. M. Hong¹³⁹, J. C. Honig⁵², A. Hönle¹¹⁵, B. H. Hooberman¹⁷³, W. H. Hopkins⁶, Y. Horii¹¹⁷, P. Horn⁴⁸, L. A. Horyn³⁷, S. Hou¹⁵⁸, A. Hoummada^{35a}, J. Howarth¹⁰¹, J. Hoya⁸⁹, M. Hrabovsky¹³¹, J. Hrdinka⁷⁷, I. Hristova¹⁹, J. Hrivnac⁶⁵, A. Hrynevich¹⁰⁹, T. Hryn'ova⁵, P. J. Hsu⁶⁴, S.-C. Hsu¹⁴⁸, Q. Hu²⁹, S. Hu^{60c}, Y. F. Hu^{15a,15d}, D. P. Huang⁹⁵, Y. Huang^{60a}, Y. Huang^{15a}, Z. Hubacek¹⁴², F. Hubaut¹⁰², M. Huebner²⁴, F. Huegging²⁴, T. B. Huffman¹³⁵, M. Huhtinen³⁶, R. F. H. Hunter³⁴, P. Huo¹⁵⁵, A. M. Hupe³⁴, N. Huseynov^{80,af}, J. Huston¹⁰⁷, J. Huth⁵⁹, R. Hyneman¹⁰⁶, S. Hyrych^{28a}, G. Iacobucci⁵⁴, G. Iakovidis²⁹, I. Ibragimov¹⁵¹, L. Iconomidou-Fayard⁶⁵, Z. Idrissi^{35e}, P. Iengo³⁶, R. Ignazzi⁴⁰, O. Igonkina^{120,ab,*}, R. Iguchi¹⁶³, T. Iizawa⁵⁴, Y. Ikegami⁸², M. Ikeno⁸², D. Iliadis¹⁶², N. Ilic^{119,167,ae}, F. Iltzsche⁴⁸, G. Introzzi^{71a,71b}, M. Iodice^{75a}, K. Iordanidou^{168a}, V. Ippolito^{73a,73b}, M. F. Isacson¹⁷², M. Ishino¹⁶³, W. Islam¹³⁰, C. Issever^{19,46}, S. Istin¹⁶⁰, F. Ito¹⁶⁹, J. M. Iturbe Ponce^{63a}, R. Iuppa^{76a,76b}, A. Ivina¹⁸⁰, H. Iwasaki⁸², J. M. Izen⁴³, V. Izzo^{70a}, P. Jacka¹⁴¹, P. Jackson¹, R. M. Jacobs²⁴, B. P. Jaeger¹⁵², V. Jain², G. Jäkel¹⁸², K. B. Jakobi¹⁰⁰, K. Jakobs⁵², T. Jakoubek¹⁴¹, J. Jamieson⁵⁷, K. W. Janas^{84a}, R. Jansky⁵⁴, J. Janssen²⁴, M. Janus⁵³, P. A. Janus^{84a}, G. Jarlskog⁹⁷, N. Javadov^{80,af}, T. Javůrek³⁶, M. Javurkova¹⁰³, F. Jeanneau¹⁴⁵, L. Jeanty¹³², J. Jejelava^{159a}, A. Jelinskas¹⁷⁸, P. Jenni^{52,b}, J. Jeong⁴⁶, N. Jeong⁴⁶, S. Jézéquel⁵, H. Ji¹⁸¹, J. Jia¹⁵⁵, H. Jiang⁷⁹, Y. Jiang^{60a}, Z. Jiang^{153,p}, S. Jiggins⁵², F. A. Jimenez Morales³⁸, J. Jimenez Pena¹¹⁵, S. Jin^{15c}, A. Jinaru^{27b}, O. Jinnouchi¹⁶⁵, H. Jivan^{33e}, P. Johansson¹⁴⁹, K. A. Johns⁷, C. A. Johnson⁶⁶, K. Jon-And^{45a,45b}, R. W. L. Jones⁹⁰, S. D. Jones¹⁵⁶, S. Jones⁷, T. J. Jones⁹¹, J. Jongmanns^{61a}, P. M. Jorge^{140a}, J. Jovicevic³⁶, X. Ju¹⁸, J. J. Junggeburth¹¹⁵, A. Juste Rozas^{14,z}, A. Kaczmarska⁸⁵, M. Kado^{73a,73b}, H. Kagan¹²⁷, M. Kagan¹⁵³, A. Kahn³⁹, C. Kahra¹⁰⁰, T. Kajji¹⁷⁹, E. Kajomovitz¹⁶⁰, C. W. Kalderon⁹⁷, A. Kaluza¹⁰⁰, A. Kamenshchikov¹²³, M. Kaneda¹⁶³, N. J. Kang¹⁴⁶, L. Kanjir⁹², Y. Kano¹¹⁷, V. A. Kantserov¹¹², J. Kanzaki⁸², L. S. Kaplan¹⁸¹, D. Kar^{33e}, K. Karava¹³⁵, M. J. Kareem^{168b}, S. N. Karpov⁸⁰, Z. M. Karpova⁸⁰, V. Kartvelishvili⁹⁰, A. N. Karyukhin¹²³, L. Kashif¹⁸¹, R. D. Kass¹²⁷, A. Kastanas^{45a,45b}, C. Kato^{60c,60d}, J. Katzy⁴⁶, K. Kawade¹⁵⁰, K. Kawagoe⁸⁸, T. Kawaguchi¹¹⁷, T. Kawamoto¹⁶³, G. Kawamura⁵³, E. F. Kay¹⁷⁶, V. F. Kazanin^{122a,122b}, R. Keeler¹⁷⁶, R. Kehoe⁴², J. S. Keller³⁴, E. Kellermann⁹⁷, D. Kelsey¹⁵⁶, J. J. Kempster²¹, J. Kendrick²¹, K. E. Kennedy³⁹, O. Kepka¹⁴¹, S. Kersten¹⁸², B. P. Kerševan⁹², S. Ketabchi Haghighat¹⁶⁷, M. Khader¹⁷³, F. Khalil-Zada¹³, M. Khandoga¹⁴⁵, A. Khanov¹³⁰, A. G. Kharlamov^{122a,122b}, T. Kharlamova^{122a,122b}, E. E. Khoda¹⁷⁵, A. Khodinov¹⁶⁶, T. J. Khoo⁵⁴, E. Khramov⁸⁰, J. Khubua^{159b}, S. Kido⁸³, M. Kiehn⁵⁴, C. R. Kilby⁹⁴, Y. K. Kim³⁷, N. Kimura⁹⁵, O. M. Kind¹⁹, B. T. King^{91,*}, D. Kirchmeier⁴⁸, J. Kirk¹⁴⁴, A. E. Kiryunin¹¹⁵, T. Kishimoto¹⁶³, D. P. Kisiuk¹⁶⁷, V. Kitali⁴⁶, O. Kivernyk⁵, T. Klapdor-Kleingrothaus⁵², M. Klassen^{61a}, M. H. Klein¹⁰⁶, M. Klein⁹¹, U. Klein⁹¹, K. Kleinknecht¹⁰⁰, P. Klimek¹²¹, A. Klimentov²⁹, T. Klingl²⁴, T. Klioutchnikova³⁶, F. F. Klitzner¹¹⁴, P. Kluit¹²⁰, S. Kluth¹¹⁵, E. Kneringer⁷⁷, E. B. F. G. Knoops¹⁰², A. Knue⁵², D. Kobayashi⁸⁸, T. Kobayashi¹⁶³, M. Kobel⁴⁸, M. Kocian¹⁵³, P. Kodys¹⁴³, P. T. Koenig²⁴, T. Koffas³⁴, N. M. Köhler³⁶, T. Koi¹⁵³, M. Kolb¹⁴⁵, I. Koletsou⁵, T. Komarek¹³¹, T. Kondo⁸², K. Köneke⁵², A. X. Y. Kong¹, A. C. König¹¹⁹, T. Kono¹²⁶, R. Konoplich^{125,aj}, V. Konstantinides⁹⁵, N. Konstantinidis⁹⁵, B. Konya⁹⁷, R. Kopeliansky⁶⁶, S. Koperny^{84a}, K. Korcyl⁸⁵, K. Kordas¹⁶², G. Koren¹⁶¹, A. Korn⁹⁵, I. Korolkov¹⁴, E. V. Korolkova¹⁴⁹, N. Korotkova¹¹³, O. Kortner¹¹⁵, S. Kortner¹¹⁵, T. Kosek¹⁴³, V. V. Kostyukhin^{166,166}, A. Kotskechagia⁶⁵, A. Kotwal⁴⁹, A. Koulouris¹⁰, A. Kourkoumeli-Charalampidi^{71a,71b}, C. Kourkoumelis⁹, E. Kourlitis¹⁴⁹, V. Kouskoura²⁹, A. B. Kowalewska⁸⁵, R. Kowalewski¹⁷⁶, C. Kozakai¹⁶³, W. Kozanecki¹⁴⁵, A. S. Kozhin¹²³, V. A. Kramarenko¹¹³, G. Kramberger⁹², D. Krasnopevtsev^{60a}, M. W. Krasny¹³⁶, A. Krasznahorkay³⁶, D. Krauss¹¹⁵, J. A. Kremer^{84a}, J. Kretzschmar⁹¹, P. Krieger¹⁶⁷, F. Krieter¹¹⁴, A. Krishnan^{61b}, K. Krizka¹⁸, K. Kroeninger⁴⁷, H. Kroha¹¹⁵, J. Kroll¹⁴¹, J. Kroll¹³⁷, K. S. Krowpman¹⁰⁷, J. Krstic¹⁶, U. Kruchonak⁸⁰

H. Krüger²⁴, N. Krumnack⁷⁹, M. C. Kruse⁴⁹, J. A. Krzysiak⁸⁵, T. Kubota¹⁰⁵, O. Kuchinskaia¹⁶⁶, S. Kuday^{4b}, J. T. Kuechler⁴⁶, S. Kuehn³⁶, A. Kugel^{61a}, T. Kuhl⁴⁶, V. Kukhtin⁸⁰, R. Kukla¹⁰², Y. Kulchitsky^{108,ah}, S. Kuleshov^{147c}, Y. P. Kulinich¹⁷³, M. Kuna⁵⁸, T. Kunigo⁸⁶, A. Kupco¹⁴¹, T. Kupfer⁴⁷, O. Kuprash⁵², H. Kurashige⁸³, L. L. Kurchaninov^{168a}, Y. A. Kurochkin¹⁰⁸, A. Kurova¹¹², M. G. Kurth^{15a,15d}, E. S. Kuwertz³⁶, M. Kuze¹⁶⁵, A. K. Kvam¹⁴⁸, J. Kvita¹³¹, T. Kwan¹⁰⁴, A. La Rosa¹¹⁵, L. La Rotonda^{41a,41b}, F. La Ruffa^{41a,41b}, C. Lacasta¹⁷⁴, F. Lacava^{73a,73b}, D. P. J. Lack¹⁰¹, H. Lacker¹⁹, D. Lacour¹³⁶, E. Ladygin⁸⁰, R. Lafaye⁵, B. Laforge¹³⁶, T. Lagouri^{33e}, S. Lai⁵³, I. K. Lakomic^{84a}, S. Lammers⁶⁶, W. Lampl⁷, C. Lampoudis¹⁶², E. Lançon²⁹, U. Landgraf⁵², M. P. J. Landon⁹³, M. C. Lanfermann⁵⁴, V. S. Lang⁴⁶, J. C. Lange⁵³, R. J. Langenberg¹⁰³, A. J. Lankford¹⁷¹, F. Lanni²⁹, K. Lantzsch²⁴, A. Lanza^{71a}, A. Lapertosa^{55a,55b}, S. Laplace¹³⁶, J. F. Laporte¹⁴⁵, T. Lari^{69a}, F. Lasagni Manghi^{23a,23b}, M. Lassnig³⁶, T. S. Lau^{63a}, A. Laudrain⁶⁵, A. Laurier³⁴, M. Lavorgna^{70a,70b}, S. D. Lawlor⁹⁴, M. Lazzaroni^{69a,69b}, B. Le¹⁰⁵, E. Le Guirriec¹⁰², M. LeBlanc⁷, T. LeCompte⁶, F. Ledroit-Guillon⁵⁸, A. C. A. Lee⁹⁵, C. A. Lee²⁹, G. R. Lee¹⁷, L. Lee⁵⁹, S. C. Lee¹⁵⁸, S. J. Lee³⁴, S. Lee⁷⁹, B. Lefebvre^{168a}, H. P. Lefebvre⁹⁴, M. Lefebvre¹⁷⁶, F. Legger¹¹⁴, C. Leggett¹⁸, K. Lehmann¹⁵², N. Lehmann¹⁸², G. Lehmann Miotto³⁶, W. A. Leight⁴⁶, A. Leisos^{162,x}, M. A. L. Leite^{81d}, C. E. Leitgeb¹¹⁴, R. Leitner¹⁴³, D. Lellouch^{180,*}, K. J. C. Leney⁴², T. Lenz²⁴, R. Leone⁷, S. Leone^{72a}, C. Leonidopoulos⁵⁰, A. Leopold¹³⁶, C. Leroy¹¹⁰, R. Les¹⁶⁷, C. G. Lester³², M. Levchenko¹³⁸, J. Levêque⁵, D. Levin¹⁰⁶, L. J. Levinson¹⁸⁰, D. J. Lewis²¹, B. Li^{15b}, B. Li¹⁰⁶, C-Q. Li^{60a}, F. Li^{60c}, H. Li^{60a}, H. Li^{60b}, J. Li^{60c}, K. Li¹⁵³, L. Li^{60c}, M. Li^{15a,15d}, Q. Li^{15a,15d}, Q. Y. Li^{60a}, S. Li^{60c,60d}, X. Li⁴⁶, Y. Li⁴⁶, Z. Li^{60b}, Z. Liang^{15a}, B. Liberti^{74a}, A. Liblong¹⁶⁷, K. Lie^{63c}, S. Lim²⁹, C. Y. Lin³², K. Lin¹⁰⁷, T. H. Lin¹⁰⁰, R. A. Linck⁶⁶, J. H. Lindon²¹, A. L. Lioni⁵⁴, E. Lipeles¹³⁷, A. Lipniacka¹⁷, T. M. Liss^{173,aa}, A. Lister¹⁷⁵, A. M. Litke¹⁴⁶, J. D. Little⁸, B. Liu⁷⁹, B. L. Liu⁶, H. B. Liu²⁹, H. Liu¹⁰⁶, J. B. Liu^{60a}, J. K. K. Liu¹³⁵, K. Liu¹³⁶, M. Liu^{60a}, P. Liu¹⁸, Y. Liu^{15a,15d}, Y. L. Liu¹⁰⁶, Y. W. Liu^{60a}, M. Livan^{71a,71b}, A. Lleres⁵⁸, J. Llorente Merino¹⁵², S. L. Lloyd⁹³, C. Y. Lo^{63b}, F. Lo Sterzo⁴², E. M. Lobodzinska⁴⁶, P. Loch⁷, S. Loffredo^{74a,74b}, T. Lohse¹⁹, K. Lohwasser¹⁴⁹, M. Lokajicek¹⁴¹, J. D. Long¹⁷³, R. E. Long⁹⁰, L. Longo³⁶, K. A. Looper¹²⁷, J. A. Lopez^{147c}, I. Lopez Paz¹⁰¹, A. Lopez Solis¹⁴⁹, J. Lorenz¹¹⁴, N. Lorenzo Martinez⁵, A. M. Lory¹¹⁴, M. Losada²², P. J. Lösel¹¹⁴, A. Lösle⁵², X. Lou⁴⁶, X. Lou^{15a}, A. Lounis⁶⁵, J. Love⁶, P. A. Love⁹⁰, J. J. Lozano Bahilo¹⁷⁴, M. Lu^{60a}, Y. J. Lu⁶⁴, H. J. Lubatti¹⁴⁸, C. Luci^{73a,73b}, A. Lucotte⁵⁸, C. Luedtke⁵², F. Luehring⁶⁶, I. Luise¹³⁶, L. Luminari^{73a}, B. Lund-Jensen¹⁵⁴, M. S. Lutz¹⁰³, D. Lynn²⁹, H. Lyons⁹¹, R. Lysak¹⁴¹, E. Lytken⁹⁷, F. Lyu^{15a}, V. Lyubushkin⁸⁰, T. Lyubushkina⁸⁰, H. Ma²⁹, L. L. Ma^{60b}, Y. Ma^{60b}, G. Maccarrone⁵¹, A. Macchiolo¹¹⁵, C. M. Macdonald¹⁴⁹, J. Machado Miguens¹³⁷, D. Madaffari¹⁷⁴, R. Madar³⁸, W. F. Mader⁴⁸, N. Madysa⁴⁸, J. Maeda⁸³, T. Maeno²⁹, M. Maerker⁴⁸, A. S. Maevskiy¹¹³, V. Magerl⁵², N. Magini⁷⁹, D. J. Mahon³⁹, C. Maidantchik^{81b}, T. Maier¹¹⁴, A. Maio^{140a,140b,140d}, K. Maj^{84a}, O. Majersky^{28a}, S. Majewski¹³², Y. Makida⁸², N. Makovec⁶⁵, B. Malaescu¹³⁶, Pa. Malecki⁸⁵, V. P. Maleev¹³⁸, F. Malek⁵⁸, U. Mallik⁷⁸, D. Malon⁶, C. Malone³², S. Maltezos¹⁰, S. Malyukov⁸⁰, J. Mamuzic¹⁷⁴, G. Mancini⁵¹, I. Mandić⁹², L. Manhaes de Andrade Filho^{81a}, I. M. Maniatis¹⁶², J. Manjarres Ramos⁴⁸, K. H. Mankinen⁹⁷, A. Mann¹¹⁴, A. Manousos⁷⁷, B. Mansoulie¹⁴⁵, I. Manthos¹⁶², S. Manzoni¹²⁰, A. Marantis¹⁶², G. Marceca³⁰, L. Marchese¹³⁵, G. Marchiori¹³⁶, M. Marcisovsky¹⁴¹, L. Maccoccia^{74a,74b}, C. Marcon⁹⁷, C. A. Marin Tobon³⁶, M. Marjanovic¹²⁹, Z. Marshall¹⁸, M. U. F. Martensson¹⁷², S. Marti-Garcia¹⁷⁴, C. B. Martin¹²⁷, T. A. Martin¹⁷⁸, V. J. Martin⁵⁰, B. Martin dit Latour¹⁷, L. Martinelli^{75a,75b}, M. Martinez^{14,z}, V. I. Martinez Outschoorn¹⁰³, S. Martin-Haugh¹⁴⁴, V. S. Martoiu^{27b}, A. C. Martyniuk⁹⁵, A. Marzin³⁶, S. R. Maschek¹¹⁵, L. Masetti¹⁰⁰, T. Mashimo¹⁶³, R. Mashinistov¹¹¹, J. Masik¹⁰¹, A. L. Maslennikov^{122a,122b}, L. Massa^{74a,74b}, P. Massarotti^{70a,70b}, P. Mastrandrea^{72a,72b}, A. Mastroberardino^{41a,41b}, T. Masubuchi¹⁶³, D. Matakias¹⁰, A. Matic¹¹⁴, N. Matsuzawa¹⁶³, P. Mättig²⁴, J. Maurer^{27b}, B. Maček⁹², D. A. Maximov^{122a,122b}, R. Mazini¹⁵⁸, I. Maznas¹⁶², S. M. Mazza¹⁴⁶, S. P. Mc Kee¹⁰⁶, T. G. McCarthy¹¹⁵, W. P. McCormack¹⁸, E. F. McDonald¹⁰⁵, J. A. McFayden³⁶, G. Mchedlidge^{159b}, M. A. McKay⁴², K. D. McLean¹⁷⁶, S. J. McMahon¹⁴⁴, P. C. McNamara¹⁰⁵, C. J. McNicol¹⁷⁸, R. A. McPherson^{176,ae}, J. E. Mdhluli^{33e}, Z. A. Meadows¹⁰³, S. Meehan³⁶, T. Megy⁵², S. Mehlhase¹¹⁴, A. Mehta⁹¹, T. Meideck⁵⁸, B. Meirose⁴³, D. Melini¹⁶⁰, B. R. Mellado Garcia^{33e}, J. D. Mellenthin⁵³, M. Melo^{28a}, F. Meloni⁴⁶, A. Melzer²⁴, S. B. Menary¹⁰¹, E. D. Mendes Gouveia^{140a,140e}, L. Meng³⁶, X. T. Meng¹⁰⁶, S. Menke¹¹⁵, E. Meoni^{41a,41b}, S. Mergelmeyer¹⁹, S. A. M. Merkt¹³⁹, C. Merlassino²⁰, P. Mermod⁵⁴, L. Merola^{70a,70b}, C. Meroni^{69a}, G. Merz¹⁰⁶, O. Meshkov^{113,111}, J. K. R. Meshreki¹⁵¹, A. Messina^{73a,73b}, J. Metcalfe⁶, A. S. Mete¹⁷¹, C. Meyer⁶⁶, J-P. Meyer¹⁴⁵, H. Meyer Zu Theenhausen^{61a}, F. Miano¹⁵⁶, M. Michetti¹⁹, R. P. Middleton¹⁴⁴, L. Mijović⁵⁰, G. Mikenberg¹⁸⁰, M. Mikestikova¹⁴¹, M. Mikuž⁹², H. Mildner¹⁴⁹, M. Milesi¹⁰⁵, A. Milic¹⁶⁷, D. A. Millar⁹³, D. W. Miller³⁷, A. Milov¹⁸⁰, D. A. Milstead^{45a,45b}, R. A. Mina¹⁵³, A. A. Minaenko¹²³, M. Miñano Moya¹⁷⁴, I. A. Minashvili^{159b}, A. I. Mincer¹²⁵, B. Mindur^{84a}, M. Mineev⁸⁰, Y. Minegishi¹⁶³, L. M. Mir¹⁴, A. Mirto^{68a,68b}, K. P. Mistry¹³⁷, T. Mitani¹⁷⁹, J. Mitrevski¹¹⁴, V. A. Mitsou¹⁷⁴, M. Mittal^{60c}, O. Miu¹⁶⁷, A. Miucci²⁰, P. S. Miyagawa¹⁴⁹, A. Mizukami⁸², J. U. Mjörnmark⁹⁷, T. Mkrchyan^{61a}, M. Mlynarikova¹⁴³, T. Moa^{45a,45b}, K. Mochizuki¹¹⁰, P. Mogg⁵², S. Mohapatra³⁹, R. Moles-Valls²⁴, M. C. Mondragon¹⁰⁷, K. Mönig⁴⁶, J. Monk⁴⁰, E. Monnier¹⁰², A. Montalbano¹⁵², J. Montejo Berlingen³⁶, M. Montella⁹⁵, F. Monticelli⁸⁹, S. Monzani^{69a}, N. Morange⁶⁵,

D. Moreno²², M. Moreno Llácer¹⁷⁴, C. Moreno Martinez¹⁴, P. Morettini^{55b}, M. Morgenstern¹²⁰, S. Morgenstern⁴⁸, D. Mori¹⁵², M. Morii⁵⁹, M. Morinaga¹⁷⁹, V. Morisbak¹³⁴, A. K. Morley³⁶, G. Mornacchi³⁶, A. P. Morris⁹⁵, L. Morvaj¹⁵⁵, P. Moschovakos³⁶, B. Moser¹²⁰, M. Mosidze^{159b}, T. Moskalets¹⁴⁵, H. J. Moss¹⁴⁹, J. Moss^{31,m}, E. J. W. Moyses¹⁰³, S. Muanza¹⁰², J. Mueller¹³⁹, R. S. P. Mueller¹¹⁴, D. Muenstermann⁹⁰, G. A. Mullier⁹⁷, D. P. Mungo^{69a,69b}, J. L. Munoz Martinez¹⁴, F. J. Munoz Sanchez¹⁰¹, P. Murin^{28b}, W. J. Murray^{178,144}, A. Murrone^{69a,69b}, M. Muškinja¹⁸, C. Mwewa^{33a}, A. G. Myagkov^{123.ak}, A. A. Myers¹³⁹, J. Myers¹³², M. Myska¹⁴², B. P. Nachman¹⁸, O. Nackenhorst⁴⁷, A. Nag Nag⁴⁸, K. Nagai¹³⁵, K. Nagano⁸², Y. Nagasaka⁶², J. L. Nagle²⁹, E. Nagy¹⁰², A. M. Nairz³⁶, Y. Nakahama¹¹⁷, K. Nakamura⁸², T. Nakamura¹⁶³, I. Nakano¹²⁸, H. Nanjo¹³³, F. Napolitano^{61a}, R. F. Naranjo Garcia⁴⁶, R. Narayan⁴², I. Naryshkin¹³⁸, T. Naumann⁴⁶, G. Navarro²², P. Y. Nechaeva¹¹¹, F. Nechansky⁴⁶, T. J. Neep²¹, A. Negri^{71a,71b}, M. Negrini^{23b}, C. Nellist⁵³, M. E. Nelson^{45a,45b}, S. Nemecek¹⁴¹, P. Nemethy¹²⁵, M. Nessi^{36,d}, M. S. Neubauer¹⁷³, M. Neumann¹⁸², R. Newhouse¹⁷⁵, P. R. Newman²¹, Y. S. Ng¹⁹, Y. W. Y. Ng¹⁷¹, B. Ngair^{35e}, H. D. N. Nguyen¹⁰², T. Nguyen Manh¹¹⁰, E. Nibigira³⁸, R. B. Nickerson¹³⁵, R. Nicolaidou¹⁴⁵, D. S. Nielsen⁴⁰, J. Nielsen¹⁴⁶, N. Nikiporou¹¹, V. Nikolaenko^{123.ak}, I. Nikolic-Audit¹³⁶, K. Nikolopoulos²¹, P. Nilsson²⁹, H. R. Nindhito⁵⁴, Y. Ninomiya⁸², A. Nisati^{73a}, N. Nishu^{60c}, R. Nisius¹¹⁵, I. Nitsche⁴⁷, T. Nitta¹⁷⁹, T. Nobe¹⁶³, Y. Noguchi⁸⁶, I. Nomidis¹³⁶, M. A. Nomura²⁹, M. Nordberg³⁶, N. Norjoharuddeen¹³⁵, T. Novak⁹², O. Novgorodova⁴⁸, R. Novotny¹⁴², L. Nozka¹³¹, K. Ntekas¹⁷¹, E. Nurse⁹⁵, F. G. Oakham^{34.as}, H. Oberlack¹¹⁵, J. Ocariz¹³⁶, A. Ochi⁸³, I. Ochoa³⁹, J. P. Ochoa-Ricoux^{147a}, K. O'Connor²⁶, S. Oda⁸⁸, S. Odaka⁸², S. Oerdek⁵³, A. Ogrodnik^{84a}, A. Oh¹⁰¹, S. H. Oh⁴⁹, C. C. Ohm¹⁵⁴, H. Oide¹⁶⁵, M. L. Ojeda¹⁶⁷, H. Okawa¹⁶⁹, Y. Okazaki⁸⁶, M. W. O'Keefe⁹¹, Y. Okumura¹⁶³, T. Okuyama⁸², A. Olariu^{27b}, L. F. Oleiro Seabra^{140a}, S. A. Olivares Pino^{147a}, D. Oliveira Damazio²⁹, J. L. Oliver¹, M. J. R. Olsson¹⁷¹, A. Olszewski⁸⁵, J. Olszowska⁸⁵, D. C. O'Neil¹⁵², A. P. O'Neill¹³⁵, A. Onofre^{140a,140e}, P. U. E. Onyisi¹¹, H. Oppen¹³⁴, M. J. Oreglia³⁷, G. E. Orellana⁸⁹, D. Orestano^{75a,75b}, N. Orlando¹⁴, R. S. Orr¹⁶⁷, V. O'Shea⁵⁷, R. Ospanov^{60a}, G. Otero y Garzon³⁰, H. Otono⁸⁸, P. S. Ott^{61a}, M. Ouchrif^{35d}, J. Ouellette²⁹, F. Ould-Saada¹³⁴, A. Ouraou¹⁴⁵, Q. Ouyang^{15a}, M. Owen⁵⁷, R. E. Owen²¹, V. E. Ozcan^{12c}, N. Ozturk⁸, J. Pacalt¹³¹, H. A. Pacey³², K. Pachal⁴⁹, A. Pacheco Pages¹⁴, C. Padilla Aranda¹⁴, S. Pagan Griso¹⁸, M. Paganini¹⁸³, G. Palacino⁶⁶, S. Palazzo⁵⁰, S. Palestini³⁶, M. Palka^{84b}, D. Pallin³⁸, I. Panagoulas¹⁰, C. E. Pandini³⁶, J. G. Panduro Vazquez⁹⁴, P. Pani⁴⁶, G. Panizzo^{67a,67c}, L. Paolozzi⁵⁴, C. Papadatos¹¹⁰, K. Papageorgiou^{9.g}, S. Parajuli⁴³, A. Paramonov⁶, D. Paredes Hernandez^{63b}, S. R. Paredes Saenz¹³⁵, B. Parida¹⁶⁶, T. H. Park¹⁶⁷, A. J. Parker³¹, M. A. Parker³², F. Parodi^{55a,55b}, E. W. Parrish¹²¹, J. A. Parsons³⁹, U. Parzefall⁵², L. Pascual Dominguez¹³⁶, V. R. Pascuzzi¹⁶⁷, J. M. P. Pasner¹⁴⁶, F. Pasquali¹²⁰, E. Pasqualucci^{73a}, S. Passaggio^{55b}, F. Pastore⁹⁴, P. Pasuwan^{45a,45b}, S. Pataria¹⁰⁰, J. R. Pater¹⁰¹, A. Pathak^{181.i}, T. Pauly³⁶, J. Parkes¹⁵³, B. Pearson¹¹⁵, M. Pedersen¹³⁴, L. Pedraza Diaz¹¹⁹, R. Pedro^{140a}, T. Peiffer⁵³, S. V. Peleganchuk^{122a,122b}, O. Penc¹⁴¹, H. Peng^{60a}, B. S. Peralva^{81a}, M. M. Perego⁶⁵, A. P. Pereira Peixoto^{140a}, D. V. Perepelitsa²⁹, F. Peri¹⁹, L. Perini^{69a,69b}, H. Pernegger³⁶, S. Perrella^{70a,70b}, A. Perrevoort¹²⁰, K. Peters⁴⁶, R. F. Y. Peters¹⁰¹, B. A. Petersen³⁶, T. C. Petersen⁴⁰, E. Petit¹⁰², A. Petridis¹, C. Petridou¹⁶², P. Petroff⁶⁵, M. Petrov¹³⁵, F. Petrucci^{75a,75b}, M. Pettee¹⁸³, N. E. Pettersson¹⁰³, K. Petukhova¹⁴³, A. Peyaud¹⁴⁵, R. Pezoa^{147c}, L. Pezzotti^{71a,71b}, T. Pham¹⁰⁵, F. H. Phillips¹⁰⁷, P. W. Phillips¹⁴⁴, M. W. Phipps¹⁷³, G. Piacquadio¹⁵⁵, E. Pianori¹⁸, A. Picazio¹⁰³, R. H. Pickles¹⁰¹, R. Piegai³⁰, D. Pietreanu^{27b}, J. E. Pilcher³⁷, A. D. Pilkington¹⁰¹, M. Pinamonti^{67a,67c}, J. L. Pinfold³, M. Pitt¹⁶¹, L. Pizzimento^{74a,74b}, M.-A. Pleier²⁹, V. Pleskot¹⁴³, E. Plotnikova⁸⁰, P. Podberzko^{122a,122b}, R. Poettgen⁹⁷, R. Poggi⁵⁴, L. Poggioli⁶⁵, I. Pogrebnyak¹⁰⁷, D. Pohl²⁴, I. Pokharel⁵³, G. Polesello^{71a}, A. Poley¹⁸, A. Policicchio^{73a,73b}, R. Polifka¹⁴³, A. Polini^{23b}, C. S. Pollard⁴⁶, V. Polychronakos²⁹, D. Ponomarenko¹¹², L. Pontecorvo³⁶, S. Popa^{27a}, G. A. Popeneci^{27d}, L. Portales⁵, D. M. Portillo Quintero⁵⁸, S. Pospisil¹⁴², K. Potamianos⁴⁶, I. N. Potrap⁸⁰, C. J. Potter³², H. Potti¹¹, T. Poulsen⁹⁷, J. Poveda³⁶, T. D. Powell¹⁴⁹, G. Pownall⁴⁶, M. E. Pozo Astigarraga³⁶, P. Pralavorio¹⁰², S. Prell⁷⁹, D. Price¹⁰¹, M. Primavera^{68a}, S. Prince¹⁰⁴, M. L. Proffitt¹⁴⁸, N. Proklova¹¹², K. Prokofiev^{63c}, F. Prokoshin⁸⁰, S. Protopopescu²⁹, J. Proudfoot⁶, M. Przybycien^{84a}, D. Pudza¹³⁸, A. Puri¹⁷³, P. Puzo⁶⁵, J. Qian¹⁰⁶, Y. Qin¹⁰¹, A. Quadt⁵³, M. Queitsch-Maitland³⁶, A. Qureshi¹, M. Racko^{28a}, F. Ragusa^{69a,69b}, G. Rahal⁹⁸, J. A. Raine⁵⁴, S. Rajagopalan²⁹, A. Ramirez Morales⁹³, K. Ran^{15a,15d}, T. Rashid⁶⁵, S. Raspopov⁵, D. M. Rauch⁴⁶, F. Rauscher¹¹⁴, S. Rave¹⁰⁰, B. Ravina¹⁴⁹, I. Ravinovich¹⁸⁰, J. H. Rawling¹⁰¹, M. Raymond³⁶, A. L. Read¹³⁴, N. P. Readoff⁵⁸, M. Reale^{68a,68b}, D. M. Rebuffi^{71a,71b}, A. Redelbach¹⁷⁷, G. Redlinger²⁹, K. Reeves⁴³, L. Rehnisch¹⁹, J. Reichert¹³⁷, D. Reikher¹⁶¹, A. Reiss¹⁰⁰, A. Rej¹⁵¹, C. Rembser³⁶, M. Renda^{27b}, M. Rescigno^{73a}, S. Resconi^{69a}, E. D. Resseguie¹³⁷, S. Rettie¹⁷⁵, B. Reynolds¹²⁷, E. Reynolds²¹, O. L. Rezanova^{122a,122b}, P. Reznicek¹⁴³, E. Ricci^{76a,76b}, R. Richter¹¹⁵, S. Richter⁴⁶, E. Richter-Was^{84b}, O. Ricken²⁴, M. Ridel¹³⁶, P. Rieck¹¹⁵, O. Rifki⁴⁶, M. Rijssenbeek¹⁵⁵, A. Rimoldi^{71a,71b}, M. Rimoldi⁴⁶, L. Rinaldi^{23b}, G. Ripellino¹⁵⁴, I. Riu¹⁴, J. C. Rivera Vergara¹⁷⁶, F. Rizatdinova¹³⁰, E. Rizvi⁹³, C. Rizzi³⁶, R. T. Roberts¹⁰¹, S. H. Robertson^{104.ae}, M. Robin⁴⁶, D. Robinson³², J. E. M. Robinson⁴⁶, C. M. Robles Gajardo^{147c}, A. Robson⁵⁷, A. Rocchi^{74a,74b}, E. Rocco¹⁰⁰, C. Roda^{72a,72b}, S. Rodriguez Bosca¹⁷⁴, A. Rodriguez Perez¹⁴, D. Rodriguez Rodriguez¹⁷⁴, A. M. Rodríguez Vera^{168b}, S. Roe³⁶, O. Røhne¹³⁴, R. Röhrig¹¹⁵, R. A. Rojas^{147c}

C. P. A. Roland⁶⁶, J. Roloff²⁹, A. Romaniouk¹¹², M. Romano^{23a,23b}, N. Rompotis⁹¹, M. Ronzani¹²⁵, L. Roos¹³⁶, S. Rosati^{73a}, G. Rosin¹⁰³, B. J. Rosser¹³⁷, E. Rossi⁴⁶, E. Rossi^{75a,75b}, E. Rossi^{70a,70b}, L. P. Rossi^{55b}, L. Rossini^{69a,69b}, R. Rosten¹⁴, M. Rotaru^{27b}, J. Rothberg¹⁴⁸, D. Rousseau⁶⁵, G. Rovelli^{71a,71b}, A. Roy¹¹, D. Roy^{33e}, A. Rozanov¹⁰², Y. Rozen¹⁶⁰, X. Ruan^{33e}, F. Rühr⁵², A. Ruiz-Martinez¹⁷⁴, A. Rummler³⁶, Z. Rurikova⁵², N. A. Rusakovich⁸⁰, H. L. Russell¹⁰⁴, L. Rustige^{38,47}, J. P. Rutherford⁷, E. M. Rüttinger¹⁴⁹, M. Rybar³⁹, G. Rybkin⁶⁵, E. B. Rye¹³⁴, A. Ryzhov¹²³, J. A. Sabater Iglesias⁴⁶, P. Sabatini⁵³, G. Sabato¹²⁰, S. Sacerdoti⁶⁵, H.F.-W. Sadrozinski¹⁴⁶, R. Sadykov⁸⁰, F. Safai Tehrani^{73a}, B. Safarzadeh Samani¹⁵⁶, P. Saha¹²¹, S. Saha¹⁰⁴, M. Sahinsoy^{61a}, A. Sahu¹⁸², M. Saimpert⁴⁶, M. Saito¹⁶³, T. Saito¹⁶³, H. Sakamoto¹⁶³, A. Sakharov^{125,aj}, D. Salamani⁵⁴, G. Salamanna^{75a,75b}, J. E. Salazar Loyola^{147c}, A. Salnikov¹⁵³, J. Salt¹⁷⁴, D. Salvatore^{41a,41b}, F. Salvatore¹⁵⁶, A. Salvucci^{63a,63b,63c}, A. Salzburger³⁶, J. Samarati³⁶, D. Sammel⁵², D. Sampsonidis¹⁶², D. Sampsonidou¹⁶², J. Sánchez¹⁷⁴, A. Sanchez Pineda^{67a,36,67c}, H. Sandaker¹³⁴, C. O. Sander⁴⁶, I. G. Sanderswood⁹⁰, M. Sandhoff¹⁸², C. Sandoval²², D. P. C. Sankey¹⁴⁴, M. Sannino^{55a,55b}, Y. Sano¹¹⁷, A. Sansoni⁵¹, C. Santoni³⁸, H. Santos^{140a,140b}, S. N. Santpur¹⁸, A. Santra¹⁷⁴, A. Saponov⁸⁰, J. G. Saraiva^{140a,140d}, O. Sasaki⁸², K. Sato¹⁶⁹, F. Sauerburger⁵², E. Sauvan⁵, P. Savard^{167,as}, R. Sawada¹⁶³, C. Sawyer¹⁴⁴, L. Sawyer^{96,ai}, C. Sbarra^{23b}, A. Sbrizzi^{23a}, T. Scanlon⁹⁵, J. Schaarschmidt¹⁴⁸, P. Schacht¹¹⁵, B. M. Schachtner¹¹⁴, D. Schaefer³⁷, L. Schaefer¹³⁷, J. Schaeffer¹⁰⁰, S. Schaepe³⁶, U. Schäfer¹⁰⁰, A. C. Schaffer⁶⁵, D. Schaile¹¹⁴, R. D. Schamberger¹⁵⁵, N. Scharmberg¹⁰¹, V. A. Schegelsky¹³⁸, D. Scheirich¹⁴³, F. Schenck¹⁹, M. Schernau¹⁷¹, C. Schiavi^{55a,55b}, S. Schier¹⁴⁶, L. K. Schildgen²⁴, Z. M. Schillaci²⁶, E. J. Schioppa³⁶, M. Schioppa^{41a,41b}, K. E. Schleicher⁵², S. Schlenker³⁶, K. R. Schmidt-Sommerfeld¹¹⁵, K. Schmieden³⁶, C. Schmitt¹⁰⁰, S. Schmitt⁴⁶, S. Schmitz¹⁰⁰, J. C. Schmoeckel⁴⁶, U. Schnoor⁵², L. Schoeffel¹⁴⁵, A. Schoening^{61b}, P. G. Scholer⁵², E. Schopf¹³⁵, M. Schott¹⁰⁰, J. F. P. Schouwenberg¹¹⁹, J. Schovancova³⁶, S. Schramm⁵⁴, F. Schroeder¹⁸², A. Schulte¹⁰⁰, H.-C. Schultz-Coulon^{61a}, M. Schumacher⁵², B. A. Schumm¹⁴⁶, Ph. Schune¹⁴⁵, A. Schwartzman¹⁵³, T. A. Schwarz¹⁰⁶, Ph. Schwemling¹⁴⁵, R. Schwienhorst¹⁰⁷, A. Sciandra¹⁴⁶, G. Sciolla²⁶, M. Scodreggio⁴⁶, M. Scornajenghi^{41a,41b}, F. Scuri^{72a}, F. Scutti¹⁰⁵, L. M. Scyboz¹¹⁵, C. D. Sebastiani^{73a,73b}, P. Seema¹⁹, S. C. Seidel¹¹⁸, A. Seiden¹⁴⁶, B. D. Seidlitz²⁹, T. Seiss³⁷, J. M. Seixas^{81b}, G. Sekhniaidze^{70a}, K. Sekhon¹⁰⁶, S. J. Sekula⁴², N. Semprini-Cesari^{23a,23b}, S. Sen⁴⁹, C. Serfon⁷⁷, L. Serin⁶⁵, L. Serkin^{67a,67b}, M. Sessa^{60a}, H. Severini¹²⁹, S. Sevova¹⁵³, T. Šfiligoj⁹², F. Sforza^{55a,55b}, A. Sfyrla⁵⁴, E. Shabalina⁵³, J. D. Shahinian¹⁴⁶, N. W. Shaikh^{45a,45b}, D. Shaked Renous¹⁸⁰, L. Y. Shan^{15a}, J. T. Shank²⁵, M. Shapiro¹⁸, A. Sharma¹³⁵, A. S. Sharma¹, P. B. Shatalov¹²⁴, K. Shaw¹⁵⁶, S. M. Shaw¹⁰¹, M. Shehade¹⁸⁰, Y. Shen¹²⁹, A. D. Sherman²⁵, P. Sherwood⁹⁵, L. Shi^{158,ap}, S. Shimizu⁸², C. O. Shimmin¹⁸³, Y. Shimogama¹⁷⁹, M. Shimojima¹¹⁶, I. P. J. Shipsey¹³⁵, S. Shirabe¹⁶⁵, M. Shiyakova^{80,ac}, J. Shlomi¹⁸⁰, A. Shmeleva¹¹¹, M. J. Shochet³⁷, J. Shojaii¹⁰⁵, D. R. Shope¹²⁹, S. Shrestha¹²⁷, E. M. Shrif^{33e}, E. Shulga¹⁸⁰, P. Sicho¹⁴¹, A. M. Sickles¹⁷³, P. E. Sidebo¹⁵⁴, E. Sideras Haddad^{33e}, O. Sidiropoulou³⁶, A. Sidoti^{23a,23b}, F. Siegert⁴⁸, Dj. Sijacki¹⁶, M. Jr. Silva¹⁸¹, M. V. Silva Oliveira^{81a}, S. B. Silverstein^{45a}, S. Simion⁶⁵, R. Simoniello¹⁰⁰, S. Simsek^{12b}, P. Sinervo¹⁶⁷, V. Sinetckii¹¹³, N. B. Sinev¹³², S. Singh¹⁵², M. Sioli^{23a,23b}, I. Siral¹³², S. Yu. Sivoklokov¹¹³, J. Sjölin^{45a,45b}, E. Skorda⁹⁷, P. Skubic¹²⁹, M. Slawinska⁸⁵, K. Sliwa¹⁷⁰, R. Slovak¹⁴³, V. Smakhtin¹⁸⁰, B. H. Smart¹⁴⁴, J. Smiesko^{28a}, N. Smirnov¹¹², S. Yu. Smirnov¹¹², Y. Smirnov¹¹², L. N. Smirnova^{113,u}, O. Smirnova⁹⁷, J. W. Smith⁵³, M. Smizanska⁹⁰, K. Smolek¹⁴², A. Smykiewicz⁸⁵, A. A. Snesarev¹¹¹, H. L. Snoek¹²⁰, I. M. Snyder¹³², S. Snyder²⁹, R. Sobie^{176,ae}, A. Soffer¹⁶¹, A. Sogaard⁵⁰, F. Sohns⁵³, C. A. Solans Sanchez³⁶, E. Yu. Soldatov¹¹², U. Soldevila¹⁷⁴, A. A. Solodkov¹²³, A. Soloshenko⁸⁰, O. V. Solovyanov¹²³, V. Solovyev¹³⁸, P. Sommer¹⁴⁹, H. Son¹⁷⁰, W. Song¹⁴⁴, W. Y. Song^{168b}, A. Sopczak¹⁴², A. L. Sopio⁹⁵, F. Sopkova^{28b}, C. L. Sotiropoulou^{72a,72b}, S. Sottocornola^{71a,71b}, R. Soualah^{67a,67c,f}, A. M. Soukharev^{122a,122b}, D. South⁴⁶, S. Spagnolo^{68a,68b}, M. Spalla¹¹⁵, M. Spangenberg¹⁷⁸, F. Spanò⁹⁴, D. Sperlich⁵², T. M. Spieker^{61a}, R. Spighi^{23b}, G. Spigo³⁶, M. Spina¹⁵⁶, D. P. Spiteri⁵⁷, M. Spousta¹⁴³, A. Stabile^{69a,69b}, B. L. Stamas¹²¹, R. Stamen^{61a}, M. Stamenkovic¹²⁰, E. Stanecka⁸⁵, B. Stanislaus¹³⁵, M. M. Stanitzki⁴⁶, M. Stankaityte¹³⁵, B. Stapf¹²⁰, E. A. Starchenko¹²³, G. H. Stark¹⁴⁶, J. Stark⁵⁸, S. H. Stark⁴⁰, P. Staroba¹⁴¹, P. Starovoitov^{61a}, S. Stärz¹⁰⁴, R. Staszewski⁸⁵, G. Stavropoulos⁴⁴, M. Stegler⁴⁶, P. Steinberg²⁹, A. L. Steinhebel¹³², B. Stelzer¹⁵², H. J. Stelzer¹³⁹, O. Stelzer-Chilton^{168a}, H. Stenzel⁵⁶, T. J. Stevenson¹⁵⁶, G. A. Stewart³⁶, M. C. Stockton³⁶, G. Stoica^{27b}, M. Stolarski^{140a}, S. Stonjek¹¹⁵, A. Straessner⁴⁸, J. Strandberg¹⁵⁴, S. Strandberg^{45a,45b}, M. Strauss¹²⁹, P. Strizenc^{28b}, R. Ströhmer¹⁷⁷, D. M. Strom¹³², R. Stroynowski⁴², A. Strubig⁵⁰, S. A. Stucci²⁹, B. Stugu¹⁷, J. Stupak¹²⁹, N. A. Styles⁴⁶, D. Su¹⁵³, S. Suchek^{61a}, V. V. Sulin¹¹¹, M. J. Sullivan⁹¹, D. M. S. Sultan⁵⁴, S. Sultansoy^{4c}, T. Sumida⁸⁶, S. Sun¹⁰⁶, X. Sun³, K. Suruliz¹⁵⁶, C. J. E. Suster¹⁵⁷, M. R. Sutton¹⁵⁶, S. Suzuki⁸², M. Svatos¹⁴¹, M. Swiatlowski³⁷, S. P. Swift², T. Swirski¹⁷⁷, A. Sydorenko¹⁰⁰, I. Sykora^{28a}, M. Sykora¹⁴³, T. Sykora¹⁴³, D. Ta¹⁰⁰, K. Tackmann^{46,aa}, J. Taenzer¹⁶¹, A. Taffard¹⁷¹, R. Tafirout^{168a}, H. Takai²⁹, R. Takashima⁸⁷, K. Takeda⁸³, T. Takeshita¹⁵⁰, E. P. Takeva⁵⁰, Y. Takubo⁸², M. Talby¹⁰², A. A. Talyshev^{122a,122b}, N. M. Tamir¹⁶¹, J. Tanaka¹⁶³, M. Tanaka¹⁶⁵, R. Tanaka⁶⁵, S. Tapia Araya¹⁷³, S. Tapprogge¹⁰⁰, A. Tarek Abouelfadl Mohamed¹³⁶, S. Tarem¹⁶⁰, K. Tariq^{60b}, G. Tarna^{27b,c}, G. F. Tartarelli^{69a}, P. Tas¹⁴³, M. Tasevsky¹⁴¹, T. Tashiro⁸⁶, E. Tassi^{41a,41b}, A. Tavares Delgado^{140a}, Y. Tayalati^{35e}, A. J. Taylor⁵⁰, G. N. Taylor¹⁰⁵,

W. Taylor^{168b}, A. S. Tee⁹⁰, R. Teixeira De Lima¹⁵³, P. Teixeira-Dias⁹⁴, H. Ten Kate³⁶, J. J. Teoh¹²⁰, S. Terada⁸², K. Terashi¹⁶³, J. Terron⁹⁹, S. Terzo¹⁴, M. Testa⁵¹, R. J. Teuscher^{167,ae}, S. J. Thais¹⁸³, T. Theveneaux-Pelzer⁴⁶, F. Thiele⁴⁰, D. W. Thomas⁹⁴, J. O. Thomas⁴², J. P. Thomas²¹, A. S. Thompson⁵⁷, P. D. Thompson²¹, L. A. Thomsen¹⁸³, E. Thomson¹³⁷, E. J. Thorpe⁹³, R. E. Ticse Torres⁵³, V. O. Tikhomirov^{111,ai}, Yu. A. Tikhonov^{122a,122b}, S. Timoshenko¹¹², P. Tipton¹⁸³, S. Tisserant¹⁰², K. Todome^{23a,23b}, S. Todorova-Nova⁵, S. Todt⁴⁸, J. Tojo⁸⁸, S. Tokár^{28a}, K. Tokushuku⁸², E. Tolley¹²⁷, K. G. Tomiwa^{33e}, M. Tomoto¹¹⁷, L. Tompkins^{153,p}, B. Tong⁵⁹, P. Tornambe¹⁰³, E. Torrence¹³², H. Torres⁴⁸, E. Torró Pastor¹⁴⁸, C. Toscirci¹³⁵, J. Toth^{102,ad}, D. R. Tovey¹⁴⁹, A. Traet¹⁷, C. J. Treado¹²⁵, T. Trefzger¹⁷⁷, F. Tresoldi¹⁵⁶, A. Tricoli²⁹, I. M. Trigger^{168a}, S. Trincaz-Duvoid¹³⁶, D. T. Trischuk¹⁷⁵, W. Trischuk¹⁶⁷, B. Trocme⁵⁸, A. Trofymov¹⁴⁵, C. Troncon^{69a}, M. Trovatelli¹⁷⁶, F. Trovato¹⁵⁶, L. Truong^{33c}, M. Trzebinski⁸⁵, A. Trzupek⁸⁵, F. Tsai⁴⁶, J.C.-L. Tseng¹³⁵, P. V. Tsiarshka^{108,ah}, A. Tsigotis^{162,x}, V. Tsiskaridze¹⁵⁵, E. G. Tskhadadze^{159a}, M. Tsopoulou¹⁶², I. I. Tsukerman¹²⁴, V. Tsulaia¹⁸, S. Tsuno⁸², D. Tsybychev¹⁵⁵, Y. Tu^{63b}, A. Tudorache^{27b}, V. Tudorache^{27b}, T. T. Tulbure^{27a}, A. N. Tuna⁵⁹, S. Turchikhin⁸⁰, D. Turgeman¹⁸⁰, I. Turk Cakir^{4b,v}, R. J. Turner²¹, R. T. Turra^{69a}, P. M. Tuts³⁹, S. Tzamarias¹⁶², E. Tzovara¹⁰⁰, G. Uccielli⁴⁷, K. Uchida¹⁶³, I. Ueda⁸², F. Ukegawa¹⁶⁹, G. Unal³⁶, A. Undrus²⁹, G. Unel¹⁷¹, F. C. Ungaro¹⁰⁵, Y. Unno⁸², K. Uno¹⁶³, J. Urban^{28b}, P. Urquijo¹⁰⁵, G. Usai⁸, Z. Uysal^{12d}, V. Vacek¹⁴², B. Vachon¹⁰⁴, K. O. H. Vadla¹³⁴, A. Vaidya⁹⁵, C. Valderanis¹¹⁴, E. Valdes Santurio^{45a,45b}, M. Valente⁵⁴, S. Valentineti^{23a,23b}, A. Valero¹⁷⁴, L. Valéry⁴⁶, R. A. Vallance²¹, A. Vallier³⁶, J. A. Valls Ferrer¹⁷⁴, T. R. Van Daalen¹⁴, P. Van Gemmeren⁶, I. Van Vulpen¹²⁰, M. Vanadia^{74a,74b}, W. Vandelli³⁶, M. Vandembroucke¹⁴⁵, E. R. Vandewall¹³⁰, A. Vaniachine¹⁶⁶, D. Vannicola^{73a,73b}, R. Vari^{73a}, E. W. Varnes⁷, C. Varni^{55a,55b}, T. Varol¹⁵⁸, D. Varouchas⁶⁵, K. E. Varvell¹⁵⁷, M. E. Vasile^{27b}, G. A. Vasquez¹⁷⁶, F. Vazeille³⁸, D. Vazquez Furelos¹⁴, T. Vazquez Schroeder³⁶, J. Veatch⁵³, V. Vecchio^{75a,75b}, M. J. Veen¹²⁰, L. M. Veloce¹⁶⁷, F. Veloso^{140a,140c}, S. Veneziano^{73a}, A. Ventura^{68a,68b}, N. Venturi³⁶, A. Verbytskyi¹¹⁵, V. Vercesi^{71a}, M. Verducci^{72a,72b}, C. M. Vergel Infante⁷⁹, C. Vergis²⁴, W. Verkerke¹²⁰, A. T. Vermeulen¹²⁰, J. C. Vermeulen¹²⁰, M. C. Vetterli^{152,as}, N. Viaux Maira^{147c}, M. Vicente Barreto Pinto⁵⁴, T. Vickey¹⁴⁹, O. E. Vickey Boeriu¹⁴⁹, G. H. A. Viehhauser¹³⁵, L. Vigani^{61b}, M. Villa^{23a,23b}, M. Villaplana Perez^{69a,69b}, E. Vilucchi⁵¹, M. G. Vincter³⁴, G. S. Virdee²¹, A. Vishwakarma⁴⁶, C. Vittori^{23a,23b}, I. Vivarelli¹⁵⁶, M. Vogel¹⁸², P. Vokac¹⁴², S. E. von Buddenbrock^{33e}, E. Von Toerne²⁴, V. Vorobel¹⁴³, K. Vorobev¹¹², M. Vos¹⁷⁴, J. H. Vosseveld⁹¹, M. Vozak¹⁰¹, N. Vranjes¹⁶, M. Vranjes Milosavljevic¹⁶, V. Vrba¹⁴², M. Vreeswijk¹²⁰, R. Vuillermet³⁶, I. Vukotic³⁷, P. Wagner²⁴, W. Wagner¹⁸², J. Wagner-Kuhr¹¹⁴, S. Wahdan¹⁸², H. Wahlberg⁸⁹, V. M. Walbrecht¹¹⁵, J. Walder⁹⁰, R. Walker¹¹⁴, S. D. Walker⁹⁴, W. Walkowiak¹⁵¹, V. Wallangen^{45a,45b}, A. M. Wang⁵⁹, C. Wang^{60c}, F. Wang¹⁸¹, H. Wang¹⁸, H. Wang³, J. Wang^{63a}, J. Wang¹⁵⁷, J. Wang^{61b}, P. Wang⁴², Q. Wang¹²⁹, R.-J. Wang¹⁰⁰, R. Wang^{60a}, R. Wang⁶, S. M. Wang¹⁵⁸, W. T. Wang^{60a}, W. Wang^{15c}, W. X. Wang^{60a}, Y. Wang^{60a}, Z. Wang^{60c}, C. Wanotayaroj⁴⁶, A. Warburton¹⁰⁴, C. P. Ward³², D. R. Wardrope⁹⁵, N. Warrack⁵⁷, A. Washbrook⁵⁰, A. T. Watson²¹, M. F. Watson²¹, G. Watts¹⁴⁸, B. M. Waugh⁹⁵, A. F. Webb¹¹, S. Webb¹⁰⁰, C. Weber¹⁸³, M. S. Weber²⁰, S. A. Weber³⁴, S. M. Weber^{61a}, A. R. Weidberg¹³⁵, J. Weingarten⁴⁷, M. Weirich¹⁰⁰, C. Weiser⁵², P. S. Wells³⁶, T. Wenaus²⁹, T. Wengler³⁶, S. Wenig³⁶, N. Wermes²⁴, M. D. Werner⁷⁹, M. Wessels^{61a}, T. D. Weston²⁰, K. Whalen¹³², N. L. Whallon¹⁴⁸, A. M. Wharton⁹⁰, A. S. White¹⁰⁶, A. White⁸, M. J. White¹, D. Whiteson¹⁷¹, B. W. Whitmore⁹⁰, W. Wiedenmann¹⁸¹, M. Wielers¹⁴⁴, N. Wieseotte¹⁰⁰, C. Wiglesworth⁴⁰, L. A. M. Wiik-Fuchs⁵², F. Wilk¹⁰¹, H. G. Wilkens³⁶, L. J. Wilkins⁹⁴, H. H. Williams¹³⁷, S. Williams³², C. Willis¹⁰⁷, S. Willocq¹⁰³, J. A. Wilson²¹, I. Wingerter-Seez⁵, E. Winkels¹⁵⁶, F. Winklmeier¹³², O. J. Winston¹⁵⁶, B. T. Winter⁵², M. Wittgen¹⁵³, M. Wobisch⁹⁶, A. Wolf¹⁰⁰, T. M. H. Wolf¹²⁰, R. Wolff¹⁰², R. Wölker¹³⁵, J. Wollrath⁵², M. W. Wolter⁸⁵, H. Wolters^{140a,140c}, V. W. S. Wong¹⁷⁵, N. L. Woods¹⁴⁶, S. D. Worm²¹, B. K. Wosiek⁸⁵, K. W. Woźniak⁸⁵, K. Wraight⁵⁷, S. L. Wu¹⁸¹, X. Wu⁵⁴, Y. Wu^{60a}, T. R. Wyatt¹⁰¹, B. M. Wynne⁵⁰, S. Xella⁴⁰, Z. Xi¹⁰⁶, L. Xia¹⁷⁸, X. Xiao¹⁰⁶, I. Xioidis¹⁵⁶, D. Xu^{15a}, H. Xu^{60a}, L. Xu²⁹, T. Xu¹⁴⁵, W. Xu¹⁰⁶, Z. Xu^{60b}, Z. Xu¹⁵³, B. Yabsley¹⁵⁷, S. Yacoub^{33a}, K. Yajima¹³³, D. P. Yallup⁹⁵, N. Yamaguchi⁸⁸, Y. Yamaguchi¹⁶⁵, A. Yamamoto⁸², M. Yamatani¹⁶³, T. Yamazaki¹⁶³, Y. Yamazaki⁸³, Z. Yan²⁵, H. J. Yang^{60c,60d}, H. T. Yang¹⁸, S. Yang⁷⁸, X. Yang^{60b,58}, Y. Yang¹⁶³, W.-M. Yao¹⁸, Y. C. Yap⁴⁶, Y. Yasu⁸², E. Yatsenko^{60c,60d}, H. Ye^{15c}, J. Ye⁴², S. Ye²⁹, I. Yeletsikh⁸⁰, M. R. Yexley⁹⁰, E. Yigitbasi²⁵, K. Yorita¹⁷⁹, K. Yoshihara¹³⁷, C. J. S. Young³⁶, C. Young¹⁵³, J. Yu⁷⁹, R. Yuan^{60b,h}, X. Yue^{61a}, S. P. Y. Yuen²⁴, M. Zaazoua^{35e}, B. Zabinski⁸⁵, G. Zacharis¹⁰, E. Zaffaroni⁵⁴, J. Zahreddine¹³⁶, A. M. Zaitsev^{123,ak}, T. Zakareishvili^{159b}, N. Zakharchuk³⁴, S. Zambito⁵⁹, D. Zanzi³⁶, D. R. Zaripovas⁵⁷, S. V. ZeiBner⁴⁷, C. Zeitnitz¹⁸², G. Zemaityte¹³⁵, J. C. Zeng¹⁷³, O. Zenin¹²³, T. Ženiš^{28a}, D. Zerwas⁶⁵, M. Zgubič¹³⁵, B. Zhang^{15c}, D. F. Zhang^{15b}, G. Zhang^{15b}, H. Zhang^{15c}, J. Zhang⁶, L. Zhang^{15c}, L. Zhang^{60a}, M. Zhang¹⁷³, R. Zhang¹⁸¹, S. Zhang¹⁰⁶, X. Zhang^{60b}, Y. Zhang^{15a,15d}, Z. Zhang^{63a}, Z. Zhang⁶⁵, P. Zhao⁴⁹, Y. Zhao^{60b}, Z. Zhao^{60a}, A. Zhemchugov⁸⁰, Z. Zheng¹⁰⁶, D. Zhong¹⁷³, B. Zhou¹⁰⁶, C. Zhou¹⁸¹, M. S. Zhou^{15a,15d}, M. Zhou¹⁵⁵, N. Zhou^{60c}, Y. Zhou⁷, C. G. Zhu^{60b}, C. Zhu^{15a,15d}, H. L. Zhu^{60a}, H. Zhu^{15a}, J. Zhu¹⁰⁶, Y. Zhu^{60a}, X. Zhuang^{15a}, K. Zhukov¹¹¹, V. Zhulanov^{122a,122b}, D. Zieminska⁶⁶, N. I. Zimine⁸⁰, S. Zimmermann⁵², Z. Zinonos¹¹⁵, M. Ziolkowski¹⁵¹, L. Živković¹⁶, G. Zobernig¹⁸¹, A. Zoccoli^{23a,23b}, K. Zoch⁵³, T. G. Zorbass¹⁴⁹, R. Zou³⁷, L. Zwalinski³⁶

- ¹ Department of Physics, University of Adelaide, Adelaide, Australia
- ² Physics Department, SUNY Albany, Albany, NY, USA
- ³ Department of Physics, University of Alberta, Edmonton, AB, Canada
- ⁴ (a)Department of Physics, Ankara University, Ankara, Turkey; (b)Istanbul Aydin University, Istanbul, Turkey; (c)Division of Physics, TOBB University of Economics and Technology, Ankara, Turkey
- ⁵ LAPP, Université Grenoble Alpes, Université Savoie Mont Blanc, CNRS/IN2P3, Annecy, France
- ⁶ High Energy Physics Division, Argonne National Laboratory, Argonne, IL, USA
- ⁷ Department of Physics, University of Arizona, Tucson, AZ, USA
- ⁸ Department of Physics, University of Texas at Arlington, Arlington, TX, USA
- ⁹ Physics Department, National and Kapodistrian University of Athens, Athens, Greece
- ¹⁰ Physics Department, National Technical University of Athens, Zografou, Greece
- ¹¹ Department of Physics, University of Texas at Austin, Austin, TX, USA
- ¹² (a)Bahcesehir University Faculty of Engineering and Natural Sciences, Istanbul, Turkey; (b)Istanbul Bilgi University, Faculty of Engineering and Natural Sciences, Istanbul, Turkey; (c)Department of Physics, Bogazici University, Istanbul, Turkey; (d)Department of Physics Engineering, Gaziantep University, Gaziantep, Turkey
- ¹³ Institute of Physics, Azerbaijan Academy of Sciences, Baku, Azerbaijan
- ¹⁴ Institut de Física d'Altes Energies (IFAE), Barcelona Institute of Science and Technology, Barcelona, Spain
- ¹⁵ (a)Institute of High Energy Physics, Chinese Academy of Sciences, Beijing, China; (b)Physics Department, Tsinghua University, Beijing, China; (c)Department of Physics, Nanjing University, Nanjing, China; (d)University of Chinese Academy of Science (UCAS), Beijing, China
- ¹⁶ Institute of Physics, University of Belgrade, Belgrade, Serbia
- ¹⁷ Department for Physics and Technology, University of Bergen, Bergen, Norway
- ¹⁸ Physics Division, Lawrence Berkeley National Laboratory and University of California, Berkeley, CA, USA
- ¹⁹ Institut für Physik, Humboldt Universität zu Berlin, Berlin, Germany
- ²⁰ Albert Einstein Center for Fundamental Physics and Laboratory for High Energy Physics, University of Bern, Bern, Switzerland
- ²¹ School of Physics and Astronomy, University of Birmingham, Birmingham, UK
- ²² Facultad de Ciencias y Centro de Investigaciones, Universidad Antonio Nariño, Bogota, Colombia
- ²³ (a)Dipartimento di Fisica, INFN Bologna and Università di Bologna, Bologna, Italy; (b)INFN Sezione di Bologna, Bologna, Italy
- ²⁴ Physikalisches Institut, Universität Bonn, Bonn, Germany
- ²⁵ Department of Physics, Boston University, Boston, MA, USA
- ²⁶ Department of Physics, Brandeis University, Waltham, MA, USA
- ²⁷ (a)Transilvania University of Brasov, Brasov, Romania; (b)Horia Hulubei National Institute of Physics and Nuclear Engineering, Bucharest, Romania; (c)Department of Physics, Alexandru Ioan Cuza University of Iasi, Iasi, Romania; (d)National Institute for Research and Development of Isotopic and Molecular Technologies, Physics Department, Cluj-Napoca, Romania; (e)University Politehnica Bucharest, Bucharest, Romania; (f)West University in Timisoara, Timisoara, Romania
- ²⁸ (a)Faculty of Mathematics, Physics and Informatics, Comenius University, Bratislava, Slovakia; (b)Department of Subnuclear Physics, Institute of Experimental Physics of the Slovak Academy of Sciences, Kosice, Slovak Republic
- ²⁹ Physics Department, Brookhaven National Laboratory, Upton, NY, USA
- ³⁰ Departamento de Física, Universidad de Buenos Aires, Buenos Aires, Argentina
- ³¹ California State University, Long Beach, CA, USA
- ³² Cavendish Laboratory, University of Cambridge, Cambridge, UK
- ³³ (a)Department of Physics, University of Cape Town, Cape Town, South Africa; (b)iThemba Labs, Western Cape, South Africa; (c)Department of Mechanical Engineering Science, University of Johannesburg, Johannesburg, South Africa; (d)University of South Africa, Department of Physics, Pretoria, South Africa; (e)School of Physics, University of the Witwatersrand, Johannesburg, South Africa
- ³⁴ Department of Physics, Carleton University, Ottawa, ON, Canada
- ³⁵ (a)Faculté des Sciences Ain Chock, Réseau Universitaire de Physique des Hautes Energies, Université Hassan II, Casablanca, Morocco; (b)Faculté des Sciences, Université Ibn-Tofail, Kénitra, Morocco; (c)Faculté des Sciences Semlalia, Université Cadi Ayyad, LPHEA-Marrakech, Marrakesh, Morocco; (d)Faculté des Sciences, Université Mohamed Premier and LPTPM, Oujda, Morocco; (e)Faculté des sciences, Université Mohammed V, Rabat, Morocco

- ³⁶ CERN, Geneva, Switzerland
- ³⁷ Enrico Fermi Institute, University of Chicago, Chicago, IL, USA
- ³⁸ LPC, Université Clermont Auvergne, CNRS/IN2P3, Clermont-Ferrand, France
- ³⁹ Nevis Laboratory, Columbia University, Irvington, NY, USA
- ⁴⁰ Niels Bohr Institute, University of Copenhagen, Copenhagen, Denmark
- ⁴¹ ^(a)Dipartimento di Fisica, Università della Calabria, Rende, Italy; ^(b)INFN Gruppo Collegato di Cosenza, Laboratori Nazionali di Frascati, Frascati, Italy
- ⁴² Physics Department, Southern Methodist University, Dallas, TX, USA
- ⁴³ Physics Department, University of Texas at Dallas, Richardson, TX, USA
- ⁴⁴ National Centre for Scientific Research “Demokritos”, Agia Paraskevi, Greece
- ⁴⁵ ^(a)Department of Physics, Stockholm University, Stockholm, Sweden; ^(b)Oskar Klein Centre, Stockholm, Sweden
- ⁴⁶ Deutsches Elektronen-Synchrotron DESY, Hamburg and Zeuthen, Germany
- ⁴⁷ Lehrstuhl für Experimentelle Physik IV, Technische Universität Dortmund, Dortmund, Germany
- ⁴⁸ Institut für Kern- und Teilchenphysik, Technische Universität Dresden, Dresden, Germany
- ⁴⁹ Department of Physics, Duke University, Durham, NC, USA
- ⁵⁰ SUPA-School of Physics and Astronomy, University of Edinburgh, Edinburgh, UK
- ⁵¹ INFN e Laboratori Nazionali di Frascati, Frascati, Italy
- ⁵² Physikalisches Institut, Albert-Ludwigs-Universität Freiburg, Freiburg, Germany
- ⁵³ II. Physikalisches Institut, Georg-August-Universität Göttingen, Göttingen, Germany
- ⁵⁴ Département de Physique Nucléaire et Corpusculaire, Université de Genève, Geneva, Switzerland
- ⁵⁵ ^(a)Dipartimento di Fisica, Università di Genova, Genoa, Italy; ^(b)INFN Sezione di Genova, Genoa, Italy
- ⁵⁶ II. Physikalisches Institut, Justus-Liebig-Universität Giessen, Giessen, Germany
- ⁵⁷ SUPA-School of Physics and Astronomy, University of Glasgow, Glasgow, UK
- ⁵⁸ LPSC, Université Grenoble Alpes, CNRS/IN2P3, Grenoble INP, Grenoble, France
- ⁵⁹ Laboratory for Particle Physics and Cosmology, Harvard University, Cambridge, MA, USA
- ⁶⁰ ^(a)Department of Modern Physics and State Key Laboratory of Particle Detection and Electronics, University of Science and Technology of China, Hefei, China; ^(b)Institute of Frontier and Interdisciplinary Science and Key Laboratory of Particle Physics and Particle Irradiation (MOE), Shandong University, Qingdao, China; ^(c)School of Physics and Astronomy, Shanghai Jiao Tong University, KLPPAC-MoE, SKLPPC, Shanghai, China; ^(d)Tsung-Dao Lee Institute, Shanghai, China
- ⁶¹ ^(a)Kirchhoff-Institut für Physik, Ruprecht-Karls-Universität Heidelberg, Heidelberg, Germany; ^(b)Physikalisches Institut, Ruprecht-Karls-Universität Heidelberg, Heidelberg, Germany
- ⁶² Faculty of Applied Information Science, Hiroshima Institute of Technology, Hiroshima, Japan
- ⁶³ ^(a)Department of Physics, Chinese University of Hong Kong, Shatin, N.T., Hong Kong; ^(b)Department of Physics, University of Hong Kong, Pok Fu Lam, Hong Kong; ^(c)Department of Physics and Institute for Advanced Study, Hong Kong University of Science and Technology, Clear Water Bay, Kowloon, Hong Kong, China
- ⁶⁴ Department of Physics, National Tsing Hua University, Hsinchu, Taiwan
- ⁶⁵ IJCLab, Université Paris-Saclay, CNRS/IN2P3, 91405 Orsay, France
- ⁶⁶ Department of Physics, Indiana University, Bloomington, IN, USA
- ⁶⁷ ^(a)INFN Gruppo Collegato di Udine, Sezione di Trieste, Udine, Italy; ^(b)ICTP, Trieste, Italy; ^(c)Dipartimento Politecnico di Ingegneria e Architettura, Università di Udine, Udine, Italy
- ⁶⁸ ^(a)INFN Sezione di Lecce, Lecce, Italy; ^(b)Dipartimento di Matematica e Fisica, Università del Salento, Lecce, Italy
- ⁶⁹ ^(a)INFN Sezione di Milano, Milan, Italy; ^(b)Dipartimento di Fisica, Università di Milano, Milan, Italy
- ⁷⁰ ^(a)INFN Sezione di Napoli, Naples, Italy; ^(b)Dipartimento di Fisica, Università di Napoli, Naples, Italy
- ⁷¹ ^(a)INFN Sezione di Pavia, Pavia, Italy; ^(b)Dipartimento di Fisica, Università di Pavia, Pavia, Italy
- ⁷² ^(a)INFN Sezione di Pisa, Pisa, Italy; ^(b)Dipartimento di Fisica E. Fermi, Università di Pisa, Pisa, Italy
- ⁷³ ^(a)INFN Sezione di Roma, Rome, Italy; ^(b)Dipartimento di Fisica, Sapienza Università di Roma, Rome, Italy
- ⁷⁴ ^(a)INFN Sezione di Roma Tor Vergata, Rome, Italy; ^(b)Dipartimento di Fisica, Università di Roma Tor Vergata, Rome, Italy
- ⁷⁵ ^(a)INFN Sezione di Roma Tre, Rome, Italy; ^(b)Dipartimento di Matematica e Fisica, Università Roma Tre, Rome, Italy
- ⁷⁶ ^(a)INFN-TIFPA, Povo, Italy; ^(b)Università degli Studi di Trento, Trento, Italy
- ⁷⁷ Institut für Astro- und Teilchenphysik, Leopold-Franzens-Universität, Innsbruck, Austria
- ⁷⁸ University of Iowa, Iowa City, IA, USA

- ⁷⁹ Department of Physics and Astronomy, Iowa State University, Ames, IA, USA
- ⁸⁰ Joint Institute for Nuclear Research, Dubna, Russia
- ⁸¹ ^(a)Departamento de Engenharia Elétrica, Universidade Federal de Juiz de Fora (UFJF), Juiz de Fora, Brazil; ^(b)Universidade Federal do Rio De Janeiro COPPE/EE/IF, Rio de Janeiro, Brazil; ^(c)Universidade Federal de São João del Rei (UFSJ), São João del Rei, Brazil; ^(d)Instituto de Física, Universidade de São Paulo, São Paulo, Brazil
- ⁸² KEK, High Energy Accelerator Research Organization, Tsukuba, Japan
- ⁸³ Graduate School of Science, Kobe University, Kobe, Japan
- ⁸⁴ ^(a)AGH University of Science and Technology, Faculty of Physics and Applied Computer Science, Kraków, Poland; ^(b)Marian Smoluchowski Institute of Physics, Jagiellonian University, Kraków, Poland
- ⁸⁵ Institute of Nuclear Physics Polish Academy of Sciences, Kraków, Poland
- ⁸⁶ Faculty of Science, Kyoto University, Kyoto, Japan
- ⁸⁷ Kyoto University of Education, Kyoto, Japan
- ⁸⁸ Research Center for Advanced Particle Physics and Department of Physics, Kyushu University, Fukuoka, Japan
- ⁸⁹ Instituto de Física La Plata, Universidad Nacional de La Plata and CONICET, La Plata, Argentina
- ⁹⁰ Physics Department, Lancaster University, Lancaster, UK
- ⁹¹ Oliver Lodge Laboratory, University of Liverpool, Liverpool, UK
- ⁹² Department of Experimental Particle Physics, Jožef Stefan Institute and Department of Physics, University of Ljubljana, Ljubljana, Slovenia
- ⁹³ School of Physics and Astronomy, Queen Mary University of London, London, UK
- ⁹⁴ Department of Physics, Royal Holloway University of London, Egham, UK
- ⁹⁵ Department of Physics and Astronomy, University College London, London, UK
- ⁹⁶ Louisiana Tech University, Ruston, LA, USA
- ⁹⁷ Fysiska institutionen, Lunds universitet, Lund, Sweden
- ⁹⁸ Centre de Calcul de l'Institut National de Physique Nucléaire et de Physique des Particules (IN2P3), Villeurbanne, France
- ⁹⁹ Departamento de Física Teórica C-15 and CIAFF, Universidad Autónoma de Madrid, Madrid, Spain
- ¹⁰⁰ Institut für Physik, Universität Mainz, Mainz, Germany
- ¹⁰¹ School of Physics and Astronomy, University of Manchester, Manchester, UK
- ¹⁰² CPPM, Aix-Marseille Université, CNRS/IN2P3, Marseille, France
- ¹⁰³ Department of Physics, University of Massachusetts, Amherst, MA, USA
- ¹⁰⁴ Department of Physics, McGill University, Montreal, QC, Canada
- ¹⁰⁵ School of Physics, University of Melbourne, Melbourne, VIC, Australia
- ¹⁰⁶ Department of Physics, University of Michigan, Ann Arbor, MI, USA
- ¹⁰⁷ Department of Physics and Astronomy, Michigan State University, East Lansing, MI, USA
- ¹⁰⁸ B.I. Stepanov Institute of Physics, National Academy of Sciences of Belarus, Minsk, Belarus
- ¹⁰⁹ Research Institute for Nuclear Problems of Byelorussian State University, Minsk, Belarus
- ¹¹⁰ Group of Particle Physics, University of Montreal, Montreal, QC, Canada
- ¹¹¹ P.N. Lebedev Physical Institute of the Russian Academy of Sciences, Moscow, Russia
- ¹¹² National Research Nuclear University MEPhI, Moscow, Russia
- ¹¹³ D.V. Skobel'syn Institute of Nuclear Physics, M.V. Lomonosov Moscow State University, Moscow, Russia
- ¹¹⁴ Fakultät für Physik, Ludwig-Maximilians-Universität München, Munich, Germany
- ¹¹⁵ Max-Planck-Institut für Physik (Werner-Heisenberg-Institut), Munich, Germany
- ¹¹⁶ Nagasaki Institute of Applied Science, Nagasaki, Japan
- ¹¹⁷ Graduate School of Science and Kobayashi-Maskawa Institute, Nagoya University, Nagoya, Japan
- ¹¹⁸ Department of Physics and Astronomy, University of New Mexico, Albuquerque, NM, USA
- ¹¹⁹ Institute for Mathematics, Astrophysics and Particle Physics, Radboud University Nijmegen/Nikhef, Nijmegen, The Netherlands
- ¹²⁰ Nikhef National Institute for Subatomic Physics and University of Amsterdam, Amsterdam, The Netherlands
- ¹²¹ Department of Physics, Northern Illinois University, DeKalb, IL, USA
- ¹²² ^(a)Budker Institute of Nuclear Physics and NSU, SB RAS, Novosibirsk, Russia; ^(b)Novosibirsk State University Novosibirsk, Novosibirsk, Russia
- ¹²³ Institute for High Energy Physics of the National Research Centre Kurchatov Institute, Protvino, Russia

- 124 Institute for Theoretical and Experimental Physics named by A.I. Alikhanov of National Research Centre “Kurchatov Institute”, Moscow, Russia
- 125 Department of Physics, New York University, New York, NY, USA
- 126 Ochanomizu University, Otsuka, Bunkyo-ku, Tokyo, Japan
- 127 Ohio State University, Columbus, OH, USA
- 128 Faculty of Science, Okayama University, Okayama, Japan
- 129 Homer L. Dodge Department of Physics and Astronomy, University of Oklahoma, Norman, OK, USA
- 130 Department of Physics, Oklahoma State University, Stillwater, OK, USA
- 131 Palacký University, RCPTM, Joint Laboratory of Optics, Olomouc, Czech Republic
- 132 Center for High Energy Physics, University of Oregon, Eugene, OR, USA
- 133 Graduate School of Science, Osaka University, Osaka, Japan
- 134 Department of Physics, University of Oslo, Oslo, Norway
- 135 Department of Physics, Oxford University, Oxford, UK
- 136 LPNHE, Sorbonne Université, Université de Paris, CNRS/IN2P3, Paris, France
- 137 Department of Physics, University of Pennsylvania, Philadelphia, PA, USA
- 138 Konstantinov Nuclear Physics Institute of National Research Centre “Kurchatov Institute”, PNPI, St. Petersburg, Russia
- 139 Department of Physics and Astronomy, University of Pittsburgh, Pittsburgh, PA, USA
- 140 ^(a)Laboratório de Instrumentação e Física Experimental de Partículas - LIP, Lisbon, Portugal; ^(b)Departamento de Física, Faculdade de Ciências, Universidade de Lisboa, Lisbon, Portugal; ^(c)Departamento de Física, Universidade de Coimbra, Coimbra, Portugal; ^(d)Centro de Física Nuclear da Universidade de Lisboa, Lisbon, Portugal; ^(e)Departamento de Física, Universidade do Minho, Braga, Portugal; ^(f)Departamento de Física Teórica y del Cosmos, Universidad de Granada, Granada, Spain; ^(g)Dep Física and CEFITEC of Faculdade de Ciências e Tecnologia, Universidade Nova de Lisboa, Caparica, Portugal; ^(h)Instituto Superior Técnico, Universidade de Lisboa, Lisbon, Portugal
- 141 Institute of Physics of the Czech Academy of Sciences, Prague, Czech Republic
- 142 Czech Technical University in Prague, Prague, Czech Republic
- 143 Charles University, Faculty of Mathematics and Physics, Prague, Czech Republic
- 144 Particle Physics Department, Rutherford Appleton Laboratory, Didcot, UK
- 145 IRFU, CEA, Université Paris-Saclay, Gif-sur-Yvette, France
- 146 Santa Cruz Institute for Particle Physics, University of California Santa Cruz, Santa Cruz, CA, USA
- 147 ^(a)Departamento de Física, Pontificia Universidad Católica de Chile, Santiago, Chile; ^(b)Universidad Andres Bello, Department of Physics, Santiago, Chile; ^(c)Departamento de Física, Universidad Técnica Federico Santa María, Valparaíso, Chile
- 148 Department of Physics, University of Washington, Seattle, WA, USA
- 149 Department of Physics and Astronomy, University of Sheffield, Sheffield, UK
- 150 Department of Physics, Shinshu University, Nagano, Japan
- 151 Department Physik, Universität Siegen, Siegen, Germany
- 152 Department of Physics, Simon Fraser University, Burnaby, BC, Canada
- 153 SLAC National Accelerator Laboratory, Stanford, CA, USA
- 154 Physics Department, Royal Institute of Technology, Stockholm, Sweden
- 155 Departments of Physics and Astronomy, Stony Brook University, Stony Brook, NY, USA
- 156 Department of Physics and Astronomy, University of Sussex, Brighton, UK
- 157 School of Physics, University of Sydney, Sydney, Australia
- 158 Institute of Physics, Academia Sinica, Taipei, Taiwan
- 159 ^(a)E. Andronikashvili Institute of Physics, Iv. Javakhishvili Tbilisi State University, Tbilisi, Georgia; ^(b)High Energy Physics Institute, Tbilisi State University, Tbilisi, Georgia
- 160 Department of Physics, Technion, Israel Institute of Technology, Haifa, Israel
- 161 Raymond and Beverly Sackler School of Physics and Astronomy, Tel Aviv University, Tel Aviv, Israel
- 162 Department of Physics, Aristotle University of Thessaloniki, Thessaloniki, Greece
- 163 International Center for Elementary Particle Physics and Department of Physics, University of Tokyo, Tokyo, Japan
- 164 Graduate School of Science and Technology, Tokyo Metropolitan University, Tokyo, Japan
- 165 Department of Physics, Tokyo Institute of Technology, Tokyo, Japan
- 166 Tomsk State University, Tomsk, Russia
- 167 Department of Physics, University of Toronto, Toronto, ON, Canada

- 168 (a) TRIUMF, Vancouver, BC, Canada; (b) Department of Physics and Astronomy, York University, Toronto, ON, Canada
- 169 Division of Physics and Tomonaga Center for the History of the Universe, Faculty of Pure and Applied Sciences, University of Tsukuba, Tsukuba, Japan
- 170 Department of Physics and Astronomy, Tufts University, Medford, MA, USA
- 171 Department of Physics and Astronomy, University of California Irvine, Irvine, CA, USA
- 172 Department of Physics and Astronomy, University of Uppsala, Uppsala, Sweden
- 173 Department of Physics, University of Illinois, Urbana, IL, USA
- 174 Instituto de Física Corpuscular (IFIC), Centro Mixto Universidad de Valencia - CSIC, Valencia, Spain
- 175 Department of Physics, University of British Columbia, Vancouver, BC, Canada
- 176 Department of Physics and Astronomy, University of Victoria, Victoria, BC, Canada
- 177 Fakultät für Physik und Astronomie, Julius-Maximilians-Universität Würzburg, Würzburg, Germany
- 178 Department of Physics, University of Warwick, Coventry, UK
- 179 Waseda University, Tokyo, Japan
- 180 Department of Particle Physics, Weizmann Institute of Science, Rehovot, Israel
- 181 Department of Physics, University of Wisconsin, Madison, WI, USA
- 182 Fakultät für Mathematik und Naturwissenschaften, Fachgruppe Physik, Bergische Universität Wuppertal, Wuppertal, Germany
- 183 Department of Physics, Yale University, New Haven, CT, USA
- ^a Also at Borough of Manhattan Community College, City University of New York, New York, NY, United States of America
- ^b Also at CERN, Geneva, Switzerland
- ^c Also at CPPM, Aix-Marseille Université, CNRS/IN2P3, Marseille, France
- ^d Also at Département de Physique Nucléaire et Corpusculaire, Université de Genève, Geneva, Switzerland
- ^e Also at Departament de Física de la Universitat Autònoma de Barcelona, Barcelona, Spain
- ^f Also at Department of Applied Physics and Astronomy, University of Sharjah, Sharjah, United Arab Emirates
- ^g Also at Department of Financial and Management Engineering, University of the Aegean, Chios, Greece
- ^h Also at Department of Physics and Astronomy, Michigan State University, East Lansing, MI, USA
- ⁱ Also at Department of Physics and Astronomy, University of Louisville, Louisville, KY, USA
- ^j Also at Department of Physics, Ben Gurion University of the Negev, Beer Sheva, Israel
- ^k Also at Department of Physics, California State University, East Bay, USA
- ^l Also at Department of Physics, California State University, Fresno, USA
- ^m Also at Department of Physics, California State University, Sacramento, USA
- ⁿ Also at Department of Physics, King's College London, London, UK
- ^o Also at Department of Physics, St. Petersburg State Polytechnical University, St. Petersburg, Russia
- ^p Also at Department of Physics, Stanford University, Stanford, CA, USA
- ^q Also at Department of Physics, University of Adelaide, Adelaide, Australia
- ^r Also at Department of Physics, University of Fribourg, Fribourg, Switzerland
- ^s Also at Department of Physics, University of Michigan, Ann Arbor, MI, USA
- ^t Also at Dipartimento di Matematica, Informatica e Fisica, Università di Udine, Udine, Italy
- ^u Also at Faculty of Physics, M.V. Lomonosov Moscow State University, Moscow, Russia
- ^v Also at Giresun University, Faculty of Engineering, Giresun, Turkey
- ^w Also at Graduate School of Science, Osaka University, Osaka, Japan
- ^x Also at Hellenic Open University, Patras, Greece
- ^y Also at IJCLab, Université Paris-Saclay, CNRS/IN2P3, 91405, Orsay, France
- ^z Also at Institutio Catalana de Recerca i Estudis Avancats, ICREA, Barcelona, Spain
- ^{aa} Also at Institut für Experimentalphysik, Universität Hamburg, Hamburg, Germany
- ^{ab} Also at Institute for Mathematics, Astrophysics and Particle Physics, Radboud University Nijmegen/Nikhef, Nijmegen, The Netherlands
- ^{ac} Also at Institute for Nuclear Research and Nuclear Energy (INRNE) of the Bulgarian Academy of Sciences, Sofia, Bulgaria
- ^{ad} Also at Institute for Particle and Nuclear Physics, Wigner Research Centre for Physics, Budapest, Hungary
- ^{ae} Also at Institute of Particle Physics (IPP), Vancouver, Canada

- ^{af} Also at Institute of Physics, Azerbaijan Academy of Sciences, Baku, Azerbaijan
- ^{ag} Also at Instituto de Fisica Teorica, IFT-UAM/CSIC, Madrid, Spain
- ^{ah} Also at Joint Institute for Nuclear Research, Dubna, Russia
- ^{ai} Also at Louisiana Tech University, Ruston, LA, USA
- ^{aj} Also at Manhattan College, New York, NY, USA
- ^{ak} Also at Moscow Institute of Physics and Technology State University, Dolgoprudny, Russia
- ^{al} Also at National Research Nuclear University MEPhI, Moscow, Russia
- ^{am} Also at Physics Department, An-Najah National University, Nablus, Palestine
- ^{an} Also at Physics Dept, University of South Africa, Pretoria, South Africa
- ^{ao} Also at Physikalisches Institut, Albert-Ludwigs-Universität Freiburg, Freiburg, Germany
- ^{ap} Also at School of Physics, Sun Yat-sen University, Guangzhou, China
- ^{aq} Also at The City College of New York, New York, NY, USA
- ^{ar} Also at Tomsk State University, Tomsk, and Moscow Institute of Physics and Technology State University, Dolgoprudny, Russia
- ^{as} Also at TRIUMF, Vancouver, BC, Canada
- ^{at} Also at Universita di Napoli Parthenope, Naples, Italy
- *Deceased